Analysis of the indoor environment in a room with diffuse ceiling ventilation

Master Thesis
Department of Civil Engineering
Aalborg Universitey
8th of June 2018

Georgios Christodoulou
Marius Kubilius
Rune Baldur Kessler Andersen

Long Master thesis in Indoor Environmental and Energy Engineering
Department of Civil Engineering
Thomas Manns Vej 23
9220 Aalborg SV
http://civil.aau.dk/

Title:

Analysis of the indoor environment in a room with diffuse ceiling ventilation

Project type:

Long Master thesis

Project period:

September 2017 - June 2018

Project group:

IEEE Master group - GMR

Authors:

Georgios Christodoulou
Marius Kubilius
Rune Baldur Kessler Andersen

Supervisors:

Per Kvols Heiselberg & Chen Zhang

Page nr: 179
Appendix: 21
Completed:08-06-2018

Synopsis:

This report focuses on analysis of the indoor environment quality with diffuse ceiling ventilation in a room with varying heat load distribution, pollutant source position and ventilation flow rates.

Report is mainly divided into two parts: "Experimetal setup and measurements" and "Numerical model results".

In the first part the experimental setup of the measurements is explained. A detailed presentation of measurement points, variables that are measured is presented. List of planned experiments is laid down together with each case boundary conditions. Finally, results of each measurement is presented and analysed regarding the indoor environment quality.

Second part of the thesis is an evaluation of numerical model results compared with the experimental data. It is tried to analyse whether the numerical model can precisely estimate the measured data in the laboratory by using CFD simulations on a 3D model which represents the real geometry of the room in the laboratory.

Abstract

The aim of this project is to perform an evaluation of indoor environment quality with diffuse ceiling ventilation regarding the atmospheric and thermal comfort. Report consists of two main parts : experimental analysis and numerical analysis of indoor environment quality.

During the experimental analysis it was confirmed that diffuse ceiling ventilation can provide acceptable thermal and atmospheric comfort in the room. Present and previous studies showed that while comparing novel air distribution system to the conventional systems more uniform temperature distributions, smaller vertical temperature gradients and draught free conditions in the occupied zone can be achieved. Furthermore, while varying the position of pollutant source, air change rates and heat load distribution in the room different patterns of contamination distributions were observed. These changes also had an influence on local air quality index and contaminant removal coefficient in the occupied zone.

Numerical analysis and comparison between experimental data showed some small inaccuracies between temperatures and velocities. However, it was noticed that CFD predictions on N_2O distribution in the occupied zone while pollutant source is positioned outside the thermal plume were not accurate. Even though the model could not exactly represent measured data it was assumed that the model is properly setup due to energy and mass unbalances during the measurements. In order to validate the assumption of correct model and credibility of estimated values additional model with extra energy source and reduced contamination flow rate was created and its results are presented in the Appendix V.

Finally, conclusions and findings on indoor environment with diffuse ceiling ventilation are presented. Discussion for uncertainties during the measurements and possible directions of future work are presented.

Preface

This report has been written by IEEE Master group - GMR from the 4th semester of Master's Degree in Indoor Environmental and Energy Engineering at Aalborg University. The overall theme of the project is *Analysis of the indoor environment in a room with diffuse ceiling* with focus on *indoor environment quality*. The project period has taken place from 2017 September 1st until June 8th 2018 corresponding to a total of 50ECTS points.

We would like to thank our supervisors Per Kvols Heiselberg and Chen Zhang for their guidance throughout the course of the project. We would also like to thank Hicham Johra for his help with calibrating and setting up laboratory equipment and the laboratory technicians for the help with setting up the hot box.

Reading guide
In this report the references are listed through the Harvard-method. The source is noted in square parentheses, wherein the author's surname and the publication date is listed, e.g. [Hyldgaard et al., 1997]. When the author of a publication is a company and not a person, said company will be listed. The reference is placed before the full stop when it refers to the sentence. If the reference is placed after the full stop, it refers to the paragraph. The bibliography is found in the back of the report along with the sources listed in alphabetical order. The purpose of the bibliography is to examine the critical approach to the sources that has been exercised throughout the course of the project.

References to figures and tables are made through numerical order in occurrence with the chapter number and placement within the chapter. For example, the first illustration in chapter one is named *Figure 1.1*, the next illustration *Figure 1.2*, etc. All figures and tables are provided with explanatory captions; they are placed below the figures and above the tables.

The project is divided into two reports - a main report and an appendix report. In the main report theory, methods, assumptions, set-up, measurements and results are presented and references will continuously be performed to the appendix report, which should be read as a reference to the main report. The appendix report contains additional descriptions, calculations, tables and figures.

This report has been developed and compiled by:

Georgios Christodoulou | Marius Kubilius | Rune Baldur Kessler Andersen

Index

Part I

Introduction

1 | Introduction

Building sector in the European Union is accounted for 40% of total energy consumption. While this sector is steadily expanding an increase of energy consumption is inevitable. By reducing the energy consumption of the buildings and implementing renewable energy sources it is possible to reduce the green house gas emissions and increase the energy dependency of the European Union [Parliament og the council of the European union, 2010]. In order to achieve the energy reduction European Union has set a goal to reduce green house gas emissions by 85% - 90% by 2050 compared to 1990 levels [Commission]. In addition to that Denmark is striving to achieve independence from fossil fuels by changing their 100% primary energy source to renewable energy by 2050 as presented in the Figure 1.1 below.

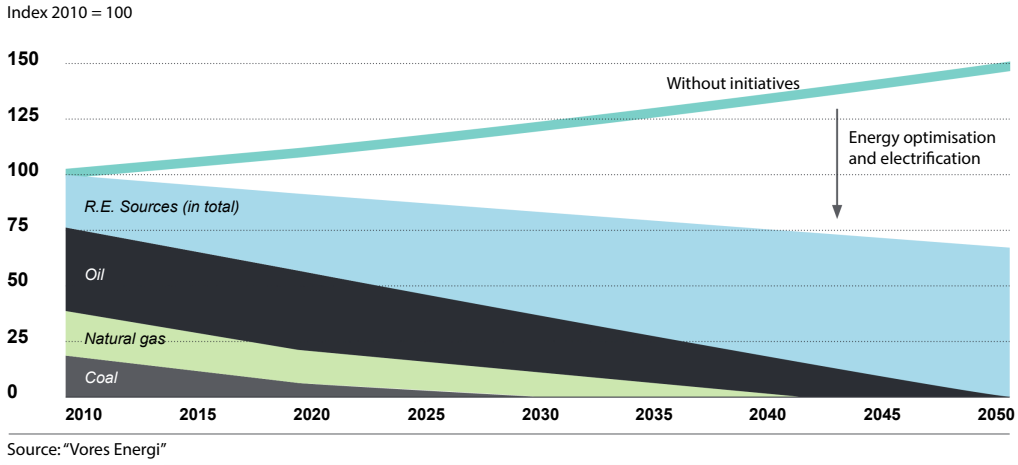

Figure 1.1. The development of energy consumption towards 2050 for oil, natural gas, coal and renewable energy sources respectively [Danish Ministry of Energy, Utilities and Climate, 2014]

In pursuance of using more renewable energy than fossil fuels and reducing the overall energy consumption of building sector changes must be made. All of this can be achieved by using more sustainable solutions, optimizing old buildings and their systems, implementing new requirements in the new buildings which would inevitably lead to less energy consumed in building sector. However, all of this must be done without jeopardizing the comfort of people that are living or working there since it is proven that productivity and satisfaction of the occupants are directly affected by indoor environment [Vilcekova et al., 2017] [Horr et al., 2016] [Mihai og Iordache, 2015]. Therefore a balance between energy reduction and indoor environment quality must be found.

Nowadays buildings are getting more insulated and more air tight reducing air leakage. The demand for heating during colder periods of the year is reduced. On the other hand, since the buildings are more insulated and air tight the risk of overheating during the

warmer periods of the year increases thus the cooling demands are growing. Therefore, designing a correct ventilation system is crucial in order to provide fresh air to the premises, remove heat surplus, dilute air pollutants, ensure good indoor environment quality and keep it energy efficient.

Two conventional and most used air distribution systems are mixing ventilation and displacement ventilation. They have been used most of the time due to their efficiency in dealing with the problems which are mentioned above. Despite that both of them have their pros and cons they must be chosen with set requirements [Nielsen et al., 2013] and [Ren et al., 2015]. One of the major complaints for mixing and displacement ventilation is draught. In order to prevent draught risk air has to be preheated before being supplied to the premises depending on the weather conditions. However by preheating the air the cooling capacity is reduced due to that an increased air flow rate has to be obtained to remove the excessive heat. This leads to increased energy consumption and risk of draught. The concern of draught can be reduced or even eliminated by a novel ventilation system called diffuse ceiling ventilation [Chen Zhang, 2016].

Diffuse ceiling ventilation concept is characterized by air being supplied through a large area which can be whole area of ceiling or just some parts that are permeable to air. Therefore, the air is being supplied to the room with very low velocities and without fixed direction flow [Hviida og Svendsena, 2012]. As mentioned before the risk of draught is either minimized or eliminated even with high air flow rates and low supply temperatures which results in high cooling capacity[Zhang et al., 2015a] [Hviid og Terkildsen, 2012] [Hviida og Svendsena, 2012] [Jacobs og Knoll, 2009] [Daria et al., 2016]. Moreover, another advantage of the system is the use of the plenum. Plenum which is the space between diffuse ceiling and internal slab can be used either to pre-heat or pre-cool the air before it gets distributed through diffuse ceiling and supplied to the occupied zone. This helps to reduce the risk of draught, increase the cooling and heating capacity or reduce the energy demand on heating [Zhang et al., 2015a] [Zhang et al., 2015b] [Yu et al., 2015a]. Moreover, the pressure losses of such system compared to the conventional ones are many times smaller making it possible to combine it with natural ventilation and further reduce the energy consumption of the fans [Yu et al., 2015b] [Yu et al., 2015a] [Chen Zhang, 2016]. Taking everything into consideration, it seems that it is very reasonable to use this type of air distribution system for its advantages compared to conventional systems which presents many risks for discomfort in the occupied zone.

In this master thesis the performance of the diffuse ceiling ventilation system will be analysed numerically by FLUENT software and experimentally by using the climatic chamber(Hot box) in Aalborg University laboratory. The main focuses of the thesis will be indoor environment of the room regarding the air quality and thermal comfort. Firstly, the layout of comfort criteria will be presented. Further on literature review on diffuse ceiling ventilation and its pros and cons will be presented as they have been investigated in other studies. Later on a learning process for modelling diffuse ceiling in CFD software is conducted. Further on experimental analysis of diffuse ceiling for different set-ups is carried out. After obtaining the experimental data numerical model is created, then validated with the results of measurements in order to check the credibility of the CFD model. Moreover, the conclusions of the results and discussion to clarify the uncertainties

and limitations of the thesis are presented. Finally possible future work is suggested.

Thesis objective

Since diffuse ceiling ventilation is a novel system in air distribution not many experiments analysing the influential parameters of the system are done. In this master thesis further investigation on such system and its parameters will be conducted:

- To investigate atmospheric comfort by evaluating contaminant removal efficiency
- Investigate the distributions of contaminants by evaluating local air quality index
- Investigate the system performance for different positions of contaminant source(s)
- Investigate thermal comfort of the system for the investigated cases

Moreover, the study will be conducted both numerically with CFD and experimentally in laboratory. Also, the study will focus on steady-state analysis neglecting the effects of transient flow and thermal mass dynamic effects.

2 | Comfort criteria

This chapter focuses on presenting comfort criteria for evaluation of indoor environment quality. Thermal and atmospheric comforts criteria are presented according to which experimental data will be analysed in further chapter.

2.1 Definition of occupied zone

In order to proceed further with analysis of indoor environment comfort the boundaries of occupied zone must be defined.

As described in EN 13779 standard the definition of the occupied zone is dependent on room's geometry and the use of the space by the occupants. Most of the times "occupied zone" can be referred to zones where it is designed for human occupancy and is defined as a volume of air that is confined by specified horizontal and vertical planes which are usually parallel with the walls of the room. Therefore, the occupied zone in the room is the space where occupants are normally located and where the requirements for the indoor environment should be satisfied. Table 2.1 and Figure 2.1 below presents typical dimensions and description of the occupied zone [EN13779, 2007].

Table 2.1. Typical dimensions of the occupied zone [EN13779, 2007]

Distance from the inner surface of		Typical range [m]	Default value [m]
Floors (lower boundary)	A	0.00 to 0.20	0.05
Floors (upper boundary)	B	1.30 to 2.00	1.8
External windows and doors	C	0.50 to 1.50	1
HVAC appliances	D	0.50 to 1.50	1
External walls	E	0.15 to 0.75	0.5
Internal walls	F	0.15 to 0.75	0.5
Doors. transit zones etc.	G	Special agreement	-

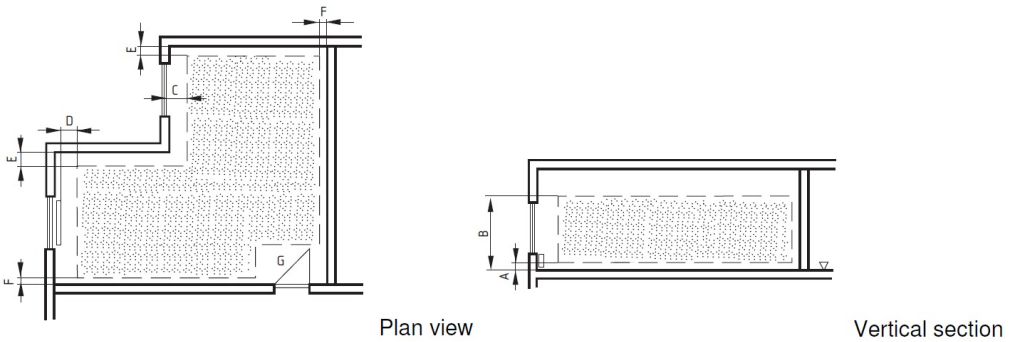

Figure 2.1. Description of the occupied zone [EN13779, 2007]

In cases of external walls with windows or doors the element with the largest distance is chosen for the whole surface. Moreover, for rooms are with low ceiling height problems might occur to meet the requirements to an upper boundary of 2.0m. In addition to that in cases of room being not based on its dimensions but on other factors the occupied zone can be defined by an arrangement of working areas, equipment or by location of breathing zone.

2.2 Criteria for thermal comfort

After describing the occupied zone where the requirements must be met comfort conditions can be described. Thermal comfort can be described as a condition where the human mind expresses satisfaction with the thermal environment. On the other hand, discomfort can be caused by warm or cool sensations of the body as a whole which can be expressed by the PMV (Predicted Mean Vote) or PPD (Predicted Percentage of Dissatisfied). Thermal environment can be evaluated in steady state and non-steady state conditions. This thesis will focus on steady-state conditions without evaluating long-term effects [EN13779, 2007].

2.2.1 Predicted mean vote

PMV is described as an index which shows the mean value of the votes of a large group of persons on the 7 point thermal sensation scale which can be seen in Figure 2.2 below [ISO7730, 2005].

+ 3	Hot
+ 2	Warm
+ 1	Slightly warm
0	Neutral
– 1	Slightly cool
–2	Cool
– 3	Cold

Figure 2.2. Thermal sensation scale for PMV [ISO7730, 2005]

The scale is based on the heat balance of the human body. It can be described as a balance between internal heat production in the body and loss of heat to the environment. PMV index can be calculated by equations provided by EN ISO 7730, taking values from the tables with different combinations of activities, clothing, relative velocities and operative temperature or by directly measuring it with integrating sensor [ISO7730, 2005].

2.2.2 Predicted percentage dissatisfied

While PMV predicts the mean value of the thermal votes of a large group of people PPD establishes a quantitative prediction of the percentage of thermally dissatisfied people who are feeling either too cold or too warm. PPD index can be calculated by the equation that is provided in EN ISO 7730 which takes PMV index into account. Furthermore, PPD

can be presented as a function of PMV as can be seen in the Figure 2.3 below [ISO7730, 2005].

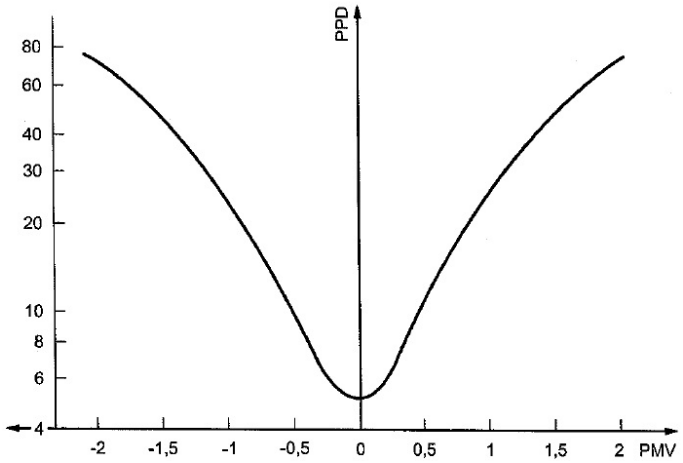

Figure 2.3. PPD scale as a function of PMV [ISO7730, 2005]

It is worth to point out that the percentage of people dissatisfied will never be 0. The minimum percentage is 5% which indicates that there will always be people who are not satisfied with thermal comfort as it is subjective.

2.2.3 Draught

Draught can be described as most often reason for local discomfort in rooms with air distribution systems [Fanger et al., 1988]. The biggest risk of draught is for sedentary people with light activity because their thermal sensation for the whole body is close to neutral whereas people with higher levels of activity are less bound to feel this discomfort. Discomfort because of draught can be expressed as the percentage of people that feel it. By using the Equation (2.1) the percentage of bothered people can be expressed [ISO7730, 2005].

$$DR = (34 - t_{a,l})(\bar{v}_{a,l} - 0.05)^{0.62}(0.37 \cdot \bar{v}_{a,l} \cdot T_u + 3.14) \tag{2.1}$$

where:
$t_{a,l}$ - the local air temperature [°C]
$\bar{v}_{a,l}$ - the local mean air velocity [m/s]
T_u - the local turbulence intensity [%] (40% may used when is unknown)

The Equation (2.1) above is applied for people at light with sedentary activity and a thermal sensation close to neutral for the whole body. It also has to be noted that this prediction is for neck height draught risk at arms and feet level model can be inaccurate [ISO7730, 2005].

Draught risk can also be avoided by limiting the mean air velocities in the room. Various standards give different values for winter and summer conditions for mean air velocities due to different assumptions on the air temperature and turbulence intensity. The values are presented in Table 2.2 below.

Table 2.2. Mean velocities for DR <20% in different seasons [ISO7730, 2005] [CR1752, 1999] [ASHRAE55, 2013]

Draught rate	Maximum mean air velocity by ISO 7730		Maximum mean air velocity by CR1752		Maximum mean air velocity by ASHRAE 55-2013	
	Winter	Summer	Winter	Summer	Winter	Summer
<20%	0.19 m/s	0.16m/s	0.22 m/s	0.18 m/s	0.2 m/s	

2.2.4 Operative temperature and vertical temperature gradient

Depending on the activity level and clothing of the occupants an optimal operative temperature which corresponds to PMV = 0 exists. The operative temperature should always be within the permissible range in the occupied zone at all times. The Figure 2.4 presents the acceptable operative temperature range with different activity and clothing levels.

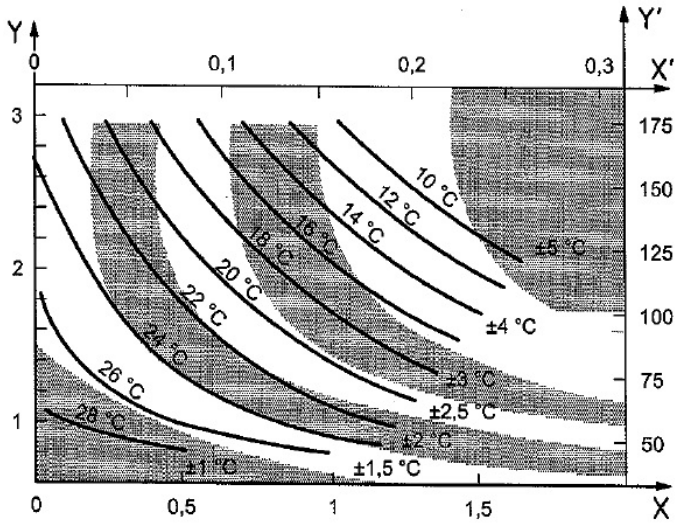

Figure 2.4. Range around the optimum temperature for PPD <10% [ISO7730, 2005]

Where X and Y axis represent basic clothing insulation in clothing units $[clo]$ and metabolic rate in metabolic units $[met]$ respectively. Also, X' and Y' represents the same parameters just in different units, metabolic rate in n $[W/m^2]$ and clothing in $[m^2 \cdot °C/W]$.

Furthermore, local thermal discomfort can also be caused by vertical temperature gradient and radiant temperature asymmetry. Where vertical temperature gradient describes the temperature difference between ankle and head level and radiant asymmetry temperature differences between the plane radiant temperatures in two opposite directions. The values for each case are presented by EN ISO 7730 in the Table 2.3 below.

Table 2.3. Values for local thermal discomfort

Vertical temperature gradient between head and ankles, [°C]	Floor surface temperature range, [°C]	Radiant temperature asymmetry, [°C]			
		Warm Ceiling	Cool wall	Cool ceiling	Warm wall
<3	19-29	<5	<10	<14	<23

2.3 Atmospheric comfort criteria

After the requirements for thermal comfort the following comfort criteria that has to be fulfilled is atmospheric comfort criteria. There are several ways to examine the air quality of the room: CO_2 concentration, ventilation effectiveness or air exchange efficiency. However, in cases when measured variable is CO_2 usually there is a limit for the concentration above outdoor levels. It should be noted that CO_2 is not impacting atmospheric comfort before reaching 3000ppm but it is a good indicator for other parameters affecting the atmospheric comfort [Hyldgaard et al., 1997]. Danish standard provides common values for air quality in three different categories which are presented in the Table 2.4 below.

Table 2.4. Recommended CO_2 concentrations above outdoor concentration [Standard, 2007]

Category	**Corresponding CO_2 above outdoors in ppm**
I	350
II	500
III	800

The indoor air quality can be described also by the ventilation effectiveness and air exchange efficiency. Ventilation effectiveness describes how efficient is the removal of contaminants from the occupied zone and how the specific areas in the room are influenced by contaminant sources. The higher ventilation effectiveness the more efficient is the ventilation system in terms of air quality. It can be calculated according the Equation (2.2) [Zhang et al., 2014].

$$\epsilon = \frac{C_R - C_0}{C_{oc} - C_0} \tag{2.2}$$

where:
C_R - Contaminant concentration in exhaust [ppm]
C_0 - Contaminant concentration in supply [ppm]
C_{oc} - Contaminant concentration in occupied zone [ppm]

3 Literature review on Diffuse Ceiling Ventilation

This chapter will be focused on previous studies on diffuse ceiling. A small introduction of three different air distribution systems will be described. Furthermore, a more in depth literature review will be conducted on diffuse ceiling. Its benefits compared to conventional air distribution systems will be pointed out and results of previous studies will be presented.

3.1 Air distribution system types

A 'family tree' which connects all types of air distribution systems in three dimensional chart was introduced by Nielsen. Since the pattern of air distribution in the room has a big role in ventilation performance the chart can be used as a guideline. As presented in the Figure 3.1 below the chart consists of four primary variables that determine air distribution :

- Supply airflow rate (q_0)
- Temperature difference between inlet and exhaust (ΔT_0)
- The ratio between supply area (a_0) and the surface area it is located (A)
- Location of the supply opening

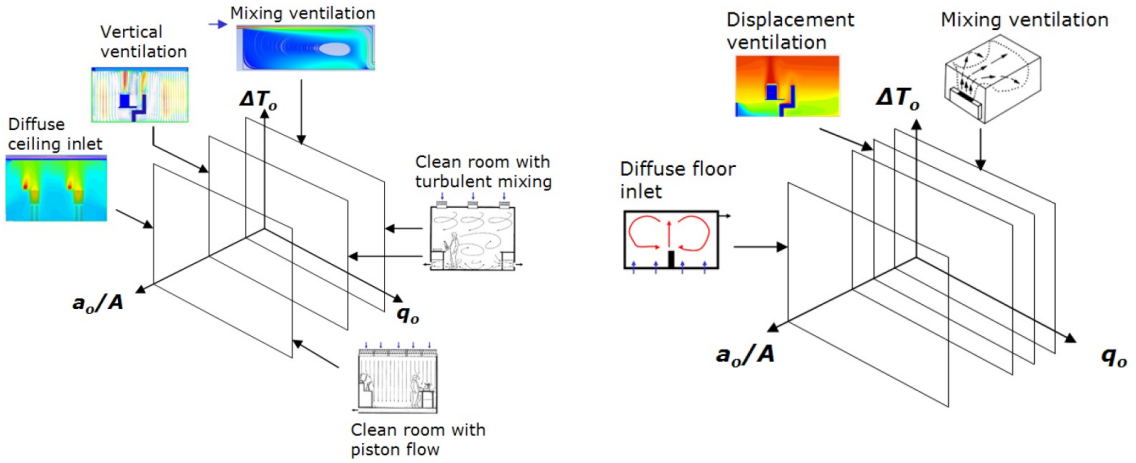

Figure 3.1. Three dimensional chart of different air distribution systems for cooling with high supply locations on the left and low supply locations on the right [Nielsen, 2011]

Further description of conventional air distribution systems is presented below in the following sections.

3.1.1 Mixing ventilation

Two most common ventilation principles are applied in the non-industrial spaces : mixing and displacement ventilation as presented in the Figure 3.2.

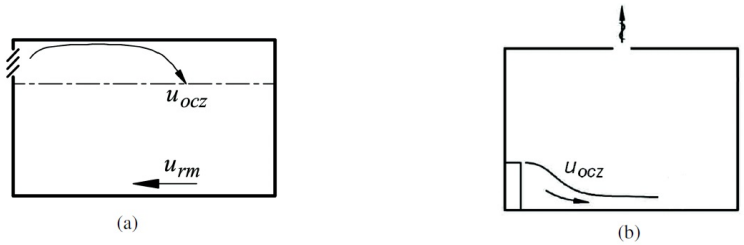

Figure 3.2. a)mixing and b)displacement ventilations. u_{ocz} stands for velocity entering occupied zone and u_{rm} stands for reversed motion velocity. [Nielsen, 2007]

Where mixing ventilation is aimed towards diluting pollutants and warm air by introducing fresh and cooler air. The supplied air has high initial mean velocity and high turbulence due to established velocity gradients which results to good mixing and uniform temperature and pollutant distribution in the occupied zone [Nielsen, 2011].

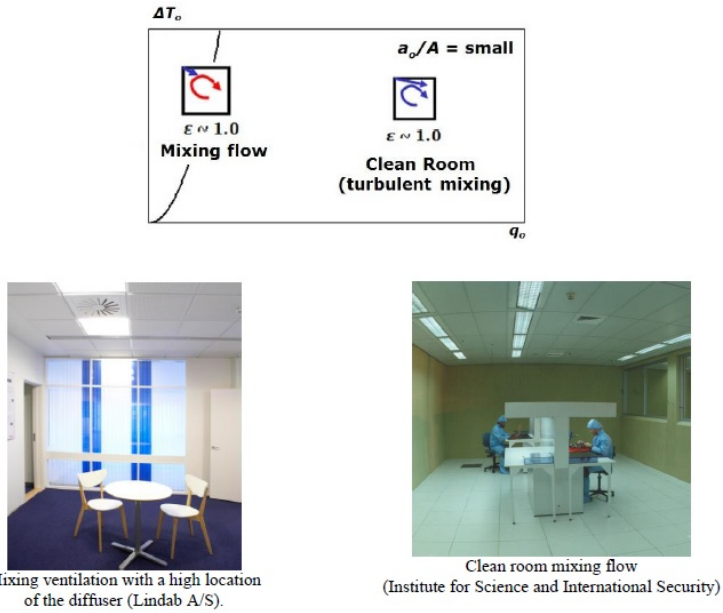

Figure 3.3. Graph representing mixing ventilation effectiveness from a high location of air supply opening. Lower photos show mixing ventilation with different diffusers and type of mixing ventilation [Nielsen, 2011]

The graph in the Figure 3.3 above represents the air distribution pattern with the mixing effect that is generated by supplying the air with a high momentum to the room. In order to achieve high momentum airflow the air change rate must be between $1h^{-1}$ - $5h^{-1}$ and the supply opening has to have relatively small area. Due to that the supply openings are located outside the occupied zone. With this principle of ventilation a high mixing in the room is achieved thereby the effectiveness of ventilation is approximately 1 [Nielsen, 2011].

3.1.2 Displacement ventilation

While mixing ventilation is based on high momentum driven flow which aims to dilute the contaminant concentration, displacement ventilation has a different approach. Displacement ventilation is based on thermal buoyancy forces. It works when the thermal plumes flow from the heat sources are dominant in the room. Usually the supply openings are located in the lower zone of the room either on a wall or along the floor whereas the exhaust is located in the upper zone either on the ceiling or on a wall. Rather than mixing the polluted air and contaminants displacement ventilation is aimed towards replacing the contaminated air by supplying fresh air close to the floor and and extracting the contaminated air in a higher area. Unlike the mixing ventilation highest velocities and lowest temperatures appear in the very lower zone of the room, approximately 0.05m from the floor inevitably creating vertical temperature gradient. Example of displacement ventilation and its effectiveness is presented in the Figure 3.4 below.

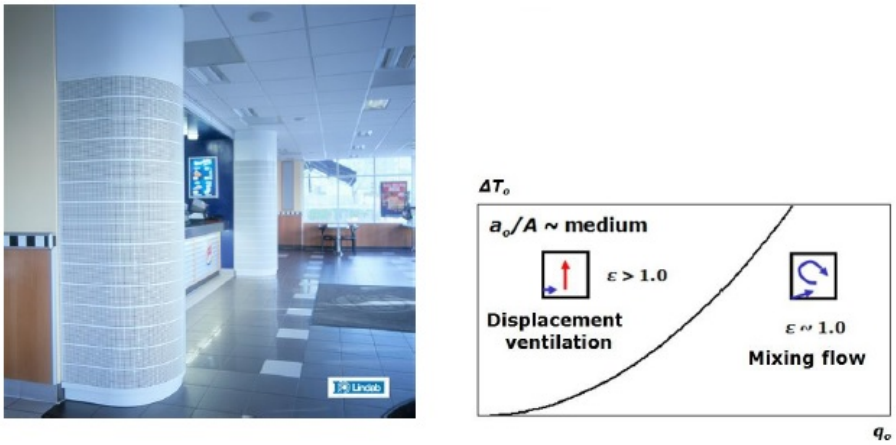

Figure 3.4. The graph on the right side represents displacement ventilation effectiveness from low level supply openings and return at high level. The photo on the left side represents an example of displacement ventilation [Nielsen, 2011]

As can be seen from the graph in the Figure 3.4 above the opening areas of supply terminals are large (medium a_0/A) thus the supply airflow has a relatively low momentum. However, it is irrelevant for air distribution in the room due to the fact that flow is driven by buoyancy forces. The flow may be thermally stratified in the occupied zone and the ventilation effectiveness might be even bigger than 1. In addition to that as can be seen from the same graph high flow rates for this kind of ventilation are not very practical because high velocities will be generated in the occupied zone and discomfort will occur because of the draught risk [Nielsen, 2011].On the other hand, the risk of draught leads to restrictions on airflow rates which results in insufficient ventilation and poor air quality [Zhang et al., 2015b].

3.1.3 Diffuse ceiling ventilation

A novel ventilation principle 'diffuse ceiling ventilation' which was widely used in industry was proposed in indoor spaces for people, especially for offices and schools due to their high heat loads and ventilation rates [Zhang et al., 2015b]. Compared to the previous

ventilation principles, diffuse ceiling ventilation utilizes the area above suspended ceiling. The air is supplied to the plenum where it acts as a pressure chamber and utilizes low momentum inlet through a porous suspended ceiling acting as a single large terminal device as presented in the Figure 3.5.

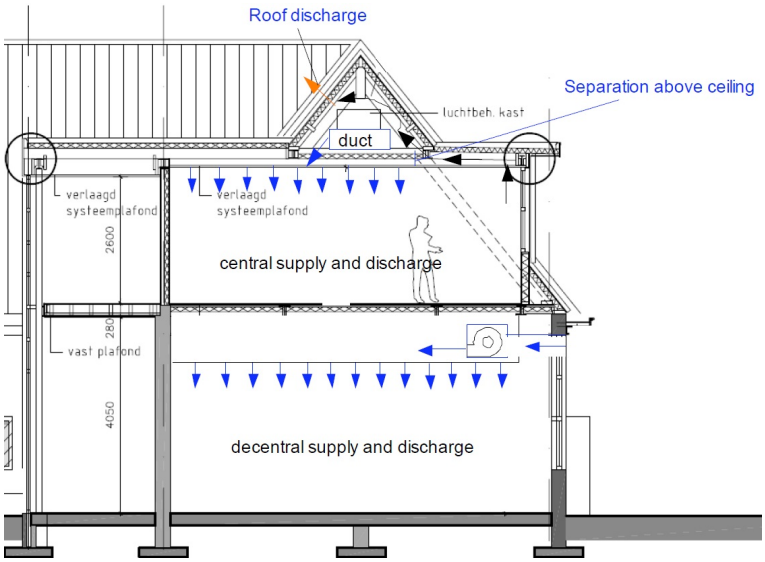

Figure 3.5. Decentralized and centralized diffuse ceiling ventilation for classroom [Jacobs og Knoll, 2009]

The air travels through the porous medium due to created overpressure in the plenum. With a small drop of pressure across the suspended ceiling the inlet air can be evenly distributed across the whole area of the suspended ceiling which works as an inlet diffuser. Main advantage compared to two previous ventilation principles is that the diffuse ceiling principle allows to supply very high airflow rates with low temperature without the risk of draught. In addition to that the system is ductless which reduces the pressure losses and air can be directly supplied from the outside without pre-heating. Moreover, due to low pressure drop in the porous medium natural ventilation could be utilized [Kristensen et al., 2016].

Furthermore, air distribution patterns in rooms with diffuse ceiling might be controlled either by buoyancy flows from heat sources or by momentum flow as represented in the Figure 3.6 below.

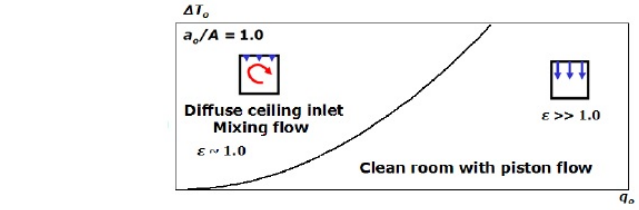

Diffuse ceiling inlet (Wessberg).

Clean room with piston flow (Shelco Inc).

Figure 3.6. Graph representing diffused ceiling ventilation effectiveness. Lower photo represent an example of a diffused ceiling ventilation system in contrast with a piston flow system [Nielsen, 2011]

This distribution system might be also defined as a mixing ventilation due to its ventilation effectiveness close to 1. If the the air change rates are reached to $50h^{-1}$ - $100h^{-1}$ piston flow patterns appear which results in very high ventilation effectiveness usually needed for high requirement rooms such as surgeries and factories dealing with dust free environment [Nielsen, 2011].

3.2 Thermal comfort

3.2.1 Risk of draught

One of the main concerns as previously mentioned is the possibility of draught in the occupied zone with the conventional mixing and displacement ventilation principles [Jacobs og Knoll, 2009]. Many previous studies has shown that the possibility of draught with diffuse ceiling ventilation is minimized. Study by Zukowska et. al has proven that even with high air change rates such as $11.5h^{-1}$ or $17.9h^{-1}$ and large temperature differences up to $10.6K$ between supply and exhaust the risk of draught in the occupied zone is negligible as the results are presented in Figure 3.7.

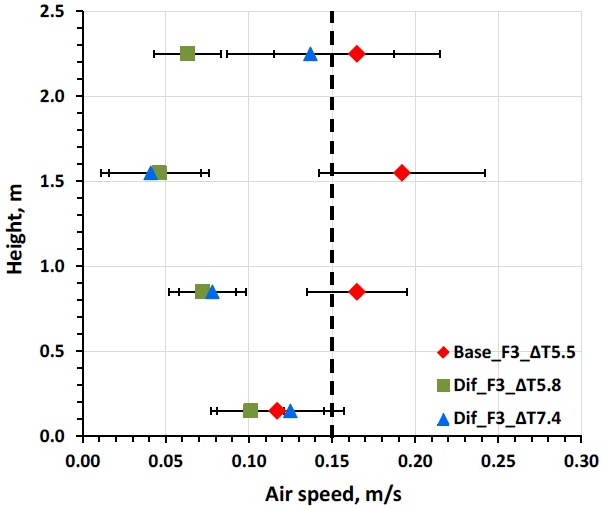

Figure 3.7. Measured velocities in one of the positions in the room with maximum air change rate of $17.9h^{-}1$ [Daria et al., 2016]

The Figure 3.7 above compares velocities with maximum air change rates with directly supplying air through ceiling mounted fan coils (Base) and diffuse ceiling options (Dif). Where it is clearly visible that air velocities for baseline conditions are much higher than diffuse ceiling.

Another study by Jacobs et al. resulted in draught free conditions for Dutch classrooms. The conducted experiment showed that even with the extreme conditions such as airflow demand of $11l/s \cdot child$ and temperature difference between supply and exhaust air of $18K$ there were no comfort problems [Jacobs og Knoll, 2009]. The measured velocities at the ankle height(0.1m) are presented in the Figure 3.8 below.

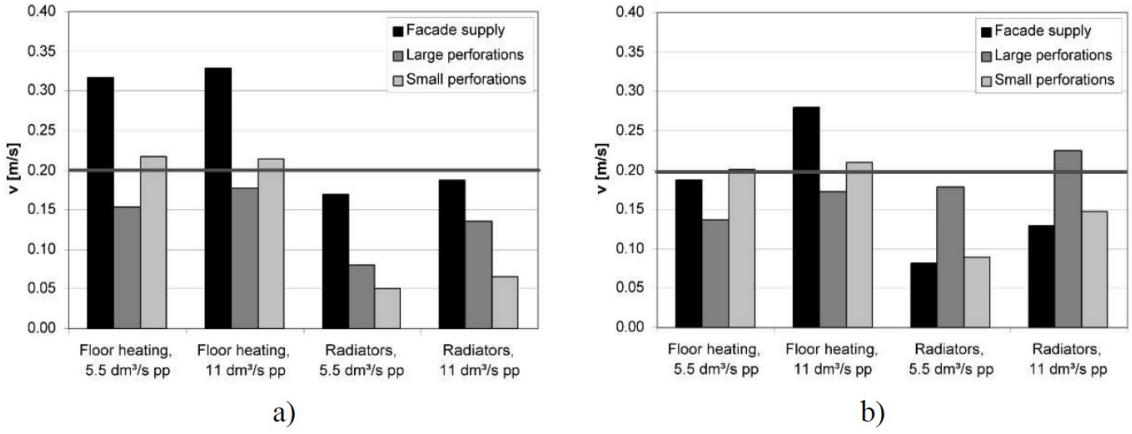

Figure 3.8. Measured air velocities at ankle height (0.1m) with a distance from facade a) 1 meter b) 2 meters [Jacobs og Knoll, 2009]

Figure 3.8 only represents the values at 0.1m because at other heights the measurements stay within comfort levels. Furthermore, it can be seen that the velocities with only the facade supply principle are higher than when using perforated ceiling as an inlet for air supply. In addition to that higher velocities close to the facade are more expected

with floor heating rather than with radiators. After the experiment the conclusion was made that ventilation in classrooms has to be improved due to increasing the efficiency in learning for students and their well-being. Also, diffuse ceiling can be used as a draught free concept in a wide range [Jacobs og Knoll, 2009].

Further experimental results by Zhang et al. has shown that draught rate at ankle level 0.1m with diffuse ceiling ventilation was decreased from 18.9% to approximately 6% when switching from ventilation type without diffuse ceiling [Zhang et al., 2015a].

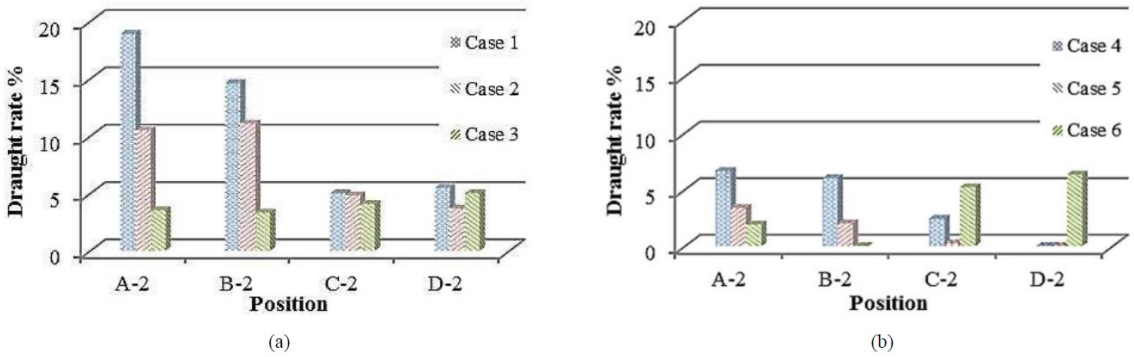

Figure 3.9. Draught rate possibilities at 0.1m height in different measurement places [Zhang et al., 2015a]

Highest draught rate of 18.9% without diffuse ceiling ventilation is found close to the facade when the supply air temperature is -7°C due to cold facade surface influencing inlet air drop downwards with relatively high velocities causing draught. However, a visible reduction of draught rate to approximately 6% is seen when switching to diffuse ceiling ventilation. Where plenum acts as a pressure chamber allowing air to be equally distributed through the entire ceiling and preventing the downward flow which causes draught. Also, it was noted that while decreasing the temperature difference between outlet and inlet the draught rate was reduced in both conditions. Moreover, the zone with possible draught rate was moved deeper into the room rather than staying close to the facade [Zhang et al., 2015a]. In addition to that, it was once again shown that even though the diffuse ceiling ventilation does not generate the risk of draught the heat sources inside the room are the cause of raising the draught risk [Zhang et al., 2015b] [Nielsen, 2011].

Another experiment was conducted on a real classroom with diffuse ceiling ventilation by Hviid which resulted in positive results concerning draught possibilities. The experiment was conducted with two flow rates ($500m^3/h$ and $1000m^3/h$), two temperatures (17°C and 10°C) for inlet and two heights where velocities were measured (0.1m and 1.1m) the results for a few of the measurement points are presented in Figure 3.10.

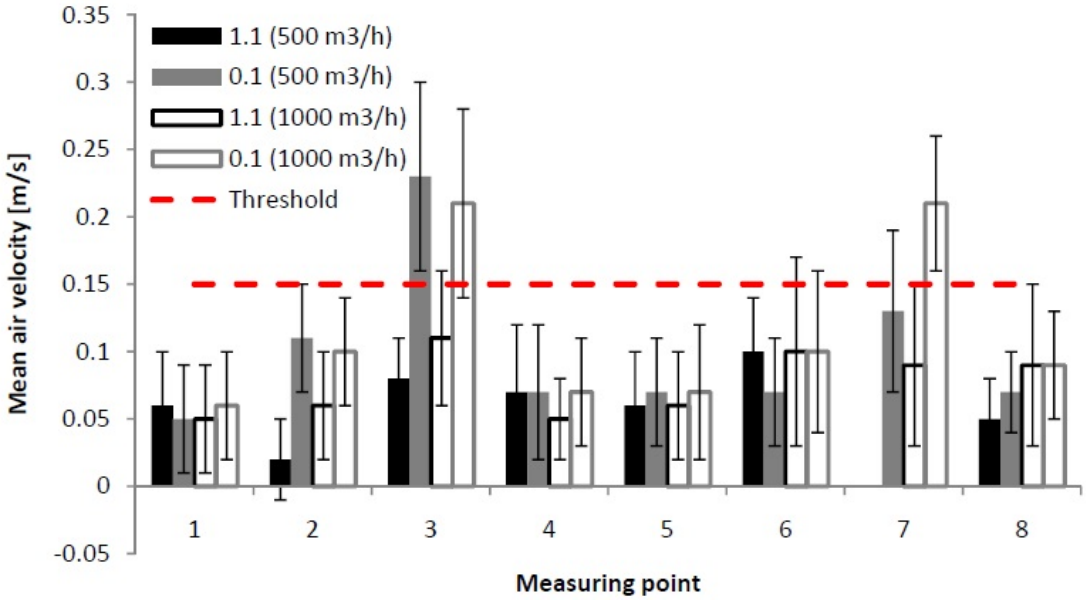

Figure 3.10. Measured air velocities at 0.1m and 1.1m above the floor with different flow rates and inlet temperature of 10°C [Hviid og Terkildsen, 2012]

Both scenarios with different inlet temperatures gave positive results of satisfying the 0.15m/s threshold and concluding that there is no draught risk. It was assumed that 3 and 7 points were above the threshold due to the fact that they were situated close to the leaky ceiling hatch [Hviid og Terkildsen, 2012].

3.2.2 Vertical temperature gradient

Another concern than the draught risk in the room is vertical temperature gradient. High temperature gradient can cause discomfort for people inside the room by having lower temperatures at the ground level and higher temperature in higher levels of the room [ISO7730, 2005]. The diffuse ceiling ventilation system has a ventilation effectiveness close to 1 which addresses good mixing of air inside the room [Nielsen, 2011]. In addition to that a number of studies identified that diffuse ceiling ventilation has a low risk of discomfort due to low vertical temperature gradient.

Fan et al. carried out an experiment of diffuse ceiling ventilation in a full scale climatic chamber imitating typical office room where indoor temperatures were measured when supplying airflow with $3.5h^{-1}$ and $5.1h^{-1}$ air change rates. The measured temperatures resulted in positive results for vertical temperature gradient. The results are presented in Figure 3.11.

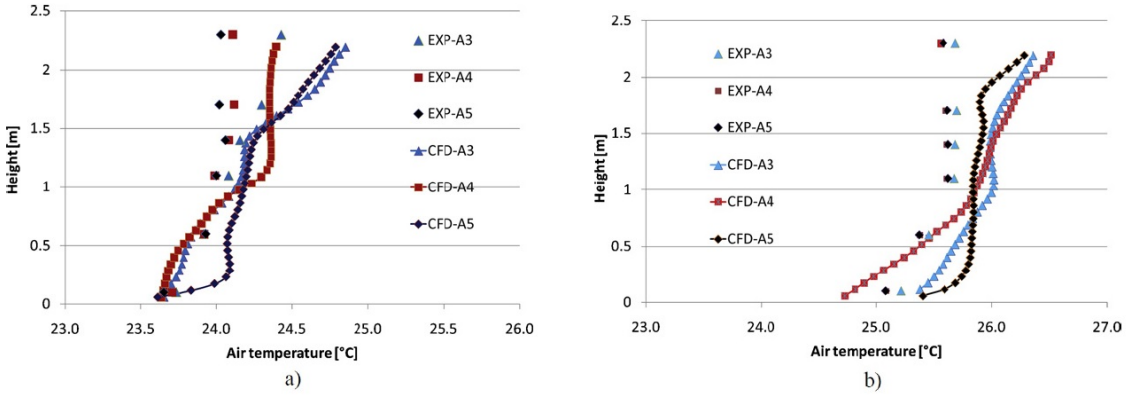

Figure 3.11. Measured and predicted air temperatures in climatic chamber. Case a) represents the scenario with ACH of $3.5h^{-1}$ and b) ACH of $5.1h^{-1}$ [Fan et al., 2013]

Higher temperatures in b) case are due to different scenarios of the experiment. The first one was conducted with ACH of $3.5h^{-1}$, inlet temperature of 16.7°C and heat load of 670W whereas the second one was conducted with $5.1h^{-1}$, inlet temperature of 17.2°C and heat load of 1137W. Despite the different set-ups both scenarios gave good results of 0.3K/m vertical temperature gradient which is due to high effectiveness of ventilation [Fan et al., 2013].

Another similar experiment was conducted by Hviid in a climatic chamber. Two different porous surfaces mounted in a suspended ceiling were used: aluminium and gypsum. The results showed that vertical temperature gradient between head and ankle height was approximately 0.5K/m. The Figure 3.12 represents the measured data.

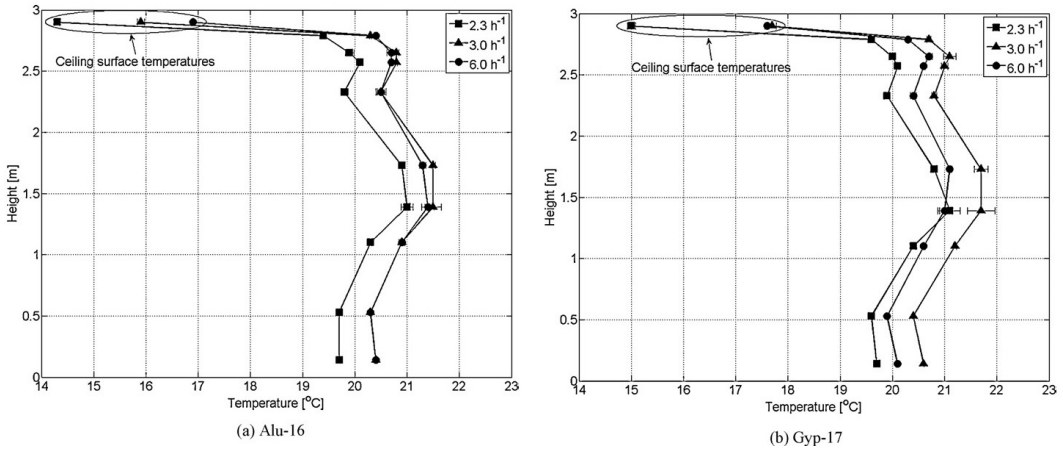

Figure 3.12. Measured temperatures in climatic chamber with different ACH [Hviida og Svendsena, 2012]

Furthermore, Hviid stated that since the temperature difference from floor to below ceiling is close to zero temperature gradients can be eliminated by self-sustaining mixing for the employed room size and heat source density distribution [Hviida og Svendsena, 2012].

Kirstensen et al. tested diffuse ceiling performance in a classroom in two different time periods with mechanical exhaust driven ventilation. Thermal comfort was assessed with

basis of thermal comfort model described in ISO 7730:2005 treating both periods as steady-state and with temperature cycles of less than 1K and temperature ramps less than 2K/h. Summarized vertical temperature gradients are presented in Figure 3.13 below.

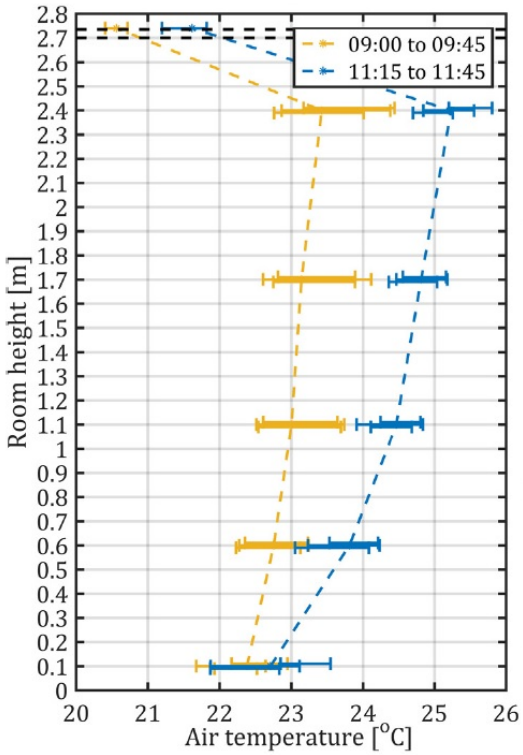

Figure 3.13. Vertical temperature gradient measured in the classroom in different periods [Kristensen et al., 2016]

Where the horizontal bars in the Figure 3.13 represent the 2.5 and 97.5 percentiles of measured values. The measured vertical temperature gradients between ankle and below diffuse ceiling heights were approximately 0.18K/m and 0.73K/m in the different cases [Kristensen et al., 2016].

Zhang in her PhD thesis conducted experiments in climatic chamber and predictions with CFD for thermal comfort. It was found that cases without diffuse ceiling large temperature gradients were observed due to insufficient mixing of air by cool supply air dropping fast to the floor while being attached to facade and warm air being stagnated in the upper zone. Meanwhile, cases with diffuse ceiling ventilation eliminated the temperature gradients as Figure 3.14 presents. [Chen Zhang, 2016]

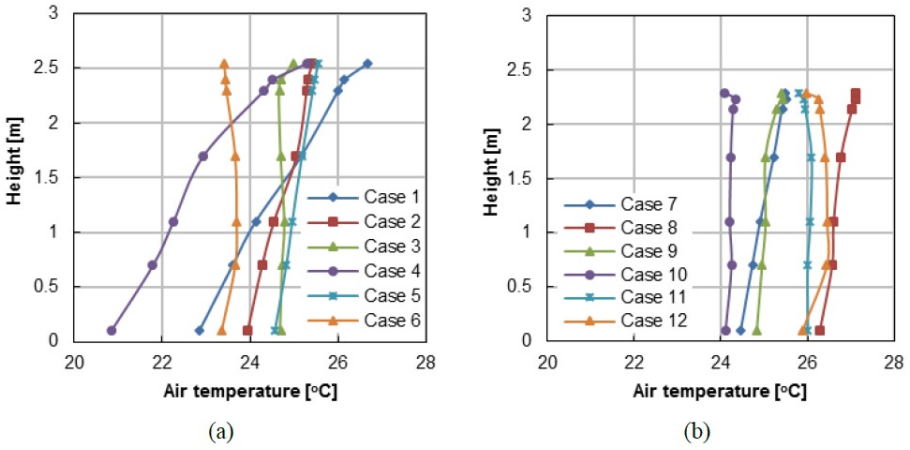

Figure 3.14. Vertical air temperature gradients (a) cases without diffuse ceiling (b) cases with diffuse ceiling [Chen Zhang, 2016]

However, despite the fact that diffuse ceiling ventilation reduced the vertical temperature gradients significantly the risk of overheating increased during summer period or even in transitional seasons. Room was approximately 2-3C° warmer with diffuse ceiling cases [Chen Zhang, 2016].

3.3 Indoor air quality

Not that much studies have been conducted about the air quality in rooms ventilated by a diffused ceiling ventilation system. However some studies mentioned measurements of the ventilation effectiveness under experiments with diffused ceiling ventilation systems.

It was shown that the diffuse ceiling ventilation system was able to remove indoor pollutant efficiently in Fan et al. studies. The average ventilation effectiveness was close to 1 which corresponds to good mixing inside the room [Fan et al., 2013]. Another study by Mikeska and Fan showed that the average calculated ventilation effectiveness for their experiment with diffuse ceiling was only 0.84 [Mikeska og Fan, 2015]. Chodor and Piotr in their master thesis got similar results as Fan et al. since their measured average ventilation effectiveness was close to 1 also [Chodor og Taradajko, 2013]. Kristensen and Jensen in their master thesis also achieved ventilation effectiveness of 1 [Kristensen og Jensen, 2015]. All the results from previous studies proves that rooms with diffuse ceiling ventilation has good mixing in the occupied zone with convective forces.

3.4 Characteristics of Diffuse Ceiling ventilation

3.4.1 Air distribution design chart

As mentioned before one of the aims of the design for the air distribution system is to find the most optimal solution without endangering the comfort of the user. Optimal flow rates, temperature difference between inlet and outlet must be found so that there is a satisfaction of the comfort criteria for draught, temperature gradients in the room [Nielsen, 2011].

A design chart for different air distribution has been designed. It helps to evaluate several design principles and allows to compare their differences in order to find the most suitable solution according to the demands. The chart is presented in the Figure 3.15 below.

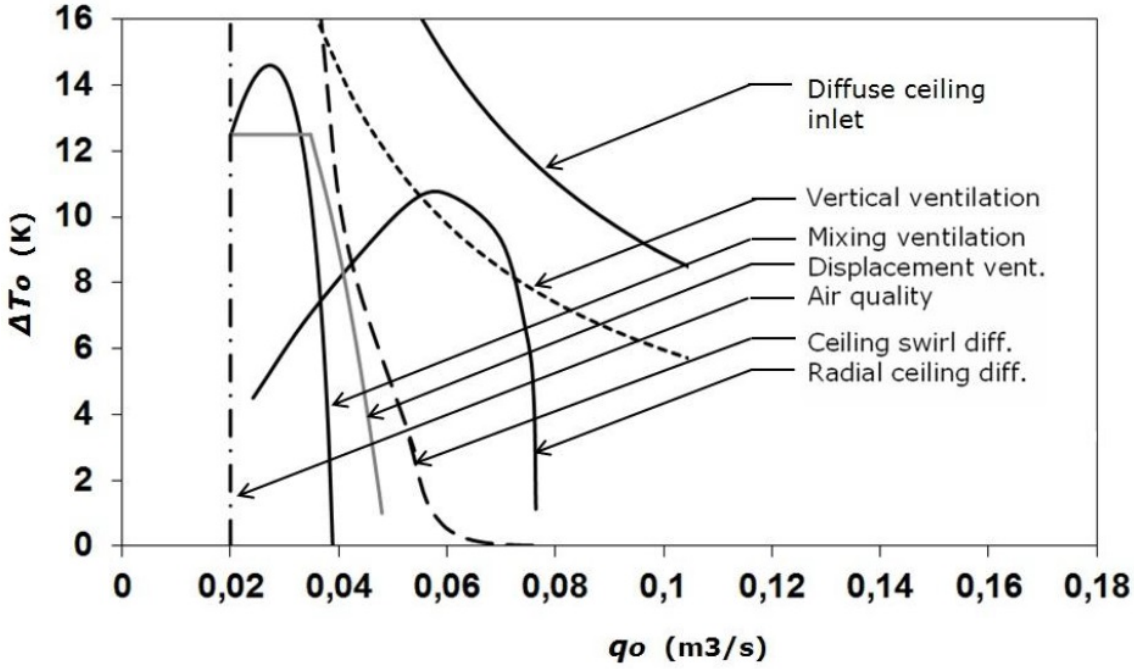

Figure 3.15. Design chart for six air distribution systems with minimal volumetric flow of $0.02m^3/s$ [Nielsen, 2011]

Figure above represents six different air distribution systems possibilities based on minimum and maximum allowable flow rate q_0 to the room and also maximum temperature difference of the return and supply temperatures. The minimum airflow of $0.02m^3h/s$ is represented in the graph to obtain given air quality. The flow rate is constant and independent of ΔT_0 when the system generates mixing. However, systems such as diffuse ceiling which are based on low momentum inlet do not present a limit for q_0. Draught is not generated by high velocities in the room, heat loads are the cause of draught and therefore the product of q_0 and ΔT_0 is limited [Nielsen, 2007].

Moreover, the chart that is represented in the Figure 3.15 has been designed with constant thermal loads, with air change rates going up from $2.75h^{-1}$ to $10.45h^{-1}$ with temperature variations of 3.5K-12.0K. Therefore, conclusion was made that the chart might be dependant on the room size, room layout and design of terminal units [Nielsen, 2007].

3.4.2 Parameter variation

Heat sources placement in the room

In numerical studies by Zhang et al. parameter variation of heat sources and room height was analysed. In all cases model had 100% opening area, air change rate of $4h^{-1}$ and air supply temperature of 15.5°C. Based on the experimental studies it was found that buoyancy flow generated by heat sources is the dominant flow in the room with diffuse

ceiling ventilation due to that the air distribution pattern depends on the distribution of heat sources. Four cases were analysed further on in the numerical model which are presented in the Figure 3.16 below [Zhang et al., 2015b]

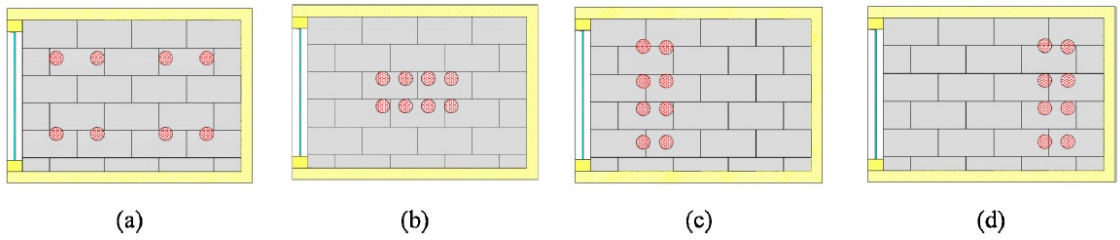

Figure 3.16. Heat source distribution in the numerical model. Where (a) evenly distributed (b) centered (c) front side (d) back side [Zhang et al., 2015a]

Each person has a heat load of 80W and the radiator is not activated during the simulations. Every setup gave different results of air distribution in the room. Plotted results are presented in the Figure 3.17 below.

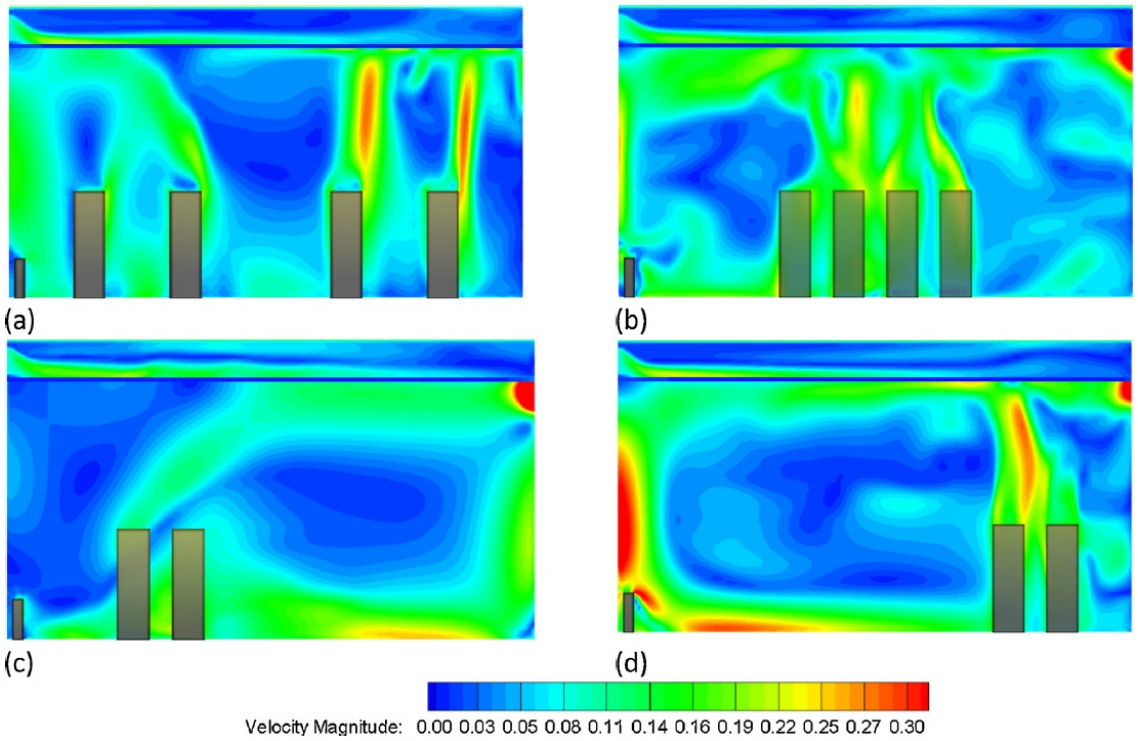

Figure 3.17. Air distribution with different heat source placement. Where (a) evenly distributed (b) centered (c) front side (d) back side [Zhang et al., 2015a]

It was concluded that strong air recirculation appears in the opposite side of the room if the heat sources are concentrated only in one side as presented in the Figure 3.17 (c) and (d) cases. Moreover, if the heat sources are concentrated in the middle of the room two asymetrical air recirculation zones appear on the sides of the heat sources, in this case the one in the front room is stronger than in the back. Furthermore, case with evenly distributed heat sources did not show any clear air recirculation zones which was also

noticed by Nielsen [Nielsen et al., 2015] in his experiments with smoke tests. In addition to that the risk of draught with each setup as a function of distance from the inlet is plotted in the Figure 3.18 below [Zhang et al., 2015b].

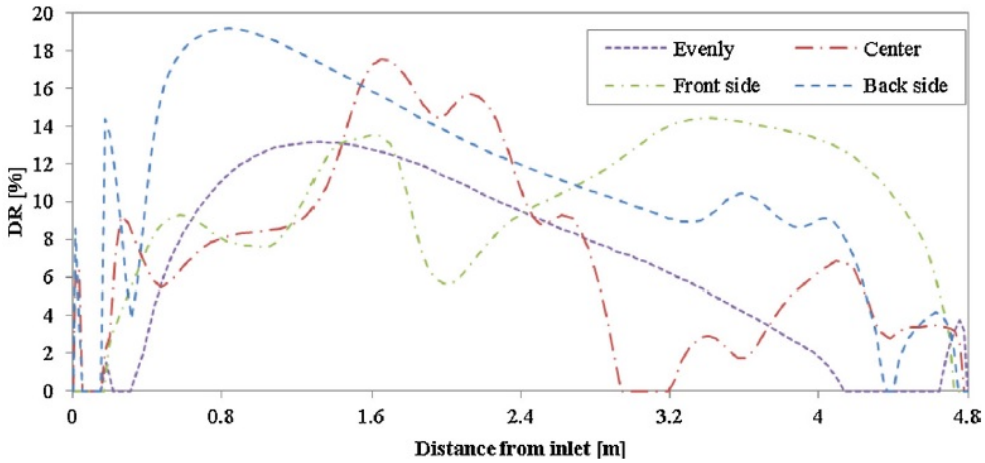

Figure 3.18. Draught risk with different setups of heat load locations as a function of distance from the inlet [Zhang et al., 2015a]

As Figure 3.18 indicates that evenly distributed sources give lowest possibility of draught compared to other distributions of heat of heat sources. In case of heat sources being concentrated in one place of the room (middle, front or back) intense thermal plume is noticed that generates strong air recirculation entering the occupied zone and increasing the risk of draught at the floor level. Also, it was noticed that the air is not evenly distributed due to the fact that big quantity of air is supplied in short distance of the inlet. That causes the downward air flow from diffuse ceiling and increasing the recirculation of air Zhang et al. [2015b].

Room height influence

Another parameter that Zhang et al. investigated the influence of room height for air distribution. Two cases were analysed with heights of 2.335m, 3.0m, 4.0m and evenly distributed heat sources with 80W for each source. The results are plotted in the Figure 3.19 below.

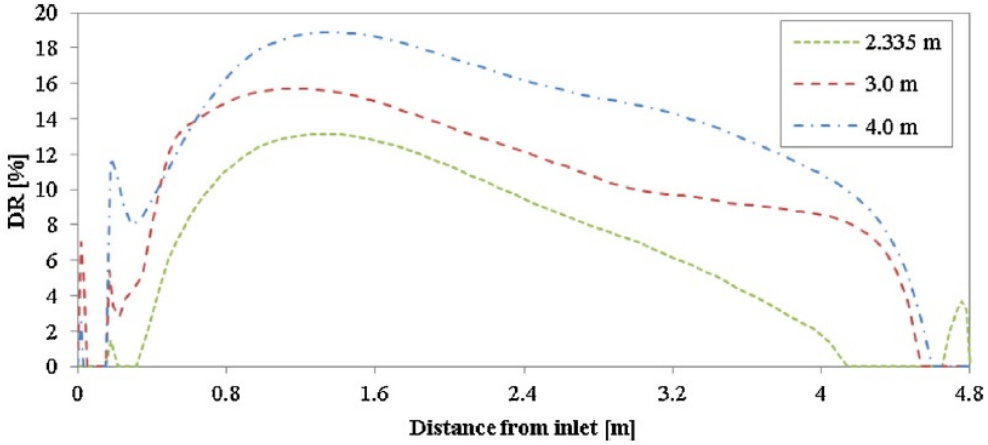

Figure 3.19. Draught risk as a function of room height [Zhang et al., 2015a]

As previous study by Nielsen et al. has shown that increasing the height of the room will increase the velocities in the room the results were verified by Zhang et al. [Nielsen et al., 2015]. The Figure 3.19 above indicates that by increasing the height of the room the intensity and strength of recirculation increases together due to the entrainment of ambient air [Zhang et al., 2015b].

Nielsen et al. also investigated the influence of the heat load distribution, ceiling height and ceiling design on air distribution in the room. The experiments were conducted on different cases with different room heights, heat load distributions and ceiling designs. Limitations of graph are based on maximum velocity in the room 0.15m/s and maximum temperature gradient of 2.5K/m where the results were plotted in Figure 3.20 below [Nielsen et al., 2017].

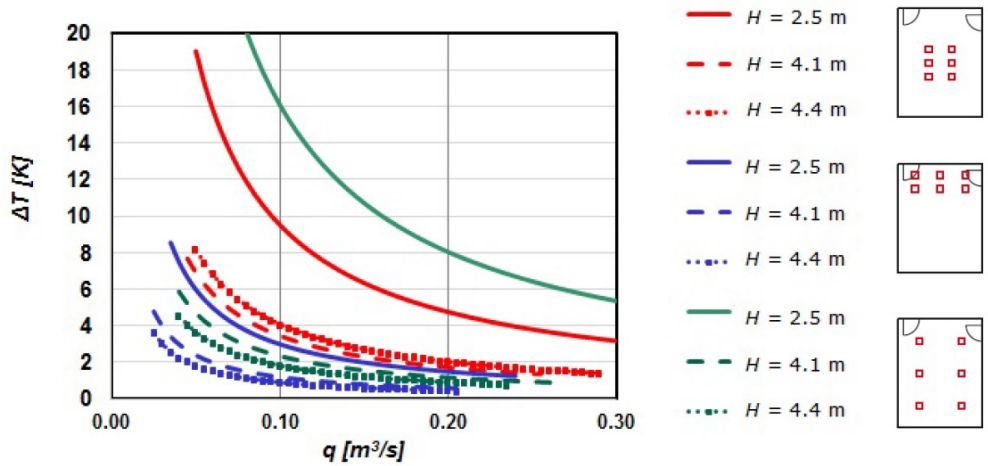

Figure 3.20. Design graph for different locations of the heat load in rooms with different height and different ceiling design [Nielsen et al., 2017]

As Figure 3.20 shows it is possible to have high air flow rate and big temperature difference between inlet and outlet without increasing the risk of draught. However, since the heat loads affect the air distribution in the room the orientation is very important as been confirmed previously by Zhang et al. studies [Nielsen et al., 2017].

3.4.3 Radiant cooling and heating

In order to save energy and ensure thermal comfort in office buildings with a cooling need throughout the whole year a novel system that combines natural ventilation and diffusion ceiling inlet coupled together with thermally activated building systems was proposed. It was stated that office room with typical 30-40W/m^2 heat load can save potentially up to 50% of energy. Moreover, this solution is sufficient enough during the winter seasons when the outside cooling potential is large but during the hot summer season the cooling potential of natural ventilation is limited and thermally activated building systems should be used for supplementary cooling or heating [Yu et al., 2015b].

Furthermore, after suggesting this novel system Yu et al. has conducted an experimental investigation of cooling performance of such system. By using thermally activated building systems and diffuse ceiling as air distribution system typical climates were simulated (extreme winter, normal winter, transitional seasons, normal summer and extreme summer). Internal heat loads were kept at two values 28.4W/m^2 and 57.7W/m^2 corresponding to the air change rate of 2h^{-1} and 4h^{-1} respectively. All tests were carried out on steady-state conditions. The results showed that by using TABS the inlet air can be either cooled or pre-heated before further supplied through the diffuse ceiling. With the air change rate of 4h^{-1} the inlet air to plenum for extreme winter conditions was heated up from -7.23°C to 10.84°C (ΔT= 18.07°C) and for extreme summer it was cooled down from 31.99°C to 19.56°C (ΔT = 12.43°C) [Yu et al., 2015a].

Another experiment conducted by Zhang et al. examined the performance of diffuse ceiling ventilation coupled with thermally activated building systems. Three cases with diffuse ceiling and thermally activated building systems are tested with constant heat load of 450.5W and constant air change rate of 2$h^{-}1$. First case imitates the winter period with supply temperature of -6.87°C, second transitional period with supply temperature of 9.46°C and last summer with supply temperature of 24.1°C. The temperatures of surfaces for thermally activated building system, diffuse ceiling and air temperature in plenum are plotted in the Figure 3.21 [Zhang et al., 2015a].

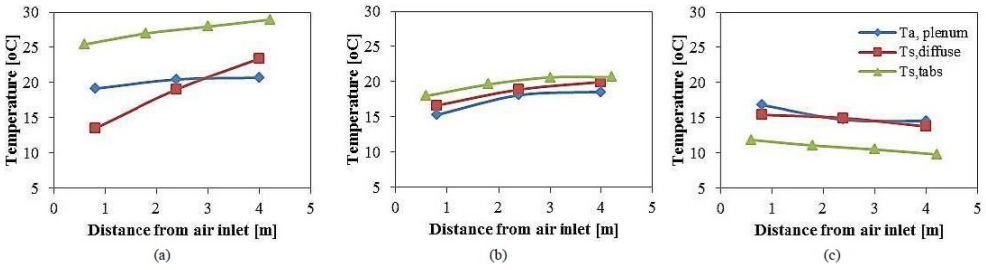

Figure 3.21. Temperature distribution in the plenum air, diffuse ceiling surface and slab surface as a function of distance from the inlet [Zhang et al., 2015b]

The plots clearly show that the air temperature distribution in the plenum is not uniformly distributed due to the fact that during the heating mode cold air is heated up with thermally activated building system and diffuse panel surfaces as it moves further into the plenum. It is also the indicator of not fully mixed air in the plenum because of different temperatures which leads to not uniform air temperature supply to the room.

However, the capability of air to be pre-heated or pre-cooled before the supply to the room is possible as indicated in the measurements [Zhang et al., 2015b].

3.5 Conclusion of literature review

After performing literature review on indoor air quality indexes, air distribution types, thermal comfort and characteristics of diffuse ceiling ventilation conclusions can be made.

- Indoor air quality can be measured by evaluating ventilation effectiveness and air change efficiency. Different air distribution lead to different ventilation effectiveness. However, coefficient of 1 has to be aimed in order to have fully mixed air in room. Furthermore, air exchange efficiency is dependant on the flow pattern, the aimed value is 50% or more.
- Two most common ventilation principles in non-industrial spaces are mixing and displacement ventilation. Despite the fact that they are most common they have their own drawbacks concerning the draught risk and vertical temperature gradient in the room. More sophisticated approach is using diffuse ceiling ventilation as air distribution system which can supply high air flow rates with big temperature differences between inlet and outlet without the risk of vertical temperature gradients or draught. Also, the flow can be momentum or buoyancy dominant depending on the ventilation rate.
- Many previous studies have shown the benefits of diffuse ceiling ventilation versus conventional air distribution systems. Through various experiments it can be seen that the risk of draught is minimized with diffuse ceiling ventilation. The highest risk of draught is at the height of the ankles 0.1m where the air recirculation appears. Furthermore, it has been shown that the vertical temperature gradients are usually less than 1K/m.
- Through experiments $\Delta T - q_0$ chart was developed with limits which ensure the thermal comfort in the occupied zone. Furthermore, it can be concluded that the rate of air flow does not influence the air distribution in the room, heat sources are the decisive factors how the air will move in the room with diffuse ceiling ventilation. In addition to that, room height and distribution of heat sources has a big influence on the risk of draught and the limitations for temperature differences and air flow. The possibility to pre-heat and pre-cool the air in the plenum is feasible. However, no uniform temperature distribution was noticed in the plenum zone

4 Numerical study of diffuse ceiling ventilation

In order to further investigate diffuse ceiling ventilation and its performance a numerical model can be created. By using a numerical model the performance of the system can accurately represent the experimental studies with low cost and less time if modelled correctly. The user can easily adjust the boundary conditions representing different scenarios and then conduct simulations to investigate the performance of the system under different circumstances. The model was created by the help of commercial CFD software.

Since diffuse ceiling is a novel ventilation system a learning process is needed to take place before the numerical study of the case is performed. This learning process has a main goal to gain knowledge and experience regarding numerical modelling of this type of ventilation system. Experimental and numerical analysis data was gathered from previous study by Zhang who has performed measurements on diffuse ceiling ventilation in similar conditions. By having information about Zhang's case numerical model can be built and then validated by comparing the current calculated results with her experimental data. After this learning process it will be possible to accurately perform the numerical analysis for further studies of this master thesis.

A procedure of verification and validation of Zhang's numerical model is presented in the Chapter 4. The criteria used by Zhang for the evaluation of indoor air environment in an office was the distribution of airflow and temperature. Therefore, the verification and validation of the model is mostly based on these two parameters. It is necessary to mention that Zhang used two numerical models in her study: a porous media model and a radiant model. The difference between these two models is the treatment of the diffuse ceiling as explained later in this Chapter 4. Zhang found out that in order to represent the experimental data accurately two models: a porous medium and a radiant model have to be combined. The radiant model aims to give some solutions to the limitations of the porous media model as explained further on. Since the aim of this phase is to gain experience and knowledge by validating Zhang's model the same approach is adopted. Initially, the porous media model is created and validated according Zhang's measurements in laboratory by using information obtained by her radiant model. After the porous media model is validated the next step is to create and validate the radiant model according information provided by Zhang.

4.1 Porous media modelling

4.1.1 Case setup

As previously mentioned the validation of the porous medium is done in accordance with Zhang's experimental measurements. Therefore, the case of the learning process needs to be identical to Zhang's case. The design of the case is based on diffuse ceiling ventilation system in an office with dimensions of 4.80m x 3.3m x 2.72m (length x width x height). The actual height of the room is 2.335m and above of it, there is air distribution space called plenum which has a height of 0.35m. The plenum and room are separated by the diffused ceiling which has a thickness of 0.035m. The room includes 2 occupants with a medium activity level of 1.2 met and their corresponding office equipment which is computers and lighting as the Figure 4.1 shows. The sizes, locations and heat load of the heat sources can been seen in the Table 4.1.

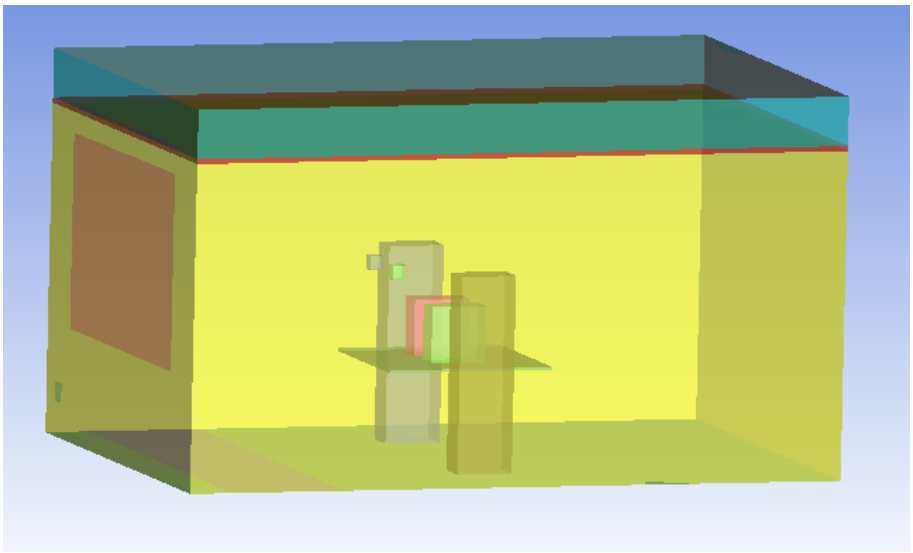

Figure 4.1. The geometry of the office investigated by Zhang

Table 4.1. The geometry of the office investigated by Zhang

Item	Length	Width	Height	Location			Heat load
	Dx, [m]	Dy, [m]	Dz, [m]	x, [m]	y, [m]	z, [m]	Q, [W]
Room	4.8	3.30	2.335				
Diffuse ceiling	4.8	3.30	0.035			2.335	
Plenum	4.8	3.30	0.350			2.37	
Window		2.30	1.400		0.5	0.80	
Exhaust		0.14	0.140		3.1	0.25	
Inlet		2,30	0.030		0.5	2.37	
Table	1.20	1.20	0.020	1.8	1.05	0.68	
Occupant 1	0.40	0.25	1.400	2.2	0.70		100
Occupant 2	0.40	0.25	1.400	2.2	2.35		100
PC 1	0.40	0.20	0.400	2.2	1.35	0.70	71
PC 2	0.40	0.20	0.400	2.2	1.75	0.70	67
Desk lamp 1	0.10	0.10	0.100	1.9	1.35	1.30	54
Desk lamp 2	0.10	0.10	0.100	1.9	1.75	1.30	59
Heat carpet	0.80	3.30		0.3			464

4.1.2 Verification of porous media model

The verification of the model aims to identify the physical phenomena for the case-problem and assess whether or not CFD is capable to represent it with accuracy [Srebric, 2011]. The case of investigation is a ventilation design thus the flow and heat transfer are needed to be predicted. The verification is performed for the following aspects:

- Basic flow features
- Turbulence models
- Auxiliary heat transfer and flow models
- Numerical methods

Basic flow features

The flow in an office is usually affected by heat transfer from the building's envelope, the heat sources located inside the room and the supply air. Therefore, the flow in the room is assumed to be mixed convection associated with conductive, convective, and radiative heat transfer[Srebric, 2011].

The porous media modelling in Fluent can not calculate the radiative heat exchange between the porous zone and other zones. To overcome this limitation a second numerical model called radiant model is required. This model treats the porous zone as solid thus the radiative heat exchange can be calculated. The resulting temperature of the room's surfaces from the radiant model can be used as input in the porous media model. In a perfect scenario the radiant model predicts with high accuracy the real temperatures of walls and then these values are used as boundaries conditions to the porous media model. In this case, the real temperatures of walls are used directly in the porous media model as boundary conditions since the creation of the radiant model has not been conducted yet. Table 4.2 lists the temperature of each surface of the room. These temperatures have

been obtained after measurements by Zang in the laboratory and are used as input in the model.

Table 4.2. Temperature of the room's surfaces

Surface	Temperature, [°C]
East wall	25.75
West wall	26.07
North wall	26.10
South wall	26.40
East plenum wall	19.30
West plenum wall	19.90
North plenum wall	19.55
South plenum wall	19.30
Plenum ceiling	20.05
Floor	26.00
Window	24.60

In addition, the internal heat sources are treated as surfaces heat fluxes on the occupants, computers and lamps. The heat sources release heat by convection and radiation. However, the effect of the radiative heat flow is taken into account in the radiant model from where the surfaces' temperatures are obtained thus it is necessary to be excluded in the porous media model. Zhang followed the ASHRAE Handbook instructions and estimated the convective fraction for the different heat sources. It is assumed that the convection heat flow released by computers is approximately 90% while the occupants and lamps release 50% of their total heat load [Chen Zhang, 2016]. The same values of heat fluxes are used for the validation of the porous media model. The corresponding values are listed in the Table 4.3.

Table 4.3. Heat fluxes of heat sources

Heat source	Heat flux, [W/m^2]
Occupants	26.0
Lamp 1	450.0
Lamp 2	491.7
PC 1	114.1
PC 2	106.9

As mentioned previously the supply air characteristics also influence the heat transfer in the room. The supply air which used in Zhang's experiments has a temperature of 8.95°C and a velocity of 0.34 m/s thus the same data used for the validation of porous media model.

Turbulence models

Since the case concerns a ventilation design in an office a steady-state flow simulation is sufficient to predict the flow characteristics. The air through the porous material has very low velocity and the flow is laminar. However, the internal heat sources generate thermal plumes increasing the turbulence levels of the flow. In such case, a turbulence model is needed to approximate the flow characteristics. The RNG k-ϵ model is used as it can be considered the most appropriated turbulence model for indoor environment simulations[Chen Q., 1995].

In addition to the turbulence modelling the near-wall treatment has to be defined. The Standard wall function is the most common approach for near wall modelling when the boundary layer is not the main concern. It can give reasonable accuracy and less computational time since it does not account the viscous sub-layer. However, the validity of the Standard wall function is affected when the mesh is too dense along the boundaries. The Scalable wall function works in the same way as the Standard wall function with the only difference that it can be applied to finer meshes too. For this reason, the Scalable wall function is used as it can be considered more flexible for simulating the air flow in cases where the resolution of grid varies among different boundaries.

Auxiliary heat transfer and flow model

As previously mentioned, Zhang used coupling between two numerical models to predict the airflow of a diffuse ceiling ventilation design. The first model called radiant model has a solid diffuse ceiling. The solid material has some slots to penetrate the air from the plenum to the room. The second model is the porous media model. In this model the diffuse ceiling is composed of a porous material and its properties can be seen in the Table 4.4. Compared to the radiant model the porous media model treats the diffuse ceiling surfaces as a fluid zone in Fluent. The Figure 4.2 illustrates the two different models. The radiant model and the porous media model are illustrated on the left and right side respectively.

Table 4.4. Properties of porous material

Type	Thermal conductivity $[W/m \cdot K]$	Thermal capacity $[J/Kg \cdot K]$	Density $[Kg/m^3]$
Porous material	0.085	932	343.8

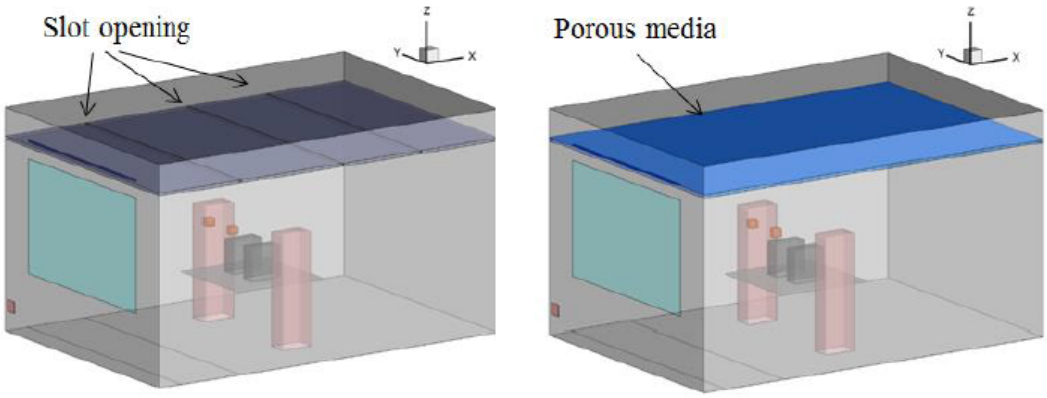

Figure 4.2. The two different models used by Zhang [Chen Zhang, 2016]

The reason for creating two numerical models is to overcome some limitations. In the porous media model the diffuse ceiling is treated as fluid zone making it incompatible with radiative heat exchange[Chen Zhang, 2016]. This is why a radiant model is built separately. Since the diffuse ceiling of the radiant model is composed of a solid material is able to account for radiation. As is previously mentioned the temperatures of the walls calculated by the radiant model are used directly as boundary conditions in the porous media model. In addition to that, the radiant model can estimate the radiative heat exchange between porous media and other zones. This radiative heat flux can be implemented as an input energy source in the porous media model. For this initial phase of the learning process, the main concern is the validation of the porous media model, this is why the radiative heat flux is taken directly from Zhang's radiant model. The radiative heat flux of the porous zone is equal to 319 W/m^3.

The porous media model is created to simulate the flow through diffuse ceiling material. The principle behind the porous modelling is the additional momentum sink in the governing momentum equation. This extra source composes two parts a viscous loss

and an inertial loss term[Ansys]. The Equation (4.1) refers to the extra momentum sink regarding porous modelling.

$$S_i = -(\frac{\mu}{\alpha} \cdot v + C_2 \cdot \frac{1}{2} \cdot \rho \cdot |v| \cdot v) \tag{4.1}$$

Where
S_i - Momentum sink $[kg/(s^2 \cdot m^2)]$
v - Superficial velocity $[m^3/(s \cdot m^2)]$
ρ - Density of fluid $[kg/m^3]$
μ - Viscosity of fluid $[kg/(m \cdot s)]$
α - Permeability $[m^2]$
C_2 - Inertial resistance factor $[m^{-1}]$

The viscous resistance and inertial resistance coefficients are obtained after measurements in a laboratory. Zhang conducted measurements regarding the pressure drop across the diffuse ceiling for different air velocities. After a quadratic regression analysis of the measured values the coefficients of the viscous and inertial resistance can be calculated. These values are used directly from Zhang measurements for the validation of the porous media model. According Zhang's measurements the viscous resistance and inertial resistance coefficient equal to 1.14 $\cdot 10^8 m^{-2}$ and 33055 m^{-1} respectively.

Numerical methods

The geometry of the room has rectangular shape. Even thought the internal heat sources are not actually rectangular it is not necessary to represent them by their fitted coordinates as the contribution of their geometrical shape on the airflow is small. In addition, the use of rectangular objects helps in building a structured mesh which leads to much faster convergence with the finite volume method. Structured Hexa-meshes were created in the entire domain and denser meshes were generated in the critical areas for instance around the heat sources diffuse ceiling inlet and outlet. Moreover, the meshes were refined along the walls in order to account the velocity gradients in the boundary layers obtaining more reliable results. The Figures 4.3 and 4.4 illustrate an example of the model with structured Hexa-mesh.

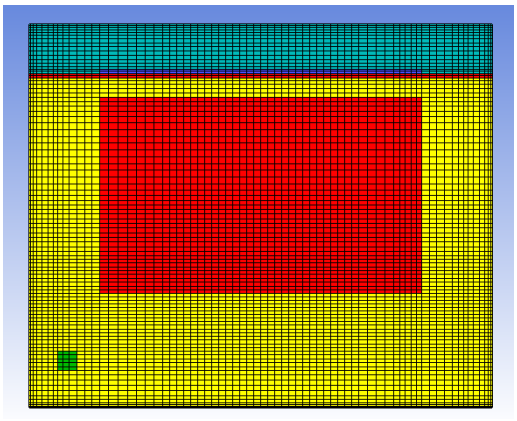

Figure 4.3. East-wall of the model

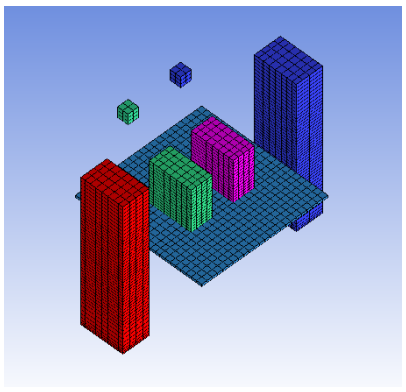

Figure 4.4. Internal objects in the room

In order to ensure the credibility of the mesh it is necessary to perform grid independence test. This test guarantees that the final results of a simulation are not affected by the size of the mesh but only by the boundary conditions. The grid independence test results can be seen in the Table 4.5.

Table 4.5. Grid independence test for porous media model

Mesh size	Average temperature, [°C]	Average velocity, [m/s]	Mass flow balance, [%]	Energy unbalance rate, [%]
205000	25.25	0.062	0	0.56
500000	25.05	0.066	0	2.95
1100000	24.90	0.067	0	4.60

As it can be seen from the Table 4.5 the mass balance has been obtained in all simulations. In addition to that, the energy unbalance rate is less than 5% in all the simulations. These low rates of unbalance indicate that the steady state has been reached in all the simulations and the results have converged. Moreover, the values of the average temperature and velocity of all grids are close enough to each other. Since the mesh of half million has almost the same results as 1.1 million cells the half million is chosen due to less computational time compared to the bigger grid.

The SIMPLE algorithm is chosen for the simulation, where the second order upwind differencing scheme was employed to minimize the false diffusion[Allard et al., 2007]. The convergence criteria are set to be lower than 10^{-3} for all absolute residuals expect for energy residual which is set to be lower than 10^{-6}. For ensuring the convergence of simulations monitoring of important values is also performed. For example, the volume average temperature and velocity of the room and mass and heat transfer rate of the system are monitored. The convergence of a simulation is considered only if all the monitoring values reach a stability in their magnitude.

4.1.3 Validation of porous media model

After the porous media model has been created the next step is to validated in accordance the provided experimental data in order to ensure the its ability to predict with accuracy the airflow pattern and the temperature distribution. As mentioned before, Zhang conducted experiments in the laboratory and measured the air temperature and velocity in different points in the room. In order to measure the air velocity and temperature Zhang used moveable columns where thermocouples and anemometers were mounted along their heights. The points where the measurements had been performed can be seen in the Figure 4.5 while the locations of the sensors along the columns can be seen in the Figure 4.6. The experimental data of both air velocity and temperature in all these measurement points have been provided by Zhang in order to be used in validating the numerical model for the sake of the learning process.

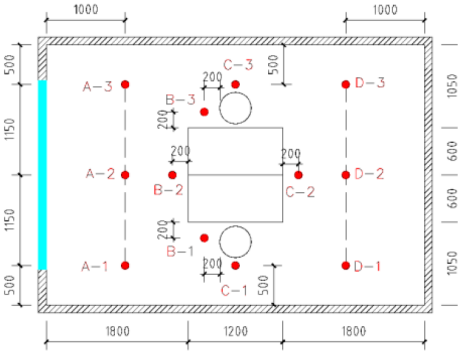

Figure 4.5. Location of columns [Chen Zhang, 2016]

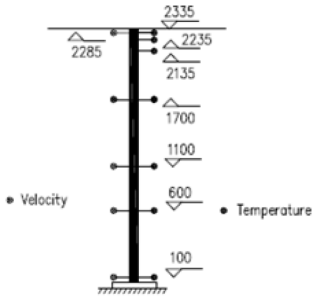

Figure 4.6. Location of sensors along each column
[Chen Zhang, 2016]

To keep brief this chapter only the results of A-2, B-2, C-2, and D-2 column are used for comparing the measurements with the calculated results. The selection of these columns aims for checking the model's validation in all the length of the occupied zone. The comparison between the Zhang's experimental data and the results of the numerical model for the selected columns is presented in the Figures below.

The Figures from 4.27 to 4.30 represent the comparison of the temperature gradient along the columns. The blue lines represent the temperatures calculated by the porous media model whereas the orange bullets represent the temperatures measured by Zhang during the her experimental procedure.

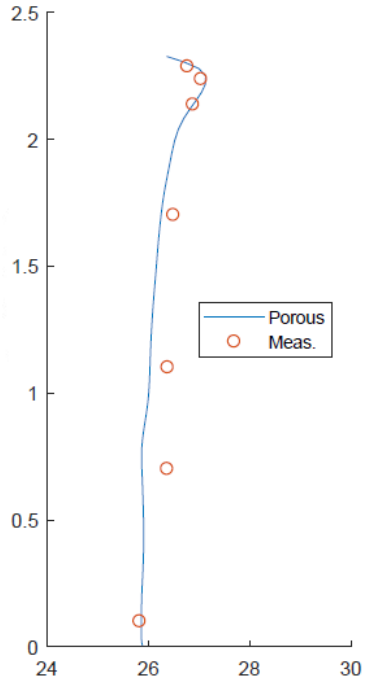

Figure 4.7. Temperature along A-2

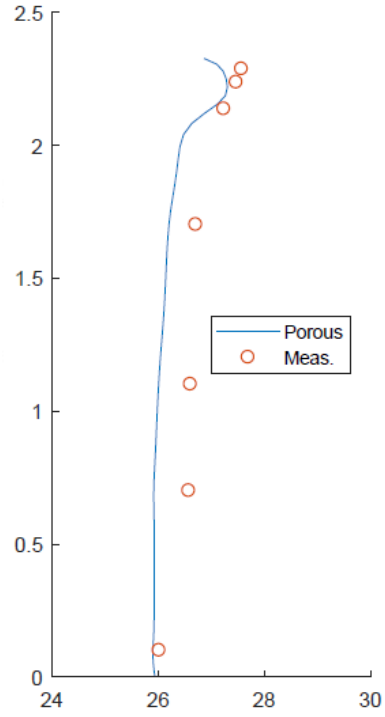

Figure 4.8. Temperature along B-2

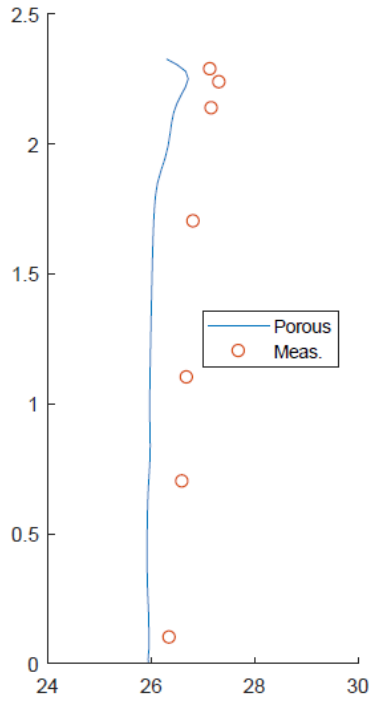

Figure 4.9. Temperature along C-2

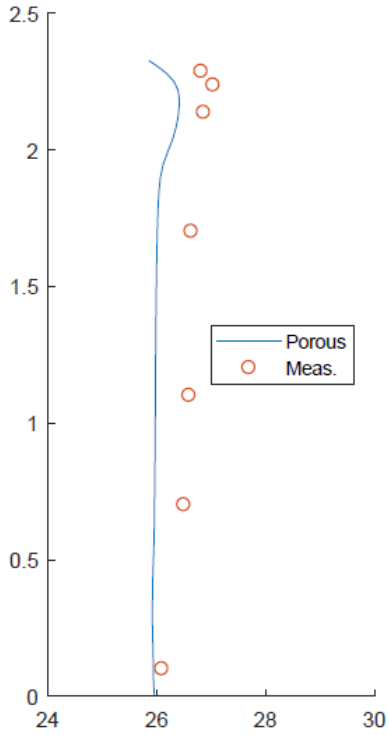

Figure 4.10. Temperature along D-2

The above Figures show that the numerical model can provide acceptable range of results regarding the tendency of the temperature distribution in the room. The tendency of the temperature gradient in the room calculated by the porous model seems almost identical to that one of the measurements. Nevertheless, it can be seen that the model underestimates the temperatures in the room in all the measured points. However, these differences between experimental data and calculated results are assumed acceptable since they do not exceed 3% of deviation. This small deviations may occur because of the wrong estimation of the convective fraction applied to specify the thermal load of the heat sources. However, this is not a big issue since a slight increase of the convective heat fraction of the heat sources can be applied easily in the CFD model. It can be concluded that the numerical model seems to underestimate the temperatures in the room but the deviations are are small enough to consider the model's results acceptable.

The Figures from 4.11 to 4.14 represent the comparison of the velocity gradient along the columns. The blue lines represent the velocities calculated by the numerical model whereas the orange bullets represent the velocities measured by Zhang during the her experiment procedure.

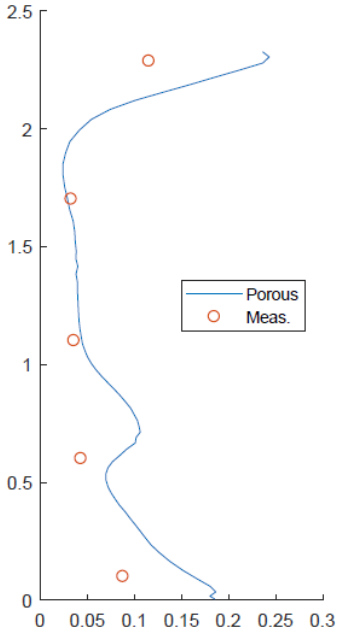

Figure 4.11. Air velocities along A-2

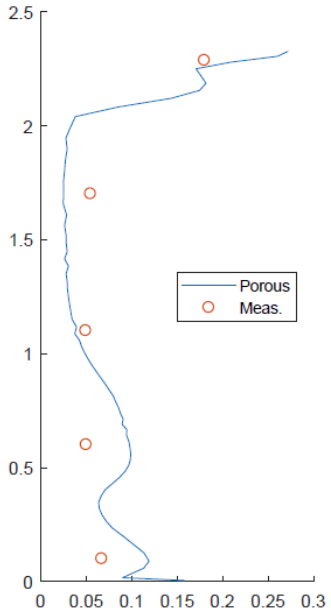

Figure 4.12. Air velocitiest along B-2

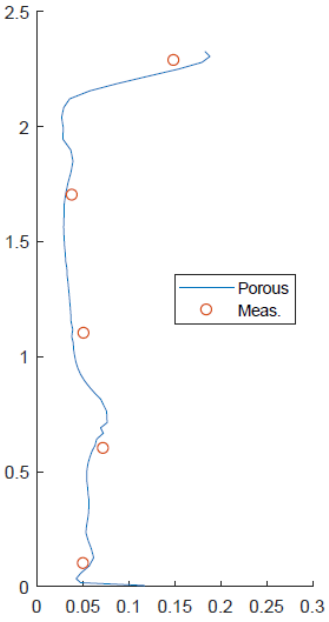

Figure 4.13. Air velocities along C-2

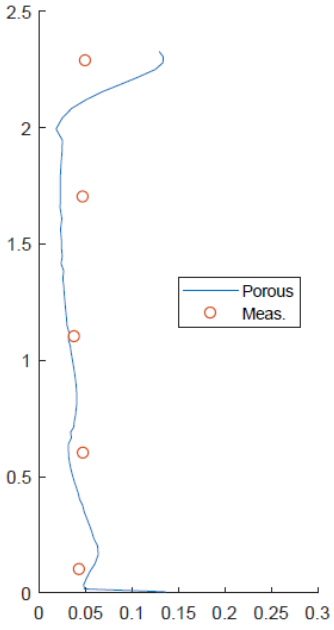

Figure 4.14. Air velocities along D-2

The Figures above show that the porous model can estimate the velocities in the room with relative high accuracy. The tendency of the velocity gradient calculated by the porous model follows the tendency of the velocity gradient measured during the experiments and their values are very close. However, there is a significant deviation regarding the velocities close to the diffuse ceiling panels especially in column A-2 and D-2. An explanation for this fact can be that the porous model overestimates the effect of buoyancy flow generated by the thermal plumes. The selected columns for comparison are located relatively close to the heat sources as it can be seen from the Figure 4.5 thus this region include thermal plumes generated by these heat sources. In general, the porous model can provide acceptable results regarding the estimation of air velocities except in the region very close to the diffuse ceiling in columns nearby the heat sources. However, this fact it can be assumed as a minor issue since those points are out of the occupied zone, therefore any miscalculation there from the numerical model will not influence the conclusion regarding the indoor comfort.

Moreover, the plenum is also a space of interest for validation since its configurations can influence the air and temperature distribution of the room. Zhang performed measurements at the mid-height of the plenum too. The points in plenum where Zhang measured air velocities and temperatures can be seen in the Figure 4.15.

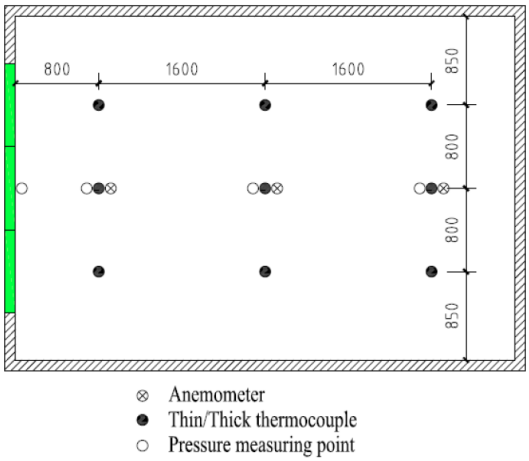

Figure 4.15. Points for measurements in plenum zone [Chen Zhang, 2016]

The Figure 4.16 illustrates the comparison of the horizontal temperature distribution along the plenum. The blue line represents the calculated temperatures in the plenum by the porous model whereas the orange bullets represent temperature distribution in plenum measured by Zhang during her experimental procedure.

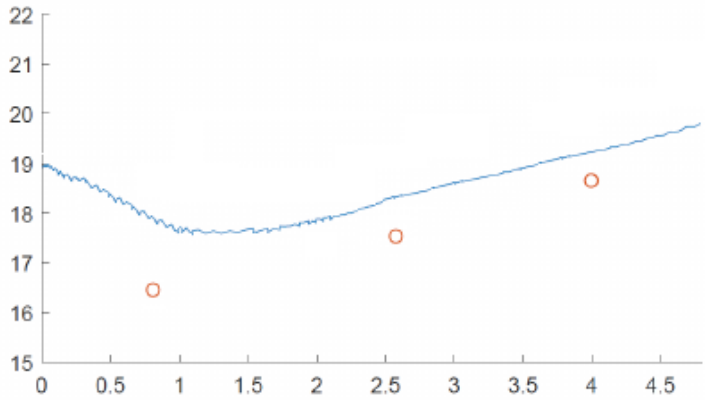

Figure 4.16. Temperature distribution along the plenum

As the above Figure 4.16 shows the porous media model can predict the tendency of the horizontal temperature distribution. The temperature of the plenum east wall is 19.3°C whereas the plenum west wall has 19.9°C temperature as they have been defined in the model's boundary conditions that is why the tendency of temperature in the plenum has these two values as starting and ending point. Moreover, as it can be seen the temperature drops to almost 17.5°C at 1m distance from the inlet because of the cool supply air. In addition, the temperature rises gradually with the distance from inlet. This happens because the cold supply air has a trend in moving downwards to the hot room through the porous zone just after entering the plenum thus the biggest amount of cold supply air does not penetrate into the deeper parts of the plenum. It seems that the model calculates the air temperature 1-2 °C higher than the measurements. However, these deviations can be considered acceptable since there is a large temperature range along the plenum making the air distribution more complex.

Overall, the porous media model seems to predict the airflow and temperature distribution in the office in acceptable range. In addition, the calculated results are close enough to the measurements in most of the points of interest. However, there are minor deviations which can be assumed acceptable considering the complexity of the porous media modelling.

4.2 Radiant model

As previously mentioned, the porous media model treats the diffuse ceiling surfaces as a fluid zone making it incompatible with the radiative heat exchange between porous and other zones. Therefore, it is necessary to have a second model which treats the diffuse ceiling surfaces as a solid material. This model is built separately and is called radiant model. The results of this model are used in the porous media model as boundary conditions as previously explained in Section 4.1. For the validation of the porous media model results from Zhang's measurements and her radiant model had been directly used. However, it is necessary to create and validate a radiant model for obtaining knowledge for this part as well. In this section the creation and validation of the radiant model are described. The validation is done in accordance with the results of Zhang's radiant model and her measurements regarding wall's temperature during her experimental procedure.

The set up for the radiant model has some differences compared to those of the porous media model. These differences are described in the following subsections. Any other parameter which is not mentioned regarding the radiant model can be assumed the same as the porous media model.

4.2.1 Case setup

Geometry

The validation of the radiant model is based on the results of Zhang's radiant model and temperature of walls measured by Zhang during her experiment, therefore the geometry of the two models needs to be identical. In the radiant model, the porous zone becomes a solid material thus the complex diffuser is replaced by simple rectangular slots. The opening area of these slots needs to represent the porosity of the diffuse ceiling panels. Zhang estimated the opening area of the slots based on pressure drop measurements across the diffuse ceiling. The effective opening area of the slots is calculated in accordance with the Equation (4.2)

$$C_d A = \frac{\dot{m}}{\sqrt{2 \cdot \rho \cdot \Delta P}} \tag{4.2}$$

Where
C_d - Discharge coefficient [-]
A - Opening area [m^2]
$\dot{m}$ - Mass flow rate [kg/s]
ρ - Density of fluid [kg/m^3]
ΔP - Pressure drop across diffuse ceiling panels [$kg/(s^2 \cdot m)$]

According to Zhang's measurements the porosity of the diffuse ceiling can be represented by three slot openings with an effective area of 0.032 m^2 (3.2 m x 0.01 m) each. Zhang assumed a uniform distribution of the slots along the diffuse ceiling as illustrated in the Figure 4.17 therefore the same approach is adopted for the validation of the radiant model.

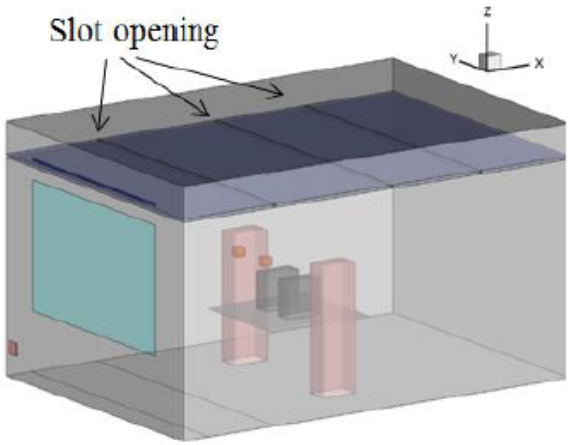

Figure 4.17. Radiant model of Zhang's study [Chen Zhang, 2016]

Numerical model

The aim of the radiant model is to calculate the temperature of the office's surfaces and also the radiative heat exchange between the porous zone and other zones. Therefore, it is necessary to account the radiation heat transfer which is why the surface to surface radiation model is activated. This radiation model calculates the radiative heat flux leaving a given surface based on the Stefan-Boltzmann law and view factors concept as the Equation (4.3) indicates.

$$q_{rad,k} = \varepsilon_k \cdot \sigma \cdot T_k^4 + \rho_k \cdot \sum_{J=1}^{N} \cdot F_{k,j} \cdot q_{rad,j} \tag{4.3}$$

Where
$q_{rad,k}$ - radiative heat flux leaving surface k [W/m^2]
ε_k - Emissivity of surface k [-]
σ - The Stefan-Boltzmann Constant [$W/m^2 \cdot K^4$]
T_k - Temperature of surface k [K]
ρ_k - Reflectivity of surface k [-]
$F_{k,j} \cdot q_{rad,j}$ - Radiative flux incident on the surface k defined by View factors [W/m^2]

Boundary conditions

As mentioned before, in the porous media model the temperatures of the external walls are directly specified as boundary conditions after a simulation of the radiant model. However, in the radiant model the convective, conductive and radiative heat transfer through walls need to be taken into consideration. Therefore the wall boundaries are defined as mixed thermal conditions where the properties of the room's envelope must be specified. The emissivity and the convective heat transfer coefficients of the room's surfaces used in the radiant model have been defined by assumptions in order to reach Zhang's measurements and are listed in Table 4.2. The free stream temperatures and external radiation temperatures correspond to the measured by Zhang air temperatures in the laboratory. The wall boundaries of the radiant model can be seen in the Table 4.6 whereas the properties of each wall are listed in the Table 4.7. The diffuse ceiling surfaces are defined with the same material as defined in the porous media model whose properties are presented in the Table 4.2.

Table 4.6. Wall boundaries of the radiant model

Surface	Heat transfer Coefficient, $[W/m^2 \cdot K]$	Free stream & External radiation temperature, $[^oC]$	Internal & External emissivity, [-]	Material	Thickness, $[m]$
Wall-East	5	9.45	0.90	Walls&floor	0.33
Wall-West	5	24.17	0.90	Walls&floor	0.26
Wall-North	5	24.17	0.90	Walls&floor	0.26
Wall-South	5	24.17	0.90	Walls&floor	0.26
Plenum-East	5	9.45	0.90	Walls&floor	0.33
Plenum-West	5	24.17	0.90	Walls&floor	0.26
Plenum-North	5	24.17	0.90	Walls&floor	0.26
Plenum-South	5	24.17	0.90	Walls&floor	0.26
Window	5	9.45	0.97	Facade	0.33
Floor	5	24.17	0.90	Walls&floor	0.26
Plenum ceiling	5	27.47	0.90	Ceiling	0.25

Table 4.7. Properties of materials used for wall boundaries

Wall type	Thermal conductivity, $[W/m \cdot K]$	Thermal capacity, $[J/m \cdot K]$	Density, $[kg/m^3]$
Walls&floor	0.046	790.4	700
Facade	0.214	840.0	700
Ceiling	0.170	798.8	700

As previously mentioned in this model the radiative heat transfer is taken into account therefore the heat sources release heat through both convection and radiation. Contrary to the porous media model where the radiative heat flow was excluded from the heat sources in the radiant model it is necessary to be included. The heat fluxes and the emissivity of the internal heat sources used in the radiant model can be seen in the Table 4.8.

Table 4.8. Heat fluxes and emissivities of heat sources in the radiant model

Heat source	Heat flux, $[W/m^2]$	Emissivity, [-]
Occupants	52.8	0.5
Lamp 1	900.0	0.1
Lamp 2	983.3	0.1
PC 1	126.8	0.1
PC 2	118.8	0.1

4.2.2 Grid independence test for the radiant model

As mentioned earlier, a grid independence test is necessary in order to prove the credibility of the mesh. Three different sizes of mesh are used for the grid independence test as the Table 4.9 shows. All the simulations have been performed under the same boundary conditions in order to check the influence of the mesh's size on the final results.

Table 4.9. Grid independence test for the radiant model

Mesh size	Average temperature, [°C]	Average velocity, [m/s]	Mass flow balance, [%]	Energy unbalance rate, [%]
400000	25.6	0.075	0	3.3
700000	24.4	0.068	0	3.5
1000000	24.3	0.067	0	0.2

As the above Table shows, in all the simulations the mass and energy balance has been obtained. However, it can be noticed that the final results are dependent on the mesh's size. The grid consisted of 400 thousand cells gives results with relative high deviations from the other grids. On the other hand, the grid with 700 thousand gives similar results as the biggest mesh which has 1 million cells. Therefore, this mesh is chosen as the final grid for the radiant model since can give reliable result in less computational time than the largest mesh.

4.2.3 Validation of the radiant model

After the choice of the final mesh for the radiant model the next step is to check for its validation. As mentioned earlier the validation of the radiant model of this study is done in accordance with the results of Zhang's radiant model and her measurements of the walls' temperature during her experimental procedure. The Table 4.10 compares the temperatures of the room's surfaces calculated by the radiant model created for learning purposes and Zhang's measurements during her experiment.

Table 4.10. Comparison Zhang's measurements and the radiant model

Surface	Zhang's measurements, [°C]	Radiant model, [°C]	Deviation, [%]
East wall	25.75	25.67	0.3
West wall	26.07	26.06	0.0
North wall	26.10	26.15	0.2
South wall	26.40	26.14	1.0
East plenum wall	19.30	19.20	0.5
West plenum wall	19.90	21.30	6.9
North plenum wall	19.55	20.60	5.3
South plenum wall	19.30	20.60	6.7
Plenum ceiling	20.05	21.90	4.4
Floor	26.00	26.13	0.5
Window	24.60	24.80	0.9

As it seems from the above Table 4.10 the temperatures calculated by the radiant model are close enough to the temperatures measured by Zhang during the experiment. The small deviations between the results of the model and measurements can be due to the rough estimation of emissivity and convective heat transfer coefficients in the wall boundaries. As it can be noticed, the bigger deviations occur for the plenum walls. It seems that the radiant model cannot estimate the temperatures of plenum walls with the

same accuracy as calculates the temperatures of room walls. However, the deviations of the results are relatively small since the biggest between them is only around 7%. Therefore, the calculated results of the radiant model can be assumed acceptable which means that the model can be considered validated since the results deviate very little from the experimental data.

In addition to that, it is necessary to validate the energy source previously used in the porous media model. As mentioned before, an energy source calculated by the Zhang's radiant model was added directly to the porous model as boundary conditions. This energy source was provided directly by Zhang thus it is necessary to be checked whether the radiant model made during the learning process can estimate the same radiative heat flux as Zhang's radiant model. The comparison of the the energy source calculated by the two different radiant models can be seen in the Table 4.11.

Table 4.11. Energy sources provided by Zhang and radiant model

Zhang's radiant model, $[W/m^3]$	Radiant model, $[W/m^3]$	Deviation, [%]
319	330	3.9

As we can see from the above Table 4.11 the energy source calculated by the radiant model of this study is very close to the energy source calculated according to Zhang's radiant model. There is a deviation of 3.9%, but it can be considered acceptable since it is relatively small. The small difference between the two values may be due to the different emissivity and convective heat transfer coefficients of room's surfaces that Zhang used in her radiant model. In a nutshell, the radiant model made for learning purposes seems to be able to validate Zhang's simulation and measurements with relatively high accuracy since its results regarding temperatures of walls and the radiative energy source are very close to her results.

According to Zhang the distribution of temperature and air velocity in a room which is ventilated by diffuse ceiling ventilation system cannot be predicted by a radiant model alone. That is why Zhang used coupling between a radiant and a porous media model. Despite the fact that is already known that a radiant model alone cannot estimate distribution of air flow it is good to show that the same conclusion is obtained also in this learning process.

The following Figures show the comparison between radiant and porous model created during the learning process regarding their prediction of the temperature and airflow distribution. The same columns which had been used to prove the validity of the porous media model are used also for the comparison between the two different models. The results of the porous model are indicated by blue lines, the results of the radiant model are indicated by red lines and the orange bullets represent the measurements by Zhang in the the laboratory.

The Figures from 4.18 to 4.21 present the comparison between the two models regarding the temperature distribution in the room.

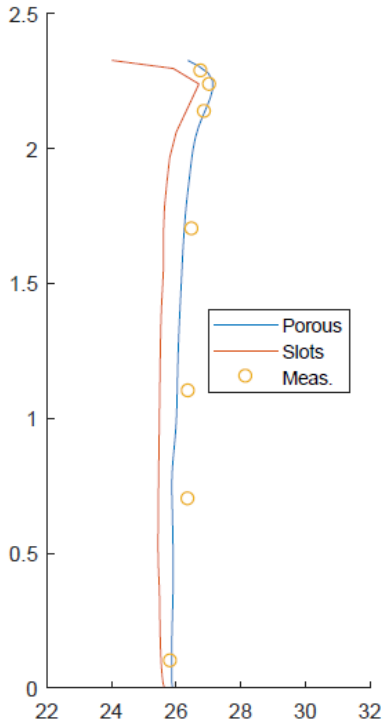

Figure 4.18. Temperature gradient along A-2

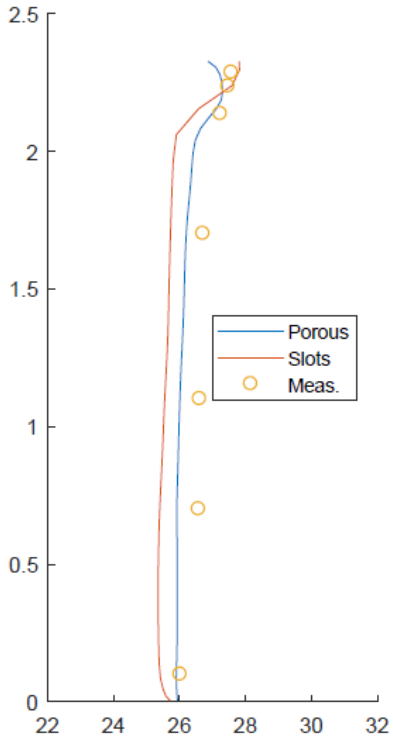

Figure 4.19. Temperature gradient along B-2

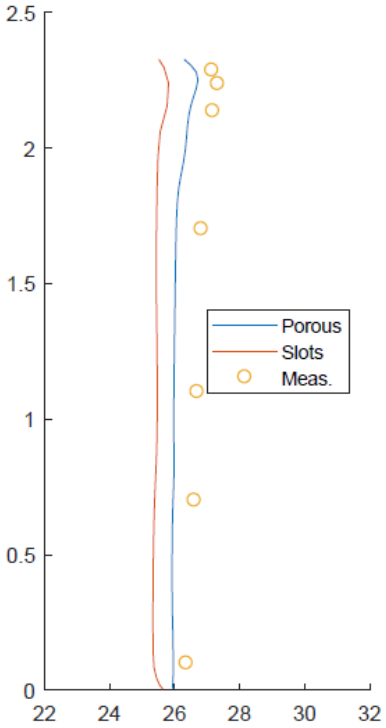

Figure 4.20. Temperature along C-2

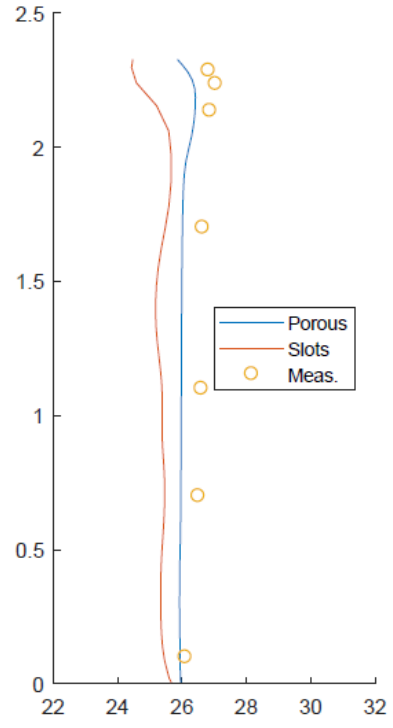

Figure 4.21. Temperature along D-2

From the above Figures it can be noticed that the two models fit quite well regarding the tendency of temperature distribution in the room. However, the radiant model seems that underestimates the temperature in the room ever more than the porous model. Even though most of the deviations between the two models are relatively small, it is obvious that the porous media model can predict better the temperature distribution in the room in all the measured points. As it seems, the porous media model can give more accurate results regarding the temperatures in the the room that is why the coupling between porous and radiant model is seems more reliable to be used in future studies instead of the radiant model by its self alone.

The Figures from 4.22 to 4.25 present the comparison between the two models regarding the airflow distribution in the room.

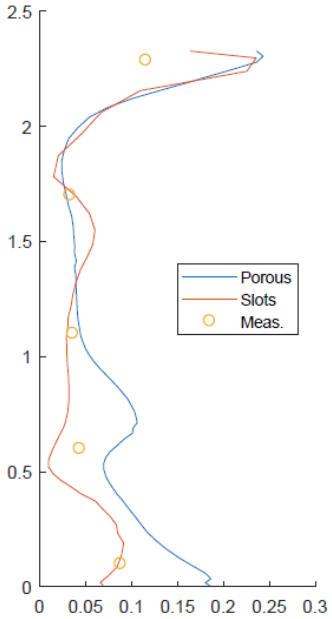

Figure 4.22. Air velocities along A-2

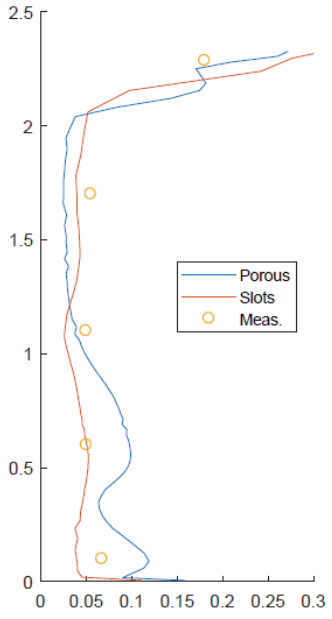

Figure 4.23. Air velocities along B-2

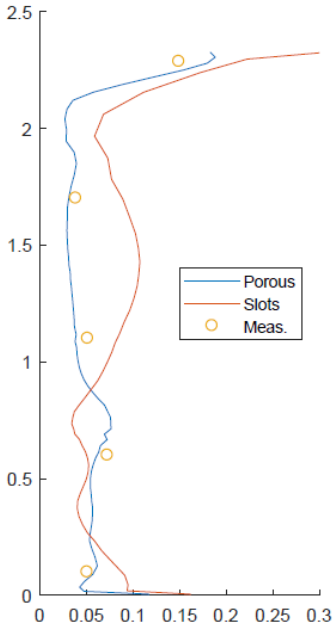

Figure 4.24. Air velocities along C-2

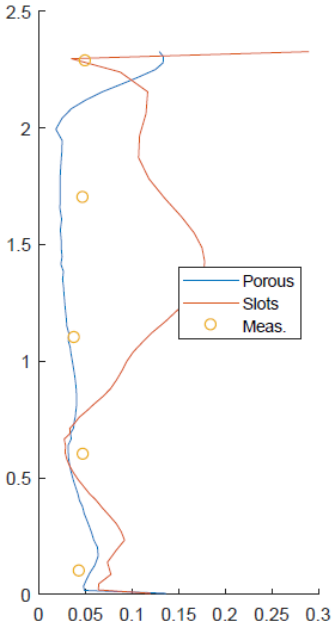

Figure 4.25. Air velocities along D-2

From the Figures above it can be noticed that the porous media model has a better performance than the radiant model on predicting the airflow distribution. In most of the cases both models can predict with relatively high accuracy the tendency of the velocity distribution in the room. However, there are points where the radiant model shows limitations in predicting the air velocities in the room. More specific in column D-2 the radiant model gives velocities with relatively high deviation from measurements. In addition to that the radiant model seems that predicts even a different tendency of velocity distribution along the column C-2 and D-2 compared to the measurements. Since radiant model's results follow a different tendency than the measurements at some points it can be concluded that is an inappropriate model for predicting the velocities in a room which is ventilated by a diffused ceiling ventilation system.

As the results show the radiant model has been proved as an inappropriate model for predicting both temperature and air distribution in an office ventilated by a diffused ceiling system. However, the performance of the model may be affected by the distribution of the slots along the diffuse ceiling. As the Figure 4.17 shows Zhang has chosen 3 vertical slots distributed uniformly on the diffuse ceiling surface. Zhang has made an assumption that this uniformly vertical distribution can properly represent the porosity of the diffused ceiling. However, this is still an assumption and a further investigation is needed. That is why a new distribution of slots along the diffused ceiling is necessary to be investigated so that a conclusion can be made regarding its influence on the performance of the radiant model.

It has been decided to investigate the scenario where vertical and horizontal slots occur together along the diffused ceiling surface. However, it is necessary to keep the total effective opening area of slots identical as previously which equals to $0.092m^2$. This

effective area has been calculated to represent the actual porosity of the diffused panels thus it is necessary to keep it the same in any other case of slot distribution. The new distribution of slots can been seen in the Figure 7.1. The horizontal slots have dimensions of 4.8m x 0.006m each whereas the vertical slots have 0.006m x 3.2m each.

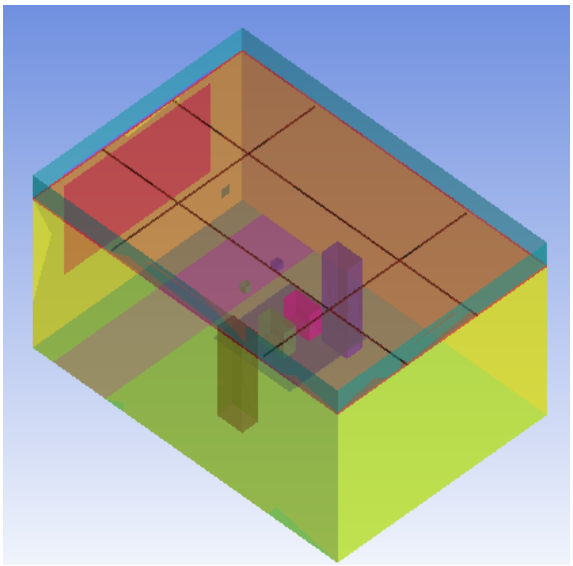

Figure 4.26. New radiant model with different distribution of slots

As mentioned before, the grid independence test is needed to confirm that the final results of a simulation are not influenced of the resolution of the grid. That is why a grid independence test is conducted for the new radiant model where the results are presented in the Table 4.12.

Table 4.12. Grid independence test for the new radiant model

Mesh size	Average temperature, [°C]	Average velocity, [m/s]	Mass flow balance, [%]	Energy unbalance rate, [%]
470000	22.85	0.083	0	4.0
800000	22.81	0.080	0	3.5
1400000	22.80	0.079	0	2.6

In Table 4.12 it can be seen from mass and energy balance that the simulations have converged. It also shows that the different grid sizes give close to the same results which proves grid independence. However the results of the denser mesh are presented with intention to show whether or not the new slot distribution can give reliable results in regards temperature and airflow distribution in the room.

The Figures from 4.18 to 4.21 present the comparison between the new radiant model (4-slots), the previous radiant model (3-slots) and porous medium model regarding the temperature distribution in the room. The results of the new radiant model are indicated by yellow lines whereas the results of the previous radiant and of porous model are indicated by red and blue lines respectively. In addition the the purple bullets represent the measurements by Zhang in the laboratory.

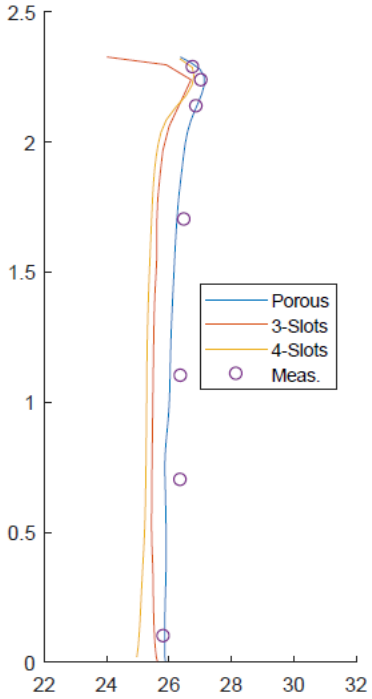

Figure 4.27. Temperature along A-2

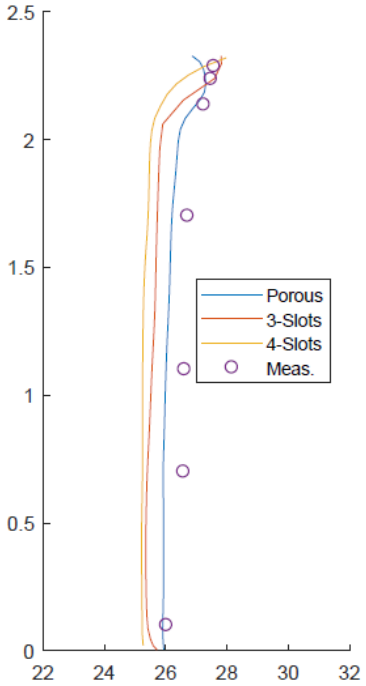

Figure 4.28. Temperature along B-2

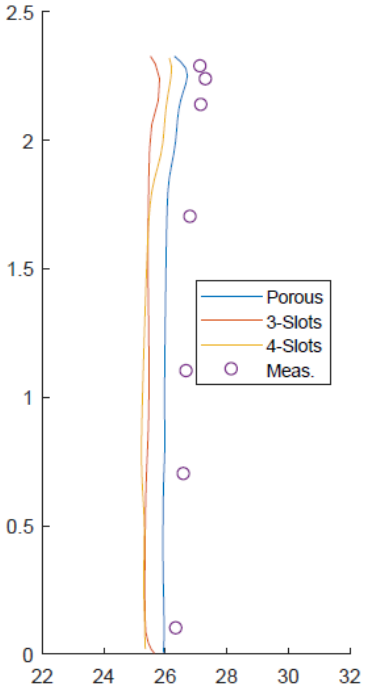

Figure 4.29. Temperature along C-2

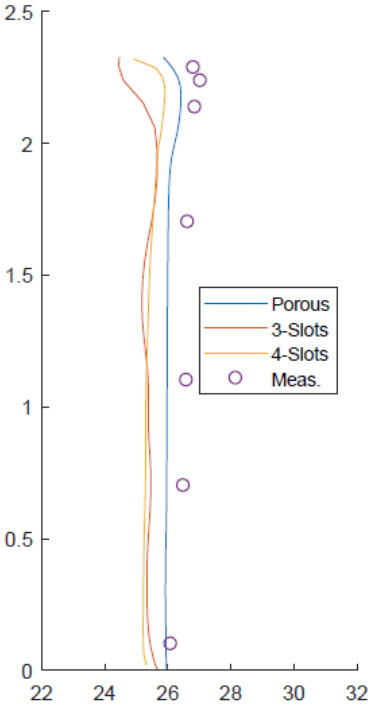

Figure 4.30. Temperature along D-2

As it can be noticed from the above Figures the new radiant model does not show any significant improvement in predicting the temperature distribution in the room . It seems that the two different radiant models give similar results and tendencies of temperatures along the columns. Therefore, the different slot distribution of the radiant model does not improve its performance in predicting the temperature distribution in the room. The porous model has a more accurate prediction of temperatures in the room than any of the radiant models and its use is necessary for accurate results in future studies.

The Figures from 4.31 to 4.34 present the performance of the new radiant model regarding the airflow distribution in the room.

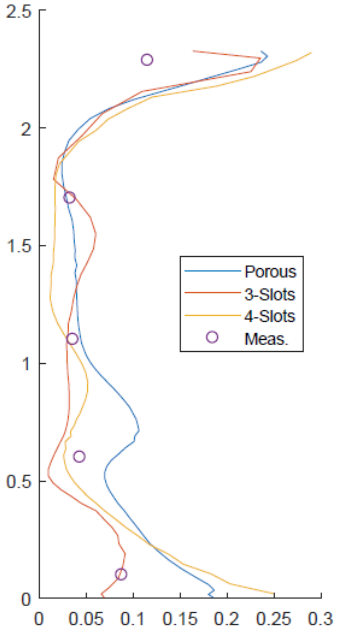

Figure 4.31. Air velocities along A-2

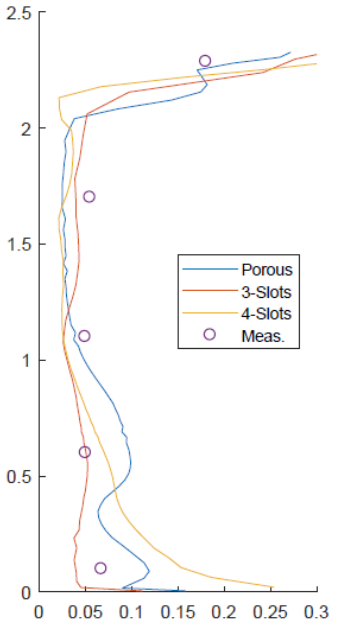

Figure 4.32. Air velocities along B-2

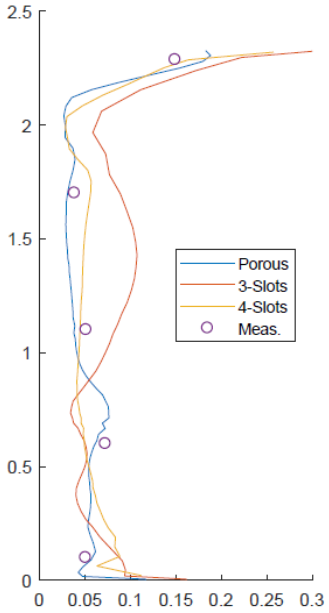

Figure 4.33. Air velocities along C-2

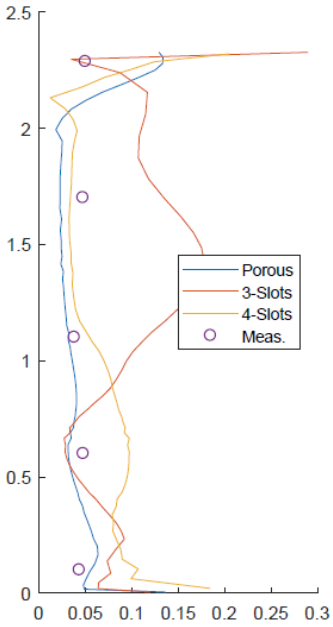

Figure 4.34. Air velocities along D-2

As it can be seen from the above Figures the air flow distribution calculated by the new radiant model has some differences compared to that one calculated by the previous radiant model. In the previous radiant model, the main concern was the wrong prediction of the airflow distribution in middle part of the column C-2 and D-2 which is not an issue in the predictions of the new radiant model. However, the new radiant model shows limitation is other points. In the lower points of columns A-2 and B-2 the new radiant model gives different tendency of air flow distribution than the measurements. In a nutshell, it can be concluded that the slot distribution of the radiant model affects the prediction of the air velocities. However, as the Figures 4.31 and 4.32 show the new radiant model with 4 slots still presents some limitations regarding the prediction of air velocities in the room. It is obvious that the porous model has a much better estimation of the air flow distribution than the 2 different radiant models thus its use is necessary for future studies.

Taking everything into consideration it can be concluded that the coupling between porous medium and radiant model is necessary since the porous media model can give more accurate results than any radiant model alone. By performing the coupling of those two models the prediction of both temperature and airflow distribution can be conducted with relatively high accuracy. Since the two different radiant models did not show any significant difference in predicting the temperature distribution the first distribution of slots (3-slots) is decided to be used for future studies since it has been successfully used by Zhang as well and also can be created with less cells than the 4-slots model.

4.3 Conclusion

By the end of this Chapter 4 some conclusions can be made. The coupling between a porous and a radiant model is necessary for obtaining reliable predictions regarding air velocities and temperatures in a room ventilated by diffused ceiling system. In addition to that, it has been proved that the slot distribution of the radiant model does not have any significant influence on the performance of the radiant model regarding the prediction of temperature distribution but has influence on the airflow distribution in the room.

Performing these numerical analyses knowledge and experience in creating and validating numerical models related to diffused ceiling ventilation systems has been obtained. This process helped to find out how to successfully perform coupling between a radiant model and a porous in order to get reliable results for proceeding to further study of this master thesis.

Part II

Experimental Analysis

5 Experimental setup and measurements

Chapters before this were focused on covering previous experimental and numerical studies on diffuse ceiling ventilation, their results and discoveries. Further chapters will focus on this thesis primary aim - indoor environment quality evaluation and its experimental and numerical study. In particular, Chapter 5 covers the set up and results of experiment in the laboratory.

5.1 Hot box and cold box layout

In the initial stages of the thesis it was aimed to use a guarded hot box (GHB) for the measurements. The advantage of this setup is that the heat losses through the walls can be controlled by the air temperature inside the air cavity which is situated in between the internal and external wall of the hot box. However, due to technical difficulties in the laboratory this function could not be set up and the cavity temperature could not be controlled. Therefore, the air from laboratory is circulated through the gap and it is assumed that the cavity temperature is equal to the ambient of the laboratory. Figure 5.1 below presents the hot box from North side and schematic layout of the guarded hot box.

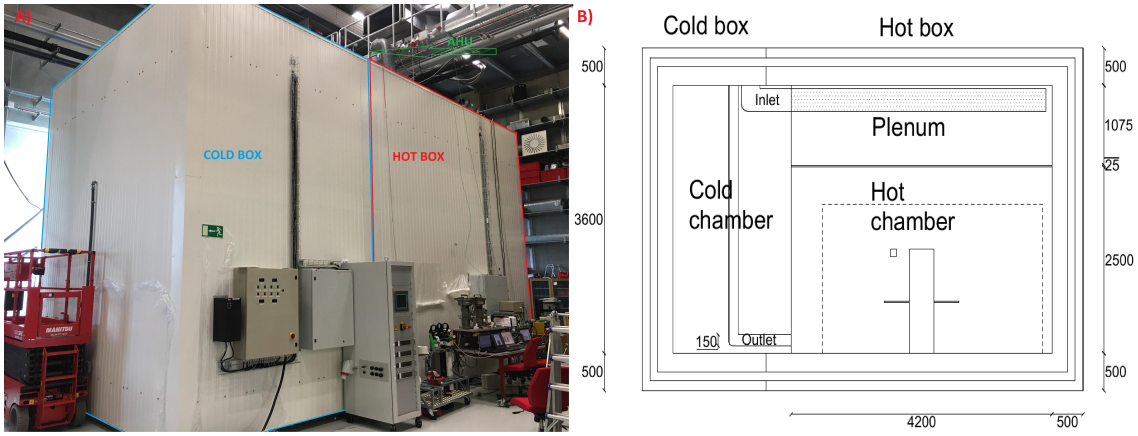

Figure 5.1. A) Guarded hot box in the laboratory B) Schematic layout of guarded hot box

Cold chamber and hot chamber are separated with 1.4cm thickness Plywood board. The properties of the façade wall are presented in Table 7.6 and 7.5 in Chapter 7. Main purpose of having a thin wall with high thermal transmittance value is to reach thermal equilibrium faster since the heat transfer is higher with bigger U-value.

Furthermore, blue lines in Figure 5.1 A) outline the cold box part where the outdoor conditions are simulated with 4 powerful lamps and air conditioning system which can be seen in the Figure 5.2 below.

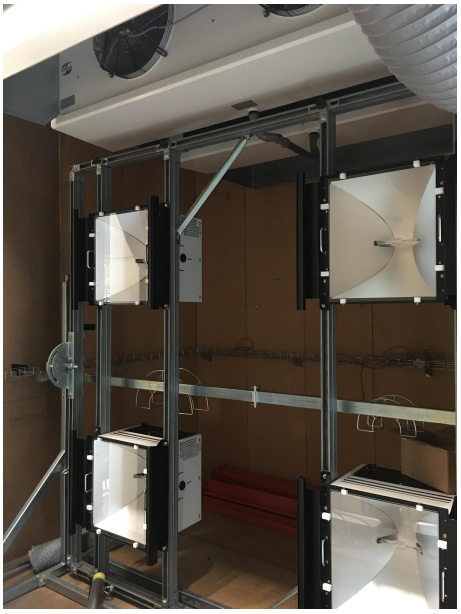

Figure 5.2. Cold box part

However, this part could not be set up before actual measurements so it was used as a "lid" for the hot chamber in order to shield it from the ambient conditions. This would result in less entrainment of surrounding air into the box and give more stable results for temperatures, velocities and CO_2 measurements.

Moreover, in the Figure 5.1 A) above red lines outline the hot chamber. This is the part where indoor environment quality is evaluated. It includes diffuse ceiling, mannequins, lamps, computers, heat carpet, anemometers, thermocouples and CO_2 analysers. The visual setup can be seen in the Figures 5.4 and 5.3 below.

Figure 5.3. Setup of the room without measuring devices

Figure 5.4. Setup of the room with measuring devices

The heat loads are distributed symmetrically in the room since everything is positioned in the centre of the room. Each person has a lamp, monitor and a computer box. Every heat source has a certain output of heat which is controlled by the equipment presented in the Figure 5.5 below.

Figure 5.5. RKT-2 voltage regulator combined with a HEWa-21 watt-meter

In order to set accurate output of heat RKT-2 voltage regulators are connected with copper wires to HEWa-21 watt-meters. This allowed to read the actual power output in watts for each controllable heat source placed in the room at any time because there were a few heat sources with a fixed power output.

In addition to that, every person and point contamination source is connected to a tracer gas tank with N_2O gases to imitate the respiration of CO_2 and furniture/building emissions in the room. Since the properties of both gases are very similar N_2O were chosen as a mutual agreement between students and supervisors. The gas tank can be seen in the Figure 5.6 below.

Figure 5.6. Gases used for the experiment and equipment control test

The other two gas tanks contained 100% N_2 and N_2O gases. These gases were not used for evaluating indoor environment quality. They were mandatory for running a control

test of gas analyser equipment. Also calculated values of volumetric flow from the mouth and point contamination source are presented in the Table 7.9 in Section 7.3. In the end according to the based assumptions each person exhales 20.4 l/h N_2O [Hyldgaard et al., 1997]. The point contamination source is assumed to release 40.8 l/h N_2O which is equal to the case with two persons.

5.1.1 Air supply to the plenum

Furthermore, the air to the plenum is distributed through the fabric duct which goes through the whole length of the room as presented in the Figure 5.7 below.

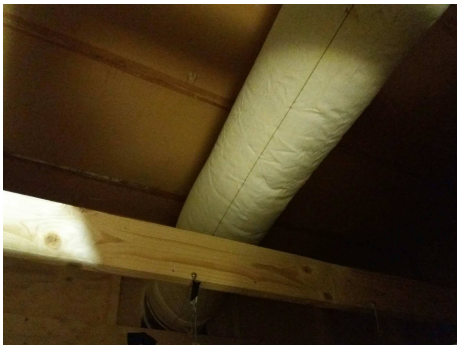

Figure 5.7. Fabric duct in the plenum

Compared to the previous study of diffuse ceiling by Zhang where the inlet was a slot opening, fabric duct was chosen to have a more uniform distribution of air in the plenum. In order to achieve inertial resistance and viscous resistance coefficients for further modelling in CFD, pressure drop tests were conducted across fabric duct material and diffuse ceiling. The results and methodology of the experiment is presented in the Appendix A.

5.1.2 Air handling unit

The air to the plenum is supplied through the air handling unit which is situated on the top of the hot box as previously presented in the Figure 5.1. The flow rate is controlled by frequency converters according to the pressure drop over the orifice plate which was monitored by Debro Meebush Micromanometer which can be seen in Appendix B.1. Furthermore, in order to control the temperature of the inlet air, R410A refrigerant was used. The flow to the cooling coil in the AHU was controlled by floating point controller. Figure 5.8 presents the AHU and controller for the setup.

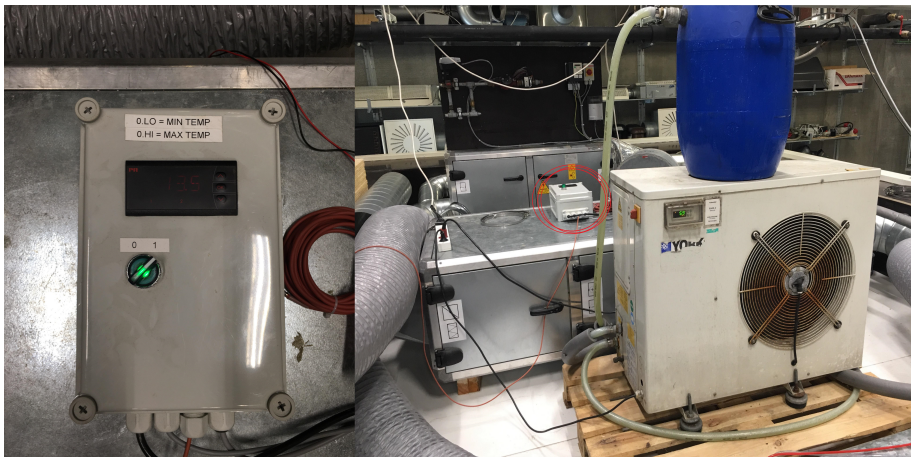

Figure 5.8. Floating point controller for inlet temperature and AHU

It should be noted since it is floating point controller and knowing the principle of how it works the temperatures of the inlet were not very stable. The supply temperatures were fluctuating erratically and were not very stable as can be seen from the Figure 5.9 below.

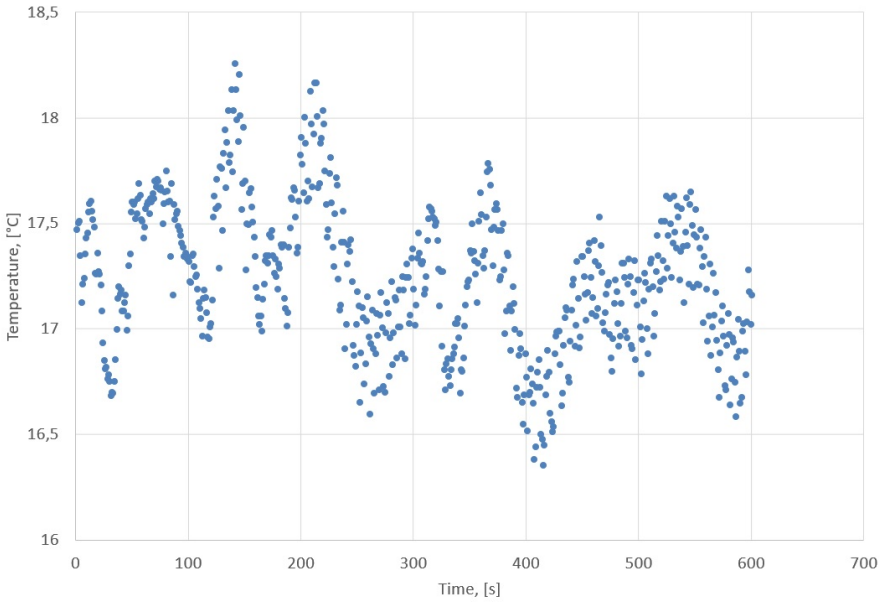

Figure 5.9. Behaviour of inlet air supply temperature

5.1.3 Diffuse ceiling panels

Since this thesis analyses diffuse ceiling porous medium is used. Wood-cement panels were used for the experiment. Panels can be seen in the Figures 5.10, 5.11 and 5.12.

Figure 5.10. Porous medium from the side

Figure 5.11. Porous medium in the room

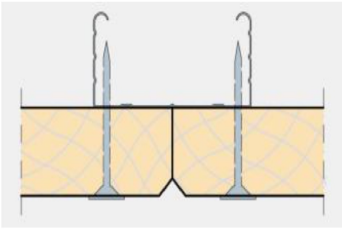

Figure 5.12. Connection of panels by type C-profile [Chen Zhang, 2016]

Since the panels are not 'fully diffuse ceiling' and are installed with C-profile some assumptions are made. Panels are drilled through with a nail in order to cling them to the metal suspension profile due to that it is assumed that some of the panels might not be air tight. This might lead to crack flow through the junctions or back flow to the plenum from the room.

Each ceiling panel had different dimensions due to the geometry of the room but filled the ceiling area minimizing junctions and crack flow possibilities. The physical properties of wood-cement panels are presented in the Table 5.1 below.

Table 5.1. Physical properties of diffuse ceiling

Density, $[kg/m^3]$	Conductivity, $[W/m \cdot K]$	Specific heat capacity, $[J/kg \cdot K]$	Porosity, [%]
359	0.085	923.3	65

In addition, the gap between top of the ceiling and beginning of the suspended ceiling is equal to 1.065m as presented in further Subsection 5.3.

5.2 Equipment for the experiment

In order to proceed to the experiments it is necessary to define a certain amount of equipment that is needed for measuring different variables of interest. The temperatures in the room, plenum and at the ventilation inlet and outlet are measured using thermocouples. The air velocity in the room is measured using anemometers whereas the volumetric flow rate at inlet and outlet is measured by manometer combined with orifice plate. The concentration of N_2O is measured by a Bruel & Kjaer indoor environment analyser which collects the contaminant concentration into 1 or more channels through tubes that can be modified to collect from 1 or more points at a time. The specifications of the measuring equipment are in Table 5.2.

Table 5.2. Equipment for measuring variables

Variable	Parameter	Equipment
Air temperature	Room air temperatures	Thermocouples
	Inlet air temperature	Thermocouples
	Exhaust air temperature	Thermocouples
Air velocity	Room air velocities	Anemometers
Flow rate	Inlet flow rate	Manometer and orifice plate
	Exhaust flow rate	Manometer and orifice plate
Contamination levels	Contamination distribution in room	B&K collector
	Contamination distribution in plenum	B&K collector
	Contamination distribution in fabric duct	B&K collector

In Table 5.3 the number of measuring equipment used to measure the parameters highlighted in Table 5.2 is shown.

Table 5.3. Amount of equipment

Equipment	Position	Variable	Number	Note
Thermocouple	Plenum	T_{plenum}	9	
	Room	T_{room}	5x6	Stationary pole
	Ambient	T_{amb}	5	
	Inlet	T_{in}	1	
	Fabric duct	T_{fbr}	2	
	Exhaust	T_{out}	1	
Anemometer	Room	V_{room}	5x6	Stationary pole
Manometer	Inlet duct	q_{in}	1	
	Exhaust duct	q_{out}	1	
B & K Collector	Room	C_{room}	3x6 ch.	Stationary pole
	Plenum	C_{plenum}	2 ch.	
	Inlet	C_{in}	1 ch.	
	Fabric duct	C_{fbr}	2 ch.	
	Exhaust	C_{out}	1 ch.	

It is important to mention that each of the used equipment has an uncertainty of the measurements. Listed below are the uncertainties of the equipment:

- To measure temperatures in the room K-type thermocouples were used with an accuracy of $\pm 0.15K$. In order to log the temperatures Helios data logger and ice point were used [Chen Zhang, 2016]. They can be seen in Appendix C.
- Air velocities were measured by using hot sphere anemometers. Accuracy of the equipment is $\pm 0.01m/s$ $+5\%$ of possible reading error [Chen Zhang, 2016]. Further information on anemometers can be found in Appendix C.
- Inlet and outlet flow rates were measured by using orifice plates which were connected to supply and exhaust fans respectively. The pressure drop across orifice plate was measured with manometer. It is assumed that the accuracy of air flow rate is $\pm 5\%$. [Chen Zhang, 2016]

- To perform pressure drop test for fabric duct material and diffuse ceiling FCO15 micro manometer was used. Accuracy of this equipment is assumed to be $\pm 0.25\%$. [Chen Zhang, 2016]
- In order to calibrate thermocouples temperature inside the ISOCAL had to be monitored. For that case F200 Precision Thermometer was used with an accuracy of $\pm 0.01K$. [ASL, 2014]
- To monitor the N_2O concentration in the room Bruel & Kjaer multipoint sampler and dozer type 1303 was used. Accuracy of dosage calculation is $\pm 2\%$. [INNOVA, 2016]

5.3 Location of measurement points

5.3.1 Room

As mentioned before in the earlier chapter the focus of this thesis is indoor environment quality in the occupied zone thus measurements in the hot chamber will be only conducted in the occupied zone. According to the definition of occupied zone in Table 2.1 at Chapter 2 boundaries in the room are described. Figure 5.13 below presents the positions of the poles equipped with measuring devices and sensors in the occupied zone which is marked by dashed line.

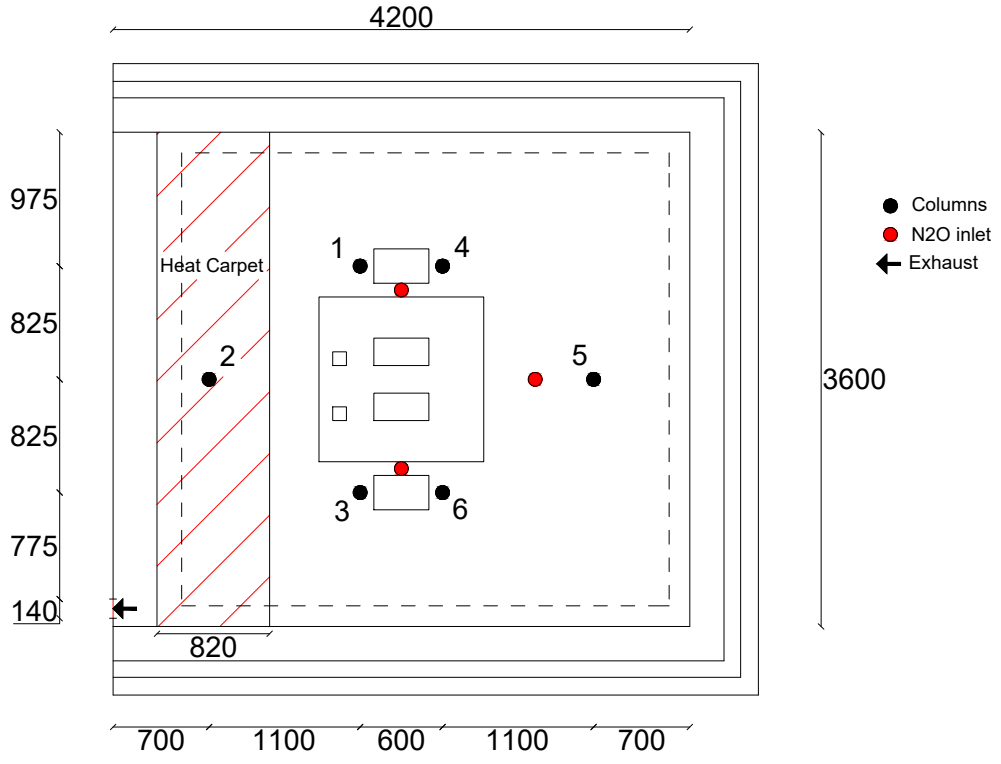

Figure 5.13. Experimental set-up of the Hot and Cold box.

It has to be noted that the positioning of the poles were chosen according to the preliminary CFD simulations. The model was set up with 3 ACH in order to identify the critical zones in the occupied zone in since the number of poles and measuring equipment was limited. In order to minimize the disruption of indoor conditions it was decided to

set up 6 poles which could satisfy all the required measurements without entering the room and reconnecting the cables or moving the poles in different positions. The results of preliminary simulations can be seen in the Figures 5.14, 5.15, 5.16 and 5.17 below.

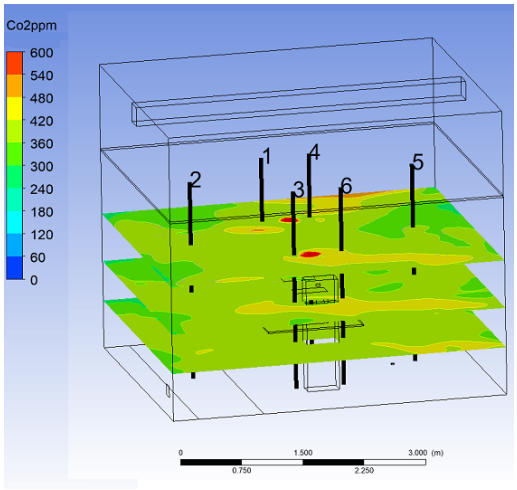

Figure 5.14. Horizontal planes for N_2O concentration distribution at 0.6m 1.1m 1.7m heights

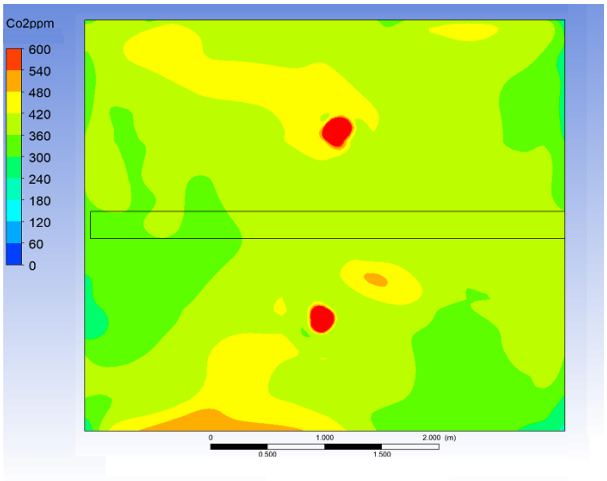

Figure 5.15. Horizontal plane for N_2O concentration distribution at 1.7m height with view from above

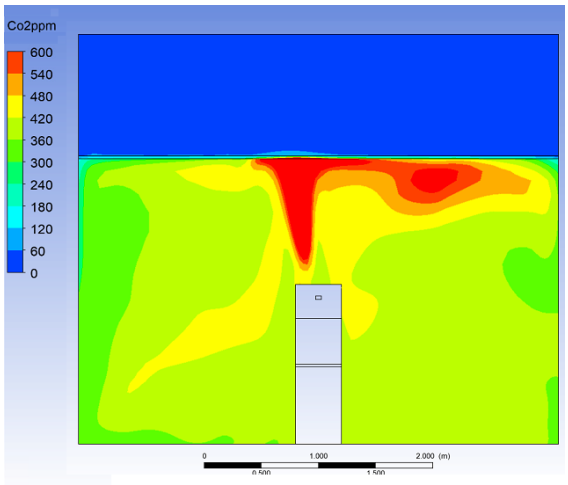

Figure 5.16. Vertical plane for N_2O concentration distribution on the exhaust side

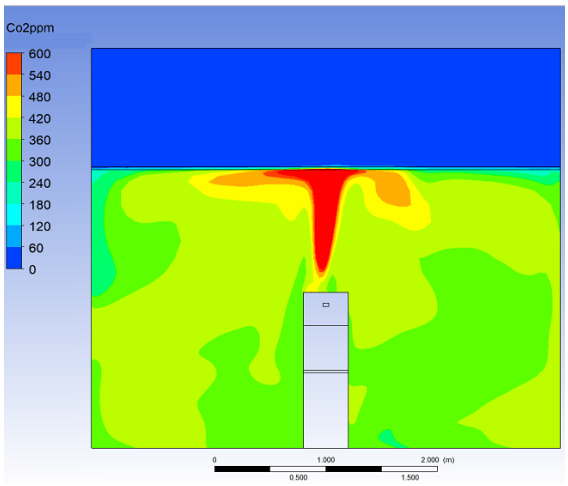

Figure 5.17. Vertical plane for N_2O concentration distribution further from the exhaust side

As it can be seen from Figures 5.13 and 5.14 poles 1;3;4;6 are positioned close to the persons in order to measure temperature and velocity gradients and evaluate comfort of people. Furthermore, same poles close to the persons have tubes which analyse the N_2O concentration in the room. Pole number 2 is positioned in the front of the room close to the façade wall and relatively close to the outlet of air. It is needed to mention that this pole stands above the heat carpet which imitates solar gains and emits 410W of heat. Due to that the temperature distribution on this pole should be affected by additional heat source beneath. Pole 5 is stationed in the end of the room with purpose of checking the farthest measuring point from the outlet and checking whether comfort criterias are met.

All of the poles have temperature, velocity and N_2O sensors. The distribution of sensors is presented in the Figure 5.18.

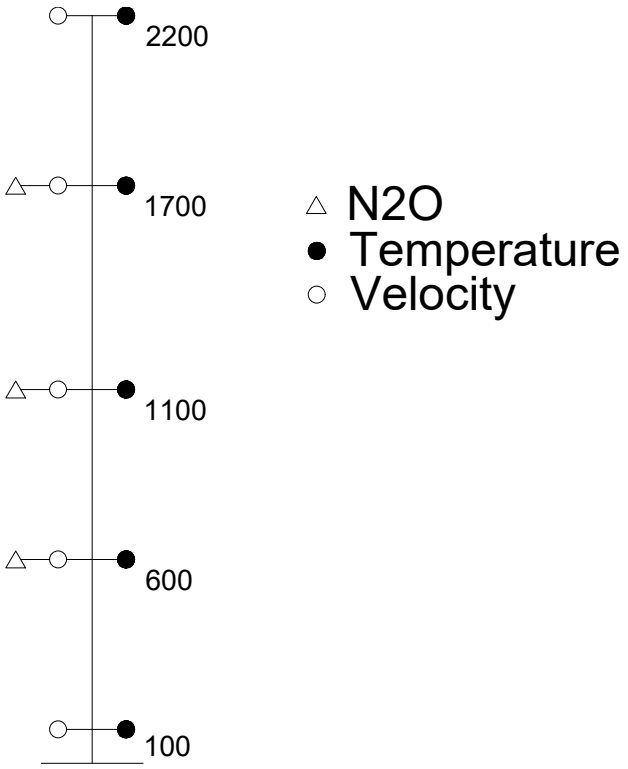

Figure 5.18. Setup of a column used for temperature and velocity measurements

To measure temperatures K-type thermocouples were chosen. The whole methodology of calibration and more information of thermocouples is presented in the Appendix C.1. Heights for measuring temperatures were chosen according the most sensitive parts of person: ankles 0.1m, sitting person neck 1.1m and standing person neck 1.7m. In addition to that intermediate points of 0.6m and 2.2m were chosen to have a more detailed information of temperature and velocity gradient in the room. Moreover, positions of anemometers were chosen according the same criteria as temperature sensors. The methodology of calibration and more information on anemometers is presented in the Appendix C.2.

5.3.2 Plenum

Even though main point of interest is in the occupied zone below the diffuse ceiling it was decided to measure temperatures and N_2O concentrations in the plenum. Firstly, N_2O is measured in order to see whether there is back flow from the room to the plenum through the porous medium. Secondly, the temperatures are measured to monitor the air distribution in the plenum. Finally, temperatures and N_2O concentrations are also measured inside the fabric duct, in the beginning and at the end. Two temperature sensors are put in the beginning and end of the duct to monitor the temperature drop along the fabric duct and levels of N_2O are also monitored to check whether there is a back flow

inside the fabric duct. Placement of sensors in the plenum are presented in the Figures 5.19 and 5.20

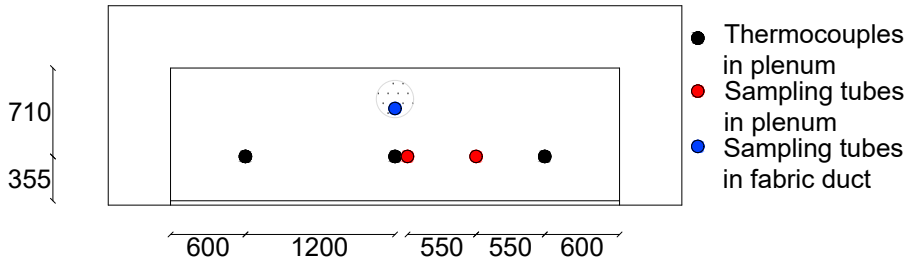

Figure 5.19. Measurement heights for the plenum shown in a section cut from the side

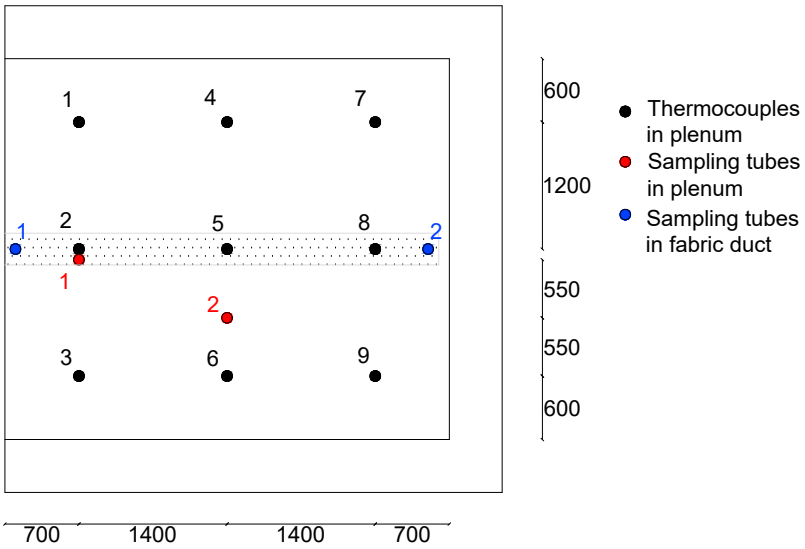

Figure 5.20. Overview of the plenum and fabric duct measuring points

The Figure 5.20 above shows the distribution of temperature and N_2O sensors within the plenum and fabric duct. Numbers 1-9 are the positions of thermocouples in plenum at height of 0.355m from the diffuse ceiling. Red colour circles represent the N_2O sensors

in the plenum. Number 1 N_2O sensor is located just above the small gap between the junction of diffuse ceiling panels whereas number 2 N_2O sensor is positioned above a person. The blue colour circles represent the N_2O and temperature sensors in the fabric duct. Number 1 N_2O sensor is located at the beginning of the fabric duct and number 2 N_2O sensor is placed at the end of it.

5.4 Experimental cases

In order to analyse indoor environment quality with diffuse ceiling ventilation cases with different setups were made with steady state calculations. These are assumptions that were made for the steady state calculations in order to reach heat balance and calculate the air supply temperature for ventilation:

- Constant room temperature of 22°C
- Constant solar gains of 410W
- Constant ambient temperatures

In order to set up the heat balance internal heat gains has to be equal to losses through the envelope via conduction and losses due to ventilation as presented in the Equation (5.1).

$$Q_{HS} = Q_{Vent} + Q_{Env} \tag{5.1}$$

Where:

Q_{HS} - Internal heat gains from lamps, people and PC, solar gains [W]
Q_{Vent} - Heat losses due to ventilation [W]
Q_{Env} - Heat losses through envelope [W]

The total internal heat load by the heat sources alone (People, PC, lamps) is equal to 451W plus additional constant solar gains of 410W. Solar gains are represented by a heat carpet in the room close to the facade which has area of $3.0m^2$.

Table 5.4 below presents 6 different cases for heat balance calculations and an example of steady state energy balance calculations is shown in the Appendix D Table D.1. As it can be seen the only variable parameters are temperature of the inlet air, air change rate,heat load of the sun and contamination source.

Table 5.4. Calculations for heat balance and estimation of inlet temperature for ventilation

Case No.	Temp coldbox, [°C]	Temp room, [°C]	Q_{Env}, [W]	Temp inlet, [°C]	ACH, $[h^{-1}]$	Q_{Vent}, [W]	Q_{HS}, [W]	N_2O Contamination source
1	21.6	22	-15	14.19	3	-435	451	2 persons
2	21.6	22	-15	14.42	6	-845	861	2 persons
3	21.6	22	-15	14.42	6	-845	861	cont.source on floor
4	21.6	22	-15	14.19	3	-435	451	cont.source on floor
5	21.6	22	-15	17.34	3	-260	275	cont.source at 1.3m
6	21.6	22	-15	17.34	3	-260	275	1 person

Each case corresponds to a different scenario of conditions as is presented below.

- Case 1 - 2 persons, their equipment, no solar gains, People as pollutant
- Case 2 - 2 Persons, their equipment, solar gains, People as pollutant
- Case 3 - 2 persons, their equipment, solar gains, pollutant on the floor
- Case 4 - 2 persons, their equipment, no solar gains, pollutant on the floor
- Case 5 - 1 Person, his equipment, no solar gains, pollutant at 1.3m height
- Case 6 - 1 Person, his equipment, no solar gains, 1 person as pollutant

Due to restrictions of the laboratory only cooling cases were able to be set up. The cold chamber temperature which should have had to represent the outdoor conditions was not able to be finished on time so the temperature could not be adjusted and was close to the temperature of the surroundings of laboratory.

The first two cases represent summer period with two persons inside the room and their equipment. Additionally, the first case scenario includes solar gains and has 6ACH where the second case is without solar gains and has 3ACH. Furthermore, the third and fourth case is identical to second and first respectively with the only difference that the N_2O release from persons is turned off but an additional contamination source attached on the floor is used as N_2O point contaminant source. The fifth case consists of 1 person operating only as a heat source, his equipment and an extra contamination source placed at 1.3m height. The sixth case is identical to the fifth case with the only difference that N_2O release from point contaminant source is turned off and the person operates as both heat and contaminant source. The purpose of the cases 3,4 and 5 is to analyse point contaminant source distribution in the room.

Furthermore, power for heating and cooling coil were calculated with intention to see how much power it will be needed to heat up or cool down the inlet air temperature for ventilation system. Capacity of heating coil and cooling coil were calculated according to the Formula (5.2) below and the results are presented in Table 5.5. Where positive power means heating and negative power means cooling.

$$Q_{Heating/Cooling} = q_v \cdot \rho \cdot c_p \cdot (T_{supply} - T_{outside}) \tag{5.2}$$

Where:

$Q_{Heating/Cooling}$ - Power needed to heat up or cool down air to wanted temperature [W]
q_v - Volumetric flow rate [m^3/s]
ρ - Density of air [kg/m^3]
c_p - Specific heat of air [$kJ/kg \cdot K$]
T_{supply} - Desired temperature of air in inlet [°C]
$T_{outside}$ - Outside air temperature [°C]

Table 5.5. Calculated heating and cooling power for each case

Case No.	$Q_{Cooling}$, [kW]
1	-547
2	-1068
3	-1068
4	-547
5	-371
6	-371

Where:

$Q_{Cooling}$ - Power for cooling down the laboratory air temperature to the desired inlet temperature

Procedure

For each measurement case the procedure shown in Table 5.6 will be followed. The procedure for each experiment starts the evening before by turning on the ventilation system so that the hot box is in a thermal steady state by next morning. The N_2O gas, which is used to represent the CO_2 gas, is then turned on, and another 2 hours are required for the system to reach concentration steady state. The time for the system to reach concentration steady state is found by plotting the Equation (5.3).

$$c(t) = \frac{q}{n \cdot V} \cdot (1 - e^{\pi t}) + c_0 \tag{5.3}$$

Where:
$c(t)$ - Concentration at time t [ppm]
q - Pollution source strength [m^3/hr]
n - Air change rate [hr^{-1}]
V - Room volume [m^3]
t - Time [hr]
c_0 - Initial concentration in the room [ppm]

In Figure 5.21 the dilution equation is plotted for the experimental cases for an air change rate of 3.

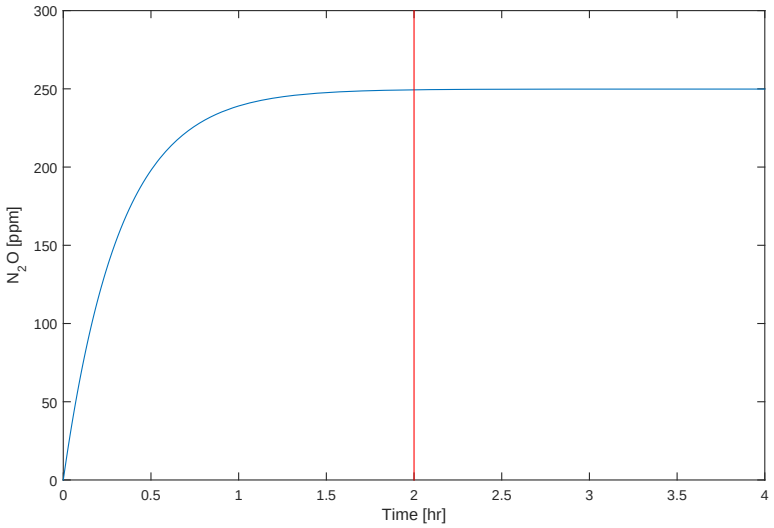

Figure 5.21. Concentration of N_2O over time with an air change rate of 3.

In Figure 5.22 the dilution equation is plotted for the experimental cases for an air change rate of 6.

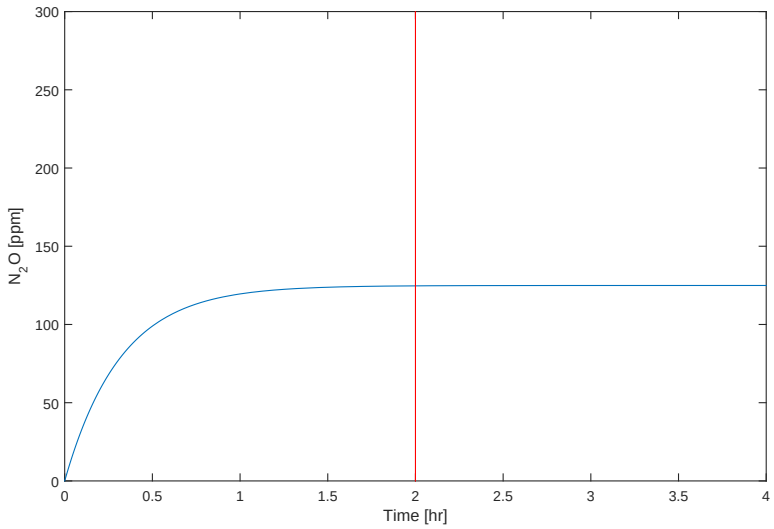

Figure 5.22. Concentration of N_2O over time with an air change rate of 6.

From Figures 5.21 and 5.22 it can be seen that steady state is reached after 2 hours for both air change rates. When the "concentration" steady state is reached the first round of N_2O measurements can begin. The time for each round of measurement is based on the Innova multipoint sample and dozer type 1412 analysis time of 40 seconds for each channel and a full cycle of the 12 channels takes roughly 500 seconds. Furthermore, it is recommended to measure atleast 20-30 cycles for these types of measurements which leads to 3,5 hours for the full measurement. When the first round of measurement is completed the second round of measurements is then conducted by the same procedure as the first. When the second measurement is over the N_2O gas is turned off and inlet air temperature together with volumetric flow rate is changed for the next case. The set-up is left to reach thermal steady state for the next experiment and the cycle continues.

Table 5.6. Procedure for experiments

Activity	**Time [h:min]**
Thermal steady state	Run during night
Concentration steady state	2:00
Measurement-1st round	3:30
Exchange N_2O tubes	0:10
Measurement-2nd round	3:30

5.5 Criteria of evaluating experimental data

Question 1

- What is the distribution of contaminants in the occupied zone?

Method

In order to check the distribution of the contaminants in the occupied zone, different measurement points within this region are needed. As mentioned previously there are 6 different locations of poles within the occupied zone and each of them is equipped with 3 N_2O collectors. The locations of the N_2O poles within the room are shown in the Figure 5.13 where the heights of the N_2O readings along each pole are shown in the Figure 5.18.

Since the measurement points are already known the ventilation efficiency of the system can be characterized by the local air quality index ε_p^c. This measure evaluates how well the ventilation system removes the contaminants from a specific point of interest in the room. This index can be calculated in accordance of the Equation (5.4). The higher the value of this index the better performance the ventilation system has regarding the removal of the contaminants in the evaluated points.

$$\varepsilon_p^c = \frac{C_{out} - C_{in}}{C_{Lc} - C_{in}} \tag{5.4}$$

where:
ε_p^c - Local air quality index [-]
C_{out} - Contaminant concentration in exhaust [ppm]
C_{in} - Contaminant concentration in supply [ppm]
C_{Lc} - Contaminant concentration in a local point of interest [ppm]

This index of air quality refers to specific points of interest. As mentioned before, there are 18 measurement points of N_2O readings in the room (6 poles x 3 points) so that 18 different local air quality indexes can be estimated and then evaluated.

Question 2

- How is the contaminant removal efficiency affected by the type of pollutant?

Method

In addition to the local air quality index, the ventilation effectiveness of a system can be characterized by a measure called contaminant removal effectiveness ϵ^c. Basically this measure follows the same idea as the local air quality index ε_p^c with the only difference that it refers to the mean concentration of the occupied zone instead of a specific point

of interest. The contaminant removal effectiveness ϵ^c can be calculated by the following Equation (5.5).

$$\epsilon^c = \frac{C_{out} - C_{in}}{C_{oc} - C_{in}} \tag{5.5}$$

where:
ϵ^c - Contaminant removal effectiveness [-]
C_{out} - Contaminant concentration in exhaust [ppm]
C_{in} - Contaminant concentration in supply [ppm]
C_{oz} - Contaminant concentration in occupied zone [ppm]

As the above Equation shows, the CRE is determined by comparing the concentration in the exhaust with the mean concentration in the room. Therefore, in order to use this measure of effectiveness it is necessary to estimate the mean concentration of contaminants in the occupied zone. In order to do that, the average value between the 18 measurement points of N_2O can be used.

The contaminant concentration in the room will be measured in the 18 different points and then evaluation of ventilation effectiveness will be performed. The local air quality index ε_p^c will be estimated for the 18 different measurements points and in the end the contaminant removal effectiveness of the system ϵ^c will be estimated after calculating the mean concentration in the room.

Question 3

- How temperatures and velocities are distributed in the occupied zone?

Method

As a part of indoor environment evaluation temperatures and velocities are measured at specific points as presented in the Figure 5.20. The values of these variables will be measured at each height and the values will be evaluated according the criterias presented in Table 2.2 and Table 2.3 in the Chapter 2.

6 | Results

6.0.1 Boundary conditions for the measurements

As a result of not being able to control the cavity temperature in the hot box and temperature in the cold box during the measurements it was noted that the ambient temperatures around the hot box were varying. The temperatures were affected by additional experiments in the laboratory, scheduled ventilation working time, changing outdoor conditions and other influential variables that can affect the temperatures inside the laboratory. Therefore, difference between measured and simulated values is expected.

Below in the Tables 6.1 and 6.2 are presented averaged boundary conditions for each case during its measured period and calculated energy unbalances respectively.

Table 6.1. Boundary conditions for each measurement

Position	Temperature, [°C]					
	Case 1	Case 2	Case 3	Case 4	Case 5	Case 6
Façade	21.65	21.95	22.05	20.05	23.11	23.75
Top	21.76	21.66	23.28	24.29	24.74	24.52
North	22.25	22.32	22.49	22.87	22.62	22.10
South	21.50	20.98	21.49	21.82	21.20	21.40
West	21.97	21.29	21.87	22.20	21.20	21.48
Exhaust	22.01	22.71	22.84	21.69	23.10	23.25
Inlet	14.35	14.28	14.61	14.44	17.09	17.34

It can be clearly seen that the conditions for surrounding temperatures varied for each measurement. Most influential temperatures are at the façade wall due to its high thermal transmittance value which leads bigger heat losses compared with other walls and top temperatures measured at the highest point of the hot box where the air intake is situated because the supply temperature stability to the room was dependant on insufficient cooling unit.

Table 6.2. Calculated energy unbalances for each case

Energy unbalance	Case 1	Case 2	Case 3	Case 4	Case 5	Case 6
Unbalance, [W]	63	15	-9	140	-85	-141
Unbalance, [%]	14	2	1	32	19	31

It has to be clarified that the calculated energy unbalances do not represent actual energy unbalances due to steady-state calculations which do not take dynamic effects into account. It is just a rough calculation to have an estimate of the situation. Therefore, from the Table 6.2 above it can be seen that for most of the cases the approximate energy

balance was not reached. As mentioned earlier it was mainly due to the unstable boundary conditions due to that it is expected to have lower temperatures in the room.

6.1 Temperature distribution

As it is stated in Chapter 1 one of the thesis objective is to investigate thermal comfort of the system. Thus, temperature distribution in the occupied zone is measured for each case. Figures 6.1 - 6.6 below present measured temperature values at specific heights for every case. The values that are given at each height are the averaged values through the period of each measurement and poles 1-6 are named C1-C6 accordingly. Positions of each pole are presented in the Figure 5.13.

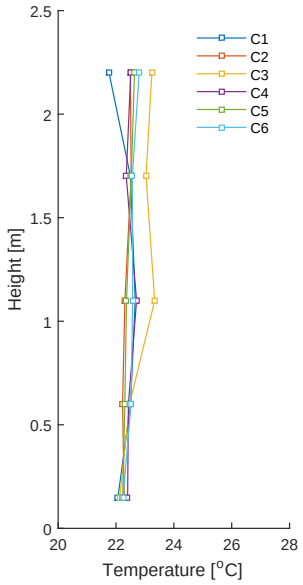

Figure 6.1. Measurement No. 1

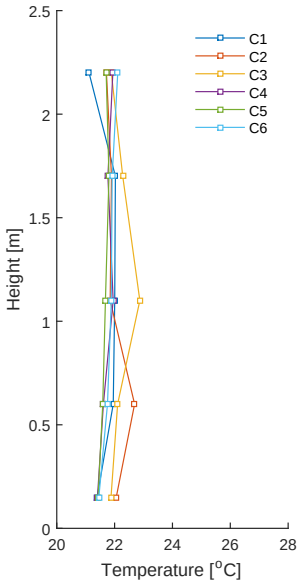

Figure 6.2. Measurement No. 2

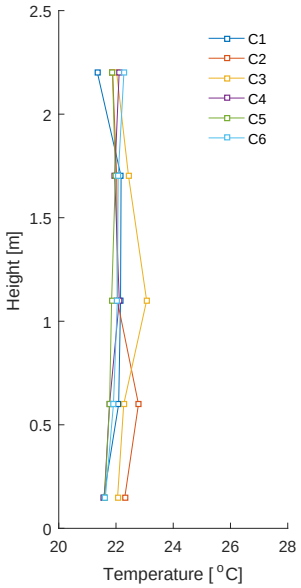

Figure 6.3. Measurement No. 3

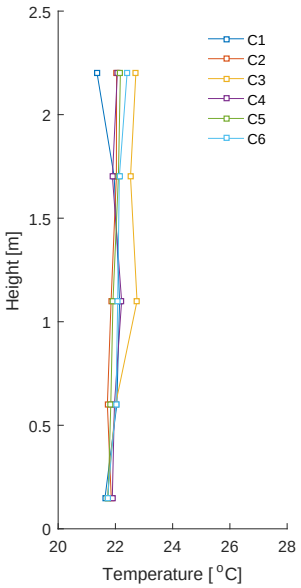

Figure 6.4. Measurement No. 4

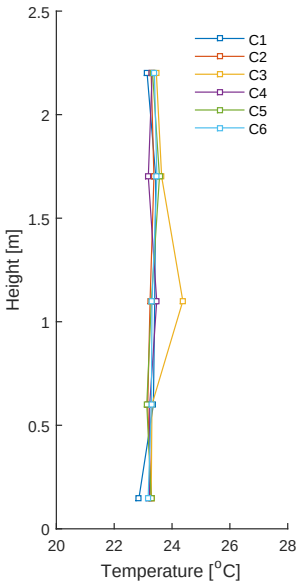

Figure 6.5. Measurement No. 5

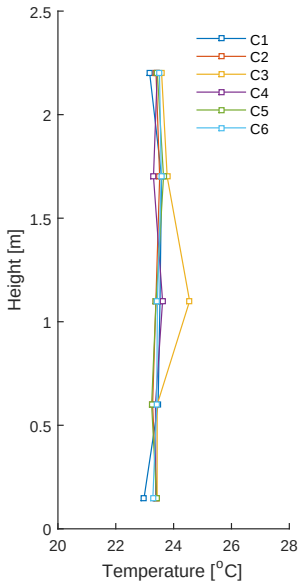

Figure 6.6. Measurement No. 6

From the Figures above it is clearly visible that the temperature distribution in the room is uniformly distributed through out the whole height of the room and has very small vertical temperature gradients. However, there are some points do not follow the same distribution pattern as other poles. Poles 1,3 which are situated close to person and pole 2 which is situated above heat carpet measured slightly different temperatures from the rest.

Firstly, lower temperature of pole 1 at that height 2.2m might be influenced by the entrainment of air through the diffuse ceiling. It might be the place where the colder air penetrates through diffuse ceiling and enters with lower temperature. Also another explanation could be that the junction between porous medium panels is not sealed properly and has a crack flow. Secondly, Pole 3 is closely positioned to the person and is on the side of the exhaust. Since the air distribution in diffuse ceiling ventilation is mainly based on buoyant forces in the room it can be concluded that the air recirculation in the room is towards the exhaust and the plume from the person could have had an influence on this point compared to other poles.

Additionally, Pole 2 at height 0.6m has almost 1°C temperature increase. It can be explained by the fact that the pole is positioned just above the heat carpet which emits heat. Point at 0.1m is not influenced due to the fact that each pole has a metal rectangular as a base which holds the pole so the first point is not affected. However, as the plume rises and the air is recirculated the amplitude of temperature is affected by it. It should be noted that it only happens for measurement 2 and 3 because during those specific cases the heat carpet is activated whereas for the case 1,4,5,6 its heat output is deactivated.

Further, all the measured temperature distributions are close to what was calculated in steady-state energy balance calculations, where the desired temperature in the room should be 22°C, except cases 5;6. Almost 1°C temperature rise in those cases can be

explained by unstable boundary conditions which lead to energy unbalance during the measurement. In Table 6.1 it can be seen that in some points the ambient temperatures for cases 1;4 are lower compared to the cases 5;6. The major difference is between façade and top temperatures which are the most influential variables in energy balance sensitivity due to their characteristic as mentioned previously. Other than that the results are as expected from the previous study on diffuse ceiling ventilation which also measured uniform temperature distributions in the room.

6.1.1 Temperature distribution in the plenum

In addition to evaluating the temperature distribution in the room, another point of interest is to monitor temperature distribution in the plenum. This was done in order to see how well the fabric duct can distribute the air in the plenum compare to the previous experiment with slot opening. Previous study with slot opening lead to varying temperatures in the plenum as it went further from the inlet. It also resulted in air diffusing through porous medium very close to the inlet causing the biggest amount of air entering in the beginning of the room rather then mixing air in the plenum uniformly and then distributing it through the diffuse ceiling. Thus, it was decided to use fabric duct in order to achieve more uniform distribution in the plenum.

Temperature sensor placement in the plenum can be seen in Figure 5.20 in Chapter 5. Measured results are plotted in the Figures 6.7 - 6.12.

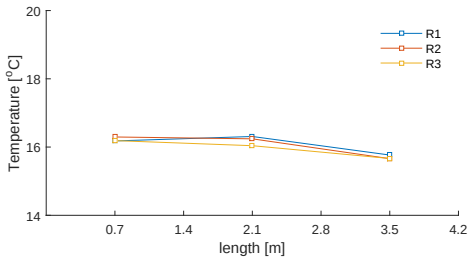

Figure 6.7. Measurement No. 1

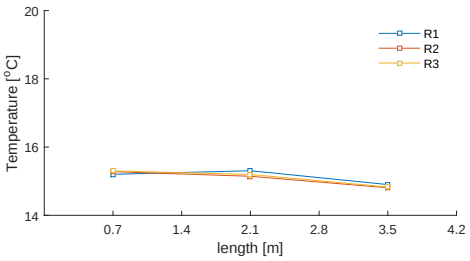

Figure 6.8. Measurement No. 2

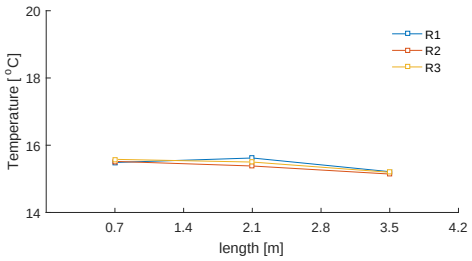

Figure 6.9. Measurement No. 3

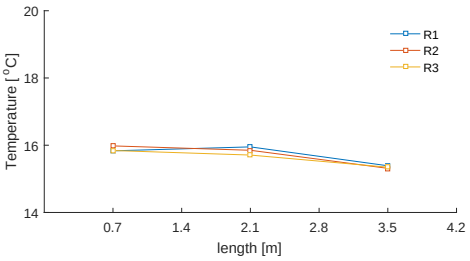

Figure 6.10. Measurement No. 4

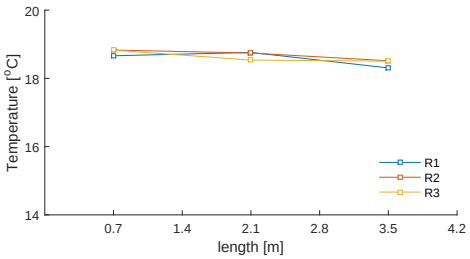

Figure 6.11. Measurement No. 5

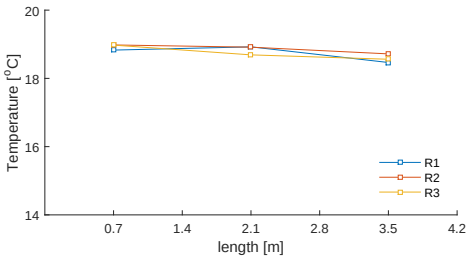

Figure 6.12. Measurement No. 6

Comparing to the slot opening, fabric duct provides very uniform temperature distribution in the plenum. The difference can be noted if the results are compared with the Figure 3.21in Chapter 3 The biggest temperature difference between beginning point and ending point is only 0.68°C which is almost 15 times less than approximately 10°C with slot opening. By the help of the fabric duct air gets more mixed in the plenum before diffusing through the porous medium leading to better air distribution to the room.

Furthermore, as explained previously, while the experiments were conducted boundary conditions were not stable. In Figure 6.11 and Figure 6.12 it can be seen that temperatures in the plenum are higher by almost 4°C compared to the first 4 measurements. One of the explanations of the temperature rise in the plenum can be explained by higher supply temperatures in these two cases. This can also be explained by insufficient cooling coil power to cool down the intake air to the air handling unit and resulting in higher supply temperatures through the fabric duct to the plenum than calculated. However, despite increased temperature difference the temperature distribution in the plenum remained uniform.

6.1.2 Stability of temperatures

In order to analyse whether the temperatures during the measurements were stable and to indicate any possible points of interest standard deviations for each pole are calculated and plotted. Since the results for all the measurements are very similar only the standing out poles are plotted below. Figures 6.13 - 6.16 presents the results of 4 poles in measurement No. 1.

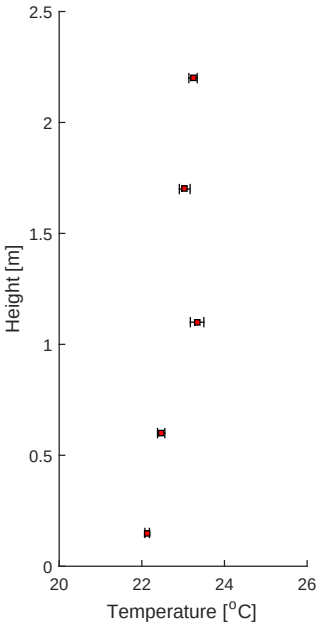

Figure 6.13. Pole 3

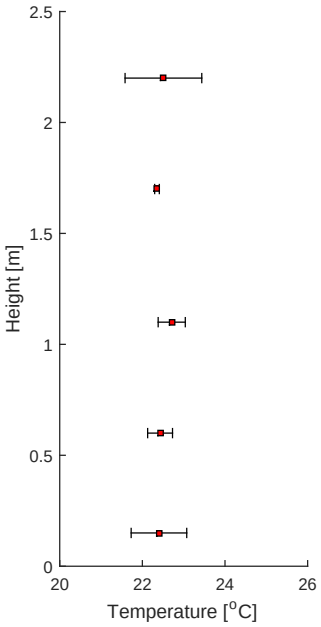

Figure 6.14. Pole 4

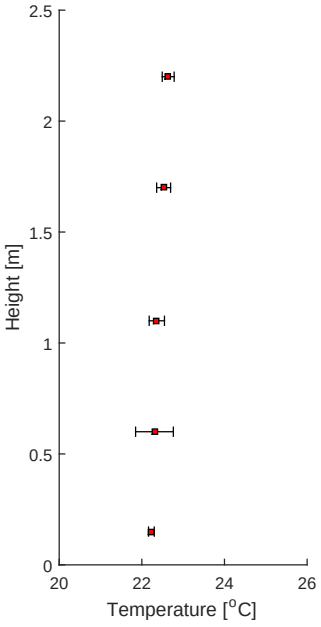

Figure 6.15. Pole 5

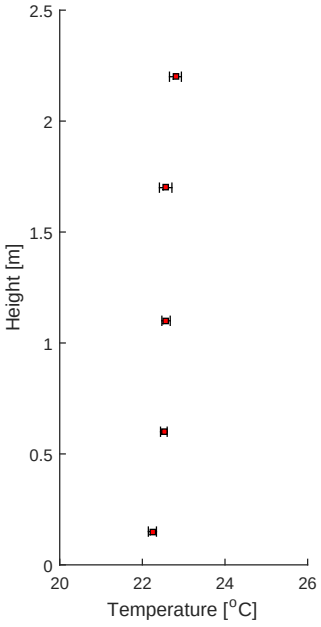

Figure 6.16. Pole 6

Previously it was mentioned that pole 3 has a deviation of temperature at 1.1m height for every measurement because of that standard deviations for pole 3 and pole 6 which are situated on the sides of person 2 are plotted in Figure 6.13 and Figure 6.16 to indicate if there are any problems. Plotted values clearly show that during the period of measured case temperatures were very stable with minor fluctuations which do not show any big temperature variations. Thus, conclusions can be made that acquired deviation at 1.1m

height was not an outlier but possibly the effect of persons thermal plume which increased the magnitude of temperature compared to the other points on the same pole. Also, since the standard deviations for all the measurements are very small it is a good indicator that the thermocouples were calibrated correctly and are providing accurate measurements with barely any deviations.

In addition, pole 4 and 5 are the only poles that have these temperature fluctuations. One of the explanations could be that these are the points where the air diffuses through the porous medium and enters the room downwards with lower temperatures and further on is mixed, resulting in temperature fluctuations. Another explanation could be that somewhere close to the poles are the possible leakage points where the leakage air mixes with room and gives temperature fluctuations.

6.2 Velocity distribution

Since the temperature distributions are already evaluated, another contributory part of thermal comfort has to be analysed. As earlier mentioned in the Chapter 2 draught can be described as most often reason for local discomfort in the rooms with air distributing systems. Therefore, an analysis of velocity distribution in the occupied zone is carried out. Figures 6.17 - 6.22 below represent measured velocities at specific heights for every case. Each point presents an average velocity magnitude through out a single measurement. In Figures C1-C6 are referred to pole numbers from 1 to 6 where the positions are the same as for thermocouples.

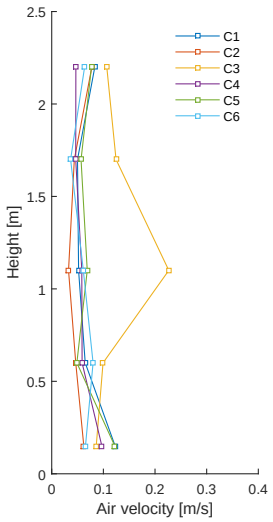

Figure 6.17. Measurement No. 1

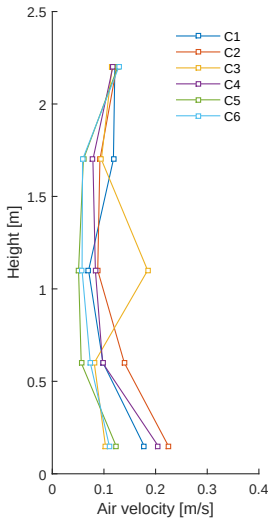

Figure 6.18. Measurement No. 2

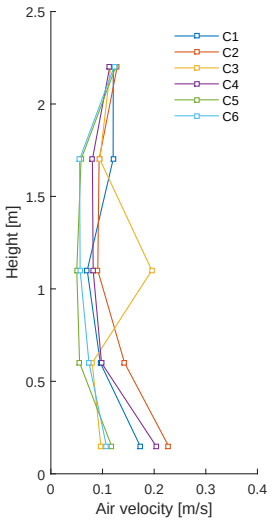

Figure 6.19. Measurement No. 3

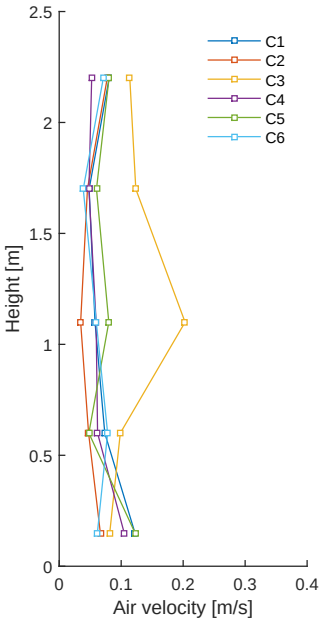

Figure 6.20. Measurement No. 4

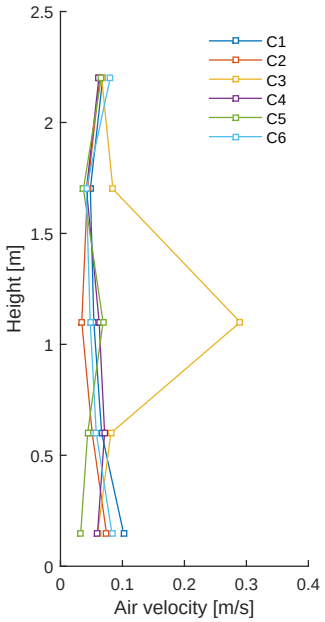

Figure 6.21. Measurement No. 5

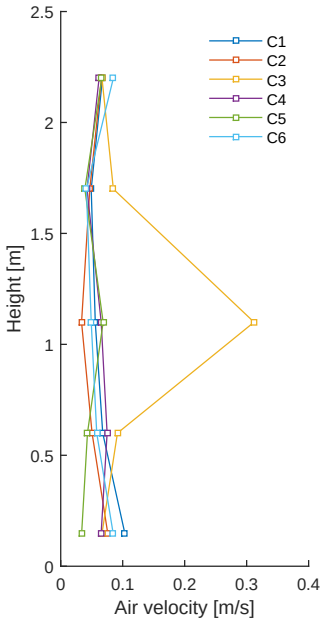

Figure 6.22. Measurement No. 6

From the Figures above it is noticeable that the velocity distribution, specifically in the occupied zone, is distributed uniformly. As anticipated, higher velocities are at the lower zone of the room where the recirculation happens and upper zone has distribution of lower velocities. Moreover, it can be noticed that for cases 1,4,5,6 with 3ACH velocities are lower than for cases with 6ACH. It is very obvious that at 0.1m height where room is ventilated with 6ACH velocities at some poles are higher than 0.2m/s which is to be expected.

In addition, the velocity magnitude is higher for the poles that are situated closer to the heat loads, specifically pole 1,2,3,4,6. Since pole 5 is situated in the end of the room, not close to any heat sources, it is excluded from the list. Poles 1,3,4,6 are positioned on the sides of manikins where each of them has heat output of 100W. Thus, when the air is recirculating on the ground level and reaches a thermal plume of a person additional recirculation happens due to buoyancy forces which adds extra momentum to the flow. As a result, higher velocities at 0.1m height are monitored. As for pole 2 which is situated just above the heat carpet, higher velocities are only observed for cases 2 and 3 where the heat carpet is active. Once again the increase of velocity magnitude compared to other cases without activated heat carpet can be explained by the effect of buoyant forces created by the thermal plume of heat carpet.

Also, for each measurement it was noticed that pole 3, which is situated next to the person and close the exhaust, has a different tendency of velocity distribution than other poles. For all the cases when comparing velocities at height 1.1m pole 3 had a deviation of approximately 0.1m/s more than other poles at that specific height. This increase of velocity magnitude could be explained by taking into account the pattern of airflow towards the exhaust side and thermal plume from the person. It is known that the airflow

pattern moves towards the exhaust duct due to created under pressure of the fan. At the same time manikin is releasing heat from its surface and generating thermal plume around its whole surface area. Since the anemometers are situated close to the manikins outer surface there is a possibility that the moving air interfered with manikins thermal plume and influenced the measurement of anemometer which is closely placed.

On the other hand, comparing the increase of velocity magnitude for first 4 cases and last 2 cases it is visible that the velocities at 1.1m are additionally higher by 0.1m/s than previous measurements. As mentioned earlier in temperature distribution part, for the last two cases a noticeable temperature increase was observed but it was assumed that unstable boundary conditions had an influence on temperature increase. However, another assumption why the temperatures and velocities at 1.1m increased during 5th and 6th measurement can be made. If in the end it is the thermal plume that had an influence on velocity increase then it can be discussed whether the heat output from manikins was not accidentally adjusted by somebody in the laboratory or a malfunction in the controller happened. It could be the only explanation why the velocity at 1.1m height with 3ACH is higher than velocity at 1.1m height with 6ACH. However, possibility of leakage air to the room which might have caused the velocity increase is not neglected.

6.2.1 Stability of velocities

Even though the flow through porous medium has very low velocities and is assumed to be laminar the velocities in the room are turbulent and are constantly fluctuating due to buoyant forces from heat loads and due its turbulent behaviour. Thus, statistical analysis of air velocities will be conducted to see the stability of their magnitude.

Figure 6.23 below presents the comparison between each measurement cases. The values that are plotted in the Figure are averaged values of all 6 poles in the room for each case.

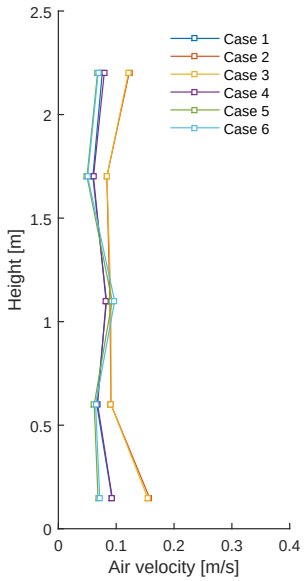

Figure 6.23. Average measured air velocities in the room for all cases

It is known that case 1,4,5,6 has 3ACH and case 2,3 has 6ACH due to that there is almost no difference between cases with lower air change rates. However, when looking at differences in the higher and lower zones for all cases, a difference in velocity magnitude is visible. This can be explained by higher volumetric flow rate which results in higher velocities.

In addition to that, the difference of velocities in the cases with same boundary conditions (case 1,4,5,6) can be explained by turbulent behaviour of air. This is very evident when looking at the raw data from the anemometers used to measure the air velocity as shown in Figure 6.24.

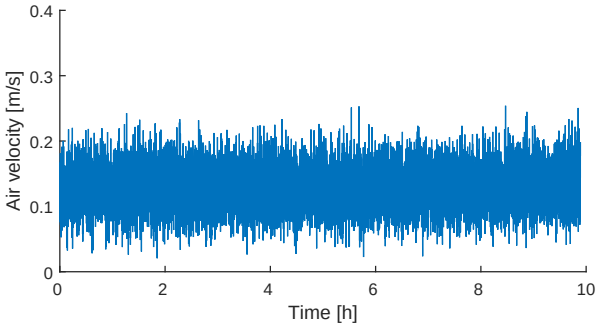

Figure 6.24. Measurement data for anemometer U01(Pole 1 height 0.1m) from case 1

Thus, to get a better understanding of the measurement data presented in the Figure above statistical analysis is carried out. Standard deviations for each pole are calculated and plotted. Specifically, to highlight the stable and fluctuating velocities poles 1 and 3 from measurement number 1 are presented in the Figures 6.25 and 6.26 below.

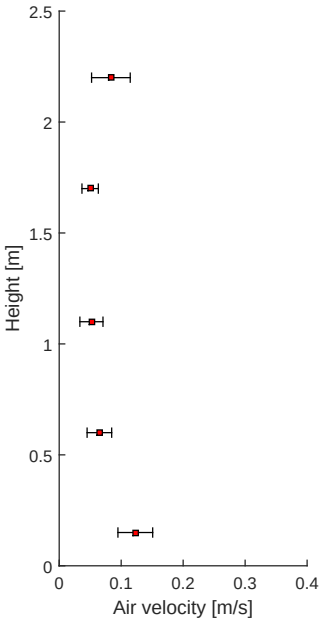

Figure 6.25. Pole 1

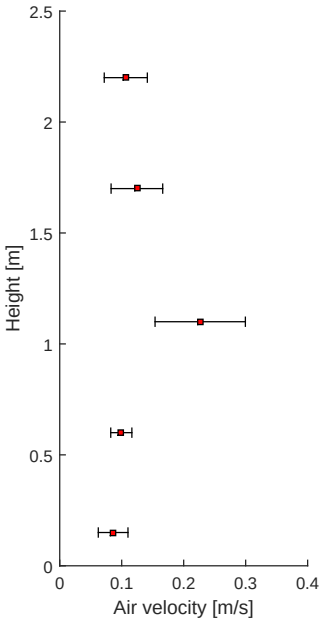

Figure 6.26. Pole 3

It is clearly visible that the pole 1 which is situated next to the manikin on the other side of exhaust has less fluctuations from the average value and is more stable than the pole 3 which is also situated next to the manikin but is next to the exhaust duct. Moreover, as mentioned earlier pole 3 for all measurements had an unstable point at 1.1m height which can be also seen in the Figure 6.26 where the deviations from the average value are high.

Further on, averaged air velocities with average standard deviations are presented in the Figures 6.27 - 6.32. This will not show each individual poles instability for the cases but it will give an overview of the behaviour of the flow in each case as the draught risk will be evaluated later in this Chapter.

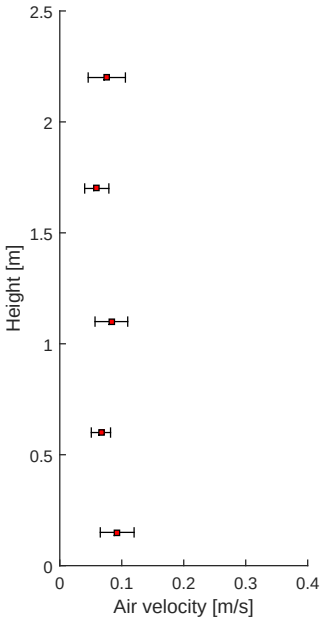

Figure 6.27. Case 1

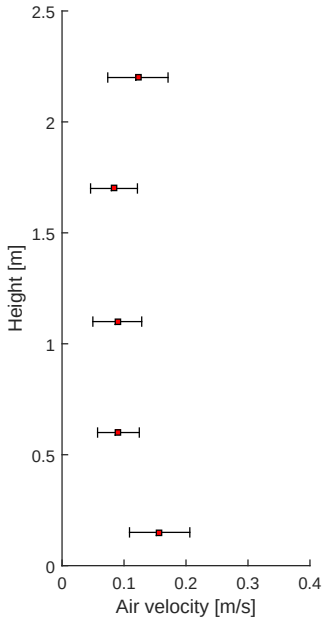

Figure 6.28. Case 2

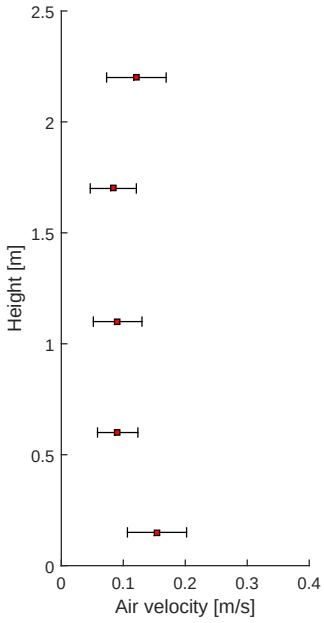

Figure 6.29. Case 3

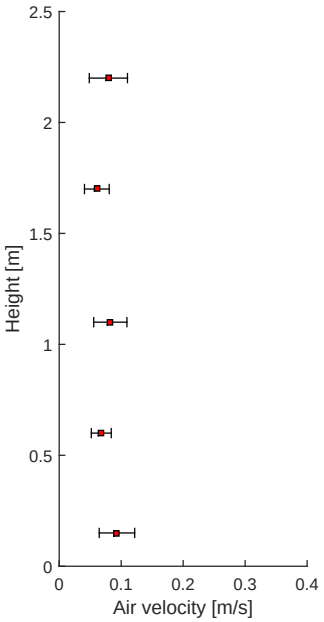

Figure 6.30. Case 4

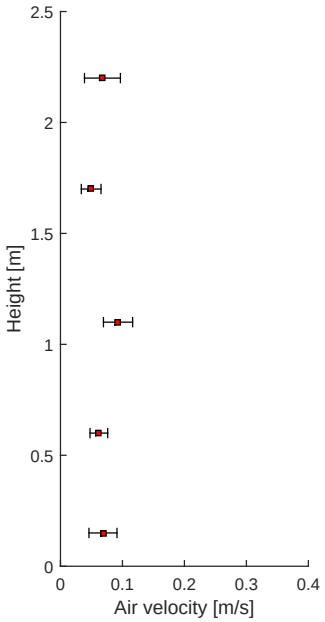

Figure 6.31. Case 5

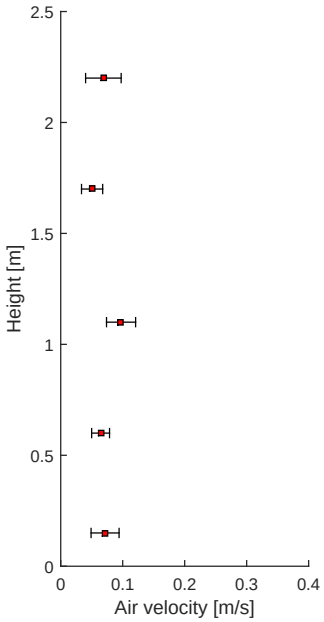

Figure 6.32. Case 6

From the Figures above it can be seen that even with pole 3 deviating from the other poles the average velocities in the room are still around 0.1 m/s and lower. It is also observed that the average velocities in cases 2 and 3 are higher than in cases 1, 4, 5 and 6 as is expected with the higher air change.

Additionally it can be seen that the standard deviations for heights 0.1m, 1.1m and 2.2m is higher than at heights 0.6m and 1.7m for cases 1, 4, 5 and 6 which are the cases with an air change of 3, where for the cases with an air change of 6 the standard deviations are more uniform for all heights except for height 0.1m where there is a noticeable increase of velocities at poles 2, 4 and 6. The reason for the high standard deviation at height 1.1m for cases 1, 4, 5 and 6 could be because of the strong buoyant flow around pole 3.

Lastly it can be seen from the Figures above that even after reaching thermal equilibrium the velocities are still unstable contrary to the temperatures with the exceptions of pole 4 and 5. Overall the distribution of the air velocities in all the cases are very similar.

6.3 N_2O distribution

With temperature and velocity distributions evaluated the final part of the measurements, which is air quality, will now be analysed. As stated in Chapter 1 more than one of the thesis objectives is related to air quality and atmospheric comfort. The concentration of N_2O is measured at the heights in the room, two points in the plenum and at the beginning and the end of the fabric duct specified earlier in this Chapter for every case. The values presented in this Section are the average values for the 20-30 cycles which were specified in the procedure Section earlier in this Chapter. Firstly the measured values for two points in the fabric, the two points in the plenum, the point in the inlet and the point in the outlet is shown in Table 6.3.

Table 6.3. N_2O concentration measured in the fabric duct, the plenum, the inlet and the exhaust for all cases

Position	Concentration [ppm]					
[-]	Case 1	Case 2	Case 3	Case 4	Case 5	Case 6
Fabric 1	48.87	27.48	17.76	76,04	52.47	23.48
Fabric 2	0.68	0.55	0.44	2.80	0.32	0.25
Plenum 1	0.64	0.54	0.61	3.08	0.72	0.42
Plenum 2	0.54	0.51	0.38	2.99	0.42	0.35
Inlet	1.00	0.68	0.49	4.81	1.02	0.40
Outlet	207.16	115.47	136.59	248.90	231.41	107.29

From the above Table it can be seen that there is a limited back flow to the plenum from the room as the concentrations in the plenum and fabric are close to the inlet concentration. While the measured values in the beginning of the fabric(Fabric 1) is very high it was observed after the measurements that the tube sampling air from the beginning of the fabric duct had a leak so that it also sampled air from the room which explains the misleading values. Essentially, the values for Fabric 1 point can be neglected because of the faulty tube. Furthermore, it can be seen that the concentration in the outlet varies even for cases with the same air change and pollutant strength(cases 1/4/5 and 2/3) which indicates a possible leak in the hot box.

Additionally, to confirm that there is a leak it can be observed from the outlet concentrations that there is an unbalance between the outlet concentration and the concentration calculated with the dilution equation in the procedure Section earlier in this Chapter. The unbalance for each of the cases is shown in Table 6.4.

Table 6.4. Pollutant unbalance in the measurements

	Case 1	Case 2	Case 3	Case 4	Case 5	Case 6
Pollutant strength [g/s]	0.022	0.022	0.022	0.022	0.022	0.012
Mass flow in outlet [g/s]	0.017	0.019	0.022	0.020	0.019	0.009
Unbalance [%]	24.62	15.97	0.60	9.43	15.80	21.97

From the Table above it can be seen that only case 3 is within the 2% uncertainty given for the instrument used to measure N_2O concentration. Moreover, with 4 out of 6 cases having an unbalance above 15% and with the unbalance varying independently of air change and pollution source type it is concluded that there must be a leak in the hot box.

The measurement results for the concentration in the room are presented in Figures 6.33, 6.34, 6.35, 6.36, 6.37 and 6.38. In the Figures C1-C6 are referring to pole numbers where the positions are the same as for thermocouples and anemometers.

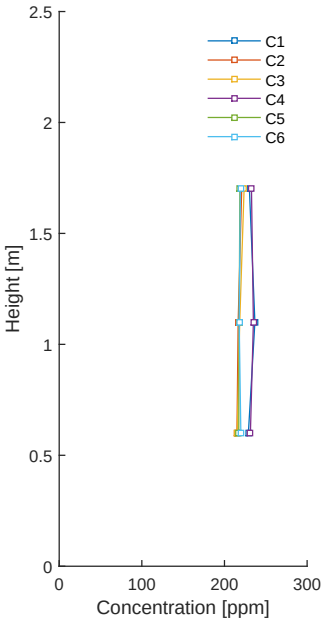

Figure 6.33. Case 1

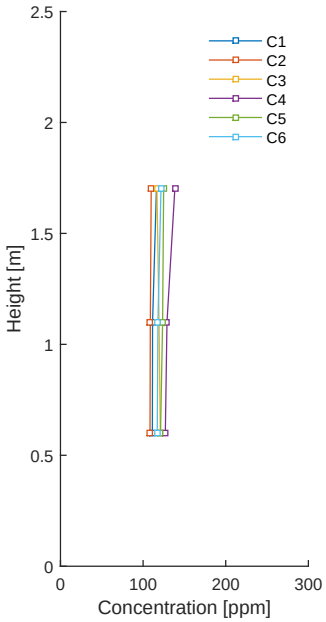

Figure 6.34. Case 2

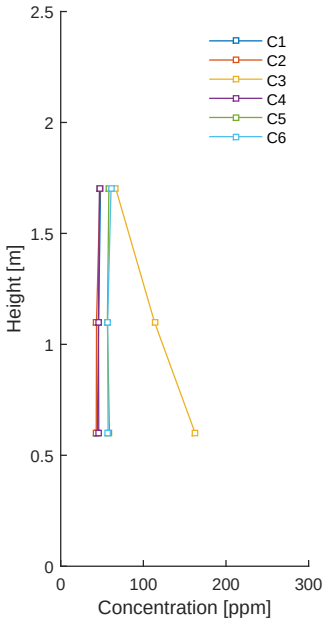

Figure 6.35. Case 3

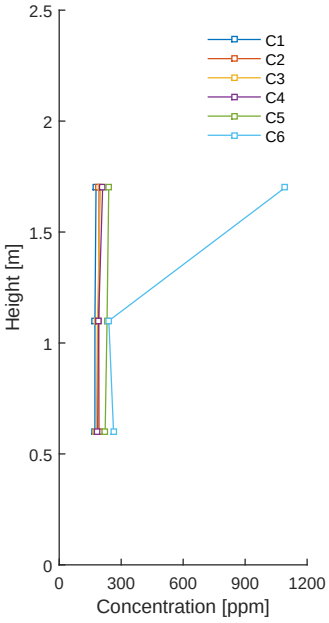

Figure 6.36. Case 4

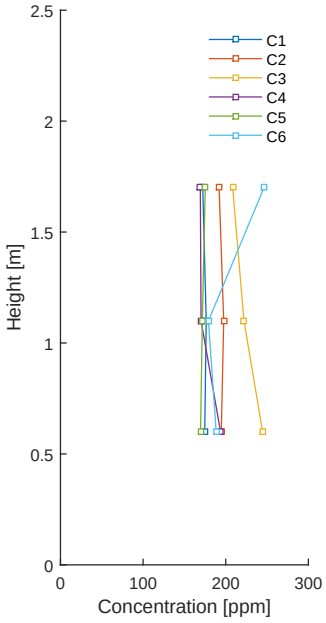

Figure 6.37. Case 5

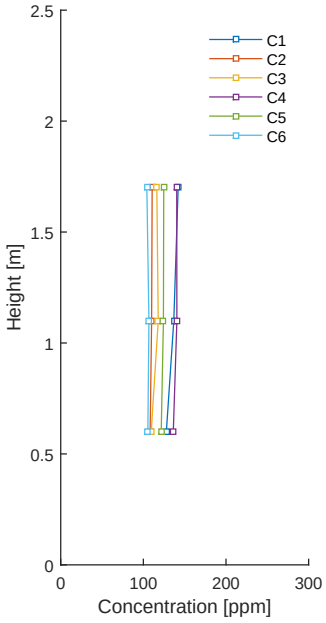

Figure 6.38. Case 6

From the Figures above it can be seen that the distributions are uniform in the occupied zone as was expected with diffuse ceiling ventilation. It has shown to have a flow behaviour similar to mixing ventilation at the air change rates used in these measurements. However, rather large deviations can be observed in two of the cases. The first deviation is in case 3 at pole 3 where the concentration gradually increases from heights 1.7m to 0.6m. When looking at the distribution for temperatures and velocities

deviations occur at the same pole and height. The concentration in the other poles of this case is also significantly lower than in case 2 which is essentially the same case but with a different pollutant source. From these observations it can be seen that the room air is not fully mixed contrary to the expectations. This flow pattern could be attributed to the stronger air flow along the floor, which can be seen from the velocity measurements, as for pole 3 the strong buoyant flow near the person entrains the polluted flow which could explain the higher concentration in the lower part of the room.

The second deviation is in case 4 at pole 4, contrary to the other deviations mentioned in this Chapter, where the concentration increases greatly at height 1.7m. It can also be seen that apart from the deviation that the concentration of the other poles in this measurement is closer to that of case 1 which is the same case but with a different pollutant source. From this it can be concluded that, while the concentration is closer to the case counterpart, it is still not fully mixed and might even have a large dead zone in the corner close to poles 5 and 6.

Additionally, problems occurring in cases 3 and 4 occurs in a smaller magnitude for case 5 which also has a pollutant source that is not a heat source. However, as mentioned earlier in the Chapter the pollutant source in this case is positioned at a height of 1.3m. From this measurement it can be seen that when the pollutant source is not at the floor it gets distributed more evenly and highlights more of the critical zones. This shows that the flow of the pollutant in cases 2 and 3 might be heavily influenced by N_2O being heavier than atmospheric air while being placed at floor level.

6.3.1 Stability of N_2O

The fluctuations in the data from the concentration measurements are not as consistent as for the air velocity measurements. For a few of the measuring points the fluctuations are large and inconsistent. To show an example the raw data for the outlet concentration from case 3 is shown in Figure 6.39.

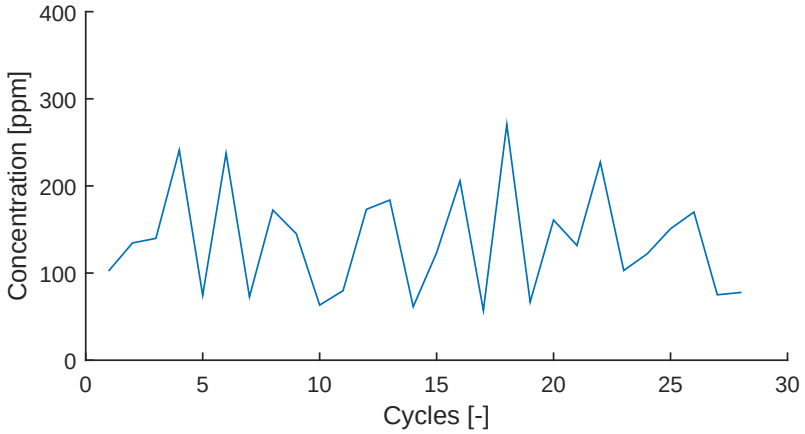

Figure 6.39. Measurement data for the sampling tube in the outlet from case 3

Therefore to get a better overview of the stability for the measurements of N_2O the results for the fabric duct, plenum, inlet and outlet will be presented in Figures 6.40, 6.41, 6.42,

6.43, 6.44 and 6.45 with standard deviations from the measurements.

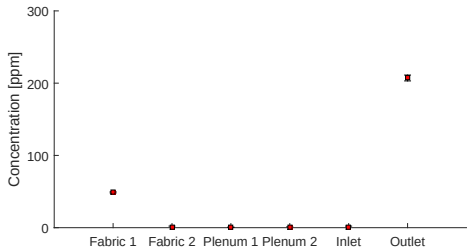

Figure 6.40. Case 1

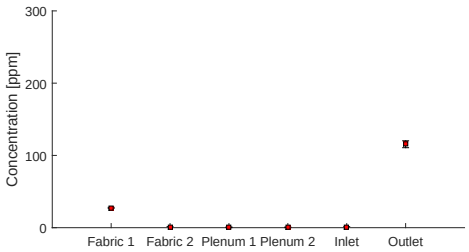

Figure 6.41. Case 2

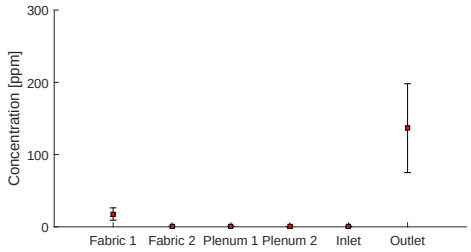

Figure 6.42. Case 3

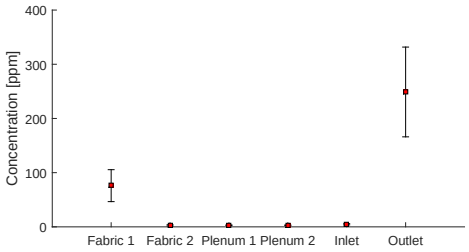

Figure 6.43. Case 4

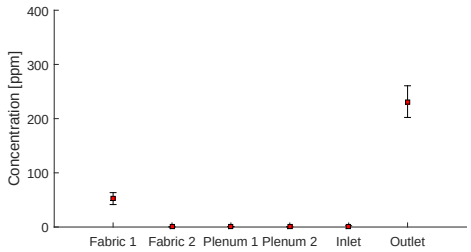

Figure 6.44. Case 5

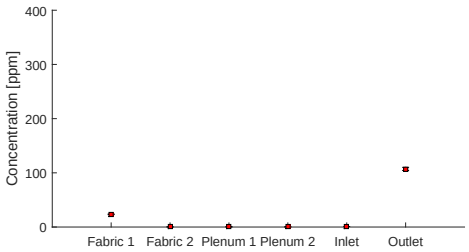

Figure 6.45. Case 6

From the above figures it can be seen that for cases 1, 2, and 6 the concentrations measured are very stable. Which shows that when the pollutant source is also a heat source, or close to one, the air is fully mixed which results in a uniform distribution of the N_2O in the occupied zone.

Additionally, it can be seen that the standard deviations in cases 3, 4 and 5 are high. The room air for these cases is not fully mixed as evident by the large fluctuations in the outlet concentration. From the concentration gradients observed in the previous Section this was expected. This also shows that even though the N_2O is more evenly distributed in case 5 it is still not fully mixed. Moreover, this confirms that when the pollutant source is not a heat source, or close to one, the pollutant does not fully mix with the room air.

To evaluate the stability in the room the average at each height is presented with the average standard deviation in Figures 6.46, 6.47, 6.48, 6.49, 6.50 and 6.51.

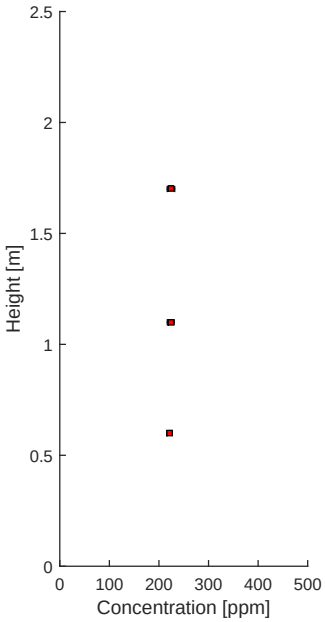

Figure 6.46. Case 1

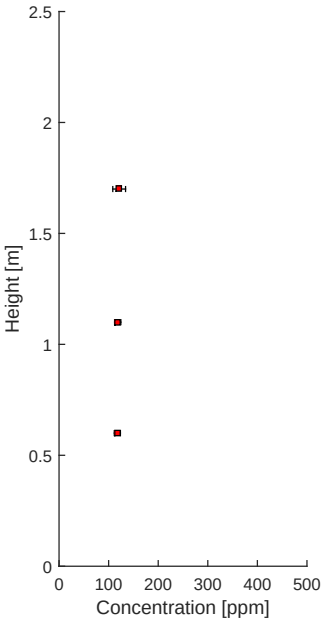

Figure 6.47. Case 2

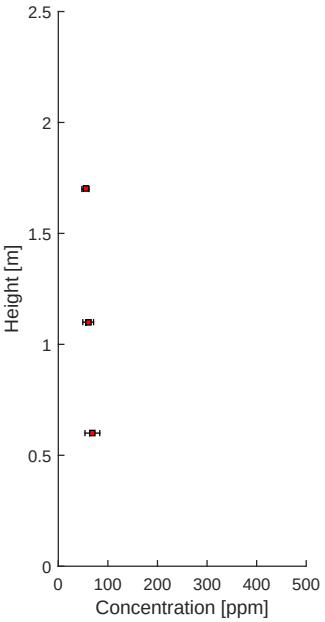

Figure 6.48. Case 3

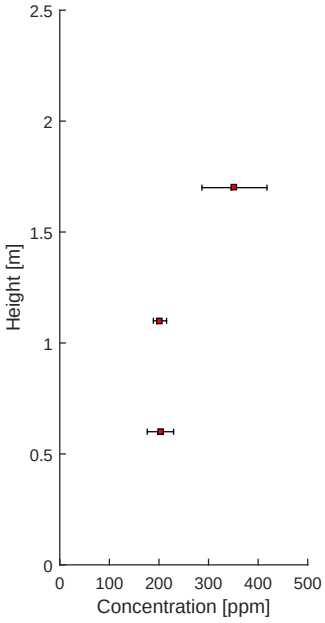

Figure 6.49. Case 4

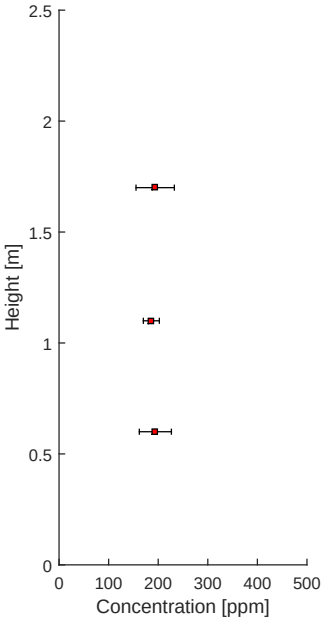

Figure 6.50. Case 5

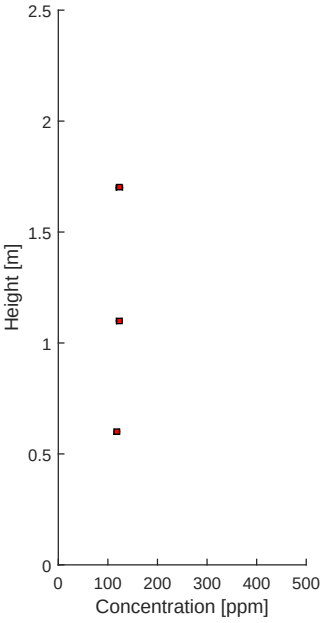

Figure 6.51. Case 6

From the Figures above it can be seen that cases 1 and 6 have close to no deviation while case 2 has a small deviation at height 1.7m. While the deviation is small it is close to the deviation in case 3 at height 0.6m which is a case where the room air is not fully mixed. This shows that case 3 is more stable in the occupied zone than presented above. However, from the distribution in the room and the deviation in the outlet concentration it is visible that the concentration distribution in the room is unstable. The deviation showed

in the Figure above for case 3 is, as mentioned above, an average of the distributions and deviations measured which is one reason why it is not the case for the Figure. Another reason could be that the points at which the flow is unstable is not within the points of interest in this thesis.

Additionally it can be seen that for case 4 and 5 the standard deviations show what was expected from the Figures with the outlet deviation. For case 4 it can be seen that the standard deviation for height 1.7m is large as expected while it can be seen that the standard deviation at height 0.6m is higher than the standard deviation at height 1.1m. From this it can be assumed that there is an entrainment from the lower part of the room to the upper part where it gathers near pole 6.

For case 5 it can be observed that while being more evenly distributed there are large standard deviations specifically at heights 0.6m and 1.7m. The standard deviations for the room is similar to the standard deviation in the outlet for case 5. While it does not eliminate the possibility of having a large dead zone as in case 4 it shows that the distribution instability is more evenly distributed in the occupied zone. Also it shows tendencies similar to both case 2 and 3 which can be attributed to that having the pollutant source on the floor could be a poor choice as the flow pattern "sticks" to the floor. This could also be because of the choice of pollutant as it is a heavier gas than air. The gas was chosen because N_2O properties are very similar to that of CO_2 but for measurements regarding pollutants like building emission or furniture emission it might not be the most optimal.

6.3.2 Local air quality and contaminant removal effectiveness

To further analyse the influence of N_2O distribution in the room additional parameters are investigated. As a part of experimental data analysis objectives contaminant removal effectiveness and local air quality index are calculated.

Measurement No. 1

From Table 6.5 it can be seen that the local air quality index is varying from 0.874 to 0.963 which shows that the room is not fully mixed and the distribution is slightly uneven. It can also be seen that the contaminant removal effectiveness is 0.928 which is within what can be expected from a mixing ventilation system. Furthermore, it can be seen from the local air quality index that the removal effectiveness is worse at the person farthest from the outlet which indicates that the room has a horizontal gradient in removal efficiency. It also correlates to the velocity and temperature measurements showing a strong thermal plume at the person closest to the outlet.

Table 6.5. Local air quality index and contaminant removal effectiveness of the system in measurement 1.

Height, [m]	**Local air quality index [-]**						**Contaminant removal effectiveness [-]**
	C1	C2	C3	C4	C5	C6	
0.6	0.905	0.963	0.962	0.895	0.953	0.942	0.928
1.1	0.874	0.956	0.948	0.881	0.951	0.951	
1.7	0.900	0.938	0.926	0.890	0.947	0.945	

Measurement No. 2

From Table 6.6 it can be seen that the local air quality index is varying from 0.833 to 1.066 which shows that the room is not fully mixed and the distribution is a bit more uneven than measurement 1. It can also be seen that the contaminant removal effectiveness is 0.970 which is within what can be expected from a mixing ventilation system which normally ranges between 0.9 and 1.0 and that the system in this case is closer to being fully mixed. Additionally, it is noticed from the local air quality index that the horizontal gradient in removal efficiency has shifted in direction. The removal efficiency in this case is worse at the far end of the room. However, it is seen from pole 6 that it is worst at the corner farthest from the outlet.

Table 6.6. Local air quality index and contaminant removal effectiveness of the system in measurement 2.

Height	**Local air quality index [-]**						**Contaminant removal**
[m]	C1	C2	C3	C4	C5	C6	**effectiveness [-]**
0.6	1.038	1.066	0.955	0.909	0.953	0.986	0.970
1.1	1.036	1.062	0.968	0.895	0.934	0.979	
1.7	0.994	1.052	0.989	0.833	0.924	0.949	

Measurement No. 3

From Table 6.7 it can be seen that the local air quality index is varying from 0.839 to 3.203 which shows that the system in this case works more similar to a piston ventilation system than a mixing ventilation system. As it seems the concentration of the pollutant is low in the measurement points but gets higher towards the exhaust. The contamination removal effectiveness is 2.241 which again suggests that for this type of contaminant the system works more like a piston ventilation system where the contamination is kept at the lower zone of the room. However, it should be noted that even with a high local air quality index and contaminant removal effectiveness the local air quality index still shows evidence of a high concentrations at column 3 heights 0.6 m and 1.1 m. Moreover, it can be seen from the local air quality index that the efficiency is significantly better closer to the exhaust and worst in the far end of the room with the exception of pole 3 where there is entrainment.

Table 6.7. Local air quality index and contaminant removal effectiveness of the system in measurement 3.

Height	**Local air quality index [-]**						**Contaminant removal**
[m]	C1	C2	C3	C4	C5	C6	**effectiveness [-]**
0.6	3.109	3.203	0.839	2.988	2.327	2.396	2.241
1.1	3.000	3.178	1.204	3.013	2.432	2.420	
1.7	2.856	2.896	2.054	2.939	2.355	2.254	

Measurement No. 4

From Table 6.8 it can be seen that the local air quality index is varying from 0.224 to 1.453 which shows that the distribution in the room is skewed towards one corner of the occupied zone. From this it is assumed that near column 6 at height 1.7m there is a dead

zone where the contaminant can gather when the pollutant is not positioned in the heat source. Because of this dead zone the contaminant removal effectiveness is 0.986 which is interesting as measurement 3 and 5 indicates that when the pollutant is not in the heat source and positioned on the ground level the system works like a piston ventilation system. Additionally it can be seen from the local air quality index that the tendency in the removal efficiency is similar to that of case 3 but with the other corner in the far end of the room having the low efficiency.

Table 6.8. Local air quality index and contaminant removal effectiveness of the system in measurement 4.

Height	**Local air quality index [-]**						**Contaminant removal**
[m]	C1	C2	C3	C4	C5	C6	**effectiveness [-]**
0.6	1.453	1.297	1.393	1.344	1.122	0.945	0.986
1.1	1.451	1.304	1.354	1.315	1.076	1.037	
1.7	1.407	1.300	1.252	1.188	1.038	0.224	

Measurement No. 5

From Table 6.7 it can be seen that the local air quality index is varying from 0.939 to 1.370 which shows that the system in this case works as a mixture between displacement and mixing ventilation. The trend in this measurement is the same as in measurement 3 and 4 with the exception of the dead zones. However, the contamination removal effectiveness is 1.210 which suggests that for this type of contaminant the system works more like a piston ventilation system. Furthermore, it can be seen from the local air quality index shows that the removal efficiency is better in the far corner of the room. This separates it from the other measurements but is also the best indication of piston flow for all the 6 cases.

Table 6.9. Local air quality index and contaminant removal effectiveness of the system in measurement 5.

Height	**Local air quality index [-]**						**Contaminant removal**
[m]	C1	C2	C3	C4	C5	C6	**effectiveness [-]**
0.6	1.327	1.190	0.946	1.195	1.367	1.229	1.210
1.1	1.314	1.172	1.042	1.362	1.350	1.294	
1.7	1.346	1.207	1.111	1.370	1.322	0.939	

Measurement No. 6

From Table 6.10 it can be seen that the local air quality index is varying from 0.754 to 1.029 which shows that the system is not fully mixed when the 2 persons office is at "half-heat load". It can also be seen that the local air quality index is worse at the columns close to the active person (columns 1 and 4). The contaminant removal effectiveness of the system in this case is 0.883 which is 5-10 % worse than the similar cases 1 and 2. This indicated that ventilation system performance drops down when heat load is not distributed symmetrically. Also, from the local air quality it is seen that even with the system under performing for these conditions the tendency in the room is still the same. There is still a horizontal removal efficiency gradient although it could have been influenced by the person which is the person farthest from the outlet.

Table 6.10. Local air quality index and contaminant removal effectiveness of the system in measurement 6.

Height [m]	**Local air quality index [-]**						**Contaminant removal effectiveness [-]**
	C1	C2	C3	C4	C5	C6	
0.6	0.838	0.991	0.979	0.786	0.881	1.017	0.883
1.1	0.783	0.975	0.908	0.762	0.862	1.005	
1.7	0.754	0.969	0.922	0.763	0.860	1.029	

6.3.3 Operative temperature and vertical temperature gradient

After conducting measurements in the laboratory operative temperature and vertical temperature gradient can be examined. By making an assumption that office workers have 1.2met and are lightly clothed with clothing level of 1clo, according to the optimum temperature range in the Figure 2.4 it can be estimated whether the temperature in the room assures optimal temperature. Average room temperatures for each case are presented in the Table 6.11 below.

Table 6.11. Average room temperatures for each case scenario

Case No.	Average room temperature, °C
1	22.49
2	21.86
3	22.03
4	22.02
5	23.34
6	23.47

Temperatures presented in the Table 6.11 are equal to the average of all poles measurements in the room for each different height. In the Figure 6.52 the red lines corresponding to 1clo level and 1.2met rate are drawn in order to see the operative temperature range easier.

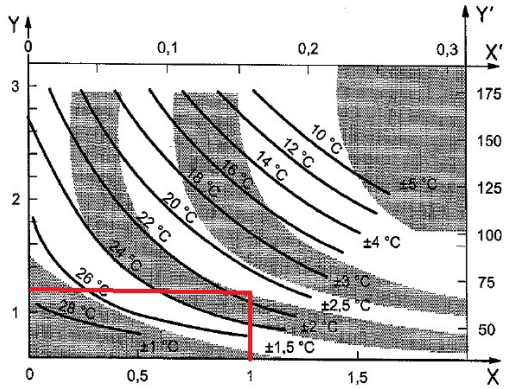

Figure 6.52. Range around the optimum temperature for 1clo and 1,2met

It can be seen that the temperature inside the room should be at least 22°C ± 2.5°C.

Based on the measured average temperatures in the room and the requirement for optimal temperature it can be concluded that for each measurement scenario the requirement was fulfilled because all the temperatures fit in the range.

Furthermore, as mentioned previously in the beginning of the report, local thermal discomfort can be caused by having high temperature differences between head and ankles. According to the Table 2.3 which is presented by EN ISO 7730 vertical temperature gradient between head and ankles should be less than 3°C. Calculated vertical temperature gradients for each pole and case for height between ankles and head are presented in the Table 6.12 below.

Table 6.12. Vertical temperature gradients for each pole and case

Pole No.	Case 1	Case 2	Case 3	Case 4	Case 5	Case 6
	Vertical temperature gradient, [°C/m]					
Pole 1	0.15	0.14	0.11	0.14	0.14	0.09
Pole 2	0.10	0.17	0.21	0.09	0.00	0.01
Pole 3	0.54	0.01	0.01	0.49	0.09	0.08
Pole 4	0.05	0.26	0.25	0.09	0.04	0.02
Pole 5	0.20	0.14	0.13	0.21	0.02	0.01
Pole 6	0.27	0.32	0.32	0.33	0.11	0.11

As expected, based on previous studies, the vertical temperature gradients are very small. In all the cases they are below 1°C which corresponds to good air mixing in the room. This also fulfils the requirements for thermal comfort by having vertical temperature gradients lower than 3°C as required.

6.3.4 Draught rate

As mentioned previously in the beginning chapters, draught is one of the main concerns of thermal discomfort in a ventilated room. Therefore, it is crucial to investigate the possibility of draught in the occupied zone. To determine whether there is possibility of draught five heights were chosen : 0.1m;0.6m;1.1m;1.7m;2.2m. Formula used to calculate the percentage of draught at each points is presented in the Chapter 2 Equation (2.1). In addition to that, since the local turbulence intensity is unknown an assumption of 40% is taken into account. The cases in the graphs are presented as:

- 6ACH2P - Measurement number 2, 6ACH, 2 Persons, their equipment, solar gains, people as pollutant
- 6ACHCS - Measurement number 3, 6ACH, 2 Persons, their equipment, solar gains, pollutant on the floor
- 3ACH2P - Measurement number 1, 3ACH, 2 Persons, their equipment, no solar gains, People as pollutant
- 3ACHCS - Measurement number 4, 3ACH, 2 Persons, their equipment, no solar gains, pollutant on the floor
- 3ACHCS1.3 - Measurement number 5, 3ACH, 1 Person, his equipment, no solar gains, pollutant at 1.3m height
- 3ACH1P - Measurement number 6, 3ACH, 1 Person, his equipment, no solar gains, 1 person as pollutant

Below are plotted results of calculated draught rates only for 2 heights : 0.1m and 1.1m. The rest of the heights are presented in the Appendix E due to the fact that all other calculated heights do not pose a risk of draught and has around 10% or less possibility of draught.

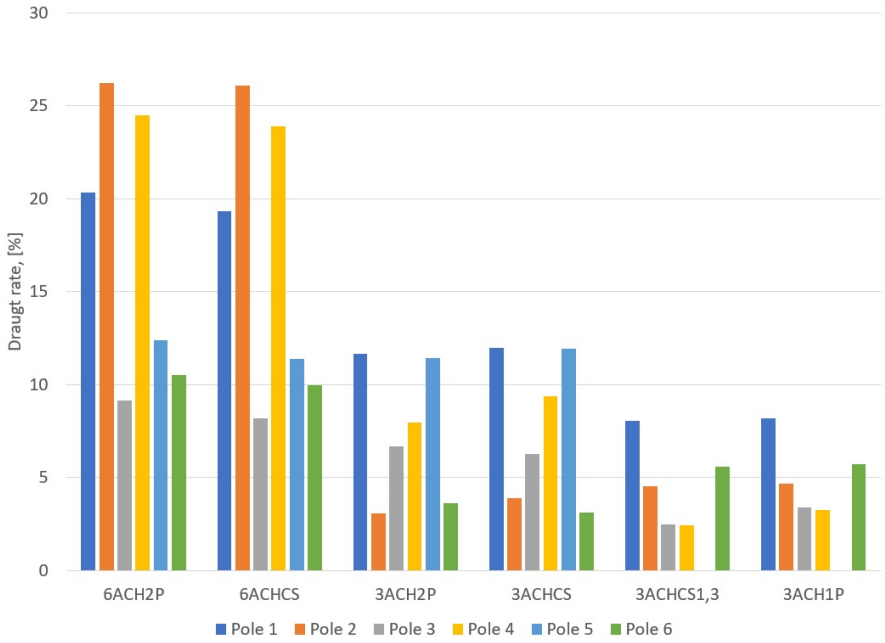

Figure 6.53. Calculated draught rates at 0.1m height for each case and each pole

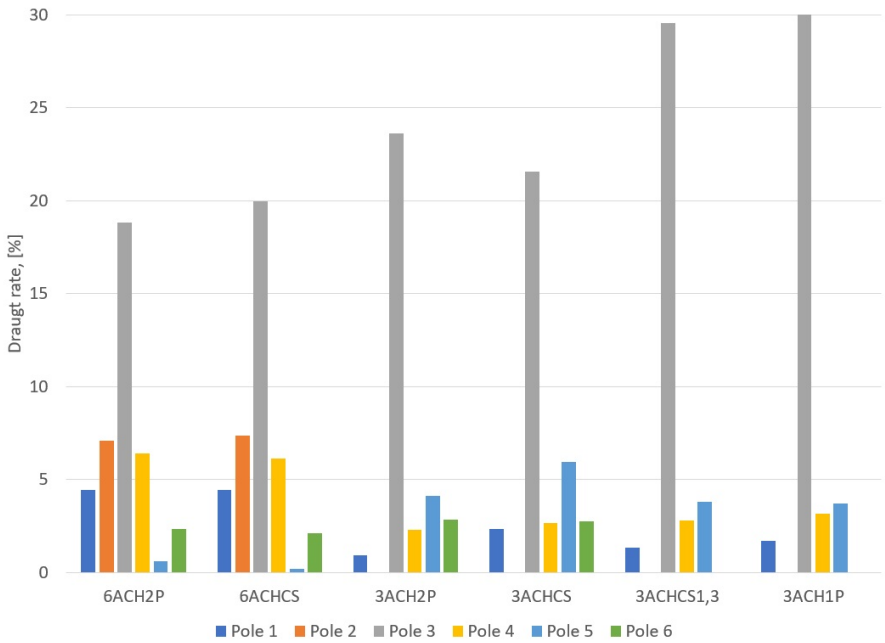

Figure 6.54. Calculated draught rates at 1.1m height for each case and each pole

As expected from the previous researches on diffuse ceiling ventilation the biggest possibility of draught appears on the lowest area of the room, close to the floor, where

the recirculation of air happens. Moreover, the highest draught rate is noticed close to the persons at Pole 1 and 4 and above the heat carpet which is below the Pole 2. However, it can be seen that by reducing the ACH by half the possibility of draught is eliminated for every pole. In addition to that, it was noted that for every conducted measurement Pole 3 at height 1.1m measured higher velocities compared to other specific points. At first it was thought that there might be a leak in manikin side and the fan inside is creating extra momentum through the gap somewhere. However, no noticeable leaks or holes in the manikin were found. Another assumption was that there was electrical noise and the voltage output was influenced. In order to validate that, the specific anemometer had to be re-calibrated and the received polynomial had to be double checked. This was not done because there was another measurement in process already and due to shortage of time it was neglected and the point was left as it is. This can be seen in the Figure 6.54 where all the cases pole 3 is very close or above 20% threshold of draught rate. It should not be neglected that specific point can be an outlier because the 6ACH cases have smaller possibility of draught rate than the 3ACH cases which does not make sense since higher air change rate should give higher velocities in the room and have higher possibility of draught.

Partial conclusion

To sum up the air quality assesment; the ventilation system works as a mixing ventilation system when the pollutant source is positioned in a heat source or close to one and as a piston ventilation system when the pollutant is away from heat sources. It is also evident that in the cases with the pollutant not being near a heat source "dead zones" can exist in the occupied zone. This particular issue however needs to be investigated in further studies.

6.3.5 PMV and PPD

For each measurement the predicted mean vote (PMV) and percentage people dissatisfied (PPD) for the thermal comfort was evaluated as well. However this is done by assuming a relative humidity of 60 % and some assumptions regarding mean radiation temperature and air temperature as only operative temperature was measured for the experiments. With the assumptions clarified the PMV and PPD for the measurements is shown in Table 6.13 and are calculated by Fanger's method [ISO7730, 2005].

Table 6.13. PMV and PPD for the 6 measurements

Measurement	PMV [-]	PPD [%]
Case 1	-0.16	5.5
Case 2	-0.38	8.0
Case 3	-0.33	7.3
Case 4	-0.29	6.7
Case 5	0.07	5.1
Case 6	0.11	5.2

From Table 6.13 it can be seen that the perceived thermal comfort is reasonable. Highest PPD is monitored during cases 2 and 3 with 6ACH. This can be explained by the highest

possibility of draught risk if compared to other cases. Also, all of the measured cases have calculated PPD percentage less than 10% which indicated that indoor environment quality is in acceptable range.

6.4 Conclusions

It was noticed that temperature distributions for each case were uniform. As expected from the previous studies where uniform temperatures were observed, present study showed no difference. All observed temperature distributions in the occupied zone showed only uniform distribution except for pole 3 height 1.1m which was situated close to the person with heat load and close to the exhaust. Generated thermal plume and air flow pattern towards exhaust side could have caused the deviation of temperature at that specific point. Other than that, all the temperatures were uniform and provided vertical temperature gradients lower than 0.54°C/m. It can be concluded that diffuse ceiling ventilation provided acceptable optimum temperature for the room and has fulfilled the requirement for optimum temperature range inside as required in the regulations.

Measured velocities in the room were within acceptable range of 0.2m/s except at some points at ankle level 0.1m and pole 3 at 1.1m height. Overall, a strong recirculation at ground level was noticed. It seems that the air flow diffuses through porous medium at the end of the room and goes downwards to the floor creating a clockwise recirculation towards the exhaust duct in the room. This was also noticed in the previous studies with symmetrically placed heat sources. Other than that, velocities at higher heights than 0.1m were lower than 0.1m/s for most of the cases causing draught free conditions in the room. Highest risk of draught was acquired in the cases with 6ACH rather than 3ACH. It was noticed only on the ground level with 6ACH and for all the cases at pole 3 for 1.1m close to the person which might have been caused by thermal plume and small distance between measurement point and exhaust duct. For other heights all the cases had draught risk of 10% and lower which is within the acceptable range in the regulations.

While measuring N_2O concentrations it was noticed that mass balance was not reached for all the cases. Therefore, an assumption was made that there is a possible leak in the envelope where tracer gas is lost. Despite that, measurements where pollutant source is within the thermal plume or at higher level than the ground level, uniform distributions in the occupied zone were observed. It was noticed that in cases where pollutant source is placed at floor level there were some noticeable peaks at ground and upper levels. It was concluded that since the pollutant source is not positioned in thermal plume its distribution pattern is mainly influenced by the air flow pattern in the room until it hits the thermal plume region. After it reaches the thermal plume the buoyant forces drive contamination upwards causing the peaks at the higher and lowest zone of the room. Also, for further analysis of contamination distribution in the room local air quality index and contaminant removal effectiveness were calculated. It was noticed that for most of the cases the ventilation system work as mixing ventilation with contaminant removal effectiveness close to 1. However, for the case 3 where room is ventilated by 6ACH and pollutant source is placed at the floor level effectiveness was approximately 2.3 which indicated that system works like piston flow ventilation. By ventilating room with high air flow rate it could be seen that the plume of contamination did not reach higher heights

in the occupied zone and was removed along the floor towards the exhaust side. On the other hand, for the case 4 where room was ventilated with 3ACH and pollutant source was placed at floor level ventilation effectiveness indicated that ventilation system worked with mixing principle. This was explained by the fact that compared to 6ACH room is ventilated with smaller volumetric flow causing air flow in the room mainly to be driven by buoyant forces. Thus, with the help of buoyancy the contaminant source was mixed with air in the room resulting in contaminant removal effectiveness close of 1 which indicated good mixing in the room. The worst case scenario was obtained in case 6 where there was only one person in the room. Achieved contaminant removal effectiveness was less than 0.9 indicating poor mixing the room. From the local air quality indexes it can be seen that most of the contamination is gather in the corner of the occupied zone leading to poor air mixing. Therefore, conclusion was made if the heat load is not distributed uniformly in the room the performance of contaminant removal drops down under acceptable range and indicates poor mixing of air in the room.

Part III

Numerical analysis

7 | Numerical model setup

In Chapter 7, the CFD model created for the numerical analysis of this thesis is presented. Information regarding the model's setup, boundary conditions and assumptions for simplifying the case are presented in this Chapter.

7.1 Setup of the model

The case setup of the present thesis is similar to that one in which Zhang performed her numerical analysis. However, there are some differences in the geometry of room, heat load released by heat sources and also configurations in the inlet which may have a big influence on the airflow and temperature distribution in both, plenum and room. The case concerns a design of diffuse ceiling ventilation system in an office room with dimensions of 4.2m x 3.6m x 3.6m (length x width x height). The actual height of the room is 2.5m and just above of it a plenum of 1.075m height is placed. The room and plenum are separated by the diffuse ceiling panels which have a thickness of 0.025m. The ventilation air is supplied to plenum through a textile duct which is placed along the ceiling. The geometry of the room can be seen in the Figure 7.1.

Inside the room there are two persons who perform office work with a medium activity level of 1.2 met. The occupants carry with them their personal office equipment which is desktop computer and lighting. In addition to that, a plane surface is placed widthwise the floor for representing the heat carpet. The heat carpet is activated for accounting solar radiation in summer days. All the heat sources designed in the model can be seen in the Figure 7.2.

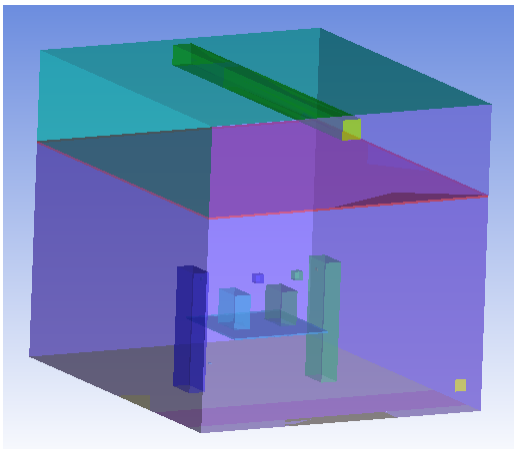

Figure 7.1. Geometry of the office room

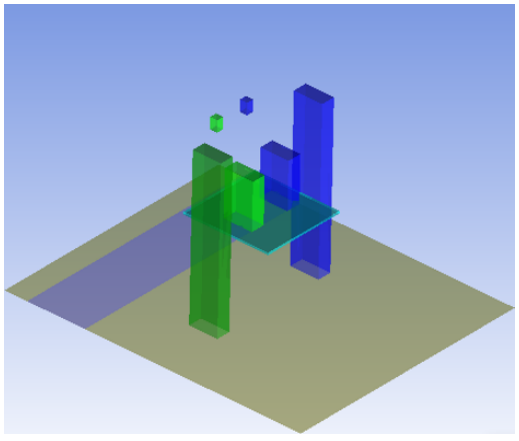

Figure 7.2. Heat sources inside the office room

The location of each object, dimensions of each surface and also the heat load released by each heat source can be seen in the Table 7.1.

Table 7.1. Detailed boundary conditions of the room case

Item	Length	Width	Height	Location			heat
	Dx, [m]	Dz, [m]	Dy, [m]	x, [m]	z, [m]	y, [m]	Q, [W]
Room	4.20	3.60	2.50				
Diffused ceiling	4.20	3.60	0.025			2.50	
Plenum	4.20	3.60	1.08			2.37	
Exhuast		0.14	0.14		3.40	0.25	
Inlet		0.24	0.24		1.75	3.30	
Textile duct	4.15	0.24	0.24		1.75	3.30	
Table	1.20	1.20	0.02	1.50	1.20	0.68	
Occupant 1	0.40	0.20	1.40	1.90	0.90		100
Mouth1	0.05		0.03	2.08	1.13	1.27	
Occupant 2	0.40	0.20	1.40	1.90	2.60		100
Mouth2	0.05		0.03	2.08	2.60	1.27	
PC 1	0.40	0.20	0.40	1.90	1.40	0.70	55
PC 2	0.40	0.20	0.40	1.90	2.00	0.70	76
Desk lamp 1	0.10	0.10	0.10	1.60	1.50	1.30	60
Desk lamp 2	0.10	0.10	0.10	1.60	2.00	1.30	60
Contaminant source	0.04	0.04		3.18	1.85		
Contaminant source 2	0.04	0.04		3.18	1.85	1.30	
Heat carpet	0.82	3.60		0.32			410

7.2 Boundary conditions

As it can be noticed the case of office room of this thesis is similar to the office room studied for learning purposes in Chapter 4. This is why most of the assumptions and boundary conditions in the setup of the numerical model can remain the same as previously explained in the Chapter 4. However, the two office rooms present some differences. Not only the dimensions of the room and heat released by the heat sources are different but also the ventilation air is supplied differently to the plenum. In addition to that, the concentration of CO_2 inside the room released by the persons will be examined as an extra parameter of indoor comfort evaluation. Therefore, some new boundary conditions are necessary to be applied in the new case room as explained further on in the Section 7.2.

7.2.1 Diffuse ceiling

As explained during the learning process in Chapter 4 the diffuse ceiling is treated as a full porous zone in the porous media model and as a solid zone with slot openings in the radiant model. In the porous media model, the functionality of the diffuse ceiling is defined according the porous parameters of its material such as viscous and inertial resistance coefficients. These coefficients are calculated by monitoring the pressure drop across the diffuse ceiling for different airflow rates. The total size of slot opening in the radiant model is also related to the pressure drop across the diffuse ceiling panels.

Therefore, the operation of both numerical models is dependent on the pressure drop across the diffuse ceiling which is highly related to the porosity and thickness of its material. Despite the similarity on the diffuse ceiling material used in both cases: present thesis and Zhang's study the use of the same porous coefficients and size of slot opening cannot be applied. As it can be noticed from the Table 7.1 the diffuse ceiling in the present case has a different thickness compared to the Zhang's case. In this case, the diffuse ceiling panels have a thickness of 0.025m whereas in Zhang's study the diffuse ceiling is 0.035m thick. This difference in thickness make it necessary to estimate new porous coefficients and slot opening size which correspond to the actual behaviour of the present diffuse ceiling.

Diffuse ceiling in porous model

In order to obtain new porous coefficients a pressure drop experiment across the diffuse ceiling panels is necessary. The Figure 7.3 shows the curve of pressure drop between plenum and room for different air flow rates. By using the polynomial which is obtained after a quadratic regression analysis of this curve the porous coefficients of the diffuse ceiling can be calculated. The pressure drop experiment is presented and explained in detail in the Appendix A. By conducting the pressure drop experiment between the plenum and room the viscous and inertial resistance coefficients of the diffuse ceiling are estimated to be equal to $7.6{\cdot}10^{7} m^{-2}$ and $50635 m^{-1}$ respectively. These coefficients are used as boundary conditions when defining the diffuse ceiling as a full porous zone in CFD model.

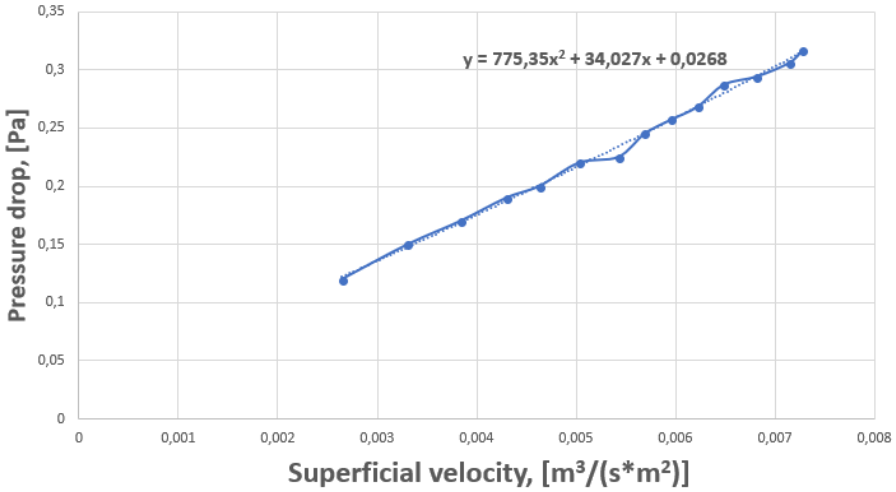

Figure 7.3. Pressure drop between plenum and room

Diffuse ceiling in radiant model

In addition to the new porous coefficients used in the porous media model, is necessary to calculate a new slot opening size for the radiant model. As explained in the Section 4.2 the size of slot opening is calculated according to the Equation (4.2). In particular this Equation accounts the pressure drop across the diffuse ceiling panels for the corresponding airflow rate. Therefore, in order to calculate the slot opening area the pressure drop between plenum and room which corresponds to the airflow rate of interest needs to

be defined. The pressure drop for a certain flow rate can be estimated by using the polynomial of the Figure 7.3. By performing these calculations the total slot opening size which represents the porosity of the diffuse ceiling material in the radiant model is estimated to be 0.56m^2. This total slot area can be distributed by three vertical slots likewise performed in the Section 4.2 with an effective area of 0.19m^2 (3.6m x 0.053m) each.

The Figure 7.4 illustrates the treatment of the diffuse ceiling in both, porous media and radiant model. The design of the permeable ceiling in the porous model can be seen on the left side of the Figure 7.4 whereas the design of the solid ceiling with slot openings is presented on the right side of the Figure 7.4.

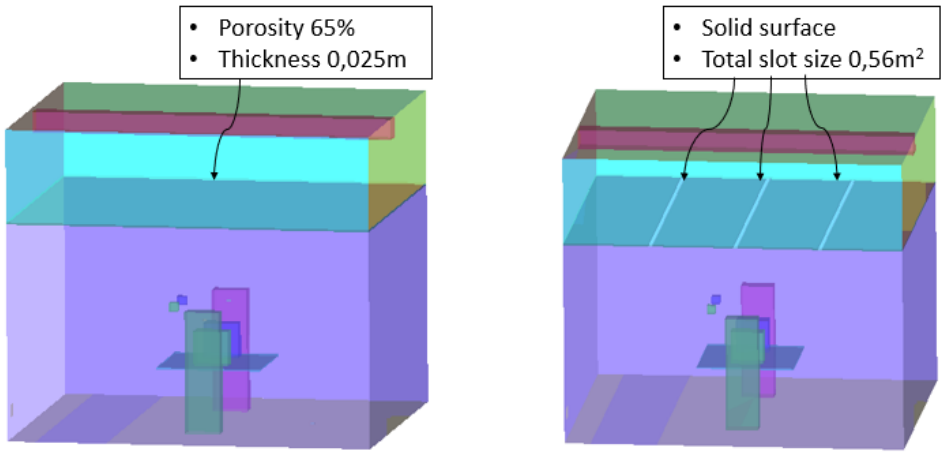

Figure 7.4. Characteristic of diffuse ceiling in porous(left) and radiant(right) model

7.2.2 Textile duct

In order to achieve uniform distribution in the plenum fabric duct was used. One of its main perks is that it can distribute supply air through its porous surface with low impulse. Therefore, the air distribution in the plenum is dependent on the porous characteristics of the textile duct material which are necessary to be precisely defined in the numerical model for obtaining reliable predictions.

In the real case, the textile duct has a shape of a cylinder with 0.3m and 4.15m diameter and length respectively. However, in the numerical model its geometry was designed differently. In order to simplify the case and build structured mesh the textile duct in the model has a square cross-section as indicated in the Figure 7.1. The dimensions of the textile duct in model were designed so that its total fabric surface and its length remain the same as in the real case. Dimensions can be found in the Table 7.1. A comparison of the geometrical characteristics of the textile duct in both real case and numerical model can be seen in the Table 7.2 below.

Table 7.2. Comparison between the textile duct in the model and in real case

Item	Shape [-]	Cross-section area [m^2]	Length [m]	Surface area [m^2]
Textile duct in reality	Cylinder	0.07	4.15	3.98
Textile duct in model	Rectangular	0.06	4.15	3.98

As mentioned before, the distribution of airflow in the plenum is influenced by the porous parameters of the textile material. Therefore, proper boundary conditions for the textile duct need to be defined so that its real functionality can be applied to the numerical model.

First of all, due to its very small thickness the textile duct is defined as porous-jump condition and not as a full porous zone like in the case of the diffused ceiling. Porous-jump condition is a 1D simplification of a full porous media zone and can be applied to porous surfaces or membranes which have finite thickness [Ansys]. By defining the fabric duct as a porous-jump condition instead of porous zone helps to reduce the amount of cells in the mesh and achieve faster convergence of the solution [Ansys].

After defining the textile duct surface as a porous-jump condition the next step is to define its porous properties. By defining the porous characteristics and the thickness of the textile material in the porous-jump conditions then the pressure drop across its layer can be calculated. The pressure drop across a porous-jump surface is calculated according to Darcy's law combined with an inertial loss term as the Equation (7.1) below indicates [Ansys].

$$\Delta_p = -(\frac{\mu}{\alpha} \cdot v + C_2 \cdot \frac{1}{2} \cdot \rho \cdot v^2) \cdot \Delta_m \tag{7.1}$$

Where
Δp - Pressure drop $[kg/(s^2 \cdot m)]$
v - Superficial velocity $[m^3/(s \cdot m^2)]$
ρ - Density of fluid $[kg/m^3]$
μ - Viscosity of fluid $[kg/(m \cdot s)]$
α - Permeability $[m^2]$
C_2 - Inertial resistance factor $[m^{-1}]$
Δm - Thickness of porous surface [m]

Therefore, as the above Equation (7.1) states, it is important to define the actual values for the permeability, inertial resistance and the thickness of the textile. In the numerical model the thickness of the fabric layer is defined 0.007m as it has been measured in the laboratory. However, for the estimation of the permeability and the inertial resistance coefficient a pressure drop experiment is required. A pressure drop experiment across the fabric layer has been conducted in the laboratory in order to obtain the coefficients for further simulations. The pressure drop curve across the textile layer for different air flow rates is shown in the Figure 7.5. By performing a quadratic regression analysis of this curve a polynomial can be obtained which is used for estimating the porous coefficients of the fabric duct. The pressure drop experiment is presented and explained in detail in Appendix A. By carrying out the pressure drop measurements the permeability and inertial resistance coefficient of the textile are estimated to be $7{\cdot}10^{-11}m^2$ and $8.8{\cdot}10^5m^{-1}$ respectively.

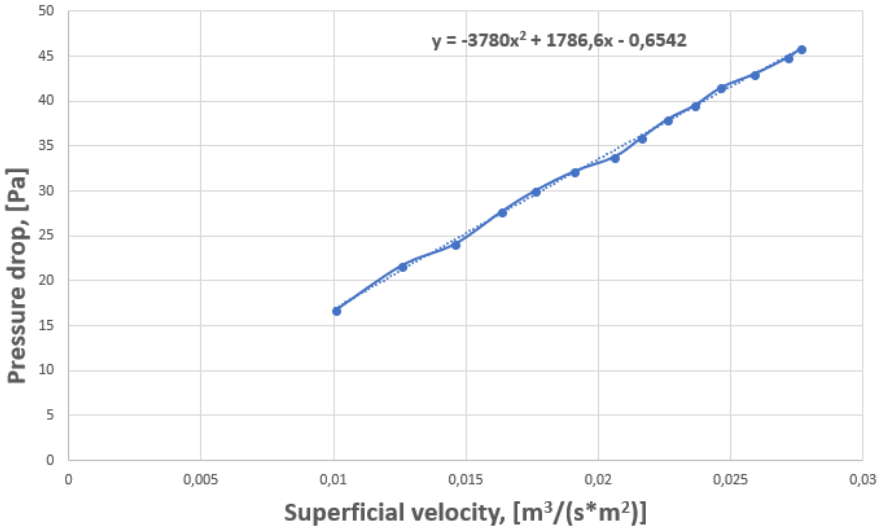

Figure 7.5. Pressure drop between textile duct and plenum

7.2.3 Heat sources

Moreover, some of the heat sources located inside the room have a different heat load compared to Zhang's case investigated during the learning process. The reason of that is due to the available equipment found in the lab where the experiments of the present thesis is conducted. Since different heat sources are used in this case, their heat fluxes used in the numerical models have to be calculated again.

Heat sources in radiant model

As explained in Chapter 4 the radiant model is used for accounting the heat transfer by means of radiation in the room. Thereby, the heat fluxes generated by the heat sources need to include both convective and radiative heat flow in the radiant model. The Table 7.3 below shows the characteristics of each heat source in the radiant model.

Table 7.3. Boundary conditions of heat sources in the radiant model

Heat source	Heat load, [W]	Heat flux, [W/m^2]	Emissivity, [-]
Occupants	100	56.8	0.5
Lamp 1	60	1000	0.1
Lamp 2	60	1000	0.1
PC 1	55	98.2	0.1
PC 2	75.5	134.8	0.1
Heat carpet	410	138.9	0.1

Heat sources in porous model

As mentioned the radiative heat flow is taken into account in the radiant model and then is applied to the porous model as input boundary conditions. Therefore, it is necessary for the heat sources to release only convective heat flow in the in the porous model. As has been applied during the learning process, the convection heat flow released by computers is 90% whereas by occupants and lamps is 50% of their total heat load. In cases where it

is necessary to activate the heat carpet its convection heat flow is assumed to be 60% of its total heat load. The Table 7.4 below lists the heat flux of each heat source used in the porous mode.

Table 7.4. Boundary conditions of heat sources in the porous model

Heat source	Heat load, [W]	Heat flux, [W/m^2]
Occupants	50.0	28.4
Lamp 1	30.0	500.0
Lamp 2	30.0	500.0
PC 1	49.5	88.4
PC 2	68.0	121.3
Heat carpet	246.0	83.3

7.2.4 Room envelope

In addition, the room envelope in the case of this thesis differs compared to the room investigated during the learning process. Not only the window is not included but also some of the walls are made of different material. That is why new wall boundaries need to be defined in the radiant model from where the wall temperatures are received. The wall boundaries which are applied in the radiant model need to correspond to the real room envelope where the experiments are conducted. In this room, the inner walls, ceiling and floor have the same thickness and are made of the same material, thereby all of these surfaces have the same insulation properties. However, the East wall which imitates the facade of the room is made of thin wood broad therefore due to that U-value coefficient of this surface differs from the rest walls. The emissivities and convective heat transfer coefficients can remain the same as used during the learning process. The Tables 7.5 and 7.6 list the wall properties and materials used for wall boundaries in the radiant model.

Table 7.5. Boundary conditions used for walls in the radiant model

Surface	Heat transfer Coefficient, [$W/m^2 \cdot K$]	Internal & External emissivity, [-]	Material	Thickness, [m]
Wall-East	5	0.9	Facade	0.014
Wall-West	5	0.9	Walls&floor&ceiling	0.260
Wall-North	5	0.9	Walls&floor&ceiling	0.260
Wall-South	5	0.9	Walls&floor&ceiling	0.260
Plenum-East	5	0.9	Facade	0.014
Plenum-West	5	0.9	Walls&floor&ceiling	0.260
Plenum-North	5	0.9	Walls&floor&ceiling	0.260
Plenum-South	5	0.9	Walls&floor&ceiling	0.260
Floor	5	0.9	Walls&floor&ceiling	0.260
Plenum ceiling	5	0.9	Walls&floor&ceiling	0.260

Table 7.6. Material properties used for each wall in the radiant model

Wall type	Thermal conductivity, $[W/m \cdot K]$	Thermal capacity, $[J/m \cdot K]$	Density, $[kg/m^3]$
Walls&floor&ceiling	0.046	790.4	700
Facade	0.112	790.4	700

7.3 Contamination modelling

As mentioned at the beginning, the main focus of this thesis is the performance of the diffuse ceiling ventilation system regarding air quality. This is why it is important to build a numerical model which can estimate the concentration of pollutants in the room of investigation. The case of this thesis is an office room with two persons who perform office work therefore, the air pollution is mainly caused by the concentration of CO_2 released during exhalation. In addition to that, other air pollutants i.e VOC_s released by furniture and construction materials can occur too. In this Section 7.3 the numerical modelling applied for estimating the concentration of contaminants in the office room is presented and explained.

In order to estimate the concentration of pollutants by a numerical model, it is necessary to activate an extra model in Fluent software. This additional model is called 'Species' and it can predict the local mass fraction of each species which takes place in the fluid phase. For this prediction, the solution of the conservation equation of all species must be obtained. This additional equation which calculates the local mass fraction of each species has a general form as expressed in the Equation (7.2)[Ansys] The below Equation does not take account any chemical reaction between the species but only their transportation in the fluid domain.

$$\frac{\partial(\rho \cdot \Upsilon_i)}{\partial t} + \nabla(\rho \cdot \vec{v} \cdot \Upsilon_i) = -\nabla \cdot \vec{J}_i + S_i \tag{7.2}$$

Where
Υ_i - Mass fraction of species i [%]
$\vec{J}_i$ - Diffusion flux of species i $[kg/(m^2 \cdot s)]$
S_i - Rate of creation of species i $[kg/(m^3 \cdot s)]$
$\vec{v}$ - Velocity component of fluid $[m/s]$
ρ - Density of mixture $[kg/m^3]$

The diffusion flux for a turbulent flow can be calculated as the Equation (7.3) below shows [Ansys].

$$\vec{J}_i = -(\varrho \cdot D_{i,m} + \frac{\mu_t}{S_{Ct}}) \cdot \nabla Y_i \tag{7.3}$$

Where
$\vec{J}_i$ - Diffusion flux of species i $[kg/(m^2 \cdot s)]$
Υ_i - Mass fraction of species i [%]
ρ - Density of mixture $[kg/m^3]$

$D_{i,m}$ - Turbulent diffusivity of species i $[m^2/s)]$
μ_t - Turbulent viscosity $[kg/(m^2 \cdot s)]$
S_{Ct} - Turbulent Schmidt number [-]

This additional equation is solved for N-1 species where N is the total number of species which take place in the system. Since the mass fraction of all the species must sum to unity the N-th mass fraction is defined as total minus the sum of N-1 solved mass fractions.[Ansys] In the present thesis, the mixture in the fluid domain concerns only two species: supply air and CO_2 released by people exhalation. Therefore, the above Equation (7.2) is solved only once in each simulation.

As mentioned previously the air pollution in an office room can be caused by CO_2 pollutants realised during occupants exhalation and also by other kind of pollutants released by manufactured items placed in the room. As mentioned in the Chapter 5, N_2O is used as a tracer gas to represent air pollutants in the room. The tracer gas is injected into the mouths of the mannequins and to certain locations in the room to imitate people exhalation and furniture emissions respectively. Therefore, the same approach needs to be applied in the setup of the numerical model in order to ensure the proper boundary conditions. In reality, these two different sources of contaminants not only release different kind of pollutants but also release pollutants with a different rate. However, in this study, both of the contaminants sources are assumed to release N_2O with the same rate. This assumption is applied since the major aim of this study is to examine the distribution of air pollutants in cases where their release takes place in two different scenarios, within and out of the thermal plume. Therefore, in the model the flow rate of contaminants released by 2 persons is equal to the flow rate released by a contaminant point source. The properties of the species which take place in the fluid mixture during the simulations can be seen in the Table 7.7.

Table 7.7. Properties of the mixture in the fluid domain

Species	Boussinesq-Density $[kg/m^3]$	Thermal Expansion Coefficeint [1/K]	Molecular Weight [kg/kmol]	Viscosity $[kg/(m \cdot s)]$
Air	1.23	0.00343	28.96	$1.789 \cdot 10^{-5}$
N_2O	1.98	0.00343	44.01	$1.72 \cdot 10^{-5}$

In order to model the exhalation of people, it is necessary to create surfaces from where N_2O is released. In reality, the procedure of exhalation can be performed either by mouth or nostrils. However, in order to simplify the case, the exhalation process is assumed only through the mouth. A mouth can be easily represented by assuming a rectangular surface attached to the person surface. The surface created for representing the mouth of each person has dimensions of 5cm x 3cm (length x height). An example of a person's mouth in the model can be seen with yellow colour in the Figure 7.6.

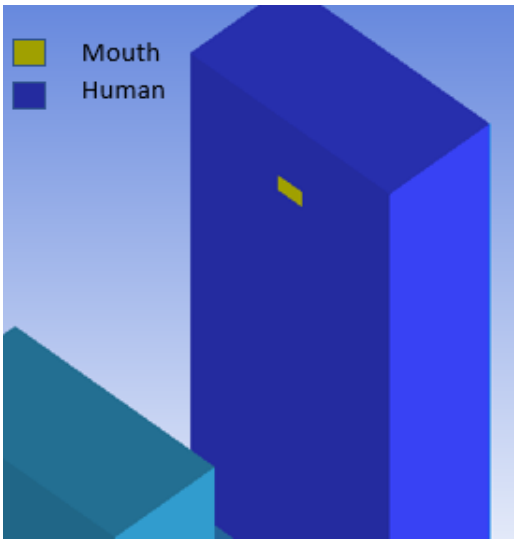

Figure 7.6. A surface attached to a person body for representing the mouth area

As mentioned before, another source of contaminants can be the furniture placed in an office room. In the experimental procedure, tracer gas is injected at certain locations in the room by a rubber tube. That means the furniture is assumed to be a point source of contaminants and not real items during experiments. The same approach needs to be adopted in the numerical model so that reliable predictions can be obtained. In order to represent this contaminant point source in the model, it is necessary to add extra surfaces on the coordinates where the tracer gas has injected in the room during the experiments. As mentioned in the Chapter 5 the traces gas which is representing furniture emissions has been placed in two different positions in the room: on the floor and at 1.3m height. Therefore, the same locations need to be defined in the model as point contaminants sources. In the numerical model these extra surfaces have small dimensions of 4cm x 4cm (length x width). In the Figure 7.7 the surface which represents the contaminant point source attached on the floor and the contaminant point source placed at head level can be seen with red and purple colour respectively.

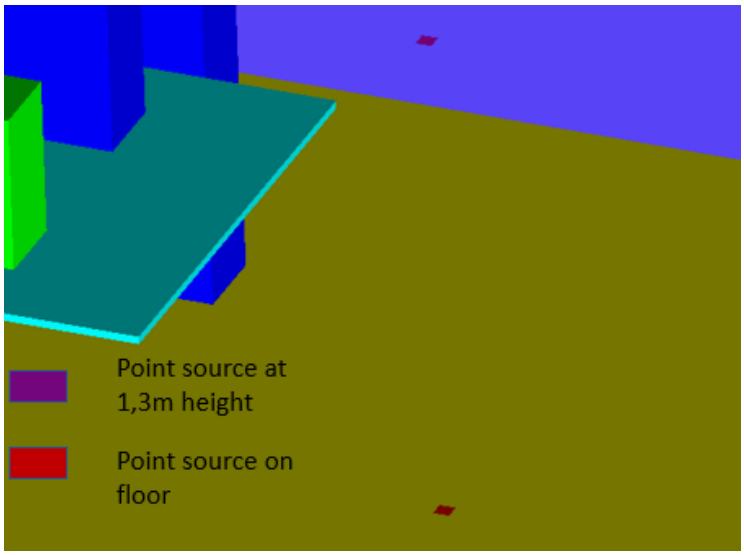

Figure 7.7. Extra surfaces for representing the contaminant point sources

However, as it is presented in Figures 7.6 and 7.7 the surfaces which have been designed to represent the inlet areas of contaminants have very small dimensions. Due to their very small dimensions, these inlet surfaces cannot obtain a structured and dense grid along them. This can be an issue since coarse inlet surfaces in a model may give errors and inaccurate results during the CFD simulations. This is why a different approach for defining the inlet surfaces for contaminants is adopted. For obtaining a flow of contaminants in the room without the use of inlet surfaces, separated cell-zones need to be created. In this case the flow is released by the volume of cells and not from surfaces. These separated cell-zones are attached to the contaminant inlet surfaces so that the pollutants are released from the same points as planned. The thickness of these cell-zones is dependent on the cell dimensions which is separated from the rest mesh. The volume of each cell zone can be seen in the Table 7.9. The location of each contaminant cell zone can be seen in the Table 7.8

Table 7.8. Location of each of the contaminant sources

Source	x,[m]	y, [m]	z, [m]
Person1 mouth	2.075	1.27	1.125
Person2 mouth	2.075	1.27	2.60
Floor point source	3.180		1.85
1.3m high point source	3.180	1.30	1.85

After defining the inlets for contaminants, the next step is to determine the rate of their release. As previously mentioned it is assumed that both contamination sources, people and point sources release the same pollutants with the same flow rate. The rate of creation of N_2O contaminants through the separated cell-zones can be calculated according to the below Equation (7.4) and then used as input in the corresponding cell zone in Fluent.

$$S_{N_2O} = \frac{\rho \cdot q}{V} \tag{7.4}$$

Where
S_{N_2O} - Rate of creation of N_2O pollutants $[kg/(m^3 \cdot s)]$
ρ - Density of N_2O $[kg/m^3]$
q - Flow rate of N_2O release $[m^3/s]$
V - Volume of cell-zone $[m^3]$

A person who performs office work with a medium activity level is assumed to exhale CO_2 with a flow rate of 20.4 l/h. Thereby, a point contaminant source is assumed to release CO_2 with a flow rate of 40.8 l/h which is equivalent with a case of 2 persons in the room. The Table 7.9 below shows the rate of release of each of the contaminant sources which take place in the room. These calculated rates of the contaminant sources are used as boundary species sources in the numerical model.

Table 7.9. Creation rate of pollutants of each of the contaminant sources

Source	Cell-Zone Volume $[m^3]$	Flow rate of contaminants [l/h]	Flow rate of contaminants $[m^3/s]$	Rate of creation $[kg/(m^3 \cdot s)$
Person 1	0,000075	20.4	$0.56{\cdot}10^{-5}$	0.150
Person 2	0,000056	20.4	$0.56{\cdot}10^{-5}$	0.200
Floor point source	0.000044	40.8	$1.12 \cdot 10^{-5}$	0.505
1.3m high point source	0.000053	40.8	$1.12 \cdot 10^{-5}$	0.425

7.4 Grid independence test

In order to ensure accuracy of the numerical analysis, grid independence test for both, radiant and porous media model needs to be performed. A grid independence test is carried out by simulating models with the same input conditions but different amount of cells. The reason for this test is to check whether the final results are dependent on the grid size. In addition to that, the grid independence test helps in choosing a grid size which converges with less as possible computational time without affecting the accuracy of the final results.

Table 7.10 below presents the grid independence test conducted for the radiant model of this study. As it can be noticed, the mass and energy unbalance have reached values less than 5% which means the below simulations have converged. The below grid independence test indicates that the final results of all the grids are close enough to each other. However, compared to 800 thousand grid the 1.2 million grid gives results with smaller deviation from the largest grid. This is the reason the model which is composed of 1.2 million cells is chosen as the final radiant model for the further studies of this thesis.

Table 7.10. Grid independence test of thesis radiant model

Mesh size	Average temperature, [°C]	Average velocity, [m/s]	Mass flow unbalance rate, [%]	Energy unbalance rate, [%]
800000	21.45	0.122	0	3.12
1200000	21.65	0.126	0	2.36
1800000	21.70	0.127	0	0.70

The grid independence test carried out for the porous model of this thesis is shown in the Table 7.11 below. As it can be seen, all the below simulations have reached a convergence state since their N_2O mass and energy unbalance rate is less than 5%. From this grid independence test it can be noticed that the final results are dependent on the grid size of the model. The first model which consist of 510K cells deviates from the rest models. All the other models calculated similar results. Since the model with 777 thousand cells gives results which do not significantly deviate from the results of the biggest mesh is chosen as the final porous model for the further studies of this thesis. This grid can provide relatively accurate results with much less computational time compared to the bigger grids.

Table 7.11. Grid independence test of thesis porous model

Mesh size	Average temperature, [°C]	Average N_2O concentration, [ppm]	Average velocity, [m/s]	Mass flow unbalance rate, [%]	Energy unbalance rate, [%]	N_2O Mass unbalance rate, [%]
510000	24.25	680	0.065	0	2.72	1.81
777000	24.40	686	0.070	0	0.90	1.30
900000	24.41	686	0.073	0	0.82	0.67
1330000	24.39	688	0.073	0	0.38	0.61

8 | Numerical model results

In order to ensure the credibility of the numerical model, it is necessary to validate it with experimental data. Chapter 8 focuses on comparing the results of model with the data obtained from the measurements in the laboratory. Afterwards it is concluded whether the model has been properly set-up and if it can provide reliable results.

As mentioned previously, in the Section 5.4 Table 5.4, 6 different cases were investigated experimentally in the laboratory. Results obtained by these measurements are compared with the results calculated by the numerical model created for this thesis. In order to have a better understanding of temperature, N_2O and air flow distribution in the room results of each case obtained by the CFD are analysed with the use of graphical illustrations.

Moreover, there are 6 stationary poles located in different positions in the room as the Figure 5.13 in Section 5.4 indicates. Along these poles thermocouples, anemometers air and tracer gas collectors are distributed as presented in the Figure 5.18. In addition to measurement points in the room, extra thermocouples and tracer gas collectors have been placed in plenum too as the Figure 5.20 shows. The aim of these extra sensors is to investigate the temperature distribution in plenum and also to check whether or not there is any reverse flow from room to plenum. Also, to check if there is any back flow to the textile duct, 2 additional N_2O collectors were put inside the fabric duct, one to the beginning(Fabric1) and one in the end of it(Fabric2). Measured values at these points will be used for the validation of the numerical model.

The energy and mass balances of all the simulations are presented in the Table 8.1. Energy and mass balance are used as indicators to see whether the simulation has converged.

Table 8.1. Simulation balances for each case

Case No.	Energy unbalance, [%]	N_2O mass unbalance, [%]
1	0.3	4.0
2	0.0	5.0
3	1.0	0.5
4	0.4	4.0
5	0.0	2.0
6	0.7	6.8

For clarification purposes planes which will be used for illustrating results of the simulations are shown in Figures 8.1 - 8.3.

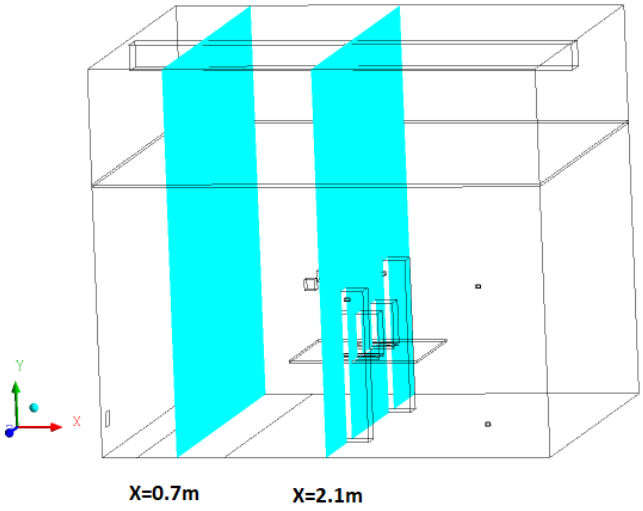

Figure 8.1. Planes along x-axis

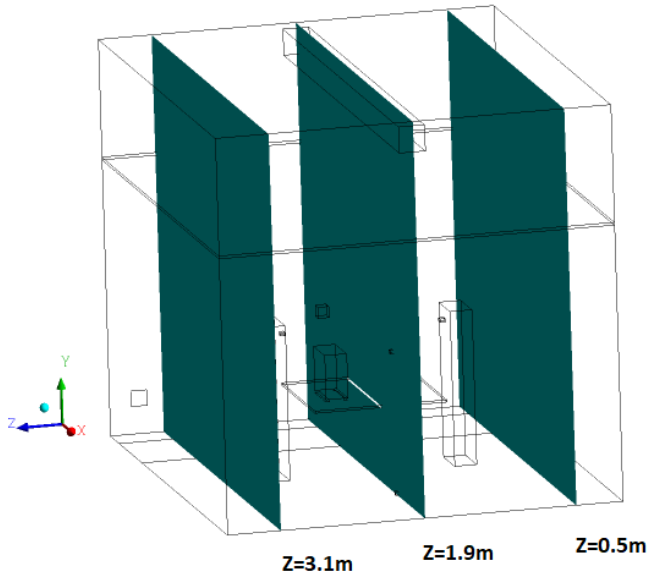

Figure 8.2. Planes along z-axis

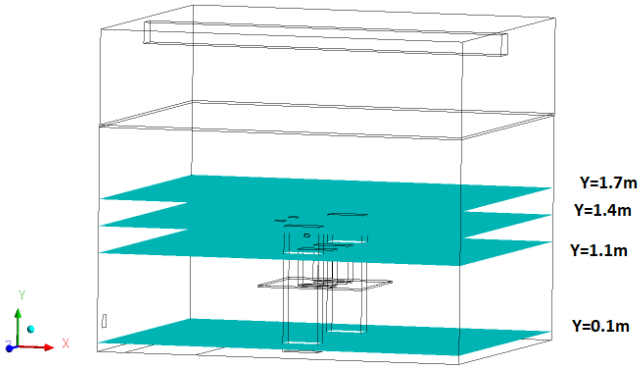

Figure 8.3. Planes along y-axis

Case 1

The comparison between temperatures measured during the experiment and calculated by the numerical model are presented in the Figures 8.4 - 8.9 below.

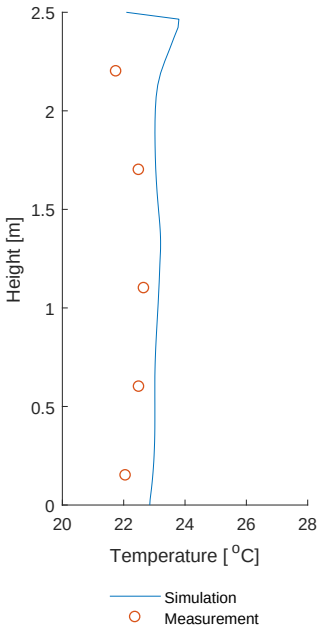

Figure 8.4. Temperatures along pole 1

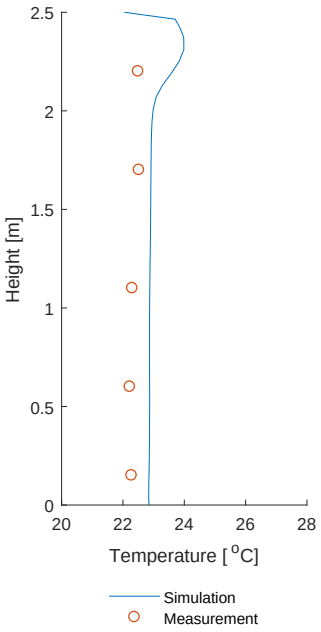

Figure 8.5. Temperatures along pole 2

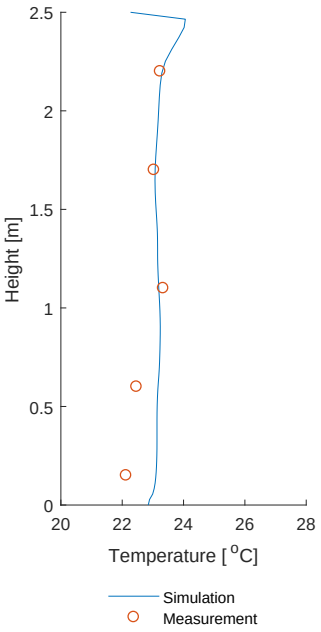

Figure 8.6. Temperatures along pole 3

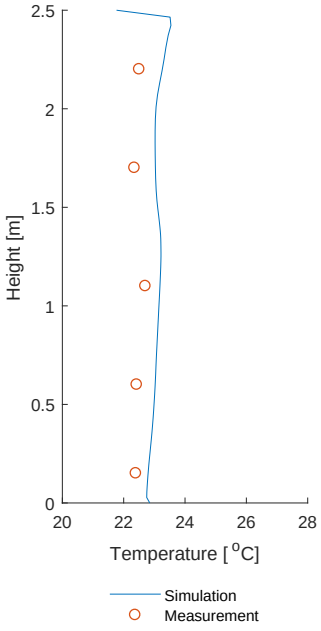

Figure 8.7. Temperatures along pole 4

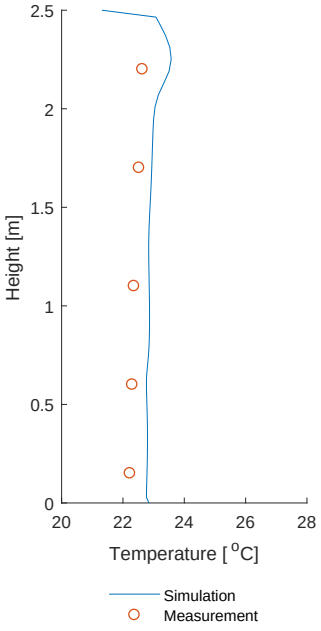

Figure 8.8. Temperatures along pole 5

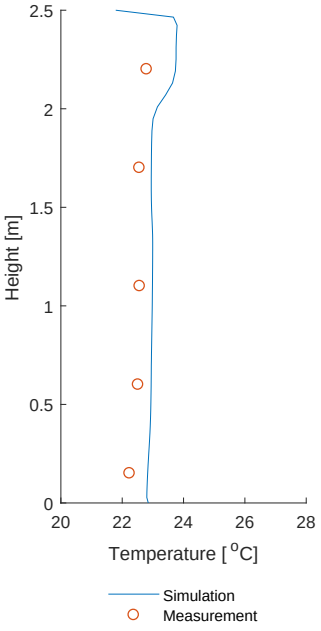

Figure 8.9. Temperatures along pole 6

The comparison of temperature distribution in the plenum is presented in the Figure 8.10

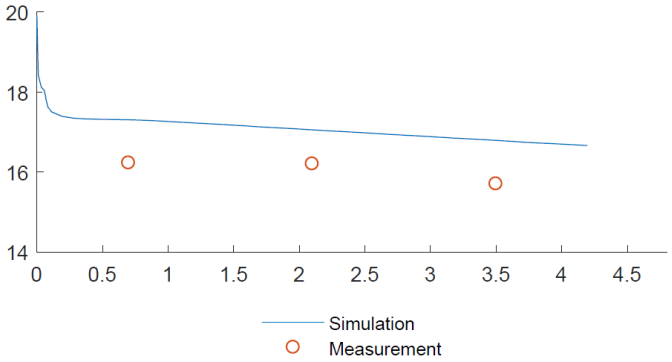

Figure 8.10. Comparison of temperature distribution in plenum

From the Figures 8.4 - 8.9 it seems that the numerical model estimates uniform temperature distribution along the poles as measured during the experiments. However, the calculated temperatures by the CFD model are higher by approximately 0.5°C than the temperatures obtained during the experiment. This happens due to the heat unbalance that occurred during the experiments. As mentioned previously the control of the cold box temperature was not available thus it was not possible to achieve desired cold box temperatures. Furthermore, in the CFD model the ambient temperatures are defined as fixed values. More specifically, the temperature of façade side was measured around 22°C just before the experiment for case 1 took place. This temperature was used as boundary condition in the radiant CFD model. By the end of the measurement in the laboratory it was noticed that the temperature of façade side had an average value around 20°C during the whole experiment for case 1. The façade wall has U-value of 8 $W/m^2 \cdot K$ which means even a small temperature difference on this side it is influential to the heat losses of the hotbox which has an impact on indoor air temperature. The unstable boundary conditions of the hotbox during the experiment influenced the heat balance and consequently the indoor temperature of the hotbox. The temperature of façade side used in the CFD radiant model and the average temperature of façade side during the case 1 experiment can be seen in Table 8.2.

Table 8.2. Comparison of temperature of facade side between experiment and CFD for case 1

Wall	Average temperature during experiment, [°C]	Fixed temperature used in CFD radiant model, [°C]
Façade wall	21.65	22.00

In addition to that, the tendency of temperature distribution in plenum calculated by the CFD model is the same as that one measured during the experiment which can be seen in the Figure 8.10. The temperature in the plenum is almost uniform in both, measurement and CFD model. However, there are deviations of 2-3°C between measured and calculated values. This can be assumed acceptable considering the heat unbalance occurred during the measurement and also the limitation of the radiant model on estimating temperatures of plenum walls as mentioned in the Section 4.2.3.

The comparison between air velocities measured during the experiment and calculated by the numerical model are presented in the Figures 8.11 - 8.16 below.

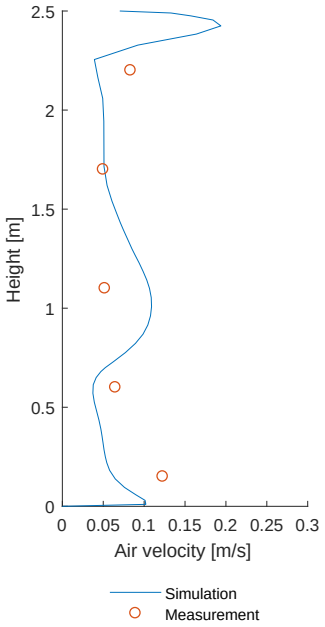

Figure 8.11. Velocities along pole 1

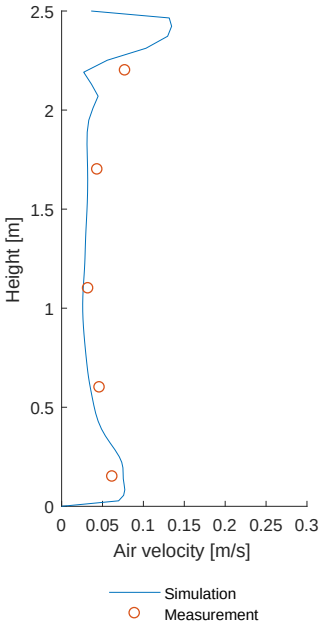

Figure 8.12. Velocities along pole 2

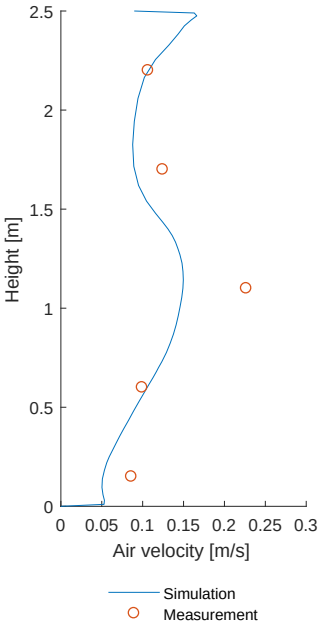

Figure 8.13. Velocities along pole 3

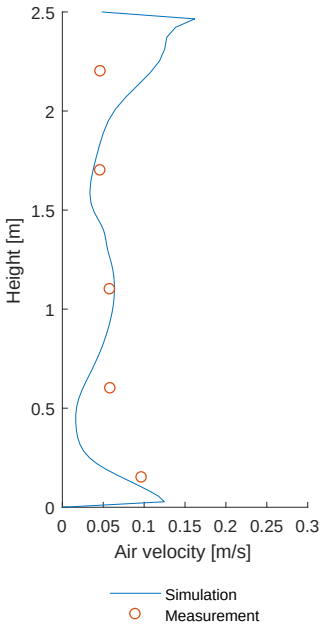

Figure 8.14. Velocities along pole 4

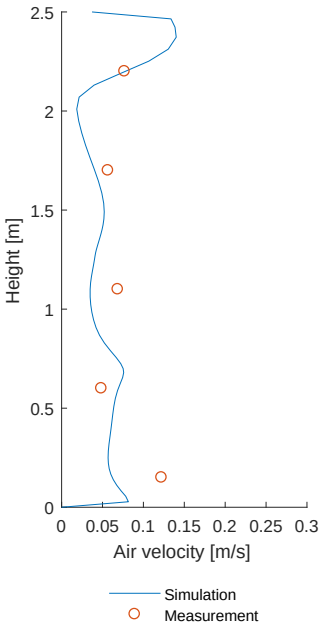

Figure 8.15. Velocities along pole 5

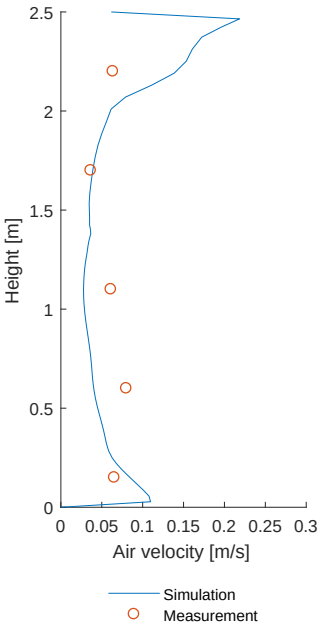

Figure 8.16. Velocities along pole 6

Figures 8.11 - 8.16 shows the velocity distribution comparison between measured and calculated values. It can be seen that numerical model estimates correctly the tendency of velocities for most of the measurement points. However, there are some points where the CFD model gives different estimation in air velocities comparing to the measured values. This may happen due to the existence of poles and cables used for the experiments inside hotbox. These poles and sensors do not exist in the CFD model thus their influence on the air flow cannot be accounted by the CFD model. Another assumption why there are deviations on the air distribution between simulation and measurement can be explained by the fact that the porous medium causes transient flow in the room. Therefore, the measured velocities are hard to be predicted accurately.

The comparison between N_2O measured during the experiment and calculated by the numerical model are presented in the Figures 8.17 - 8.22.

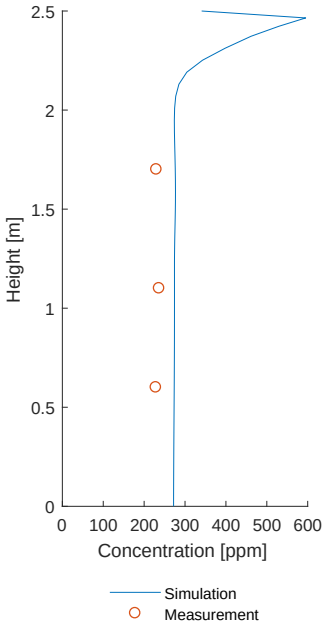

Figure 8.17. N_2O along pole 1

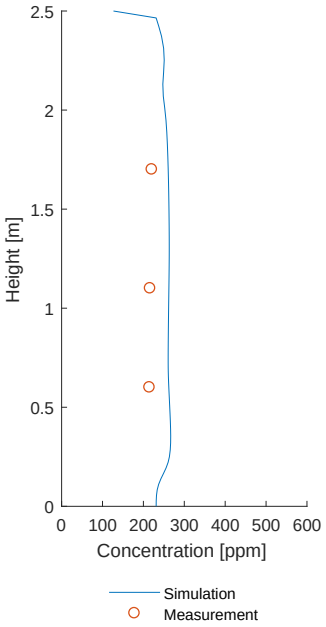

Figure 8.18. N_2O along pole 2

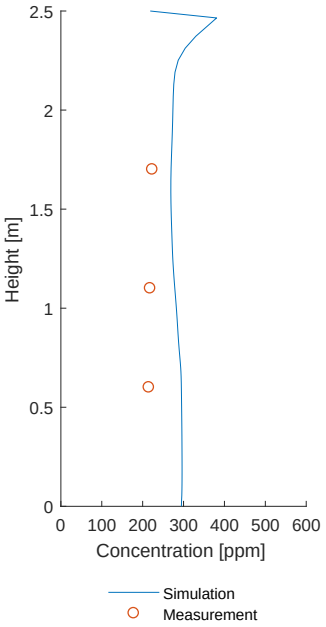

Figure 8.19. N_2O along pole 3

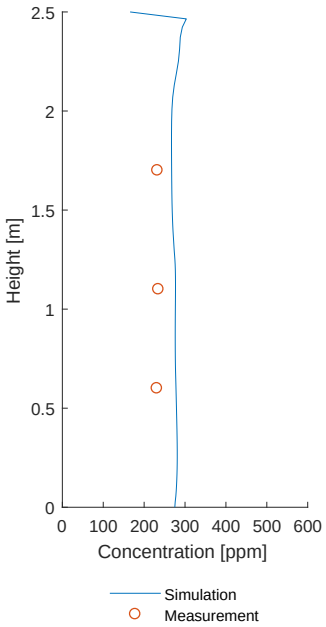

Figure 8.20. N_2O along pole 4

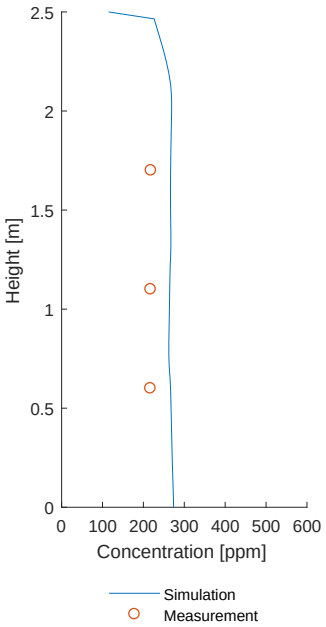

Figure 8.21. N_2O along pole 5

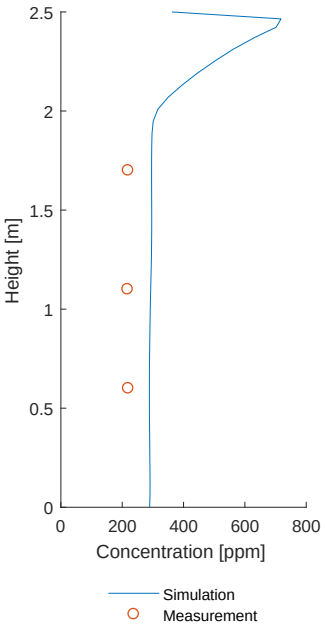

Figure 8.22. N_2O along pole 6

The comparison between N_2O concentrations at inlet, plenum points, fabric points and outlet for can be seen in Figure 8.23 and Figure 8.24.

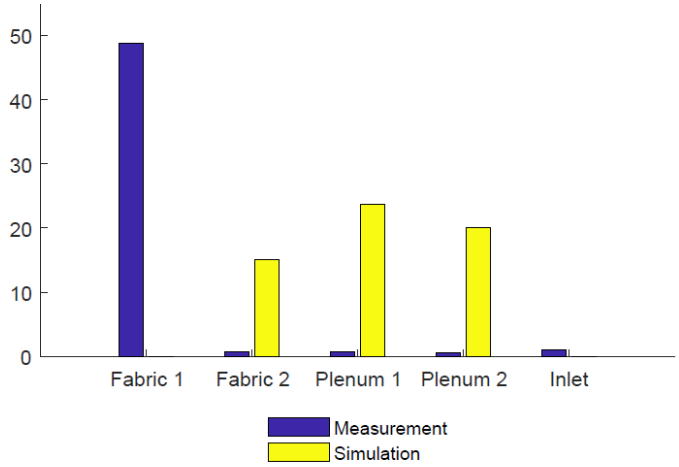

Figure 8.23. Comparison of N_2O concentration at certain locations

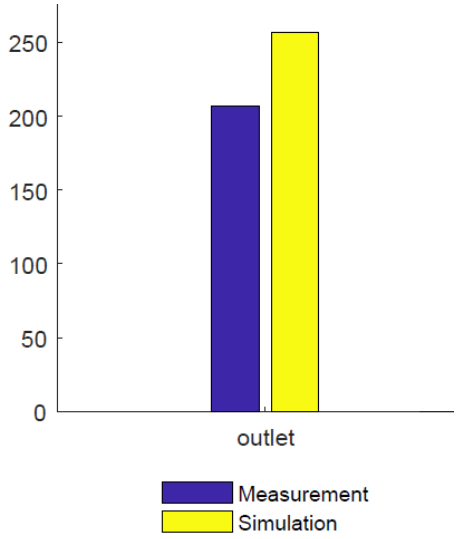

Figure 8.24. Comparison of N_2O concentration at outlet

Figures 8.17 - 8.22 show that the CFD model can estimate the tendency of the N_2O distribution. As the measurements have shown the distribution of N_2O along all the poles is uniform. The same estimation is predicted by CFD model but there are deviations between their values. The measurement showed that the N_2O concentration along all the poles is around 210-230 ppm whereas the CFD model predicts N_2O concentration in the range of 260-290 ppm. These deviations can be assumed acceptable when considering the N_2O mass unbalance which occurred during the measurement. Table 8.3 below show the N_2O mass unbalance rate occurred during the experiment which explains the lower N_2O concentration measured than expected. The N_2O mass unbalance have occurred due to the leak in the envelope of the hotbox.

Table 8.3. Comparison of N_2O mass unbalance rate between experiment and CFD for case 1

N_2O mass unbalance during experiment, [%]	N_2O mass unbalance in CFD, [%]
24.6	4.0

Moreover, points 'Plenum1' and 'Plenum2' measured N_2O concentrations in both, numerical model and measurement as shown in Figure 8.23. This means that the CFD predicted a reverse flow from room to plenum as can be concluded from the measurement too. The same applies to the 'Fabric 2' point which is located in the end of the fabric duct. This point experiences N_2O concentration in both, numerical model and measurement which indicates the existence of reverse flow from plenum to the fabric duct. The deviation between the CFD results and measurements for these points is understandable considering the general deviation happens in the room too. However, the CFD predictions and

measurements do not fit for 'Fabric 1' measurement point which is located at the beginning of the fabric duct. According to the CFD model there is not reverse flow from plenum to the beginning of the fabric duct but 'Fabric 1' point shown relatively high concentration during measurement. After all the measurements were done, it was found out that the measured concentration in the 'Fabric 1' point which obtained during all the experiments was an error in the tracer gas sensor tube. The tube for 'Fabric 1' point which was passing through the room had a leak in a junction closely situated to the exhaust duct which resulted in reading a N_2O concentration from the room instead.

Due to mass and energy unbalances occurred during the experiment the results of CFD model and experimental data do not fit. Therefore, adjustments to the CFD model are required so that it can predict the results obtained from the experiment even if mass and energy balances did not acquire. Therefore, adjustments to the CFD model are required so that it can predict the results obtained from the experiment even if mass and energy balances did not reach balance. A reduction to the supply flow rate of contaminants which counterbalance the contaminant loss and extra energy source which can equalize the heat loss need to be applied to the model. The results of the re-simulation for case 1 are shown in the Appendix F

The temperature distribution in the room for case 1 can be seen in the cross section Figures 8.25 and 8.26 below.

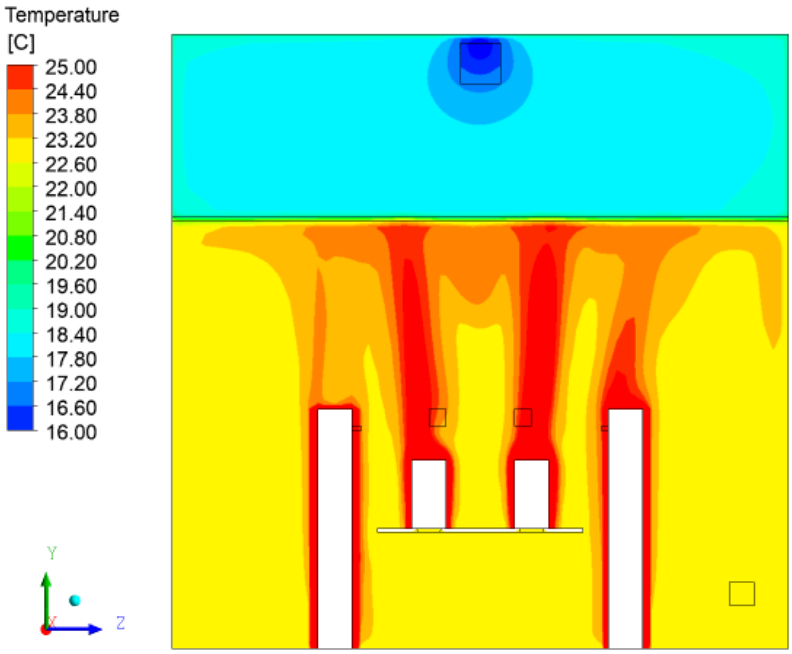

Figure 8.25. Distribution of temperature for plane at X=2.1m

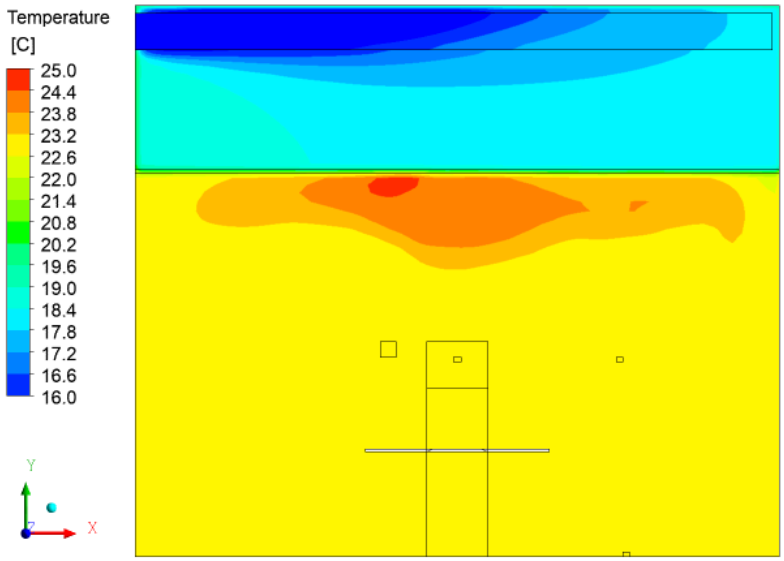

Figure 8.26. Distribution of temperature for plane at Z=1.9m

As it can be seen temperatures in the room are mostly uniformly distributed. The air temperature is around 22.5°C to 23°C in most of the space indicating good mixing of air in the room. Moreover, it can be seen that the buoyancy flow is the dominant flow in a room ventilated by a diffuse ceiling system since the thermal plume from the heat sources rises upwards and then is being mixed with the supply air coming downwards from the diffuse ceiling.

The air flow pattern for case 1 can be seen in the Figures from 8.27 to 8.31 below.

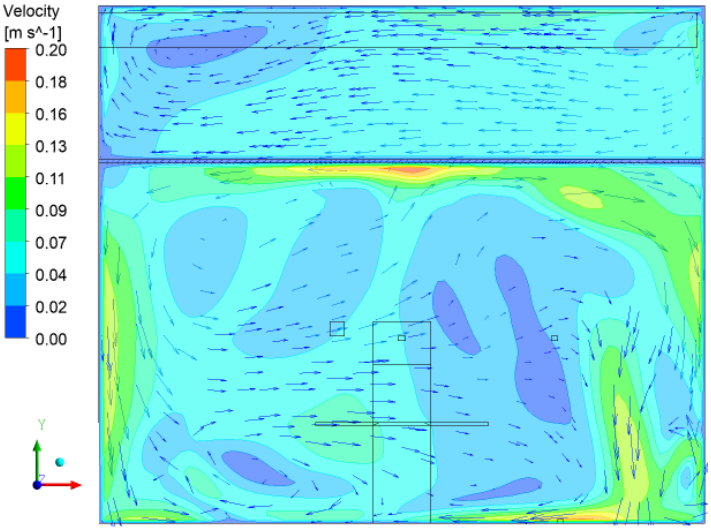

Figure 8.27. Airflow pattern for plane at Z=0.5m

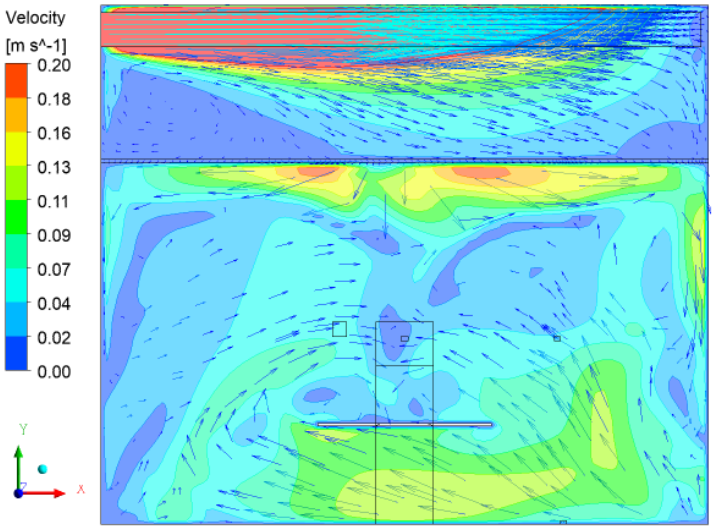

Figure 8.28. Airflow pattern for plane at Z=1.9m

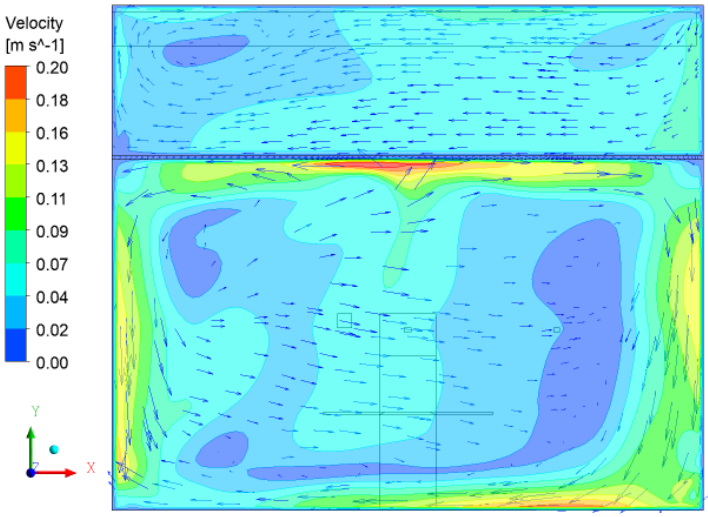

Figure 8.29. Airflow pattern for plane at Z=3.1m

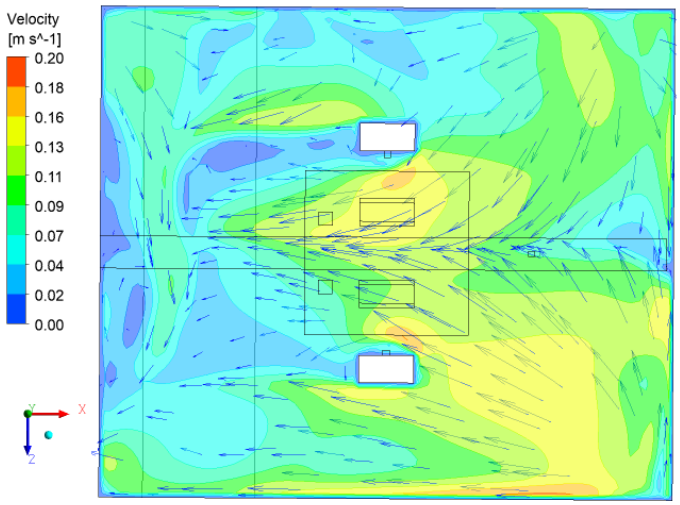

Figure 8.30. Airflow pattern for plane at Y=0.1m

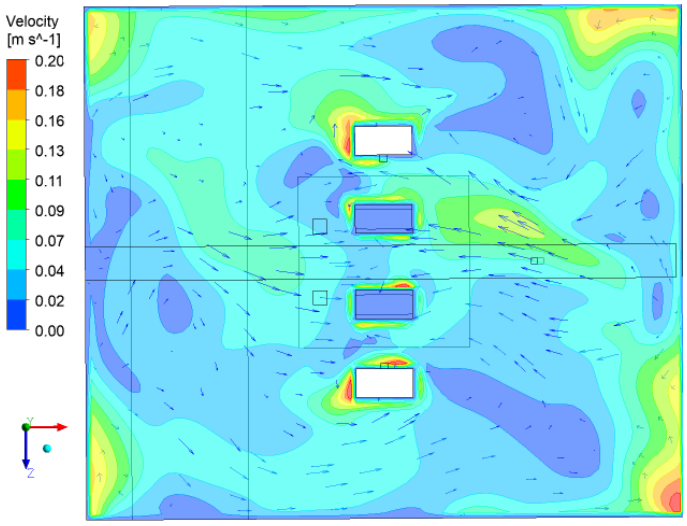

Figure 8.31. Airflow pattern for plane at Y=1.1m

The Figure 8.28 is an illustration of the air flow pattern in the middle of the room from a side view. The air enters the fabric duct with high momentum and reaches halfway until the momentum starts decreasing. At that point, the air loses its high momentum and starts diffusing from the fabric material to the plenum. Since the supply air is diffused from the fabric duct when it has already reached to the deeper parts of the plenum an air recirculation takes place in plenum starting from its deeper parts as it seems from the Figures 8.27 and 8.29. While the air circulates within the plenum it is also diffused through the porous medium due to over pressure and enters the room in the places where the thermal plume from heat sources is not acquired generating 2 symmetrical air circulations. That is why relatively high velocities are found lengthwise the diffuse ceiling and side walls. Most of the air continues along the side walls and reaches the floor where it starts spreading. That is why relatively high velocities are also generated along the floor especially beneath the table as the Figure 8.28 and 8.30. Additionally, by observing the 8.31 it can be noticed that at 1.1m height relatively high velocities are generated to the right side of the persons which explains the velocity peaks at pole 1 and 3 in Figures 8.11 and 8.13.

The distribution of contaminants for case 1 can be seen in the Figures 8.32 - 8.37.

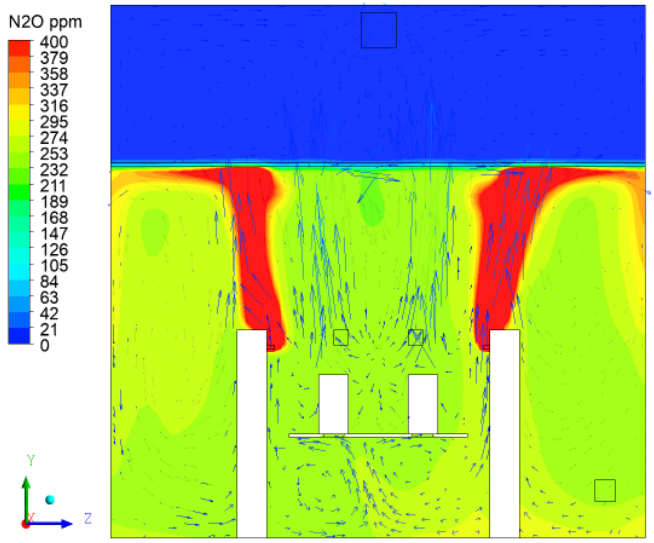

Figure 8.32. N_2O distribution for plane at X=2.1m

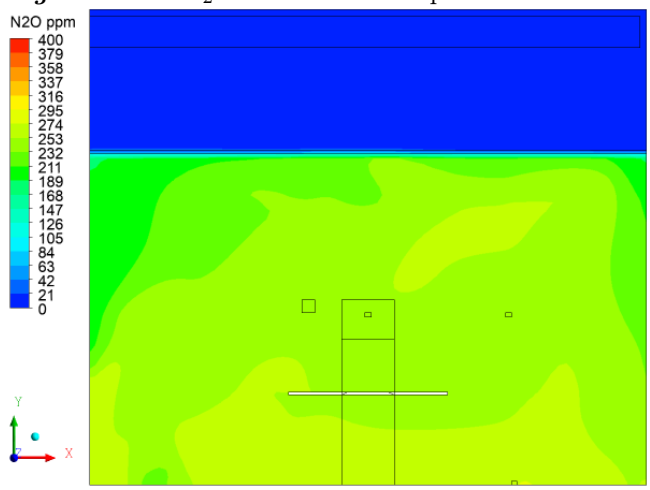

Figure 8.33. N_2O distribution for plane at Z=1.9m

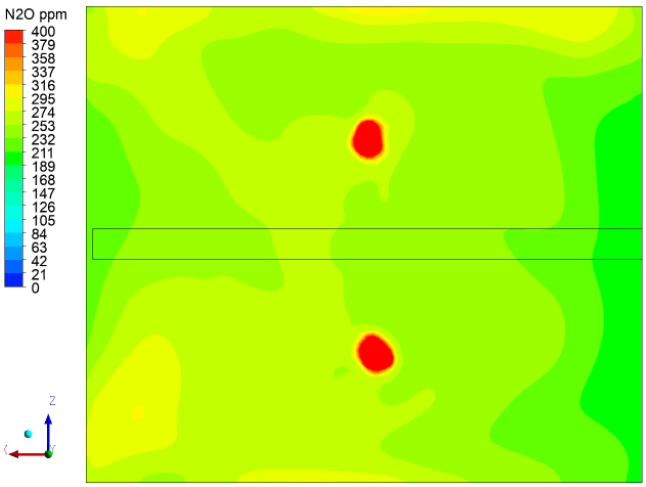

Figure 8.34. N_2O distribution for plane at Y=1.7m

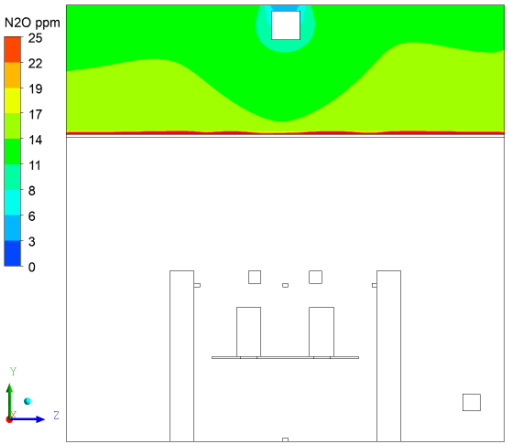

Figure 8.35. N_2O distribution in plenum for plane at X=2.1m

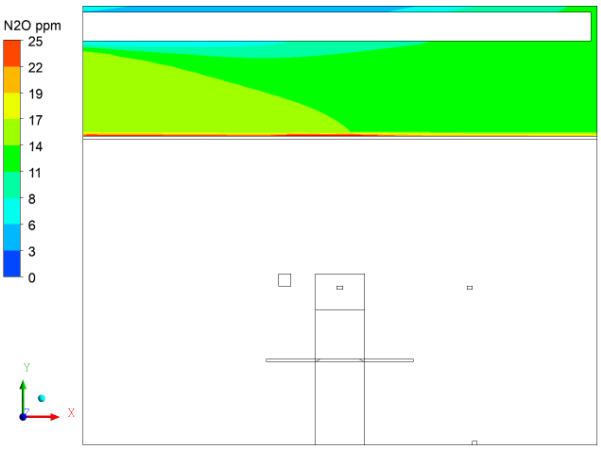

Figure 8.36. N_2O distribution in plenum for plane at Z=1.9m

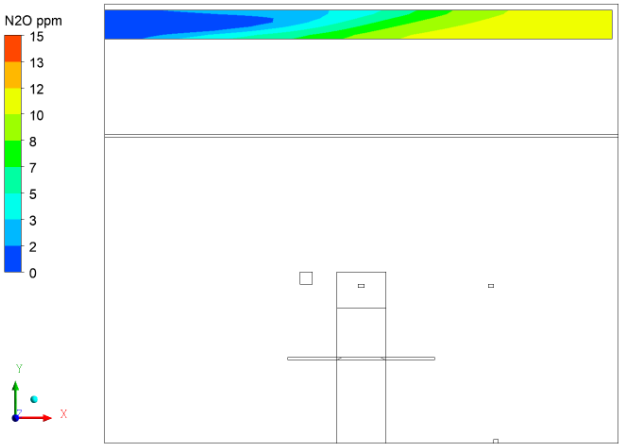

Figure 8.37. N_2O distribution in fabric duct for plane at Z=1.9m

Figures 8.32 - 8.34 show that the contaminant distribution is uniform within the room. The N_2O level is almost everywhere around 260-290 indicating good mixing of air. Figures 8.35 and 8.36 show that there is N_2O concentration in the plenum which means there is a back flow from room to plenum. Since the contamination sources are the two persons, the N_2O rises upwards with the thermal plumes and reaches the diffuse ceiling panels. As it can be noticed from these Figures the back flow happens uniformly along the diffuse ceiling since the contaminant-heat sources are positioned symmetrically in the room. In addition to that, from the Figure 8.37 it can be noticed that there is also back flow from the plenum to the fabric duct. However, this does not happen at the beginning of the fabric duct where the supply air has high momentum but only at the deeper parts of the fabric duct where the momentum starts dropping down.

Case 2

The comparison between temperatures measured during the experiment and calculated by the numerical model are presented in the Figures 8.38 - 8.43.

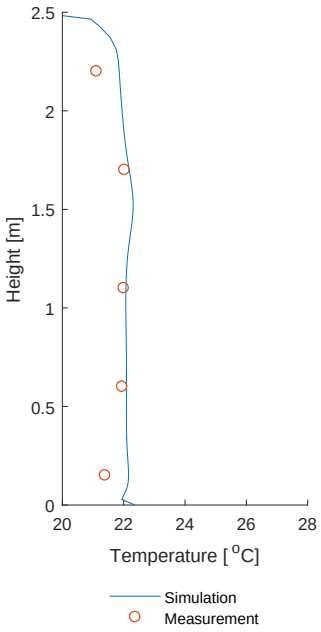

Figure 8.38. Temperatures along pole 1

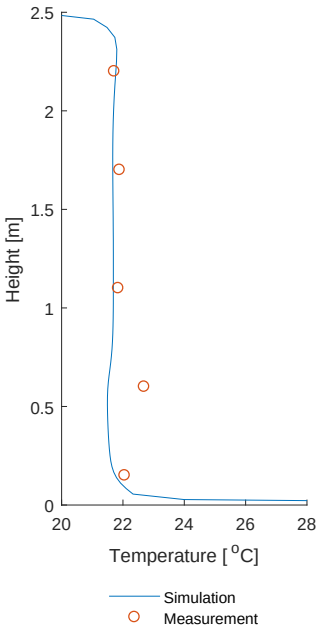

Figure 8.39. Temperatures along pole 2

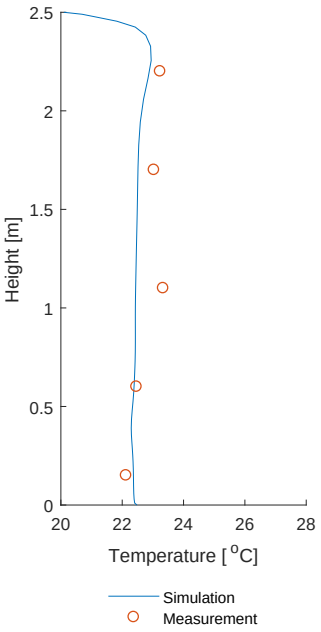

Figure 8.40. Temperatures along pole 3

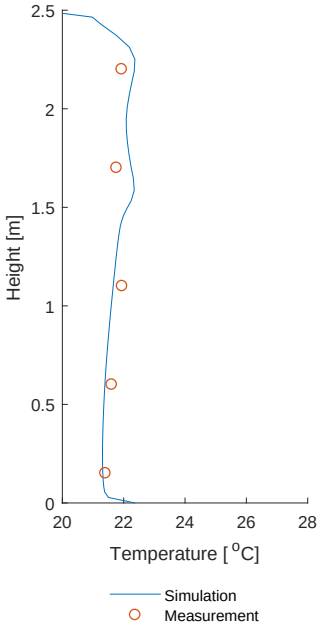

Figure 8.41. Temperatures along pole 4

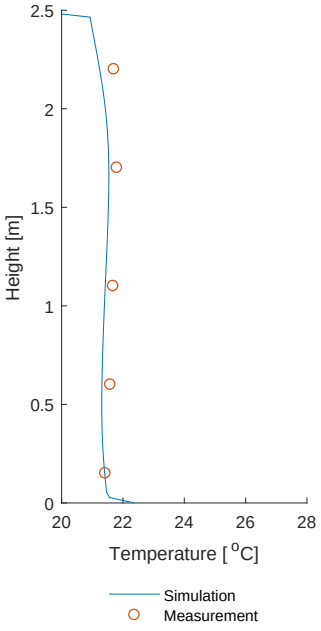

Figure 8.42. Temperatures along pole 5

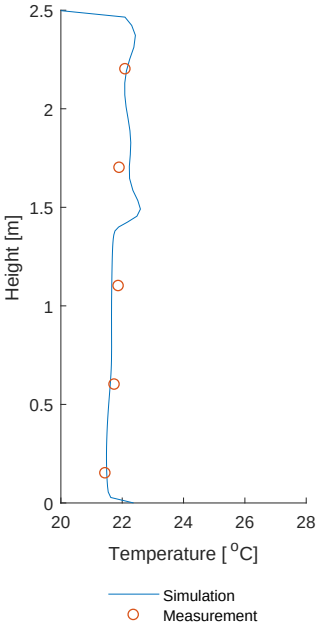

Figure 8.43. Temperatures along pole 6

The comparison of temperature distribution in the plenum is presented in the Figure 8.44

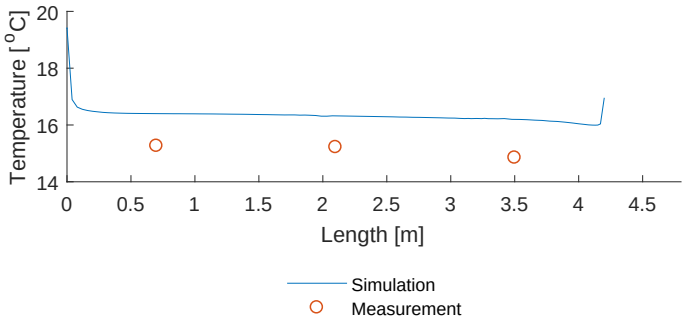

Figure 8.44. Comparison of temperature distribution in plenum

From the Figures 8.38 - 8.43 it can be noticed that the numerical model estimates a uniform temperature distribution along all poles as measured during the experiments. The higher temperature at the 0.6m height of the pole 2 happens due to the fact that pole 2 is positioned on the heat carpet and is influenced by the thermal plume but as it can be seen CFD does not capture the temperature increase. It is seen that the measured temperatures are very close to the ones that are calculated by the numerical model. For this experimental case the temperatures of CFD and experiment fit quite well. This happens because the surrounding temperatures during the experiment were close to those ones that are used in radiant CFD model. As it can be seen from the Table 8.4 the surrounding temperature of facade side used in CFD model was 22.1°C as measured just before the experiment started. The façade side temperature did not change significantly during this experiment thus the heat unbalance compared to the first case is minor which resulted in good temperature fit between measurement and numerical solution.

Table 8.4. Comparison of temperature of facade side between experiment and CFD for case 2

Wall	Average temperature during experiment, [°C]	Fixed temperature used in CFD radiant model, [°C]
Façade wall	21.95	22.10

In addition to that, the tendency of temperature distribution in plenum calculated by the CFD model is the same as the one that was measured during the experiment and is presented in the 8.44. The temperature in the plenum is almost uniform in both, measurement and CFD model. However, there are deviations of 1-1.5 °C between their values but this can be assumed acceptable considering general limitation of the CFD model on predicting the temperature in plenum region.

The comparison between air velocities measured during the experiment and calculated by the numerical model are presented in the Figures 8.45 - 8.50.

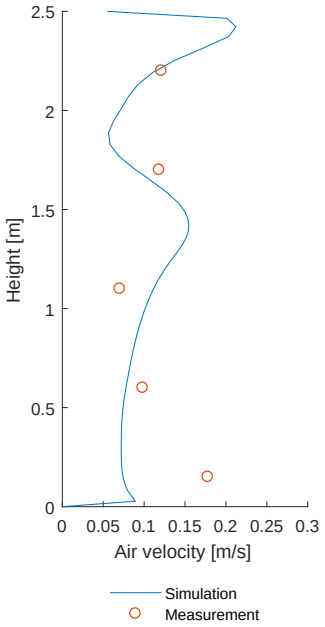

Figure 8.45. Velocities along pole 1

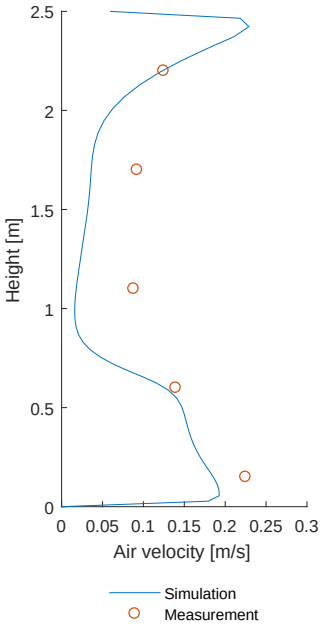

Figure 8.46. Velocities along pole 2

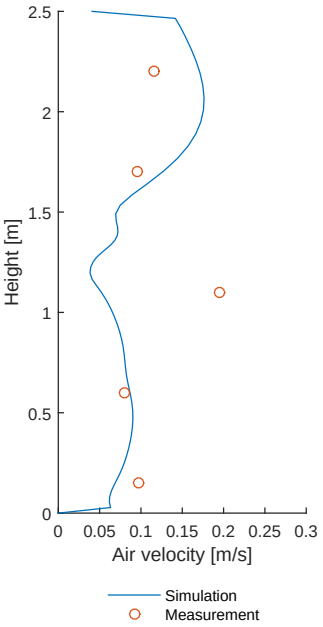

Figure 8.47. Velocities along pole 3

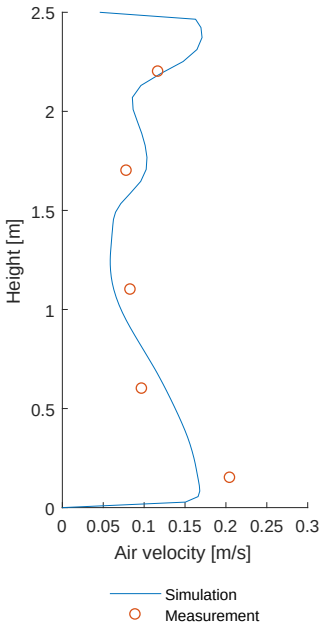

Figure 8.48. Velocities along pole 4

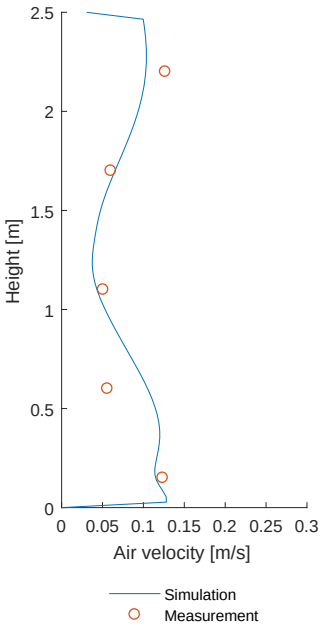

Figure 8.49. Velocities along pole 5

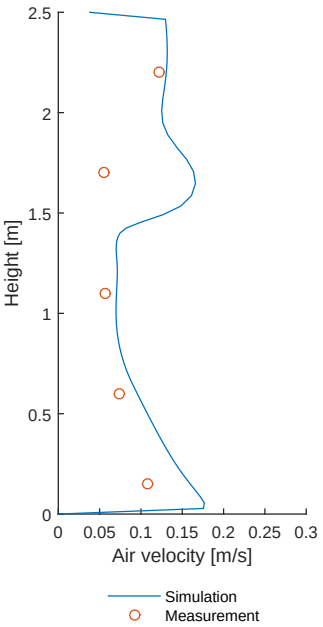

Figure 8.50. Velocities along pole 6

Figures 8.45 - 8.50 show that numerical model can estimate correctly the tendency of air velocities for most of the measurement points. However, there are some points where the CFD model estimates different air velocities compared to the measurement. This happens due to possible transient flow as mentioned previously in the case 1 results.

The comparison between N_2O measured during the experiment and calculated by the numerical model are presented in the Figures 8.51 - 8.56.

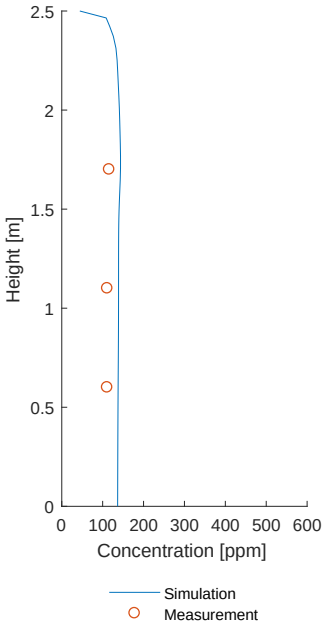

Figure 8.51. N_2O along pole 1

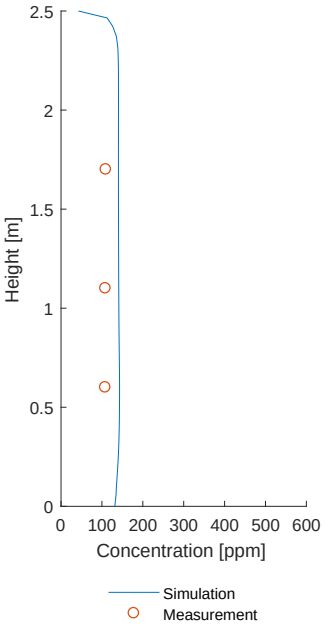

Figure 8.52. N_2O along pole 2

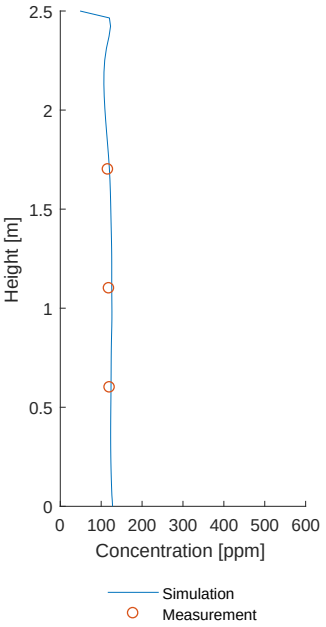

Figure 8.53. N_2O along pole 3

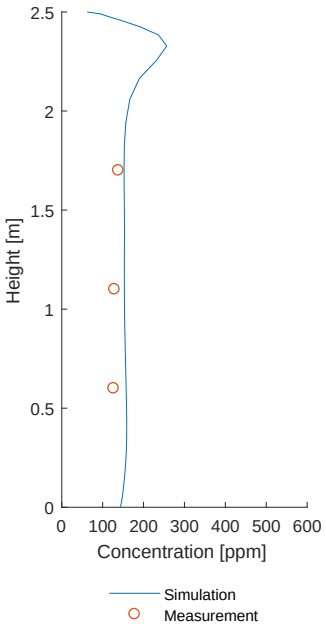

Figure 8.54. N_2O along pole 4

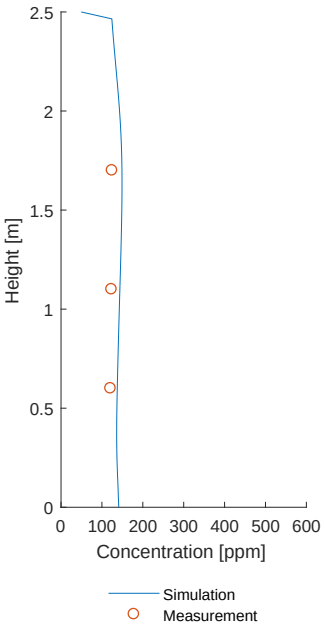

Figure 8.55. N_2O along pole 5

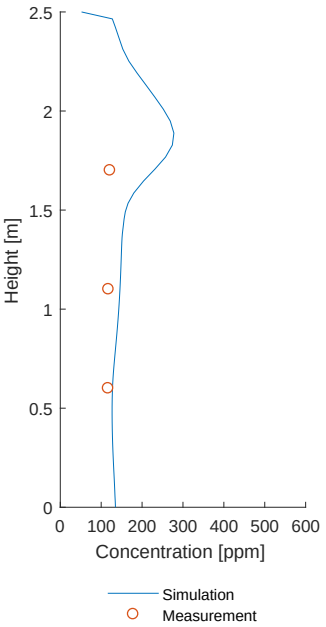

Figure 8.56. N_2O along pole 6

The comparison between N_2O concentrations at inlet, plenum points, fabric points and outlet can be seen in Figure 8.57 and 8.58.

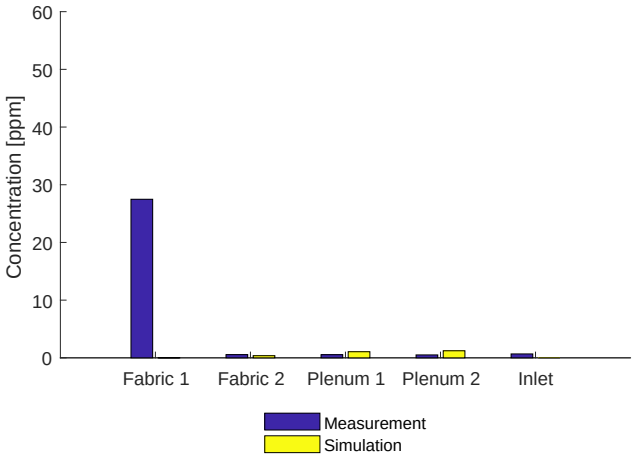

Figure 8.57. Comparison of N_2O concentration at certain locations

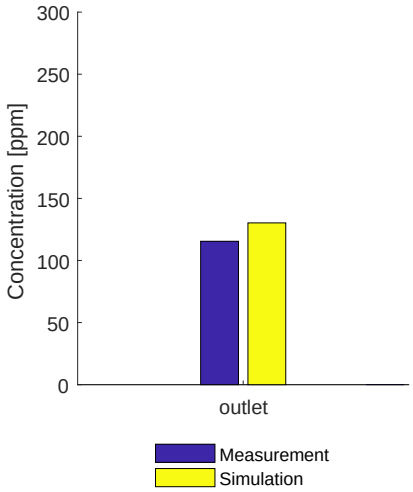

Figure 8.58. Comparison of N_2O concentration at outlet

Figures 8.51 - 8.56 show that the CFD model can estimate tendency of the N_2O distribution correctly for most of the measurement points. As the measurement have shown the distribution of N_2O along all the poles is uniform. The same estimation is shown by CFD model except pole 6 at height 1.7m. According to the CFD model, the N_2O plume from person 2 reaches the upper level of pole 6. Despite the similarities in tendencies, there are deviations between the measurement and CFD prediction values. From the measurement the N_2O concentration along all the poles is around 110-130 ppm whereas the CFD model predicts N_2O concentration in the range of 120-150 ppm. These deviations can be assume acceptable considering that the N_2O mass balance was not reached during the measurement as the Table 8.5 shows. This can explain the lower N_2O concentration measured during the experiment than expected.

Table 8.5. Comparison of N_2O mass unbalance rates between experiment and CFD for case 2

N_2O mass unbalance during experiment, [%]	N_2O mass unbalance in CFD, [%]
16.1	5.2

Moreover, the plenum points experience N_2O concentration in both, numerical model and measurements as shown in Figure 8.57. This means that CFD predicts a reverse flow from room to plenum as concluded from the measurement too. The same applies to the 'Fabric 2' indicating the existing back flow from plenum to the end of fabric duct. The 'Fabric 1' point does not experience any N_2O concentration which means there is not any reverse flow at that point according to the CFD model. However, the measured N_2O concentrations for 'Fabric 1' point are assumed to be an error in measurement setup as

explained before thus it cannot be compared with the CFD prediction.

The temperature distribution in the room for case 2 is shown in the Figures 8.59 and 8.60.

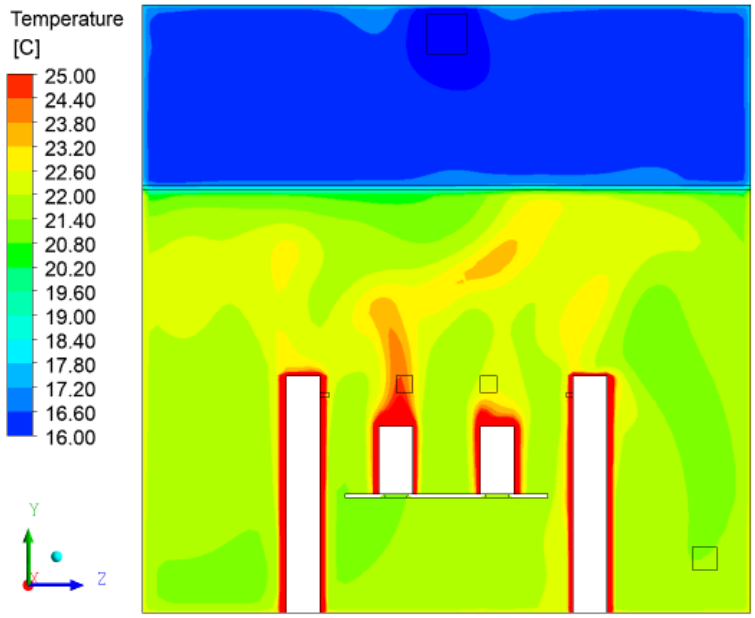

Figure 8.59. Distribution of temperature for plane at X=2.1m

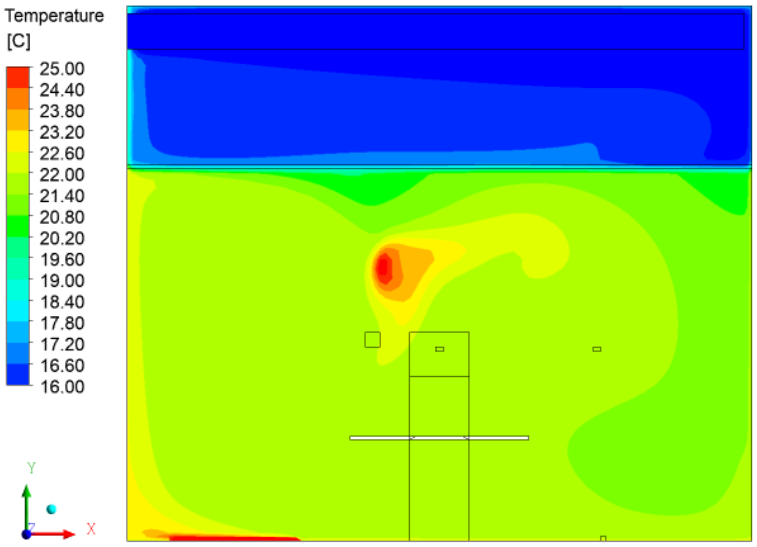

Figure 8.60. Distribution of temperature for plane at Z=1.9m

From the Figures 8.59 and 8.60 above it seems that the temperature in room is uniformly distributed. Temperature range in the room is approximately 21.5° - 22.5°C in most of the room space indicating good mixing of air. It is also noticeable that in this case, the thermal plume generated by the heat sources is much smaller than that one generated in case 1. In this case the room is ventilated with $6h^{-1}$ ACH whereas case 1 is ventilated with $3h^{-1}$ ACH. Apparently, thermal plume from persons is smaller due to higher volumetric flow rate diffused through the porous medium.

The air flow pattern for case 2 can be seen in the Figures 8.61 - 8.65 below.

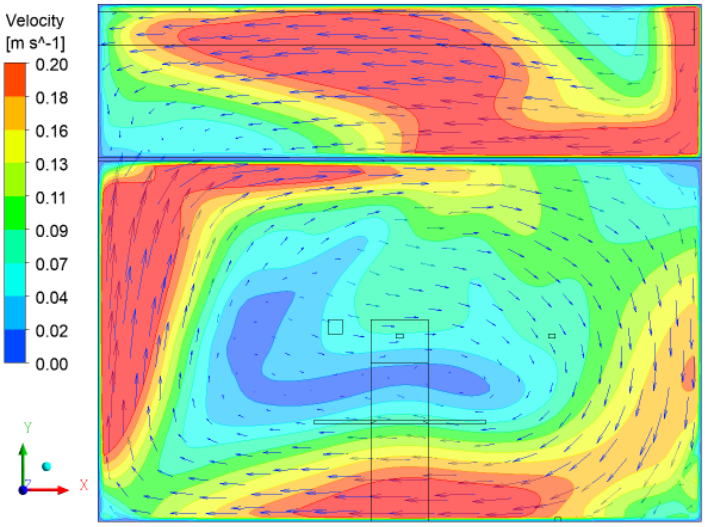

Figure 8.61. Airflow pattern for plane at Z=0.5m

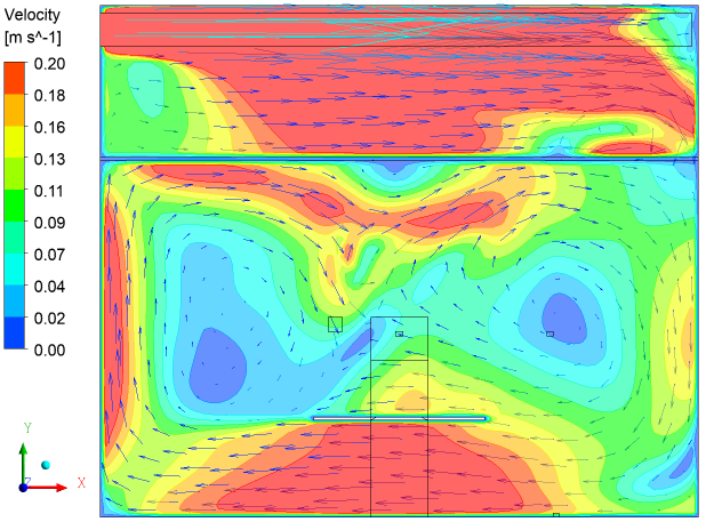

Figure 8.62. Airflow pattern for plane at Z=1.9m

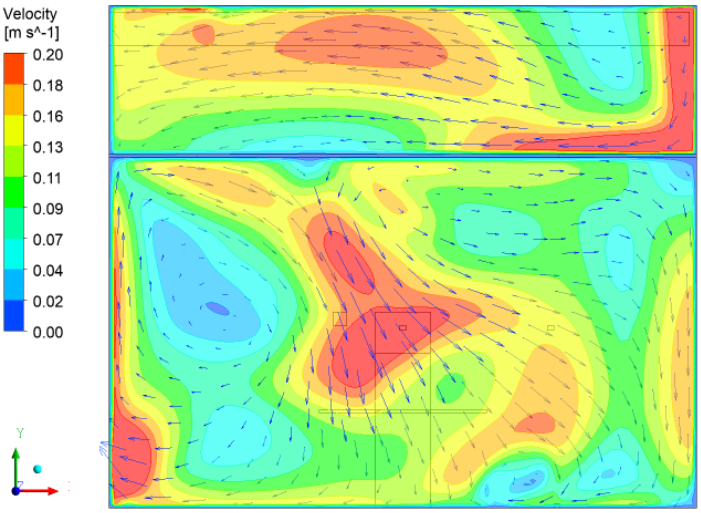

Figure 8.63. Airflow pattern for plane at Z=3.1m

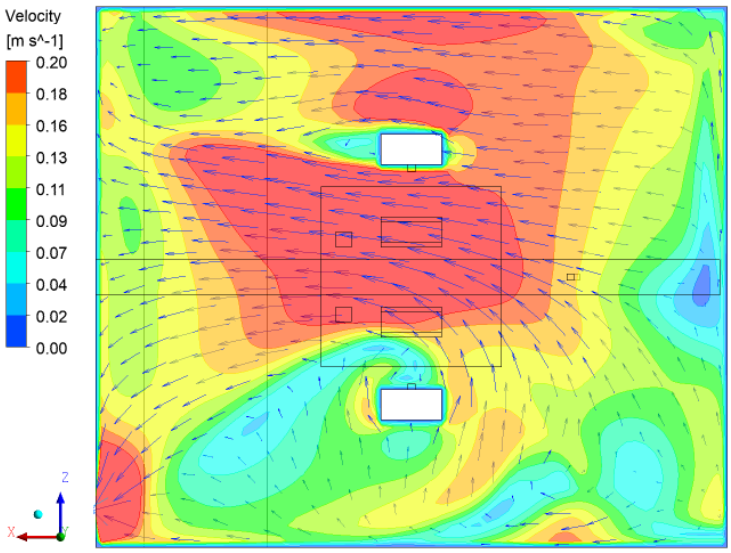

Figure 8.64. Airflow pattern for plane at Y=0.1m

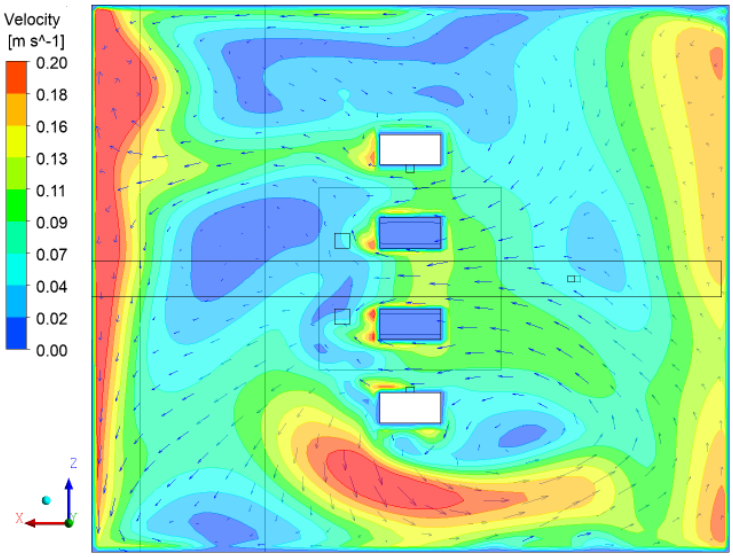

Figure 8.65. Airflow pattern for plane at Y=1.1m

The air flow pattern in the fabric duct and plenum is similar to that one in case 1 with the only difference that higher velocities are generated due to the larger flow rate.

Figures 8.61 - 8.63 show that there is a different air flow pattern in room compared to case 1. In this case there is an additional heat source which is located to the exhaust side and is influential on the flow pattern in the room. Generated thermal plume by the heat carpet forces the air to move upwards with higher velocities causing stronger air recirculation in the room. This is why relatively high velocities are monitored close to façade wall where the heat carpet is located. In addition to that, it seems that there is high risk of draught along the 0.1m height and especially beneath the table and behind person 1 as the Figure 8.64 presents. This region contains pole 1, 2 and 4 which are the poles with the highest risk of draught according to measurements as the Figure shows 6.53 in experimental part results analysis.

The distribution of N_2O can be seen in the Figures 8.66 - 8.71 below.

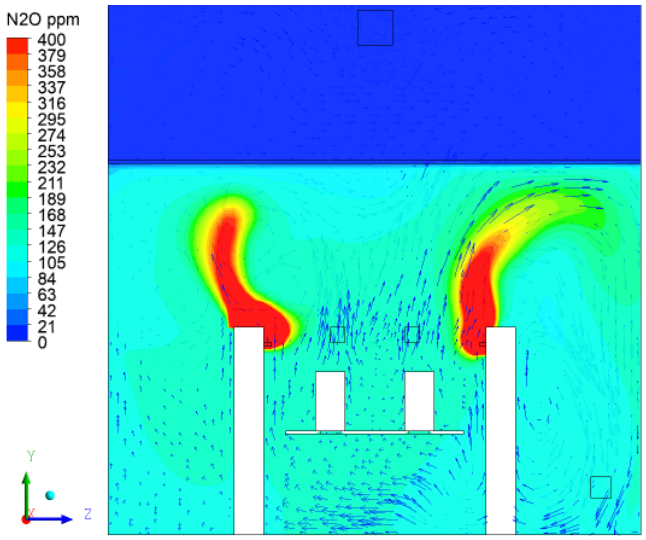

Figure 8.66. *N_2O* distribution for plane at X=2.1m

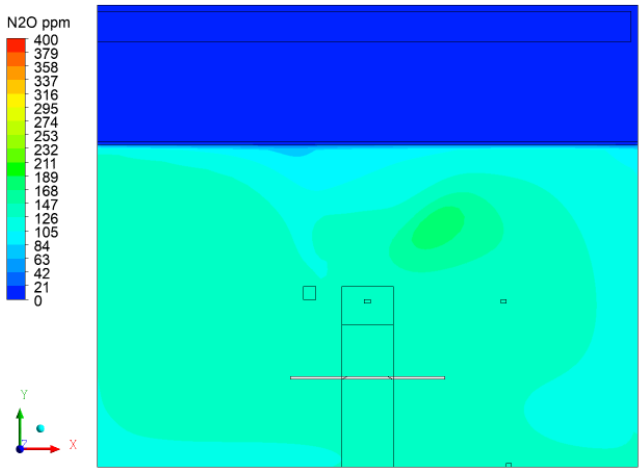

Figure 8.67. *N_2O* distribution for plane at Z=1.9m

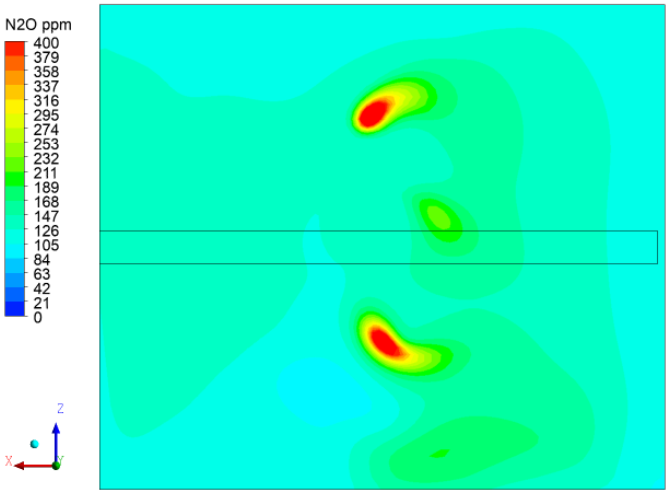

Figure 8.68. *N_2O* distribution for plane at Y=1.7m

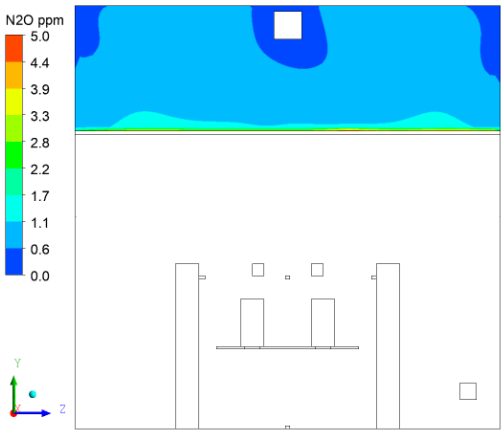

Figure 8.69. N_2O distribution in plenum for plane at X=2.1m

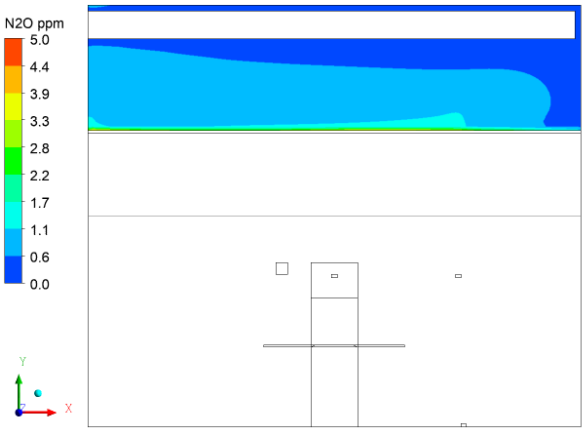

Figure 8.70. N_2O distribution in plenum for plane at Z=1.9m

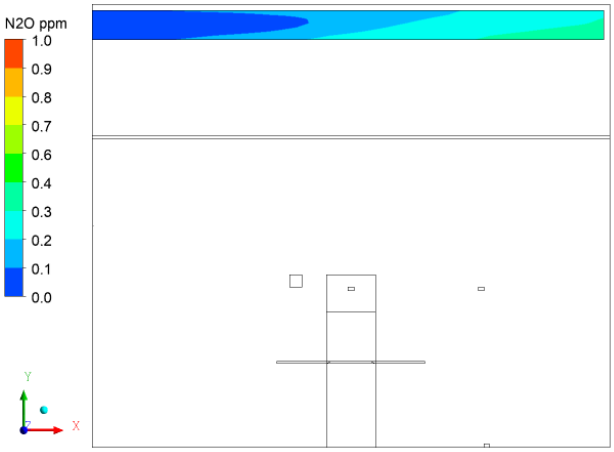

Figure 8.71. N_2O distribution in fabric duct for plane at Z=1.9m

Figures 8.66 - 8.68 clearly shows that the contaminant distribution in the room is distributed uniformly except close the the persons mouth where it is supplied. N_2O levels in the room are in range of 120-150 ppm which means there is good air mixing in the room. Figure 8.69 and 8.70 shows that there is N_2O in plenum indicating the reverse flow from room to plenum as happened in case 1 and 2. However, in this case where the ACH is 6 h^{-1} the N_2O concentration in the plenum is much less compared to case 1 where the supply ACH is 3 h^{-1}. This happens due to higher pressure in plenum which prevents the back flow effect. In addition to that, as commented for case 1 the back flow happens almost uniformly along the diffuse ceiling since the contaminant-heat sources are positioned symmetrically in the room. Moreover, the Figure 8.71 shows that there is a back flow from the plenum to the end fabric duct as it happens in the previous case.

Case 3

The comparison between temperatures measured during the experiment and calculated by the numerical model are presented in Figures 8.72 - 8.77.

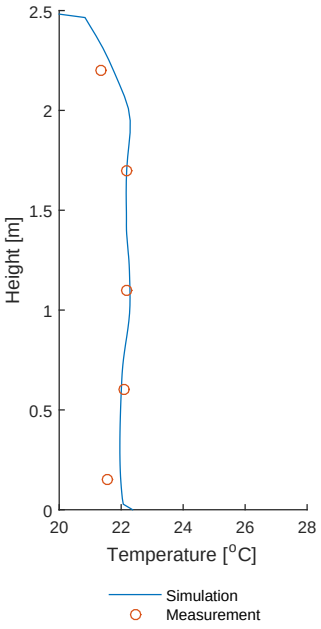

Figure 8.72. Temperatures along pole 1

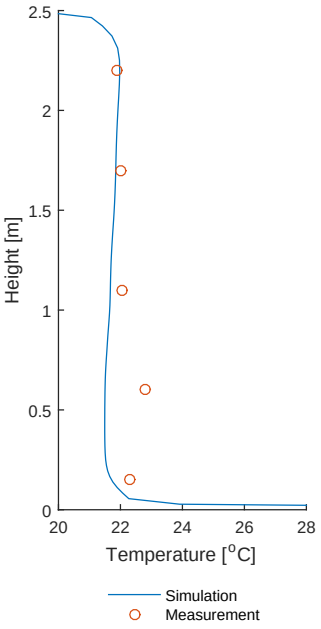

Figure 8.73. Temperatures along pole 2

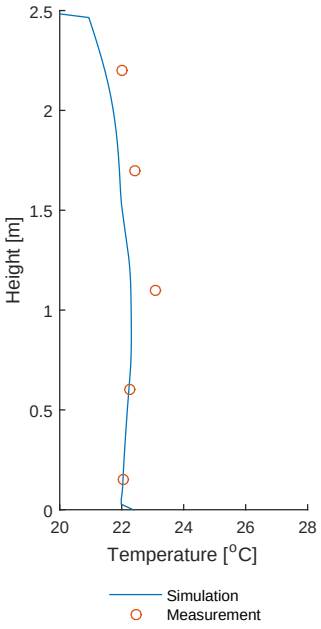

Figure 8.74. Temperatures along pole 3

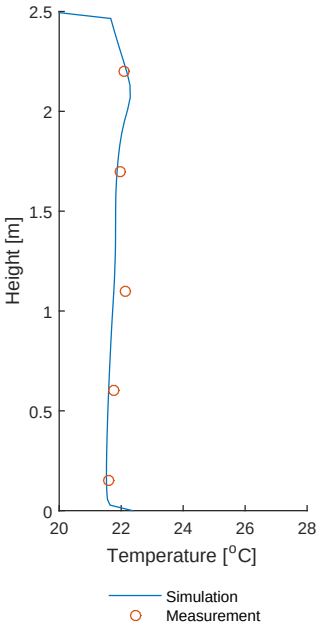

Figure 8.75. Temperatures along pole 4

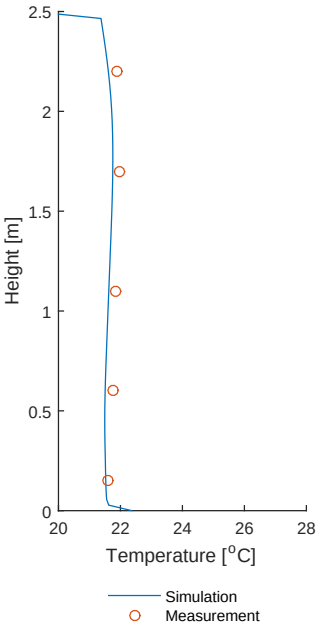

Figure 8.76. Temperatures along pole 5

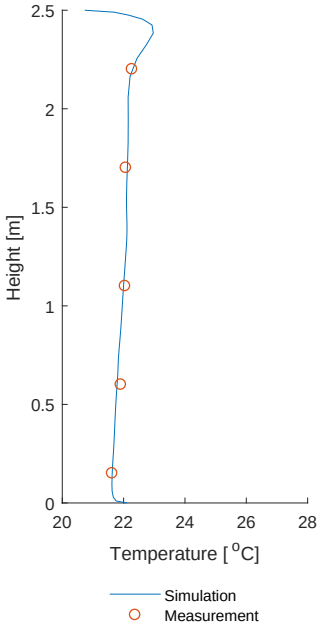

Figure 8.77. Temperatures along pole 6

The comparison of temperature distribution in the plenum for is presented in the Figure 8.78

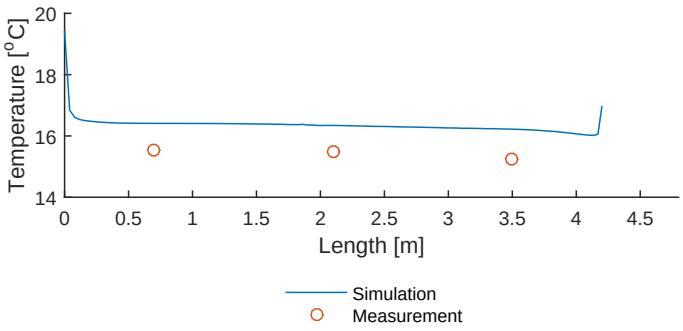

Figure 8.78. Comparison of temperature distribution in plenum

Once again Figures 8.72 - 8.77 show that the tendency of temperature distribution in the room is kept uniform as for previous cases. The measured temperatures are very close to those ones calculated by the numerical model. This happens because the surrounding temperatures remained very close to those ones used in CFD. The façade side temperature did not change significantly during this experiment thus not a big amount of heat loss or gain occurred. As it can be seen from the Table 8.6 the temperature of façade side used in CFD model is very close to the average temperature of the façade side measured during the experiment which resulted in accurate fit for the simulation results.

Table 8.6. Comparison of temperature of façade side between experiment and CFD for case 3

Wall	Average temperature during experiment, [°C]	Fixed temperature used in CFD radiant model, [°C]
Façade wall	22.05	22.10

Comparison between air velocities measured during the experiment and calculated by the numerical model are presented in the Figures 8.79 - 8.84.

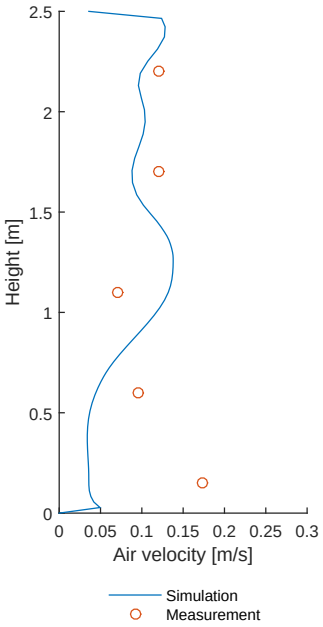

Figure 8.79. Velocities along pole 1

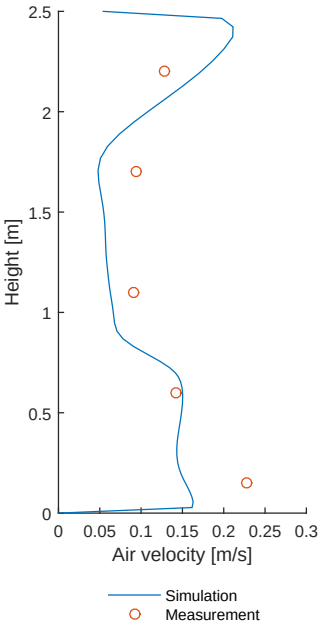

Figure 8.80. Velocities along pole 2

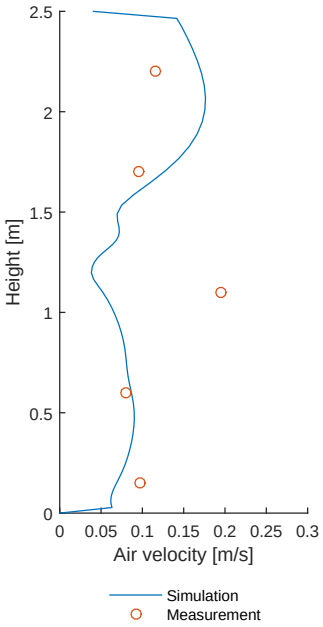

Figure 8.81. Velocities along pole 3

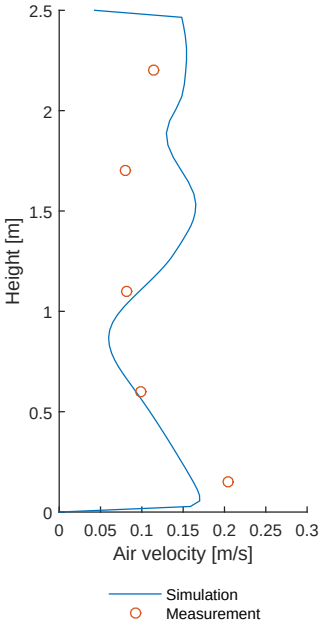

Figure 8.82. Velocities along pole 4

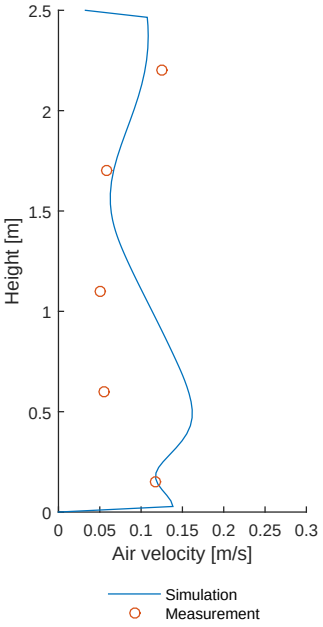

Figure 8.83. Velocities along pole 5

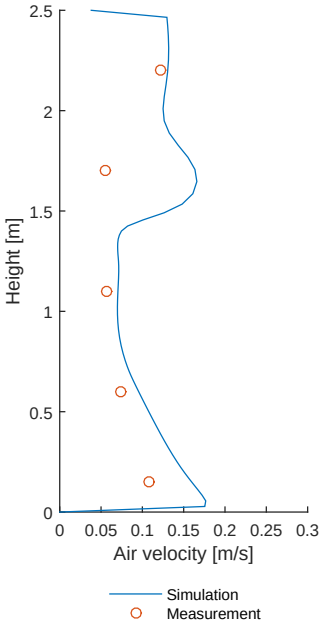

Figure 8.84. Velocities along pole 6

Figures 8.79 - 8.84 results are almost exactly the same as for case 2 since the input is the same. The deviations for measured and simulated values can also be explained by transient-flow possibility as mentioned earlier.

Comparison between N_2O measured during the experiment and calculated by the numerical modelare presented in the Figures 8.85 - 8.90.

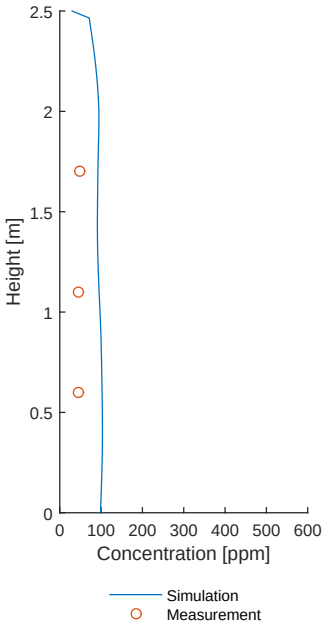

Figure 8.85. N_2O gradient along pole 1

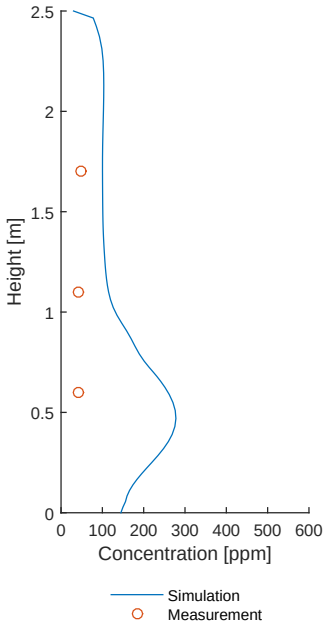

Figure 8.86. N_2O gradient along pole 2

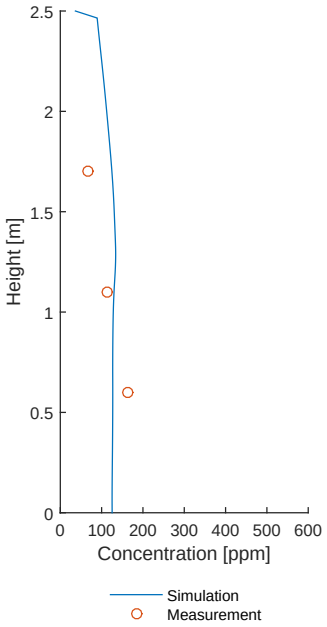

Figure 8.87. N_2O gradient along pole 3

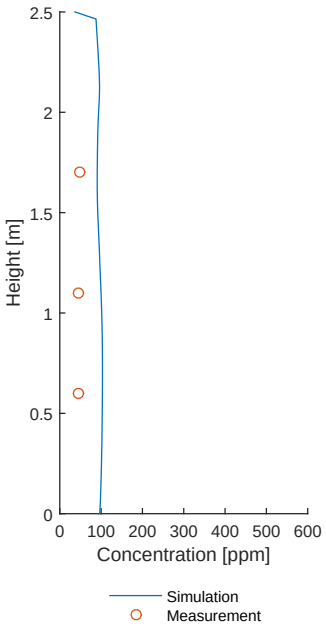

Figure 8.88. N_2O gradient along pole 4

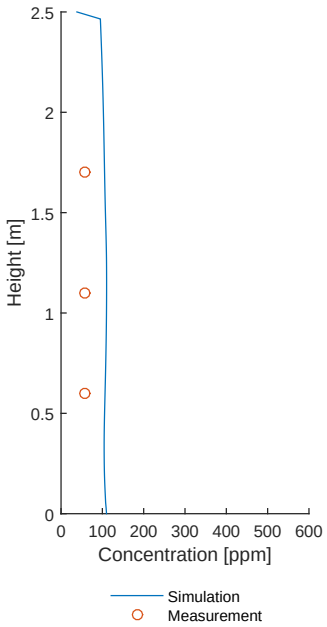

Figure 8.89. N_2O gradient along pole 5

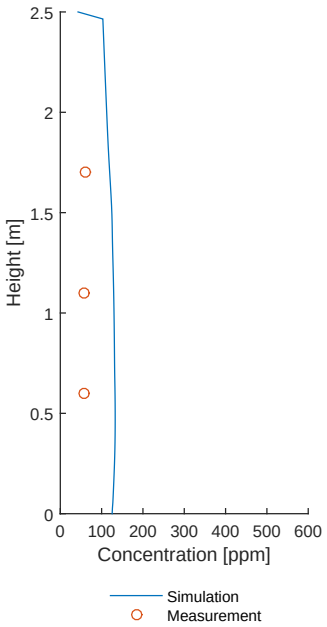

Figure 8.90. N_2O gradient along pole 6

The comparison between N_2O concentrations at inlet, plenum points, fabric points and outlet can be seen in Figure 8.91 and 8.92.

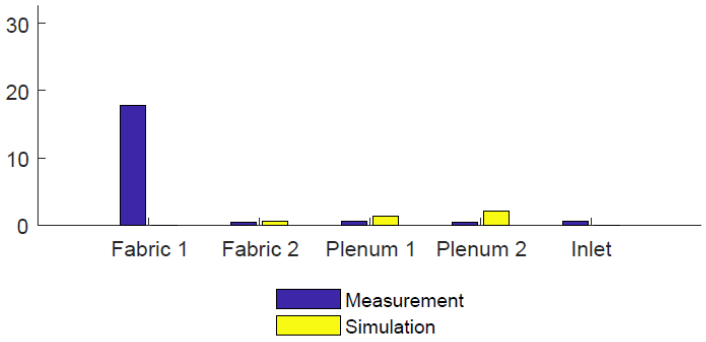

Figure 8.91. Comparison of N_2O concentration at certain locations

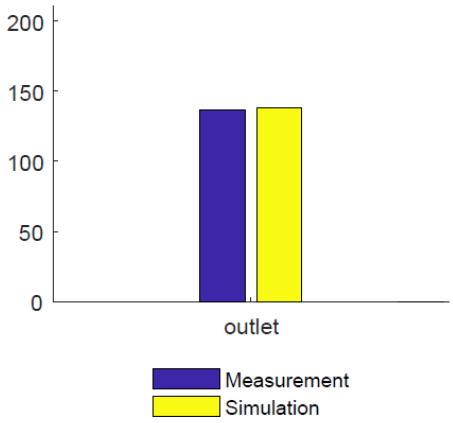

Figure 8.92. Comparison of N_2O concentration at outlet

From Figures 8.85 - 8.90 it can be concluded that the model estimates uniform N_2O distribution along the poles except for the pole 2 at 0.6m height. Even though the mass N_2O balance has been obtained in both, measurement and simulation as the Table 8.7 shows, the results obtained from measurement and CFD do not fit. As it can be seen from the Figure 8.86 the CFD predicts a 'peak' of N_2O concentration at the lower part of pole 2 where the measurements do not show higher concentrations of N_2O around pole 2 but show a relatively high level of N_2O at the lower part of pole 3 as the Figure 8.87 presents. This could mean that during the measurement the region with large N_2O concentration was found close to pole 3 instead of pole 2 as predicted by the CFD model. However, due to the limited N_2O collector used in the hotbox the 'peak' of concentration maybe was not easy to be read during the experiment. The difference in N_2O tendency may happen due to inaccurate estimation of pollution distribution in CFD model.

Table 8.7. Comparison of N_2O mass unbalance rates between experiment and CFD for case 3

N_2O mass unbalance during experiment, [%]	N_2O mass unbalance in CFD, [%]
0.5	0.5

The distribution of temperature and air velocity for case 3 are similar to those in case 2 since the boundary conditions for flow rates and heat loads are the same. The only difference between case 3 and 2 is the type of contamination source, therefore only N_2O distribution is shown with illustrations for this case.

The distribution of pollutants can be seen in the Figures 8.93 - 8.98

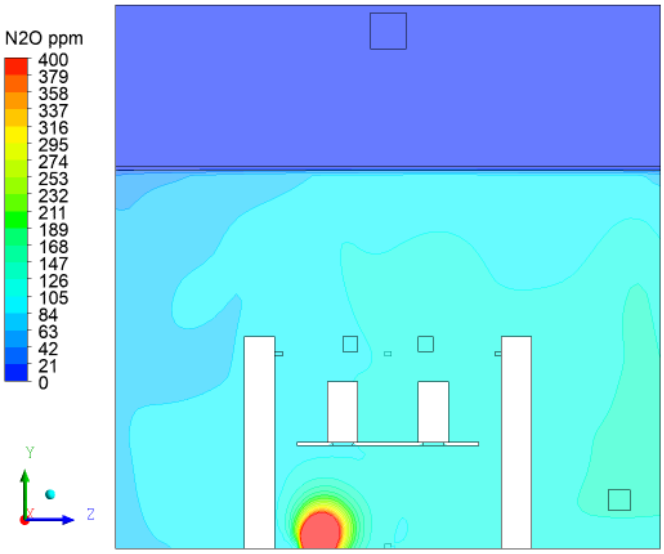

Figure 8.93. N_2O distribution for plane at X=2.1m

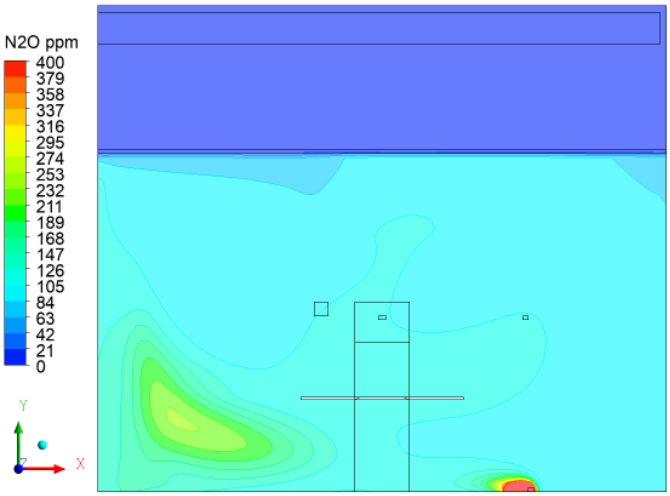

Figure 8.94. N_2O distribution for plane at Z=1.9m

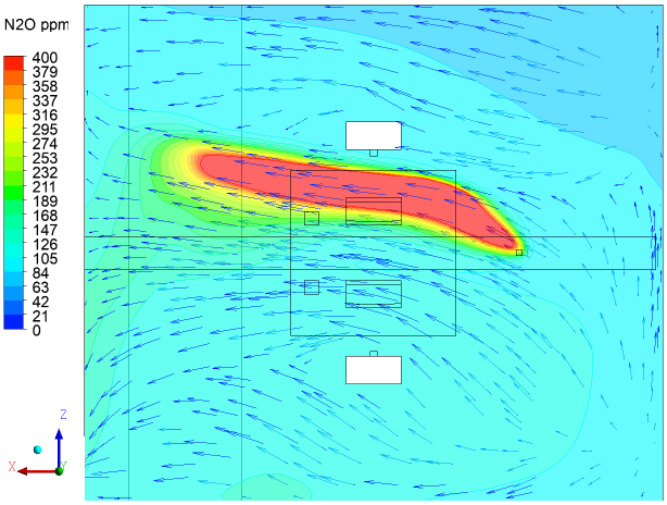

Figure 8.95. N_2O distribution for plane at Y=0.1m

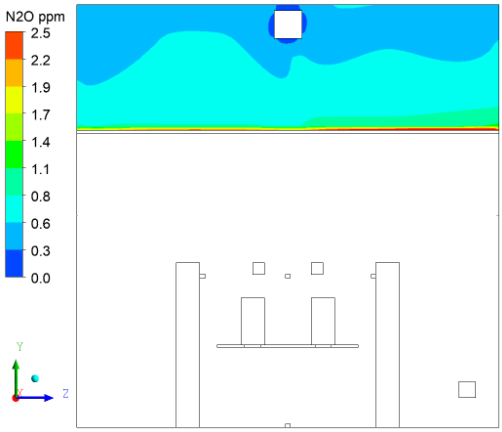

Figure 8.96. N_2O distribution in plenum for plane at X=0.7m

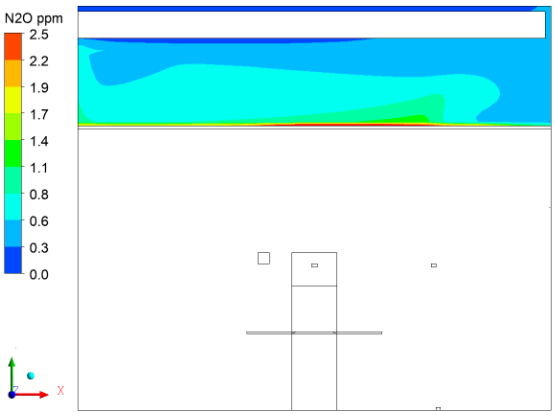

Figure 8.97. N_2O distribution in plenum for plane at Z=1.9m

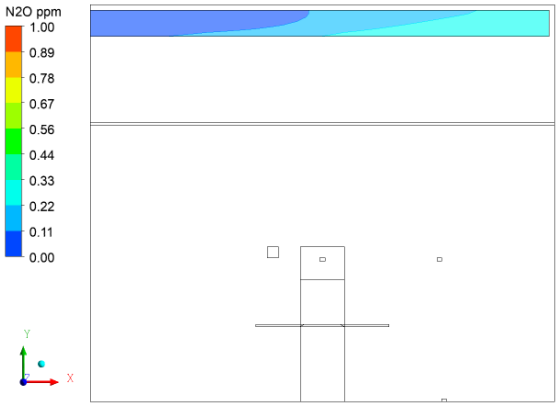

Figure 8.98. N_2O distribution in fabric duct for plane at Z=1.9m

Figures 8.93 - 8.95 show that N_2O is uniformly distributed in the room except for the lower part where the contaminants are released and close to the façade wall towards the exhaust. Actually, the façade side experiences higher N_2O level than the rest of the room which explains why the N_2O 'peak' predicted on pole 2 by the CFD model. In this case the driven force force for the pollutant distribution is the momentum of the flow along the floor and not the buoyant effect of the heat sources. The N_2O 'plume' moves along the floor towards the façade wall with a direction tilted upwards as the Figure 8.95 illustrates. When the N_2O 'plume' reaches the middle of the heat carpet it gradually starts moving towards the side of the exhaust as the Figure 8.94 and 8.95 show. This is why the reverse flow from room to plenum occurs on the exhaust side and not symmetrically as it can be seen in the Figure 8.96. Moreover, according to the Figure 8.98 there is a back flow in the end of the fabric duct.

Case 4

The comparison between measured temperatures during the experiment and calculated by the numerical model are presented in the Figures 8.99 - 8.104.

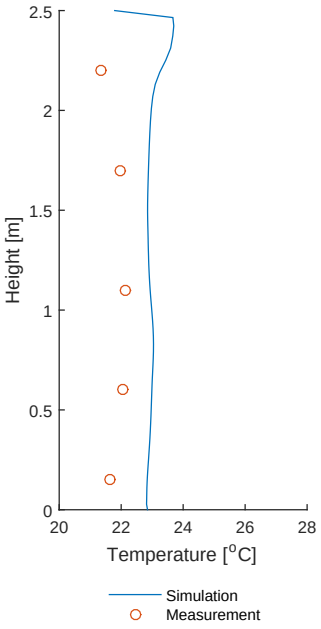

Figure 8.99. Temperatures along pole 1

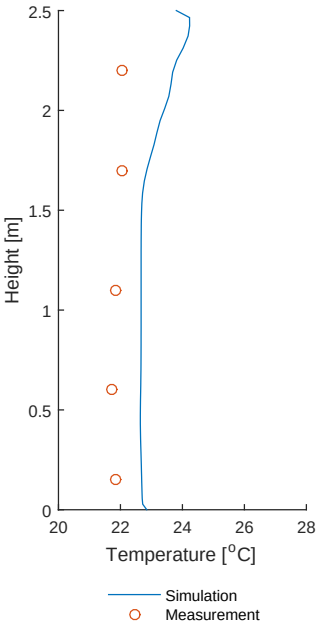

Figure 8.100. Temperatures along pole 2

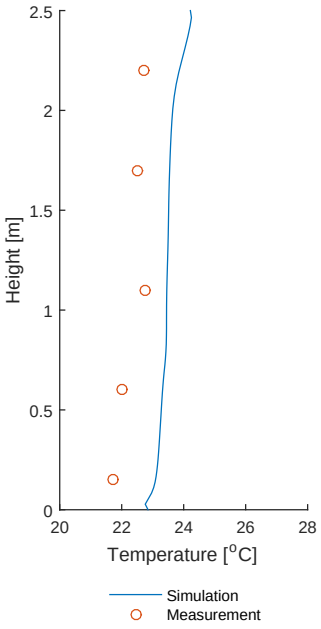

Figure 8.101. Temperatures along pole 3

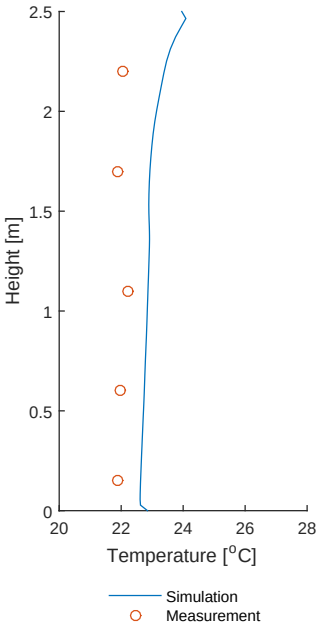

Figure 8.102. Temperatures along pole 4

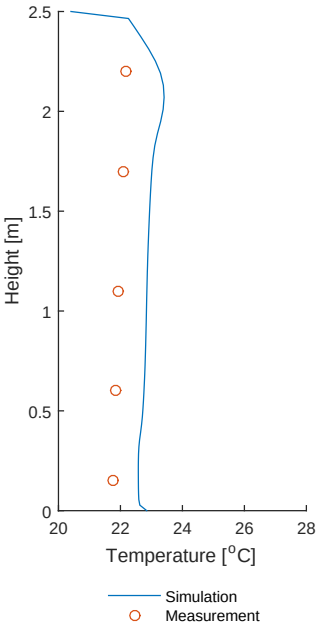

Figure 8.103. Temperatures along pole 5

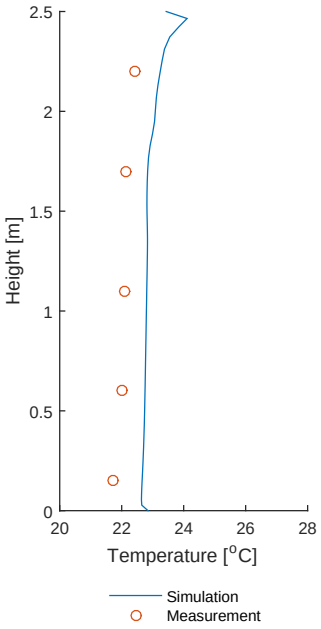

Figure 8.104. Temperatures along pole 6

The comparison of temperature distribution in the plenum is presented in the Figure 8.105

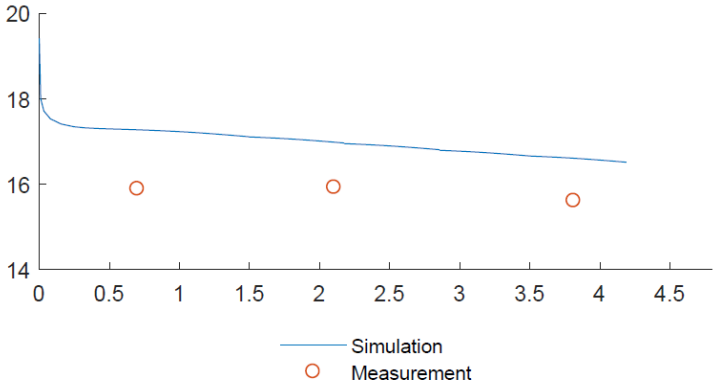

Figure 8.105. Comparison of temperature distribution in plenum

Figures 8.99 - 8.104 show that the numerical model can estimate uniform temperature distribution along the poles as measured previously during the experiment. However, the calculated temperatures by the CFD model are approximately 1°C higher than the temperatures obtained from the experiment. This happens due to the heat unbalance which occurred during the experiment. As it can be seen from the Table 8.8 the surrounding temperature of façade wall used in CFD model was 22°C as measured before the experiment started. However, the façade side temperature changed significantly during experiment. This resulted in additional heat loss leading to heat unbalance which explains the lower temperatures obtained by measurements than predicted by the numerical model.

Table 8.8. Comparison of temperature of façade side between experiment and CFD for case 4

Wall	Average temperature during experiment, [°C]	Fixed temperature used in CFD radiant model, [°C]
Façade wall	20.05	22.00

The tendency of temperature distribution in plenum calculated by the CFD model is the same as that one measured during the experiment which can be seen in the Figure 8.105. The temperature in the plenum is almost uniform in both, measurement and CFD model. However, there are significant deviations of 3°C between measured and calculated values. This happens due to the heat unbalance occured during the measurement and also the limitation of the radiant model on estimating temperatures of plenum walls as mentioned before.

The comparison between measured air velocities during the experiment and calculated by the numerical model are presented in the Figures 8.106 - 8.111.

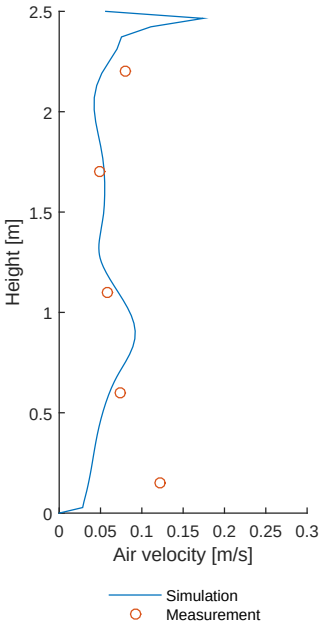

Figure 8.106. Velocities along pole 1

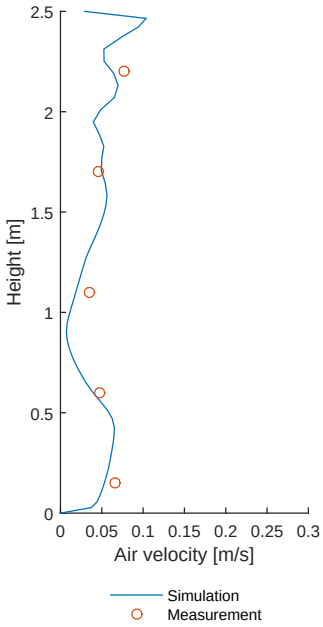

Figure 8.107. Velocities along pole 2

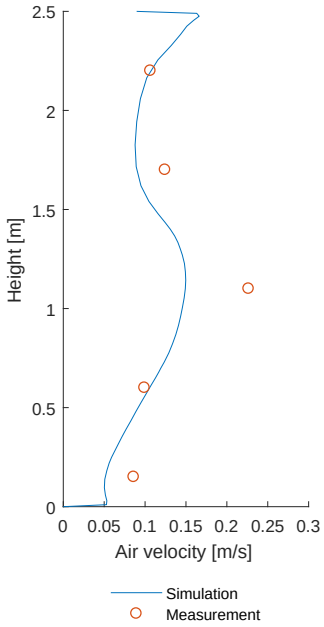

Figure 8.108. Velocities along pole 3

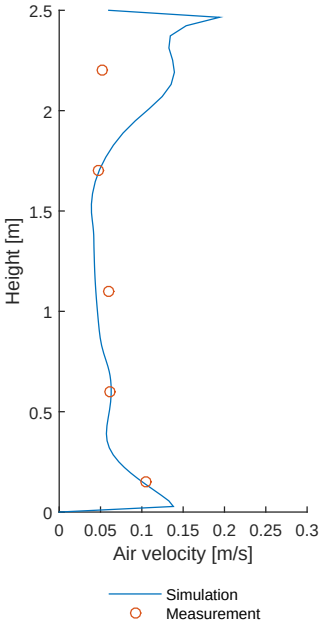

Figure 8.109. Velocities along pole 4

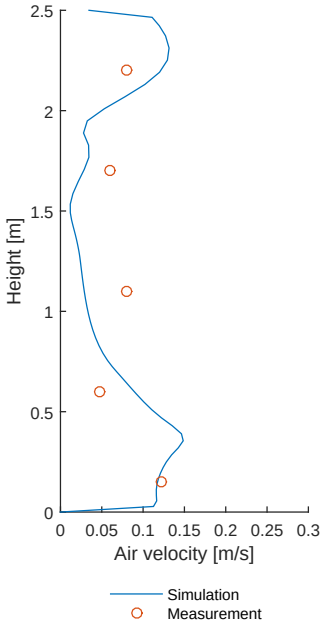

Figure 8.110. Velocities along pole 5

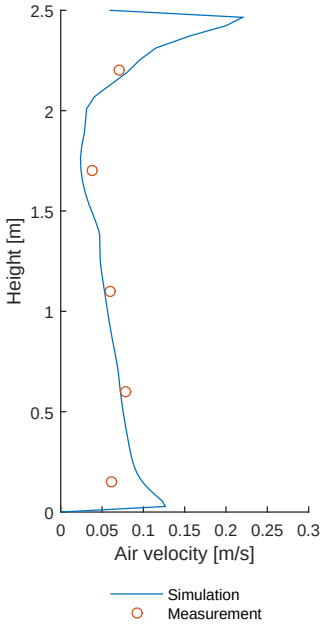

Figure 8.111. Velocities along pole 6

Figures 8.106-8.111 show that CFD model can correctly estimate the air distribution for most of the measurement points. However, for some points the CFD model estimates different air velocities than those obtained from the experiment. These deviations may occur because the air velocities are hard to be predicted during assumed transient-flow.

The comparison between measured N_2O during the experiment and calculated by the numerical model are presented in the Figures 8.112 - 8.117.

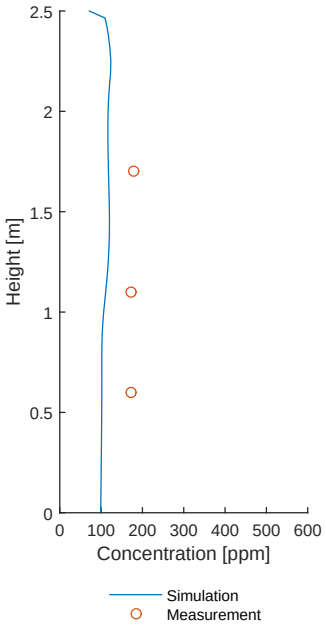

Figure 8.112. N_2O along pole 1

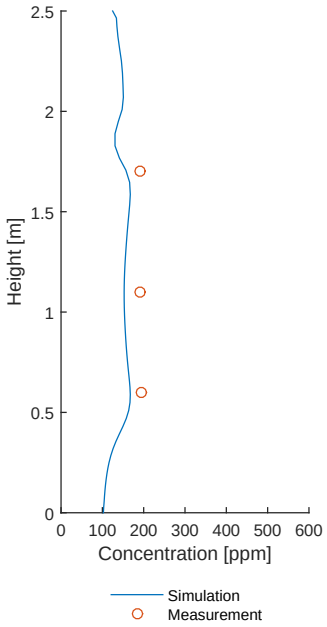

Figure 8.113. N_2O along pole 2

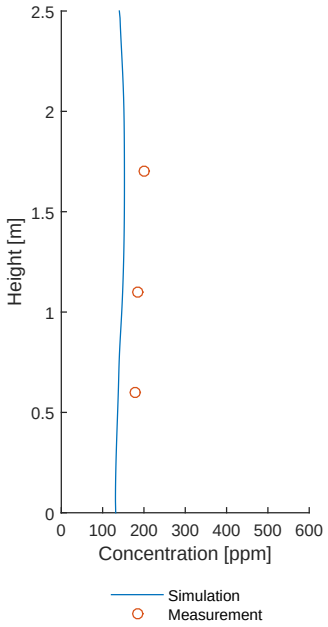

Figure 8.114. N_2O along pole 3

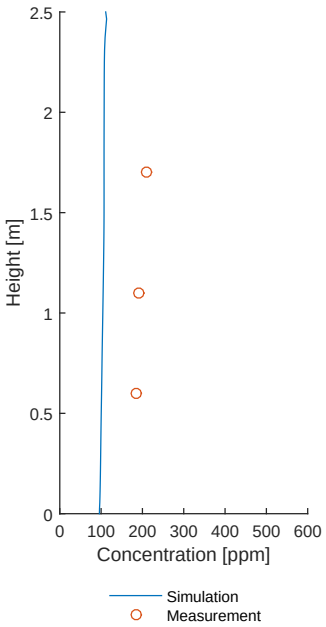

Figure 8.115. N_2O along pole 4

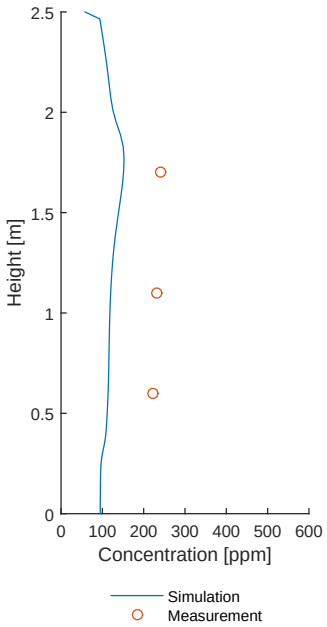

Figure 8.116. N_2O along pole 5

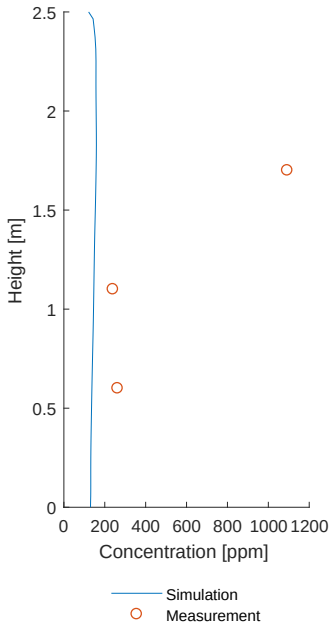

Figure 8.117. N_2O along pole 6

The comparison between N_2O concentrations at inlet, plenum points, fabric points and outlet can be seen in Figure 8.118 and 8.119.

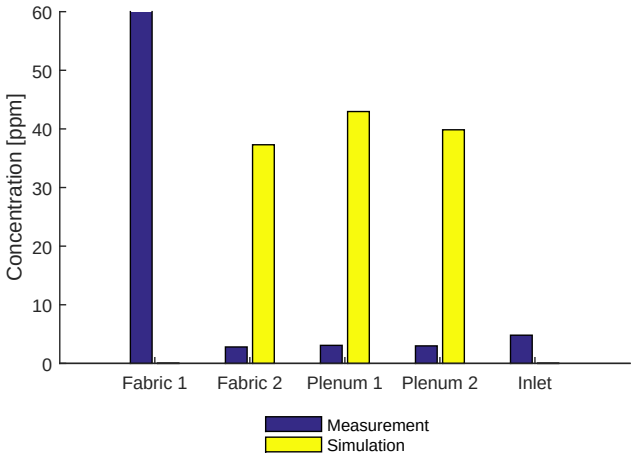

Figure 8.118. Comparison of N_2O concentration at certain locations

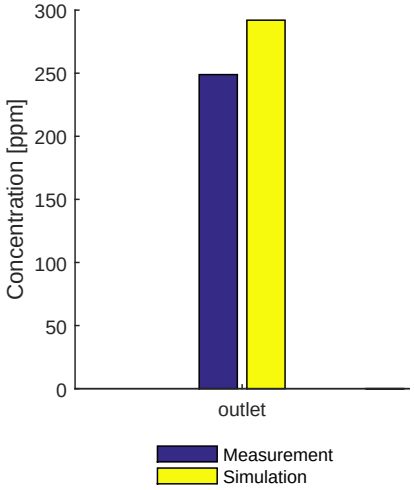

Figure 8.119. Comparison of N_2O concentration at outlet

Figures 8.112-8.117 show that the CFD model can not accurately predict the same tendency of the N_2O distribution as measured from the experiment for case 4. Measurement has shown that the distribution of N_2O along all the poles is uniform except for pole 6. According to the measurement there is a 'peak' of N_2O concentration at 1.7m height on pole 6 where the concentration reaches around 1200 ppm as the Figure 8.117 indicates. However, the CFD model predicts almost uniform contaminant distribution along the poles. In addition, estimated N_2O concentration along the poles is lower than the measurement. This could mean that the biggest amount of N_2O in the simulation is gathered somewhere away from the occupied zone thus could not be noticed on the measurement poles. The difference in N_2O tendency may happen due to the limitation of the model on estimating the contaminant distribution correctly when the source of pollutants is not found within the thermal plume. In addition to that, N_2O mass balance not acquired during the experiment as the Table 8.9 shows. This may happened due to a possible leak in the envelope of the hotbox which could also influence the N_2O pattern and concentration in the room during the experimental measurements.

Table 8.9. Comparison of N_2O mass unbalance rates between experiment and CFD for case 4

N_2O mass unbalance during experiment, [%]	N_2O mass unbalance in CFD, [%]
10.2	1.6

The distributions of temperature and air velocities for case 4 are similar to those of case 1 since the boundary conditions for ventilation and heat loads are the same. The only difference between case 1 and 4 is the type of contamination source, therefore only N_2O

distribution is shown with illustrations for this case.

The distribution of contaminants can be seen in the Figures 8.120 - 8.125.

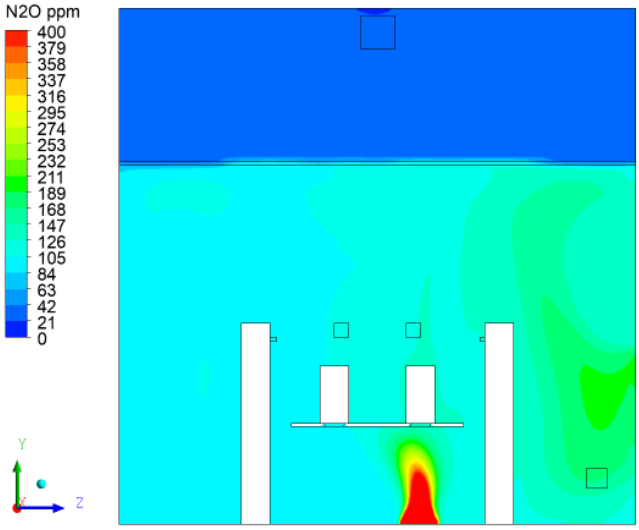

Figure 8.120. N_2O distribution for plane at X=2.1m

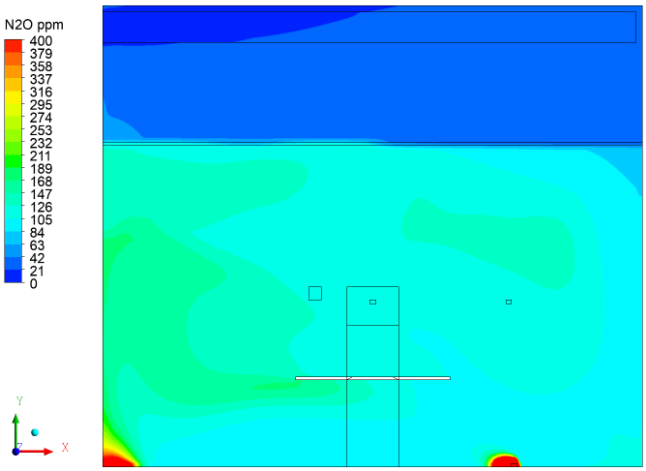

Figure 8.121. N_2O distribution for plane at Z=1.9m

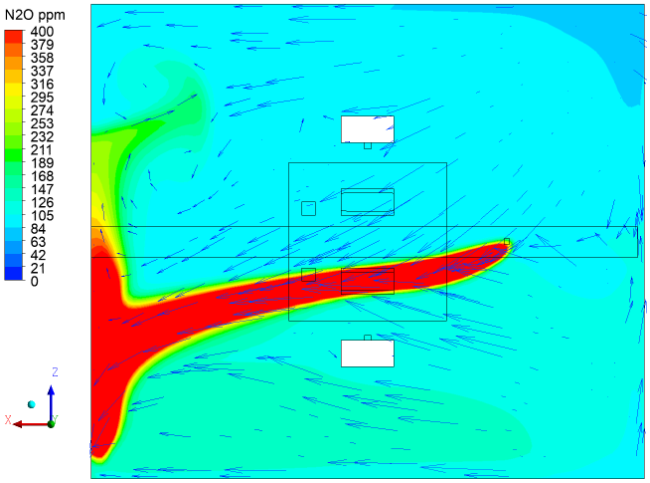

Figure 8.122. N_2O distribution for plane at Y=0.1m

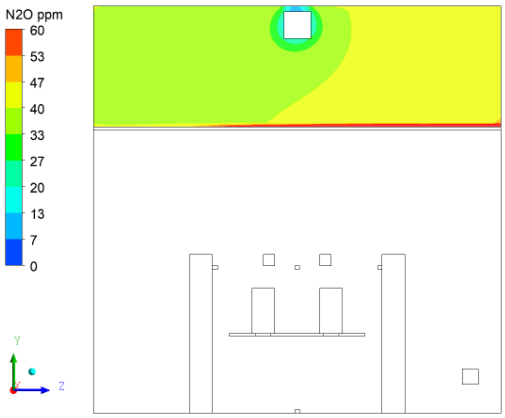

Figure 8.123. N_2O distribution in plenum for plane at X=0.7m

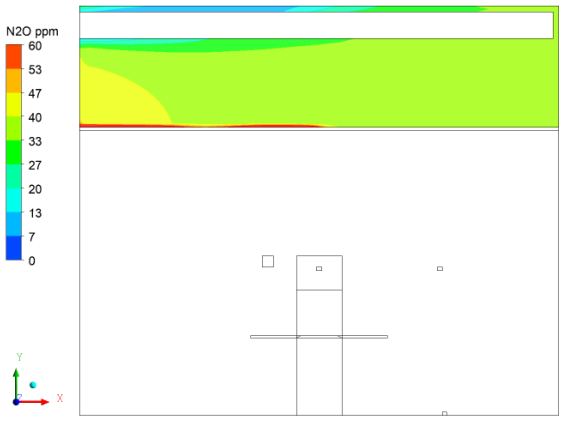

Figure 8.124. N_2O distribution in plenum for plane at Z=1.9m

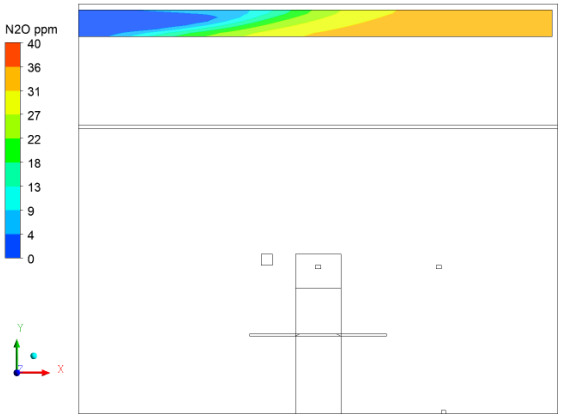

Figure 8.125. N_2O distribution in fabric duct for plane at Z=1.9m

Figures 8.120 - 8.122 represent not uniform cotaminant distribution in the room. The façade side where the exhaust is located experiences higher concentrations of N_2O comparing to the other zones of the room. There is a 'peak' of N_2O concentration gathered at the façade wall close to the exhaust side as the Figure 8.122 presents. Since the contamination source is not in the thermal plume the N_2O does not rise upwards with the help of buoyant forces but follow the air flow pattern along the floor. Since the CFD predicts that the biggest amount of N_2O is gathered close to the exhaust side it is understandable why the measurement poles show lower N_2O levels than the measurements. In addition to that, it can be noticed that N_2O rises upwards close to the façade wall just before the exhaust as seems from the Figure 8.120 and 8.121. This explains why the back flow from room to plenum starts from exhaust side as Figures 8.123 and 8.124 illustrate. When the back flow enters the plenum then the contaminants are circulated with air within the plenum causing it to enter the fabric duct in the far side as the Figure 8.125 presents.

Case 5

The comparison between measured temperatures during the experiment and calculated by the numerical model are presented in the Figures 8.126 - 8.131 below.

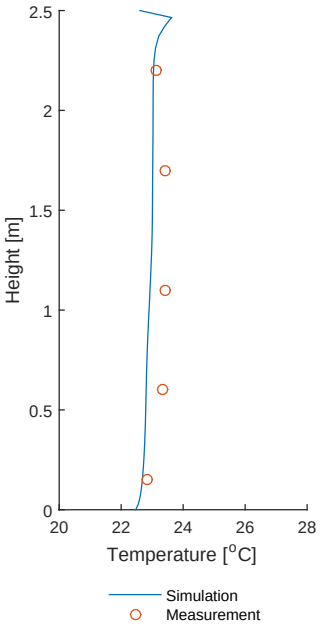

Figure 8.126. Temperatures along pole 1

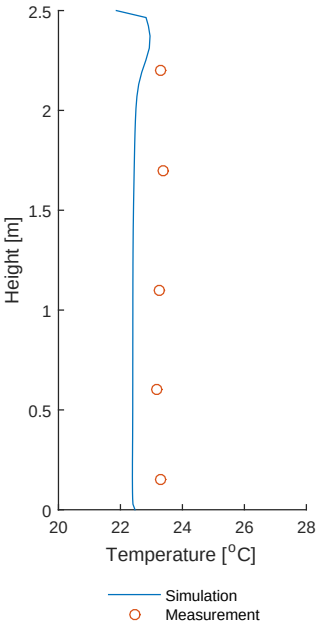

Figure 8.127. Temperatures along pole 2

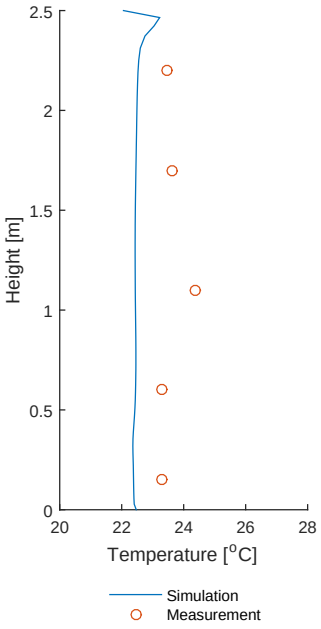

Figure 8.128. Temperatures along pole 3

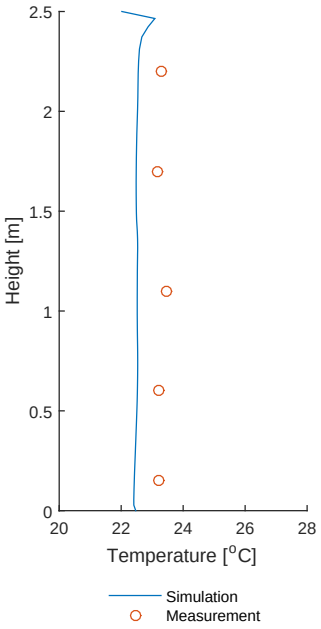

Figure 8.129. Temperatures along pole 4

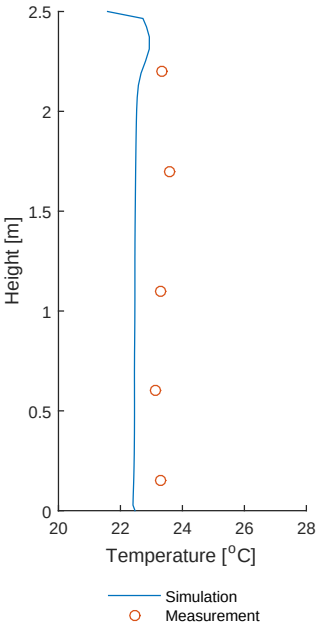

Figure 8.130. Temperatures along pole 5

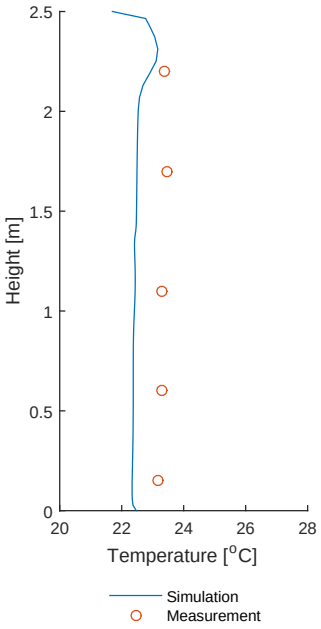

Figure 8.131. Temperatures along pole 6

The comparison of temperature distribution in the plenum is presented in the Figure 8.132

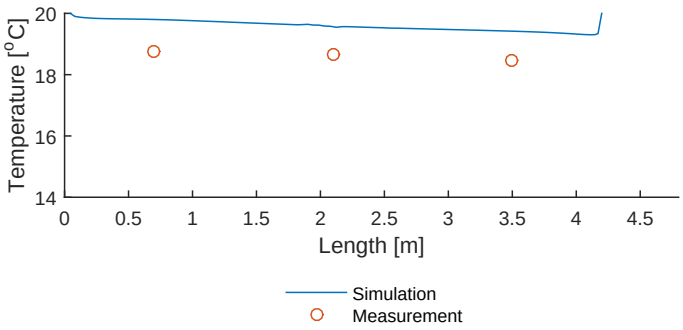

Figure 8.132. Comparison of temperature distribution in plenum

Figures 8.126 - 8.131 show that the numerical model estimates a uniform temperature distribution along the poles likewise measured during the experiments too. However, the calculated temperatures by the CFD model are around 1°C lower than the temperatures obtained from the experiment. The reason behind temperature increase is additional heat gain obtained during the experiment period. Case 5 was conducted in the middle of May when the ambient temperatures risen significantly. This had an influence in the indoor temperature of the hotbox too. In other words, in this case there was an extra heat gain compared to the case 1 and 4 where there was heat loss which explains why the simulation calculated lower temperatures than those obtained from the experiment. More specifically, the temperature of façade side was measured around 21.9°C just before the experiment started. However, by the end of the measurement, it was noticed that the temperature of façade side had an average around 23.1°C during the experiment as it can be seen in the Table 8.10.

Table 8.10. Comparison of façade boundary condition between experiment and CFD for case 5

Wall	Average temperature during experiment, [°C]	Fixed temperature used in CFD radiant model, [°C]
Façade wall	23.35	21.90

As mentioned previously, the CFD model does not predict correctly the temperatures within the plenum region. It was noticed that even in case 2 and 3 where the energy unbalance rate was minor the CFD model overestimated the temperatures in the plenum around 1 °C. In this case, the temperatures in plenum calculated by the CFD model are close enough to those obtained by the experiment. This happens due to the extra heat gain occurred during the experiment which rose the temperatures of the hotbox. The extra heat gain resulted in higher plenum temperatures which consequently reached values close to those predicted by the model. However, this happened due to circumstances and not because of the correct CFD prediction.

The comparison between measured air velocities during the experiment and calculated by the numerical model are presented in the Figures 8.133 - 8.138.

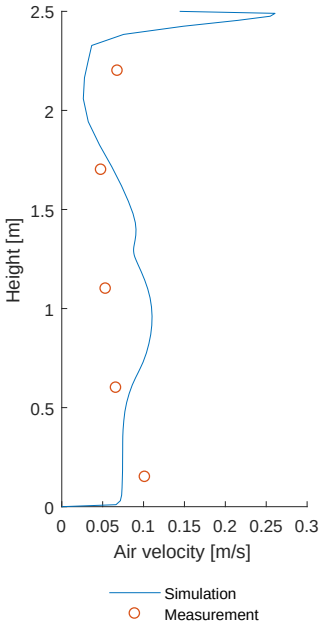

Figure 8.133. Velocities along pole 1

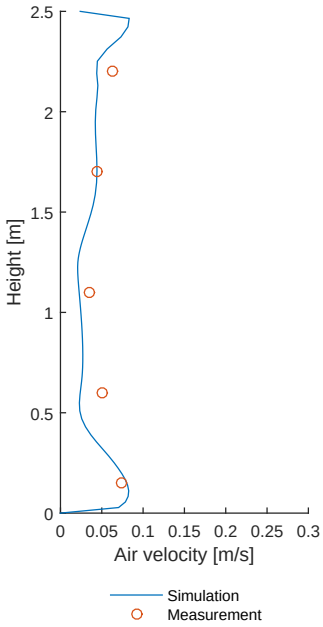

Figure 8.134. Velocities along pole 2

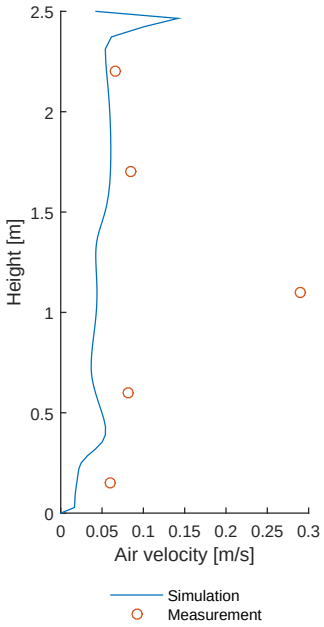

Figure 8.135. Velocities along pole 3

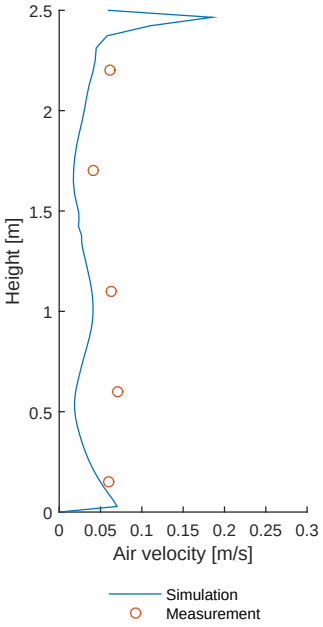

Figure 8.136. Velocities along pole 4

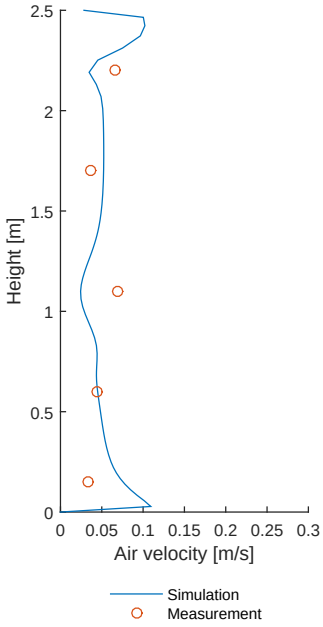

Figure 8.137. Velocities along pole 5

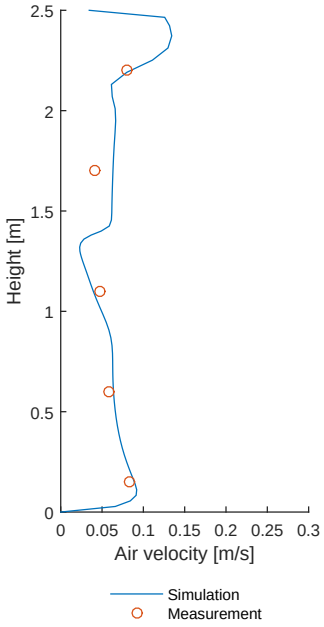

Figure 8.138. Velocities along pole 6

Figures 8.133-8.138 show that CFD model has close estimation of measured velocities except one point with big underestimation. Figure 8.135 shows that the velocity at height 1.1m deviates from that one obtained by the measurement. It seems that the CFD model does not predict the 'peak' of air velocity at that specific point.

The comparison between measured N_2O concentrations during the experiment and calculated by the numerical model are presented in the Figures 8.139 - 8.144.

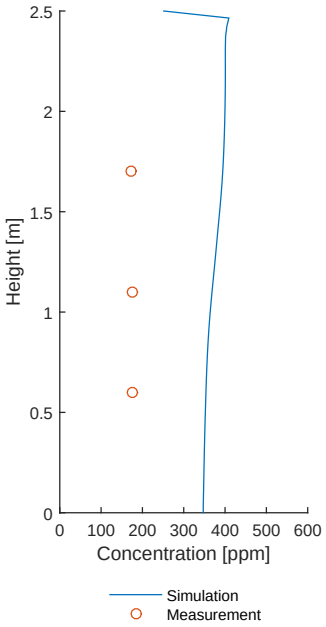

Figure 8.139. N_2O along pole 1

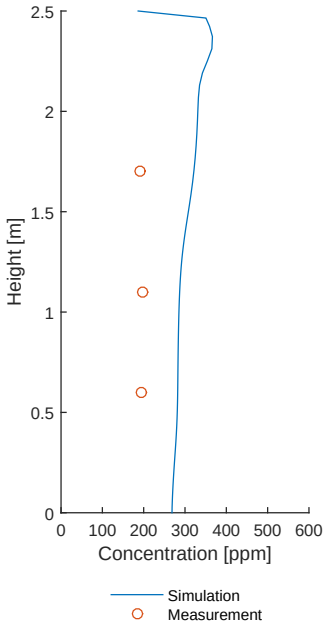

Figure 8.140. N_2O along pole 2

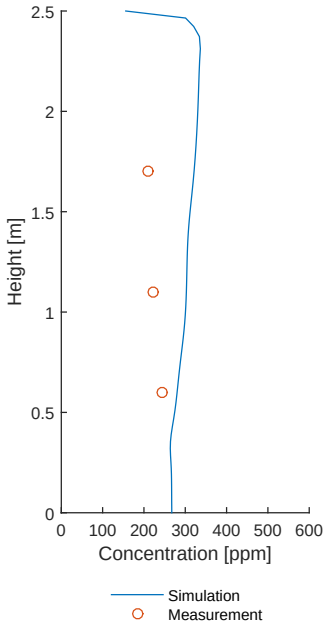

Figure 8.141. N_2O along pole 3

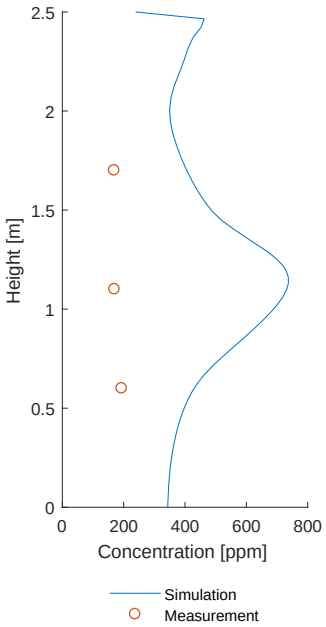

Figure 8.142. N_2O along pole 4

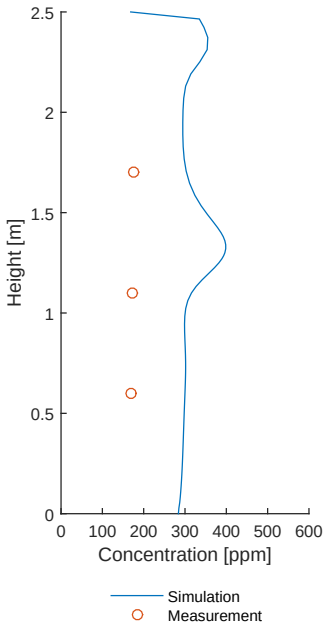

Figure 8.143. N_2O along pole 5

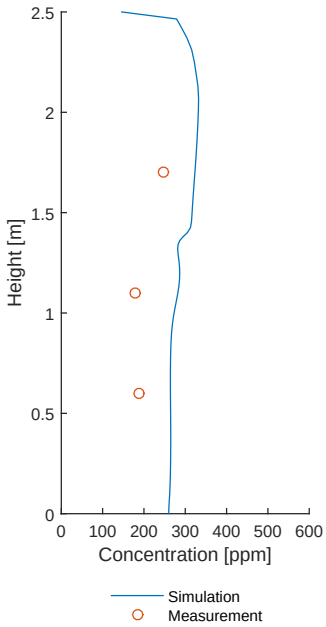

Figure 8.144. N_2O along pole 6

The comparison between N_2O concentrations at inlet, plenum points, fabric points and outlet can be seen in Figure 8.145 and 8.146.

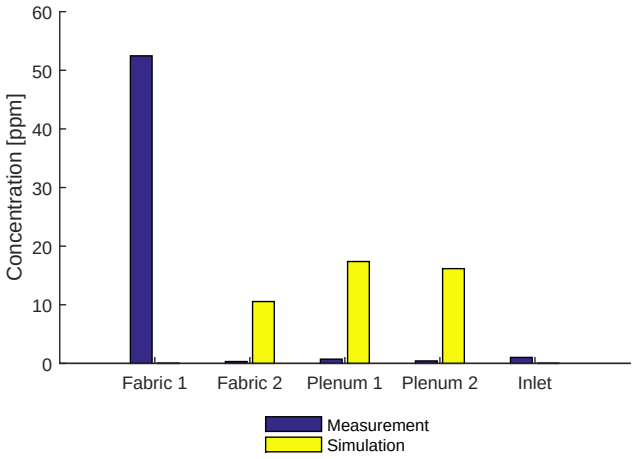

Figure 8.145. Comparison of N_2O concentration at certain locations

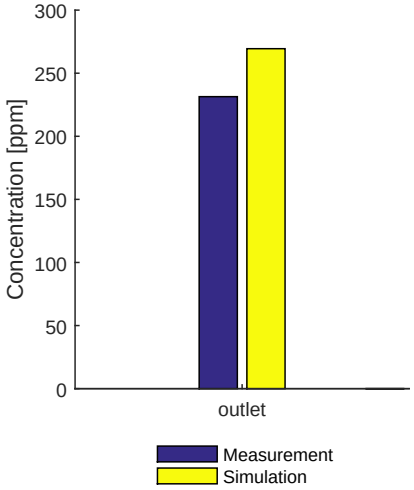

Figure 8.146. Comparison of N_2O concentration at outlet

Figures 8.139 - 8.144 show that the estimation of N_2O distribution in the room compared to the measurements is not very accurate and has some peaks which were not noticed during the measurements. Measurements clearly show that the distribution of N_2O along all the poles is uniform. However the numerical model has different tendency of distribution especially for pole 4. According to the simulation there is a 'peak' of N_2O concentration at 1.1m height on pole 4 where the concentration reaches around 700 ppm as the Figure 8.142 indicates. The difference in N_2O tendency may happen as a result of model limitations when the pollutant source is not positioned in the thermal plume which was also noticed for previous simulations. In addition to that, N_2O mass balance was not reached during the experiment as it can be seen in the Table 8.11. This may have happened due to a possible leak in the envelope of the hotbox which could also influence the N_2O pattern and concentration in the room.

Table 8.11. Comparison of N_2O mass unbalance rates between experiment and CFD for case 5

N_2O mass unbalance during experiment, [%]	N_2O mass unbalance in CFD, [%]
16	0

The distribution of temperature in the room can be seen in the Figures 8.147 and 8.148 below.

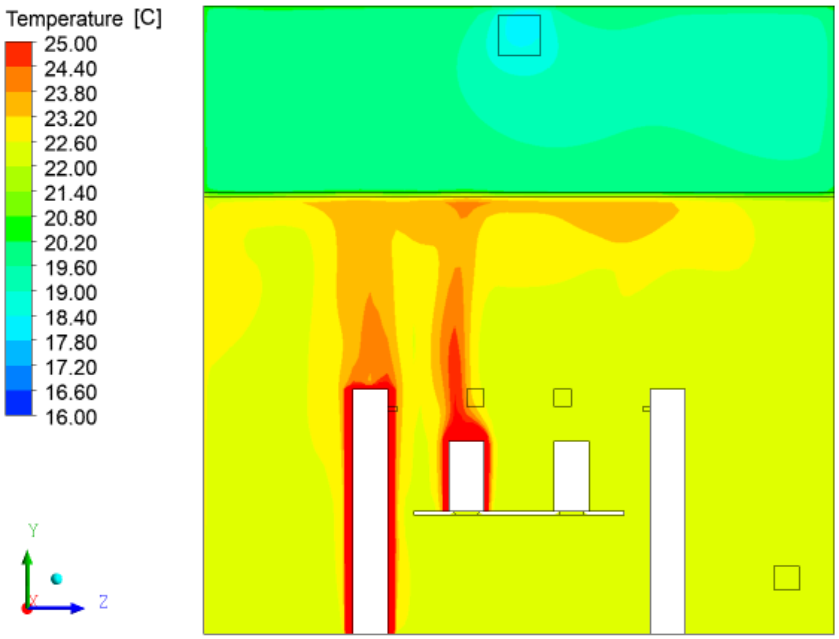

Figure 8.147. Distribution of temperature for plane at X=2.1m

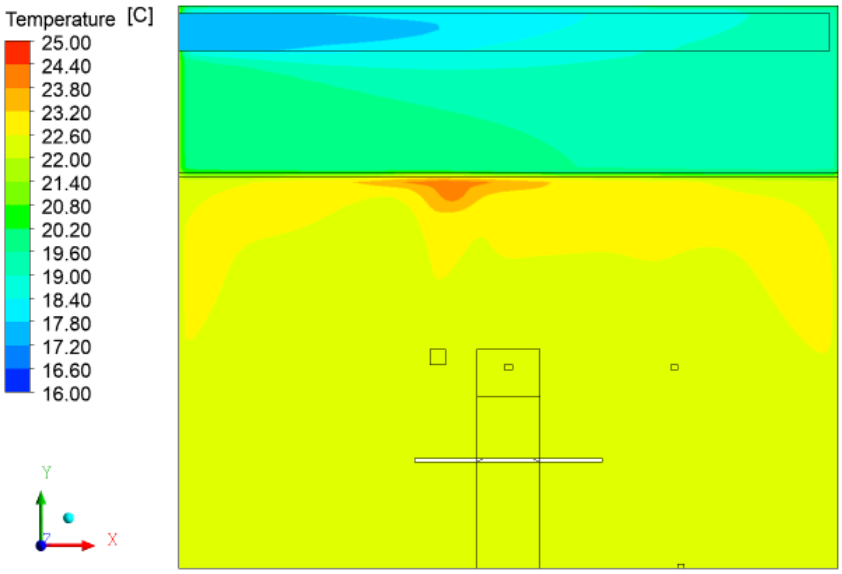

Figure 8.148. Distribution of temperature for plane at Z=1.9m

As it can be seen from the Figures 8.147 and 8.148 the temperature in the room is mostly uniform. The air temperature range is around 22°C - 22.5°C in most of the space of the room even when only one of the persons and his equipment is active as heat sources.

The air flow pattern for case 5 can be seen in the Figures from 8.149 to 8.153 below.

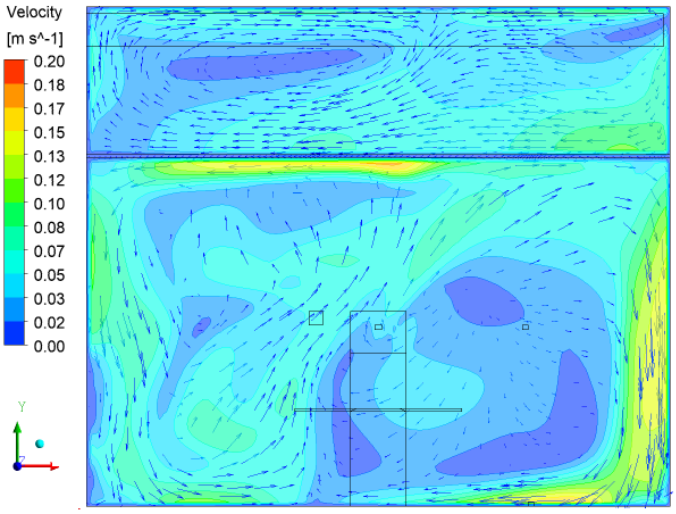

Figure 8.149. Airflow pattern for plane at Z=0.5m

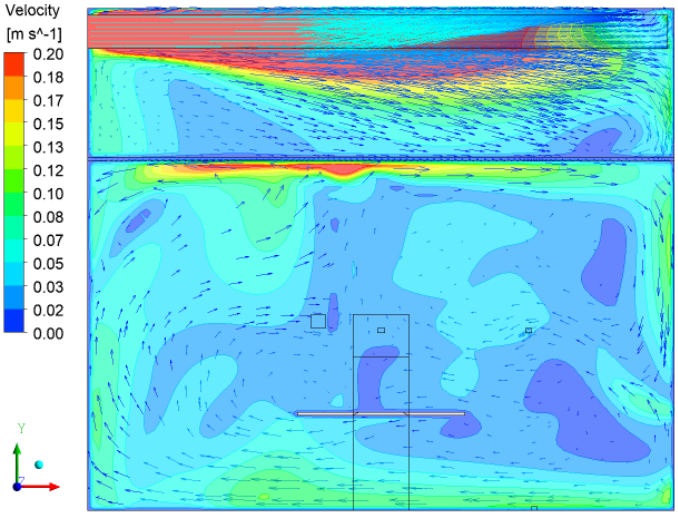

Figure 8.150. Airflow pattern for plane at Z=1.9m

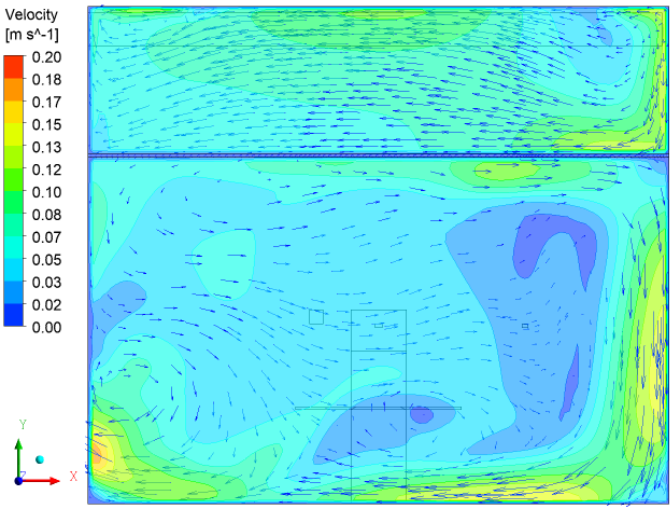

Figure 8.151. Airflow pattern for plane at Z=3.1m

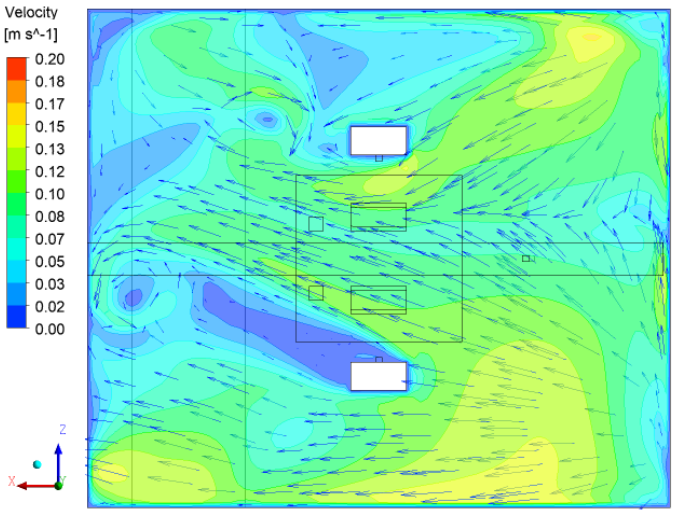

Figure 8.152. Airflow pattern for plane at Y=0.1m

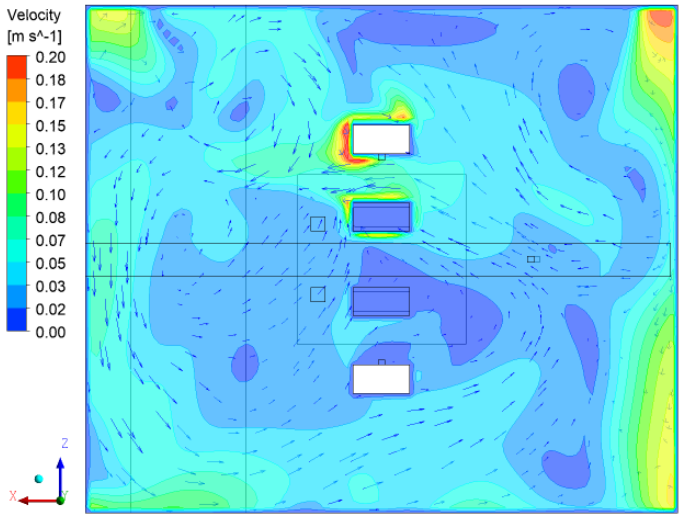

Figure 8.153. Airflow pattern for plane at Y=1.1m

Figures 8.149 - 8.151 show that the airflow pattern is forced to the side walls and causes a recirculation on the side of person 1. This happens due to the fact that only person 1 acts as a heat source and generates thermal plume. Thus, comparing the air flow pattern on person 1 side and on the exhaust side it can be noticed that around the person 1 there are two recirculation vortexes on each of the sides whereas on the exhaust side there is only one recirculation vortex due to the removed heat load.

Additionally, by observing the 8.152 and 8.153 it can be pointed out that compared to the cases with two persons, the air flow pattern is not symmetrical. This happens due to the fact that the heat load is not evenly distributed within the room. The thermal plume of person 1 which is the only person acting as a heat source drives the air towards its side.

The distribution of contaminants can be seen in the Figures 8.154 - 8.159.

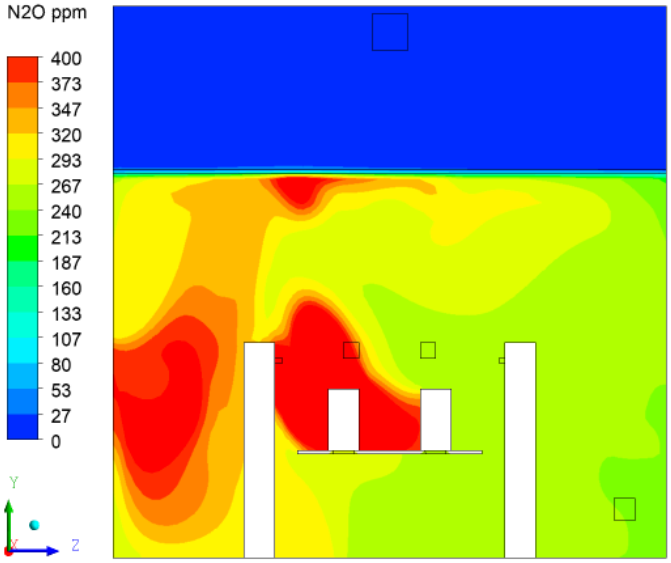

Figure 8.154. N_2O distribution for plane at X=2.1m

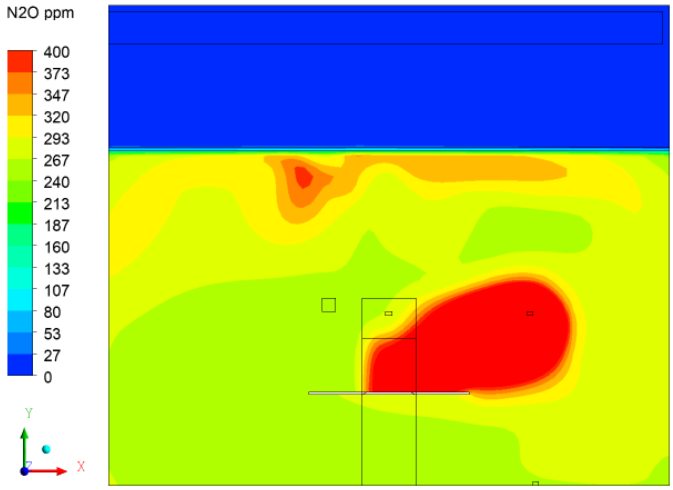

Figure 8.155. N_2O distribution for plane at Z=1.9m

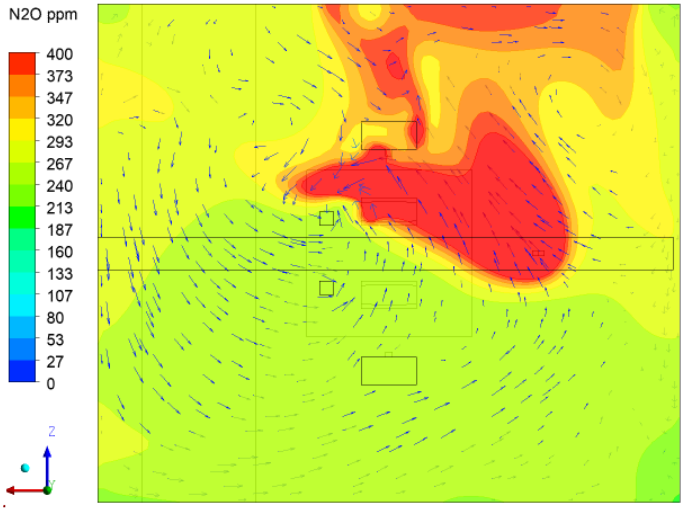

Figure 8.156. N_2O distribution for plane at Y=1.4m

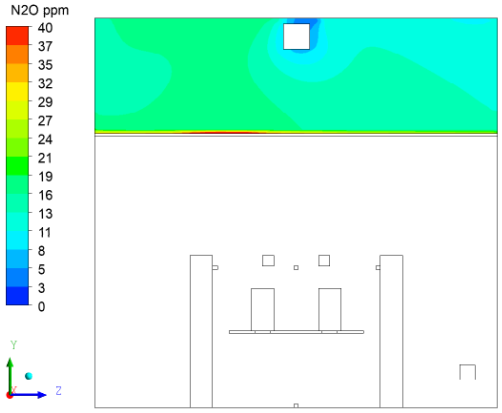

Figure 8.157. N_2O distribution in plenum for plane at X=2.1m

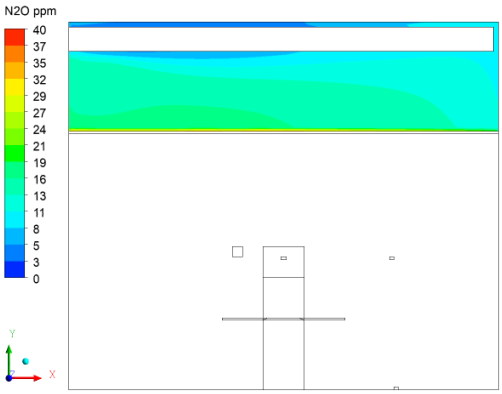

Figure 8.158. N_2O distribution in plenum for plane at Z=1.9m

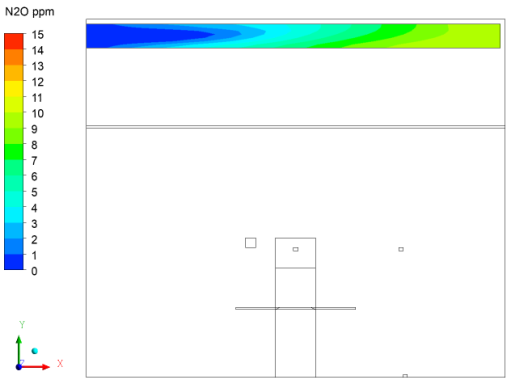

Figure 8.159. N_2O distribution in fabric duct for plane at Z=1.9m

As it can be seen from the Figure 8.154 and 8.156 the N_2O plume has a direction towards activated person which results in not uniform contamination distribution in the room. This happens due to the air flow pattern which is driven towards to person as explained previously. When the N_2O meets the thermal plume of person, it starts rising upwards to the diffuse ceiling. This is why the back flow from room to plenum takes place above person 1 as the Figure 8.157 indicates.

Case 6

The comparison between measured temperatures during the experiment and calculated by the numerical model are presented in the Figures from 8.160 to 8.165.

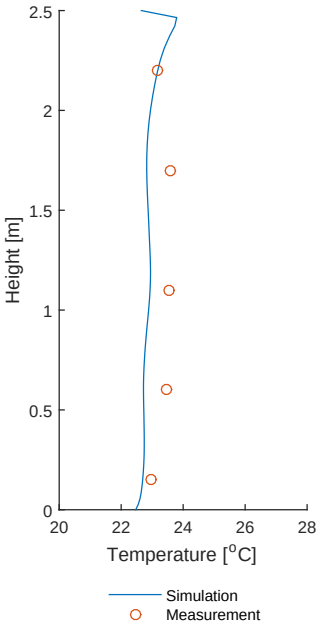

Figure 8.160. Temperatures along pole 1

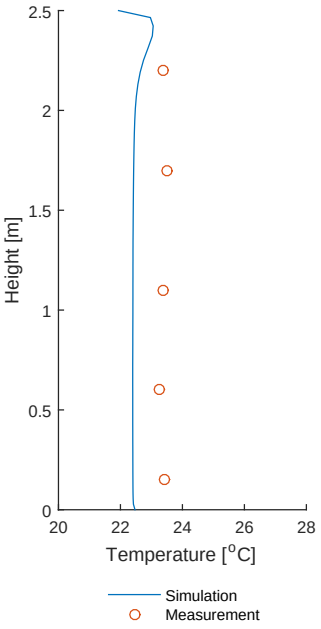

Figure 8.161. Temperatures along pole 2

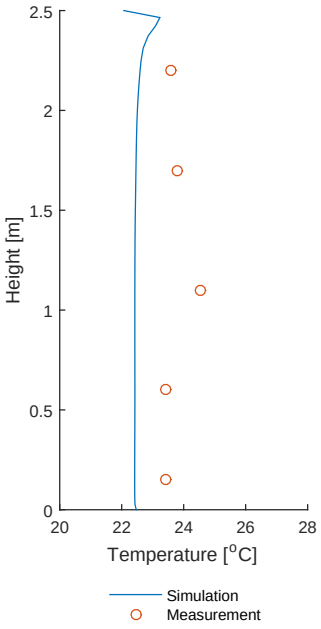

Figure 8.162. Temperatures along pole 3

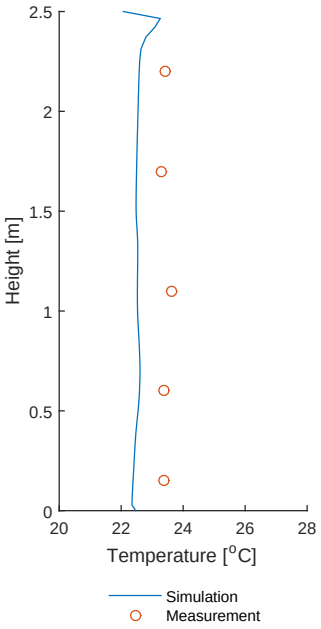

Figure 8.163. Temperatures along pole 4

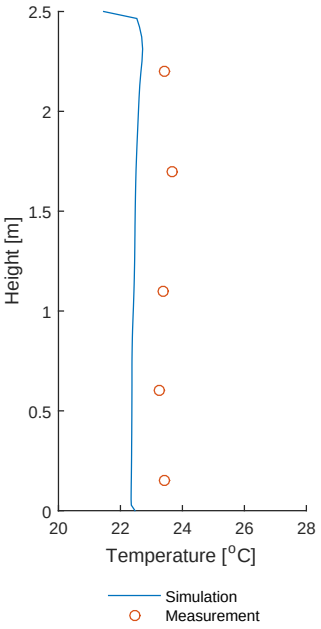

Figure 8.164. Temperatures along pole 5

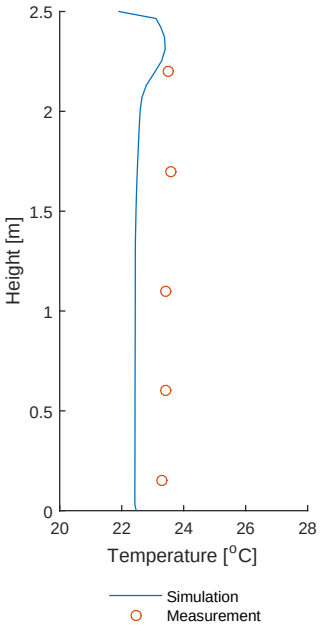

Figure 8.165. Temperatures along pole 6

The comparison of temperature distribution in the plenum for case 6 is presented in the Figure 8.166

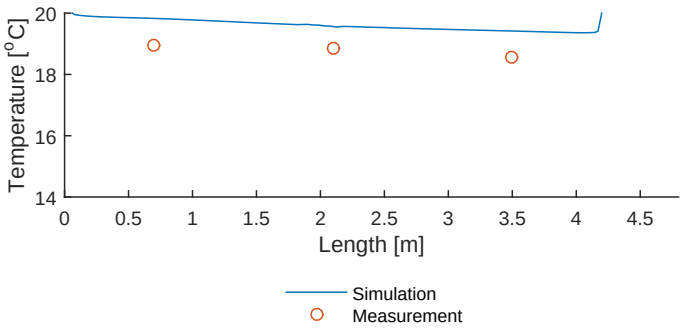

Figure 8.166. Comparison of temperature distribution in plenum

From Figures 8.160 - 8.165 seems that the numerical model estimates a uniform temperature distribution along all the poles as observed from experiment. However, temperatures calculated by CFD model are a bit lower than the temperatures obtained from the experiment. The reason for these deviations is the same as explained in case 5. More specifically, the temperature of façade side was used in CFD was 21.9°C as measured before the experiment. However, after the experiment it was noticed that the temperature of façade side had an average temperature of approximately 23.5°C during the period of measurement as the Table 8.12 shows.

Table 8.12. Comparison of boundary conditions between experiment and CFD for case 6

Wall	Average temperature during experiment, [°C]	Fixed temperature used in CFD radiant model, [°C]
Façade wall	23.47	21.90

The extra heat gain obtained during the experiment resulted in higher plenum temperatures which consequently reached values close to those predicted by the model. However, this happened due to circumstances and not because of the correct CFD prediction as explained in case 5 results.

The comparison between measured air velocities during the experiment and calculated by the numerical model are presented in the Figures from 8.167 to 8.172.

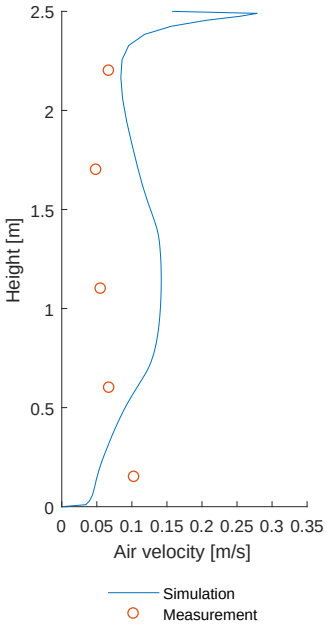

Figure 8.167. Velocities along pole 1

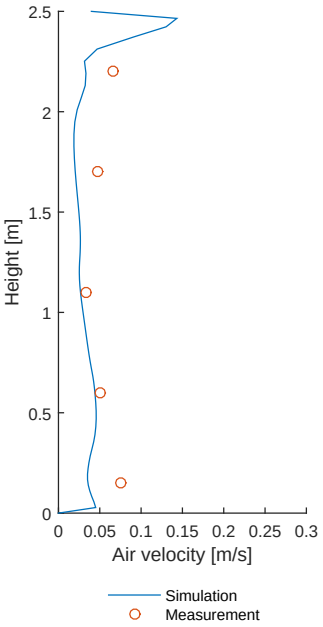

Figure 8.168. Velocities along pole 2

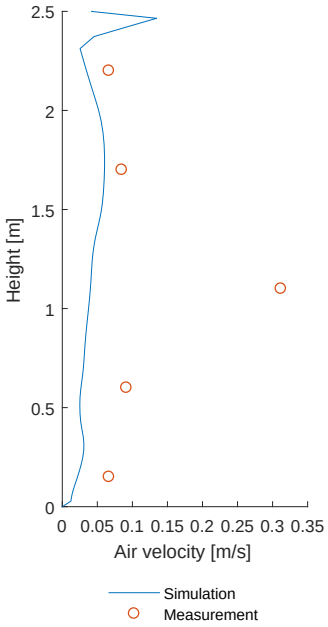

Figure 8.169. Velocities along pole 3

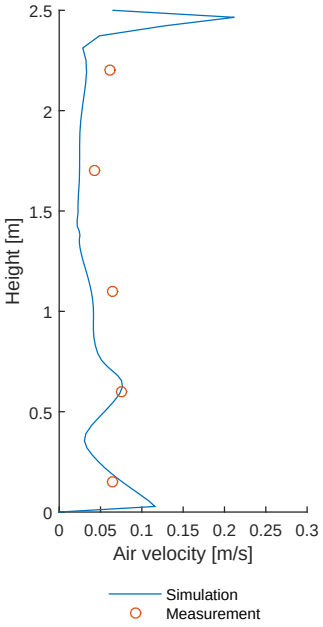

Figure 8.170. Velocities along pole 4

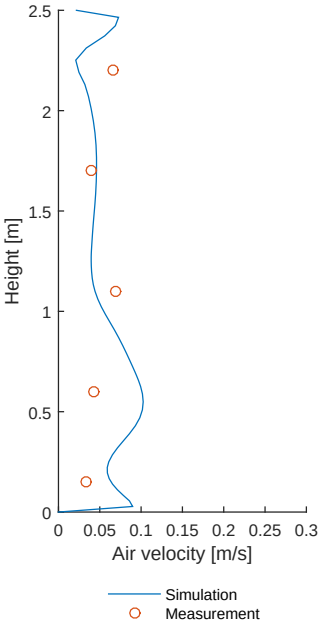

Figure 8.171. Velocities along pole 5

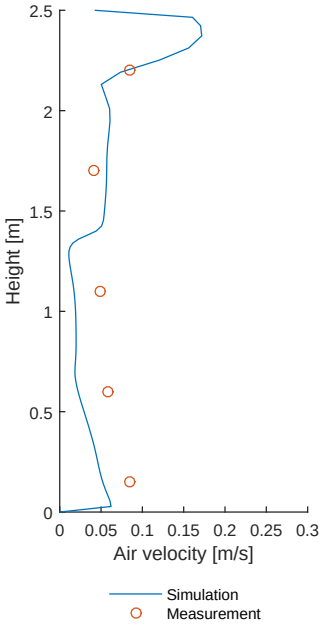

Figure 8.172. Velocities along pole 6

Figures 8.167-8.172 show that CFD model estimates correct air distribution for most of the measurement points. However, there are some points where the CFD model predicts different air velocities comparing to the measured values. It is noticeable that as measured in case 5, the velocity 'peak' at 1.1m on pole 3 is not predicted predicted by the CFD model.

The comparison between measured N_2O during the experiment and calculated by the numerical model are presented in the Figures from 8.173 to 8.178.

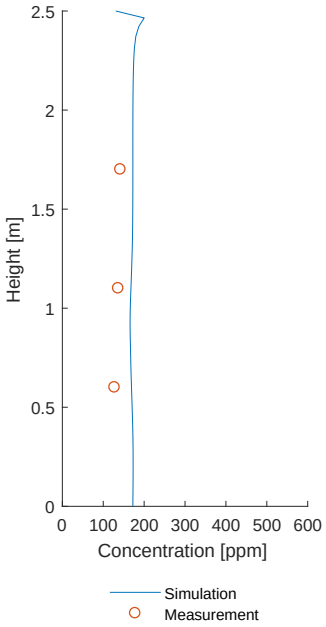

Figure 8.173. N_2O along pole 1

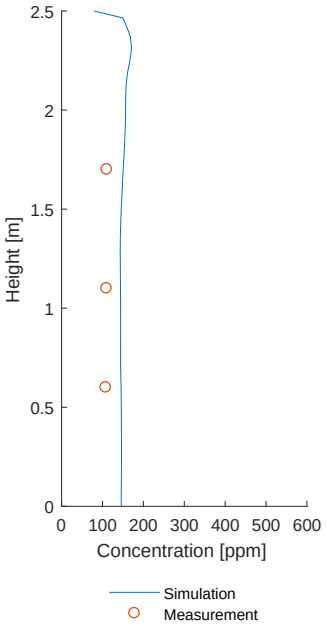

Figure 8.174. N_2O along pole 2

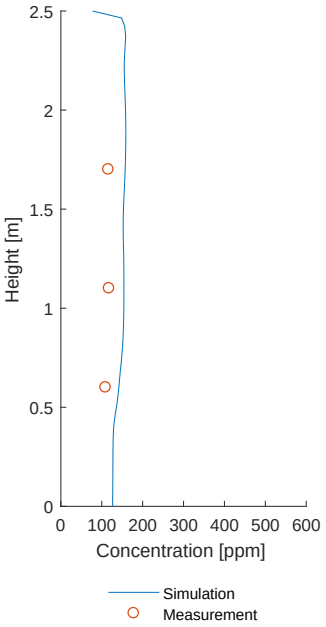

Figure 8.175. N_2O along pole 3

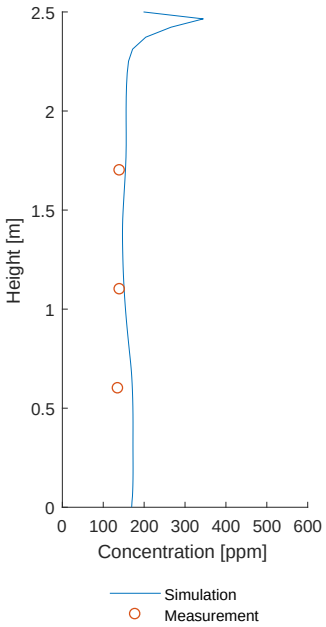

Figure 8.176. N_2O along pole 4

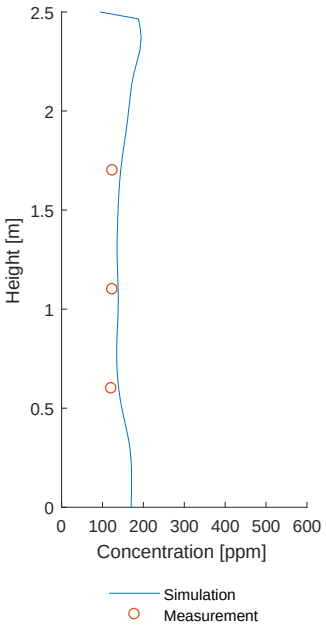

Figure 8.177. N_2O along pole 5

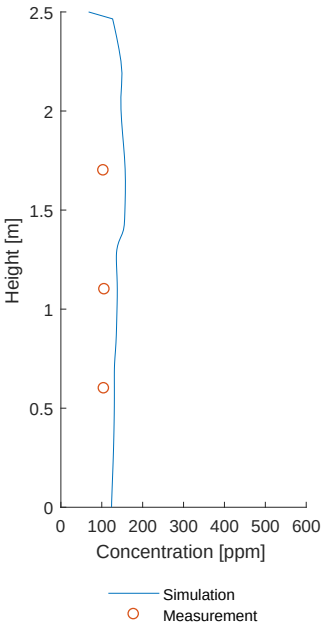

Figure 8.178. N_2O along pole 6

The comparison between N_2O concentrations at inlet, plenum points, fabric points and outlet for case 6 can be seen in Figure 8.179 and 8.180.

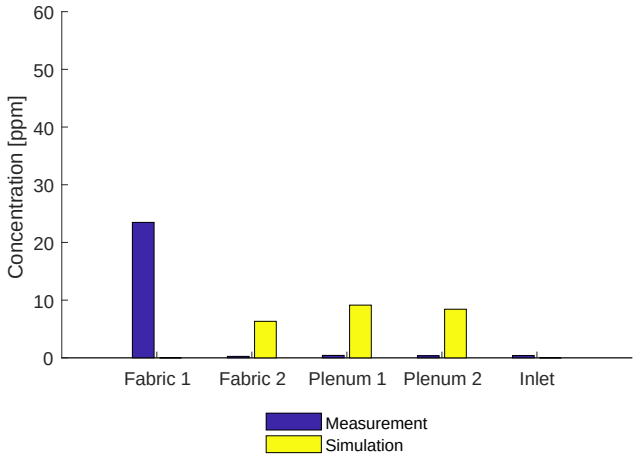

Figure 8.179. Comparison of N_2O concentration at certain locations

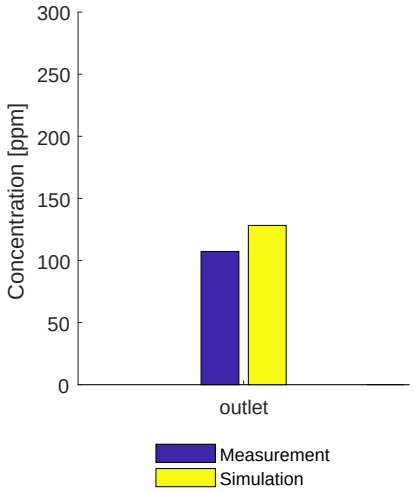

Figure 8.180. Comparison of N_2O concentration at outlet

Figures 8.173 - 8.178 show that CFD model can estimate correct tendency of the N_2O distribution along the poles. As the measurements have shown the distribution of N_2O along all the poles is uniform. The same estimation is predicted by CFD model. However, there are deviations between their values. According to the measurement the N_2O concentration along all the poles is around 120-140 ppm whereas the CFD model predicts N_2O concentration in the range of 160-180 ppm. These deviations can be assumed acceptable considering the N_2O mass balance was not reached during the measurement. As the Table 8.13 shows the N_2O concentration did not reach balance due to a possible leak in hotbox. This could explain the lower N_2O concentration measured during the experiment than expected.

Table 8.13. Comparison of N_2O mass unbalance rates between experiment and CFD for case 6

N_2O mass unbalance during experiment, [%]	N_2O mass unbalance in CFD, [%]
22.0	6.8

The distribution of temperature and air velocity for case 6 are similar to those of case 5 since the same boundary conditions for ventilation and heat loads are applied. The only difference between case 5 and 6 is the type of contamination source and the flow rate of contaminants, therefore only N_2O distribution is shown with illustrations for this case.

The distribution of contaminants can be seen in the Figures 8.181 - 8.186.

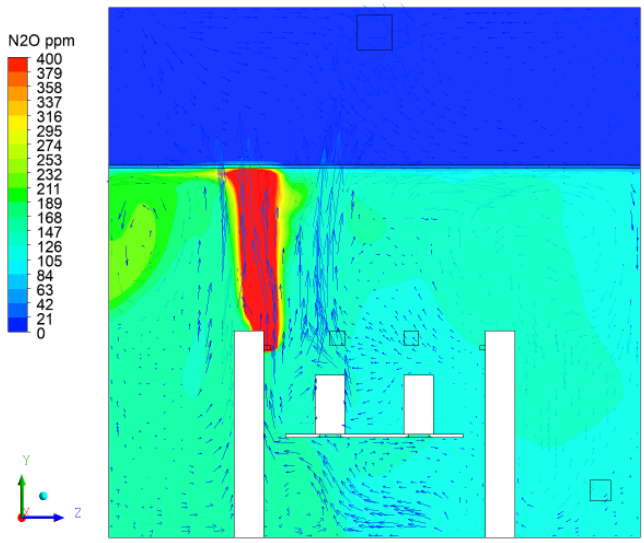

Figure 8.181. N_2O distribution for plane at X=2.1m

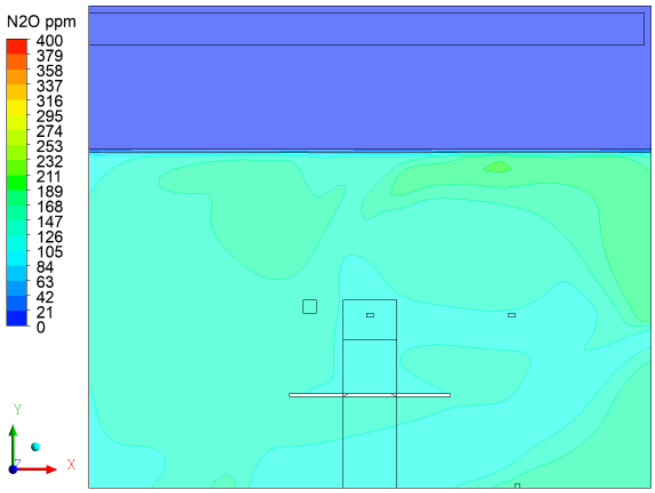

Figure 8.182. N_2O distribution for plane at Z=1.9m

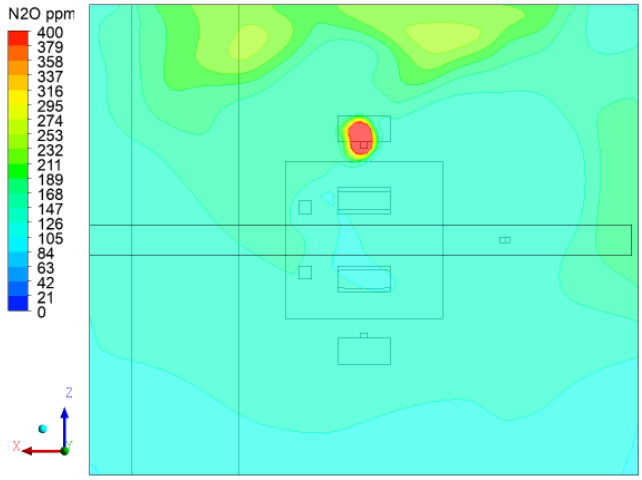

Figure 8.183. N_2O distribution for plane at Y=1.7m

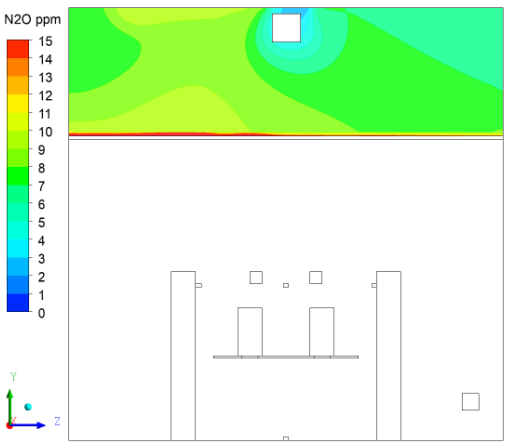

Figure 8.184. N_2O distribution in plenum for plane at X=2.1m

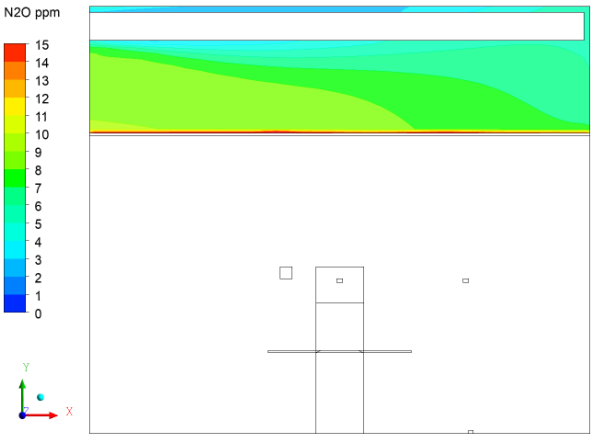

Figure 8.185. N_2O distribution in plenum for plane at Z=1.9m

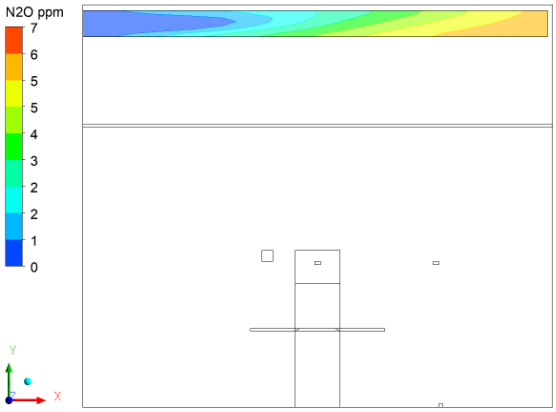

Figure 8.186. N_2O distribution in fabric duct for plane at Z=1.9m

Figures 8.181 and 8.183 indicate that the N_2O distribution is not uniform in the room. It can be seen that the region behind activated person gathers higher N_2O concentration than the rest of the room. However, the part where the cloud of N_2O is gathered can be neglected because it is not in the occupied zone. The N_2O level in the occupied zone is almost uniform. The thermal plume of person rises upwards to the diffuse ceiling together with N_2O which explains why the reverse flow from room to plenum happens above person as the Figure 8.184 indicate. When the N_2O enters the plenum starts circulating with air and eventually reach the end of the fabric duct as the Figure 8.186 presents

8.0.1 Conclusion of validation

In all the cases the CFD model has shown uniform temperature distribution in both, plenum and room as measured from the experiments too. However, in some cases the temperatures of CFD model and measurements do not fit due to unstable thermal boundary conditions which occurred during the experiments. Also, it was clear that CFD models overestimated the temperatures within the plenum in all cases which was also noticed during the learning process in this thesis. In order to obtain correct temperatures from CFD model re-simulations are required to be performed where additional energy source in the room is applied and its output is equal to the additional heat losses caused by the energy unbalance. Due to the shortage of time and CFD licences limitations it was decided to correct only case number 1 as an indication that the model can predict correctly the temperatures in the room if it is properly setup. The results of the re-simulations for case 1 can be seen in Appendix F.

Further on, prediction of air velocity distribution for the most of the measurement points is accurate. However, in some cases, large deviations have been observed. The air velocities are hard to be predicted since the existence of the porous zone creates a transient profile of velocity in both, experiments and simulations. The magnitude of air velocity does not stay stable either during the experiments or in simulations thus any relatively small difference in velocity profile between CFD and measurements can be assumed to be acceptable.

Regarding the contaminant distribution, two different situations have been observed. When the contaminant source is found within the thermal plume the CFD model can predict similar contaminant distribution in the room as measured from the experiments. When the contaminant sources are the people in the room, the CFD predicts the same tendency of N_2O as observed in the experiments. The N_2O rises upwards due to the buoyancy effect and then distributed uniformly in the room. However, when the contaminant source is not positioned in the thermal plume the CFD model presents limitations on predicting the same N_2O distribution as measured from the experiments. When the contaminant source is positioned away from the heat sources the contaminant distribution is not uniform and a 'peak' of N_2O occurs within the room as observed in both simulations and measurements. Nevertheless, there are differences between numerical model and experiments on where the N_2O 'peak' is found within the room. This probably happens due to the transient profile of velocity which occurred in the room. When the pollutant source is not placed close to the heat source the N_2O distribution is depended on the air flow pattern within the room. Since the porous zone causes a transient profile of air velocities the N_2O 'peak' is hard to be predicted. It is questionable if the deviations of N_2O concentrations and distribution are caused due to a limitation of the numerical model or to the mass unbalance which occurred during the experiments. Thus, it can be included as a point of interest for the future work.

In addition, CFD simulations as measurements observed the back flow to the plenum. During the simulations it was noticed that if the room is equipped with symmetrical heat load, back flow to the plenum through porous medium is achieved symmetrically through the diffuse ceiling surface. However, for the cases where the head load is not evenly distributed within the room it was noticed that the back flow happens only above the active heat sources. Therefore can be conclude that the cause of reverse flow back to the

plenum was thermal plume generated from heat sources which lead N_2O concentrations upwards to the diffuse ceiling.

Lastly, the CFD model predicts back flow from plenum to the fabric duct as observed during the experiments too. According to the CFD predictions, the back flow occurs only in the deeper parts of the fabric duct and not at the beginning of it. On the contrary, the beginning of fabric duct experienced a relatively high concentration of N_2O in all the measurements. However, by the end of the experimental investigation it was found out that the measured concentration at that position was an error, therefore it could not be used for the comparison.

Part IV

Conclusions

9 | Conclusion

To begin with, the main aim of this thesis was to evaluate indoor environment quality, more specifically the air quality and thermal comfort by using the climatic chamber (hot box) with diffuse ceiling ventilation in Aalborg University. The experiment was conducted both numerically, by the help of Fluent CFD program, and experimentally in the hot box. Present study focused only on steady-state conditions which excluded possible dynamic effects of the surroundings. This chapter will be focused on the general conclusions that were achieved through out the period of experiment. However, it has to be noted that due to the restrictions of equipment in the laboratory and because of the shortage of time the expected full scale experiments were not carried out. Only a part of the expected experiments were conducted and only this part was analysed.

Furthermore, based on the previous studies on diffuse ceiling ventilation it was expected to get uniform temperature distributions in the room, draught free environment, low vertical temperature gradients and good effectiveness of contamination removal. During the present experimental measurements it was confirmed that diffuse ceiling ventilation provides uniform temperature distribution in the room for all the measured cases. The smallest average vertical temperature gradient was achieved in case 6 which corresponded to 0.06°C/m and the biggest average vertical temperature gradient was achieved in case 1 and 4 with 0.22°C/m vertical temperature gradient. In all the cases temperature gradients for individual poles were lower or equal to 0.54°C/m. Also, it was observed that smaller vertical temperature gradients appear in cases with 6ACH and 3ACH cases have higher vertical temperature gradients which indicate that 6ACH mixes air better. In addition to that, compared to the previous study by Zhang where the inlet was a slot opening a more uniform temperature distribution in the plenum was achieved due to the use of the fabric duct. For all the measured cases temperature difference between the beginning of the plenum and the end of the plenum was less than 1°C and the cases had somewhat of the same temperature in the whole plenum volume.

Moreover, most of the measured velocities in the room were below threshold value of 0.2m/s which should provide draught free environment in the room based on the regulations. According to the measurements the biggest velocities appear on the lower zone of the room where the air recirculation happens which is also confirmed by previous studies on diffuse ceiling ventilation. Calculated draught rates shows that by increasing the ACH twice from 3ACH to 6ACH the possibility of draught in specific poles on average increases almost two times. Also, it can be seen that highest draught rates appear on the poles that are close to persons which might be influenced by the generated thermal plumes.

In addition to that, the distribution of N_2O gases in the room proved to be very uniformly distributed for all the cases except couple of points. Some deviations were noticed during

the measurements with additional contamination source at ground level with 6ACH and 3ACH. Dead zones could not be confirmed because of few tracer gas sensors. Also, it was noticed that in the beginning of the fabric duct contamination was varying between 20-70ppm despite the fact that the measured value in the inlet of AHU was measured to be less than 1ppm. Later on it was found out that the junction of the tubes leading to the measuring point in the fabric duct was not sealed correctly which lead to faulty measurements in the beginning of the fabric duct. Overall average contaminant removal effectiveness for most of the cases was around 1 which implicated a good mixing of air in the room. The interesting part that was observed during the measurements is that when the heat load is distributed symmetrically in the room and the contamination source is supplied from the heat source the contamination in the room is well mixed with a ventilation coefficient close to 1. However, when there is only one person in the room and the heat load is no longer distributed symmetrically the ventilation effectiveness drops down below threshold of 0.9 which indicates poor mixing. Furthermore, in cases of experiment where the contamination source was placed on the floor level it was observed that the contaminant does not rise and spread to the upper level of the room it rather travels across the floor towards the exhaust side and only spreads and rises if it is captured by the thermal plume of heat source. Moreover, in this case the ventilation system works with contamination removal effectiveness of around 3 which indicates the principle of piston flow. As for the case where the contamination source is placed at 1.3m height more uniform distribution of contamination is observed if compared to the contamination source placed on floor level. Also, for such case the contamination removal effectiveness is approximately 1.2 which indicates that the ventilation system works more like a mix between piston and mixing ventilation.

On the other hand, when comparing the measured values with numerical model values some discrepancies can be noticed. For most of the temperature distribution cases simulated values are higher than measured values. That can be explained by the steady-state calculations were the façade temperatures that were used for calculations were higher than the actual ones during the measurements. That lead to energy unbalance in measurements which resulted to lower temperatures than anticipated. Despite the fact that they are lower it can be seen that the tendency of distribution is followed by numerical simulation. Same can be applied for velocity distributions which are compared to the numerical model. Most of the poles fit the measured values and kept the tendency except one point at pole 3 which for all cases gave higher measured velocities than simulated. In addition, it can be seen that CFD over predicts the N_2O concentrations in the plenum volume and outlet. Assuming that the concentration in fabric 1 point was an error in measurement setup the over prediction in CFD can be also explained by possible leakages inside the room which may have caused mass unbalance during the experiments. It was calculated that for most of the cases during the measurements there was an unbalance of 10-20% N_2O mass which implies that there must be a leak somewhere in the hot box. It can be seen that the simulated outlet values are higher than the measured ones which can be supported by the leak assumption. Essentially, the measurements showed uniform temperature distributions, velocities were low enough to provide draught free environment. In addition to that contamination distribution in the occupied zone was mostly uniform for the cases where contaminant sources were placed on the heat sources.

Contamination removal effectiveness for these cases was close 1 indicating good mixing of indoor air. In cases where the pollutant source is not at the heat source the distribution of N_2O is not completely uniform in the room. Effectiveness of contaminant removal reaches values of more than 1 indicating piston flow ventilation principle or in worst case just below 1 alerting that it is below 0.9 threshold which shows poor mixing of air. Thus, it can be concluded that diffuse ceiling for this experiment provided good indoor environment quality and all of results can be supported by the previous studies on diffuse ceiling ventilation which indicates same tendencies of measured variables.

When comparing the measured values during the experiment and numerical simulations differences between results were observed. Most of it can be explained by the unbalances during the measurements due to unstable surrounding conditions and leaks in the hot box. It is noticed that for some cases CFD model over predicts or under predicts the temperature magnitude in the occupied zone. This happens due to the heat unbalance which occurred during the measurements. In addition, it can be seen that the CFD model can correctly predict the distribution of contamination in the occupied zone when it is placed on the heat source within thermal plume. However, it seems that the CFD model over predicts the N_2O concentration magnitude within the occupied zone when it is compared to the measurement results which was caused by mass unbalance of N_2O during measurements. Moreover, the numerical model does not estimate the same contaminant distribution as measured in experiments in cases where the pollutant source is found away from the thermal plume. It is questionable if these deviations occur due to a limitation of the CFD model or due to a different contaminant pattern resulted by the mass unbalance observed in the experiments.

10 Discussion

The present research on indoor environment evaluation with diffuse ceiling ventilation provided very reasonable results as it was expected from the previous studies and their findings. Diffuse ceiling ventilation proved to achieve thermal comfort requirements with different cases. Temperature distributions in the occupied zone were proven to be uniformly distributed with small vertical temperature gradients which varied between 0.01°C - 0.54°C for different cases and pole positions. Compared to the conventional ventilation systems, diffuse ceiling ventilation principle helped to remove draught risk even with higher air change rates of 6ACH and lower inlet supply temperatures such as 14.28°C. It was found out that the highest risk of draught appears on the lower zone of the room, specifically at 0.1m where persons ankles are, which was also shown by previous studies on this type of system.

Furthermore, most of the researches that were conducted on the diffuse ceiling analysed thermal comfort in the room, pre-heating and cooling capabilities in the plenum. There were very few researches that evaluated indoor air quality. Present study tried to evaluate thermal and atmospheric comfort provided by this type of ventilation. The measurements showed that while the contamination source is located inside a thermal plume the distribution of contamination is uniform and provides a good air mixing which can be confirmed by contamination removal coefficient of approximately 1 for most of the cases. Moreover, since diffuse ceiling ventilation principle is mainly based on buoyant forces and not momentum forces, for the cases where there was only one person instead of two persons and the heat load was distributed not symmetrically it was noticed that contamination removal coefficient was below 0.9 which indicated a poor mixing of air in the room. It was concluded that the atmospheric comfort is dependent on how the heat load is distributed since it determines the air flow pattern in the room. Despite the fact that results were satisfactory, during the measurements there were some uncertainties that might have influenced the results and are worth investigating in the future work on this type of system.

Firstly, it should be noted that during the preparation of the experiment it was decided to control the surrounding temperatures of the hot box via the cavity which was integrated between the walls of hot box to reduce the heat losses and control the cold box temperature with the cooling system. The façade wall which is on the side of the cold box was most sensitive to heat losses due to its high U-value of $8 W/m^2 \cdot K$ and logically had the biggest heat losses compared to the other walls of the hot box. However, due to technical difficulties the cooling system in the new laboratory of Aalborg University could not be made in time and neither the cold box temperatures and cavity temperatures could not be controlled through out the whole experiment. This lead to unstable boundary conditions for the experiments which were influenced by different outdoor conditions, additional experiments in the laboratory with high heat loads, schedule of ventilation system in

the laboratory. Because of unstable boundary conditions previous energy balances that were set up to generate experimental cases with different ambient temperatures were not completely accurate any more. Most of the cases had an unbalance of approximately 100W or more except cases 2;3 and mainly the unbalance was caused by façade wall heat losses or gains due to its high thermal transmittance coefficient. As a result of unbalance during the measurements, when comparing the results with CFD simulations, the results did not fit exactly because of unbalance rate which had to be taken into account. In order to correct the CFD results resimulations with extra energy source in the room which corresponds to the unbalance rate can be perform to check whether it gives better fit for the temperature distributions.

Secondly, during the measurements it was noticed that the cooling system for the supply air had not enough power to cool down the air which was also confirmed by the technician only after the measurements period. As a result of poorly designed cooling system the temperatures were not stable and were varying constantly through out the time. Due to constantly differentiating temperatures the temperature distribution in the plenum and room, air pattern and velocities could have been influenced. This disadvantage should be also taken into account for further studies and if possible proper cooling system which would match the requirements should be installed to provide more accurate supply temperatures.

Thirdly, after comparing the N_2O distribution in the room during the experimental part and simulation results it was noticed that there are some differences between the results. The simulations provided higher concentrations in the room for all the cases because of that it was decided to calculate the mass balance of the contamination source. It was found out that for all the cases, except one, there were unbalances for 10% or more. The unbalance of contamination source showed that part of the supplied amount was disappearing somewhere in the room because it was not captured in the exhaust duct. After further investigation of the room it was found out that there were some minor leaks in the walls which might have caused the mass unbalance. This could explain why the simulation results give a bit higher concentrations than in measurements. Thereby, for obtaining more accurate results regarding contaminant concentration in the room the hot box should be sealed appropriately. Also, after analysing the set up it was found out that measured values at the beginning of the fabric duct were incorrect due to the leakage in the junction of the tube that was positioned at that point. Thus, in order to rectify this measurement error the leakage should be sealed. For further studies it would be recommended to monitor the concentration of the contaminants inside the cavity and cold box side to see whether the contamination spreads in those parts and confirm the leakage suggestion. In addition, the equipment that was used to measure N_2O concentrations in the room might have had influence on the measured values. Because the logging equipment was old it was advised that the calibration procedure should be skipped in order due its complexity.It was recommended to conduct only test control of the gas analyser to see how the measured deviated from the actual value. However, the variety of gases was only limited to a gas tank with 100ppm and a gas tank with 0ppm of N_2O. Thus the gas test was only conducted for two different concentrations. However, due to the limited type of gas tanks the conversion formula can not be assumed accurate. This approach of measuring N_2O might have created a percentage of error which should

be taken into consideration of the measurements. It is questionable whether the existence of deviations between model and measurements is due to a limitation of the model or poor experimental conditions. The model not only under predicts the contaminants concentration but in cases where there is point contamination source predicts also a different N_2O distribution. Therefore, more investigation about the use of the 'Species' model for an indoor environment evaluation is required.

Fourthly, as mentioned before, the boundary conditions for each measurement varied. It can be clearly seen in the magnitude of temperatures if cases 1;2;3;4 and 5;6 would be compared. During first two measurements the outdoor temperatures were low. However, since the last two cases were performed in the middle of May the weather conditions outside were much warmer compared to other cases. Also, 5th and 6th measurement was conducted after the condensation in the plenum happened. After 4th measurement it was noticed that the plenum started to accumulate water and soon the room was filled with water which was soaking the porous medium through which the air moves. It was left to dry out for couple of days until it dried out and the measurements were continued further on. Whether the rise of temperature of approximately 1°C was caused by possibly damaged permeability of porous medium or the rise can be an after effect of changed weather conditions in the outside can be discussable. As a result, last two cases 5th and 6th have approximately 1°C higher temperatures than it was calculated from the steady-state balance.

Fifthly, in order to calculate the viscous resistance and inertial resistance coefficients for fabric duct and new porous medium, used for the experiment, pressure drop tests across the materials had to be conducted. Two pressure sensors were used to measure pressure drop across two materials which were positioned in fabric duct and plenum, and in plenum and room. Since the fabric duct was very old design the company that manufactured it did not have any information on this product therefore it was unknown what approximate pressure drop should be measured across the fabric duct. On the contrary, porous medium that was used in present thesis differed only by 10mm from previous study of Zhang due to that there was some kind of a baseline that could be followed. However, the micromanometer device which used to measure the pressure drop was not calibrated and also the pressure drop experiment was not conducted under perfect pressure conditions the room was not fully sealed. An optimal solution would be to measure the pressure drop across a single pallet. Inaccurate inertial and viscous resistance coefficients that are put into the CFD simulations might influence overall air flow pattern, temperature and velocity distribution in the room.

Taking everything into account, present research proved that diffuse ceiling can accommodate acceptable indoor environment quality. However, there are some uncertainties that could have influenced the measurement results. Unstable boundary conditions of the ambient surroundings, poor cooling system, leakages in the hot box, possibly improperly conducted pressure drop tests could have lead to some mismatches between experimental data and numerical model. All of this should be kept in mind while evaluating the results of this thesis and some of it could be taken into account as precautions during the preparations and measurement period of future studies for similar researches.

11 | Future work

After conducting this research there are still some questions that were left unknown. Listed below are the possible future work ideas for diffuse ceiling ventilation capabilities :

- During the experimental part there were only 3 heights of N_2O concentration measurements in the occupied zone. It was noticed that for some cases there were some deviations in some points and it could not be explained. Therefore, future studies could analyse the distribution of contaminants for the whole room where it could possibly identify the locations of dead zones where the contamination accumulates and what can influence their distribution.

- One of the major goals of this thesis was to analyse the contaminant distribution when the pollutants source is positioned away from the thermal plume. However, during the experimental investigation, the point contaminant source was positioned only in 2 different locations within the room: on the floor and at 1,3m height. Due to that fact, not a clear explanation can be given on how the pollutants are distributed within the room when the pollutant release starts away from the heat sources. Thereby, future studies could investigate the contaminant distribution by locating the point contamination source in many different positions thus a better conclusion can be made

- Primarily this thesis had plans on creating the chart for ventilation effectiveness with different inlet temperatures. However, due to technical difficulties in the laboratory it could not be concluded. This could be another possibility of future studies where ventilation effectiveness is analysed with different supply temperatures.

- In this thesis the energy consumption for cooling and heating purposes is not taken into account. However, it would be interesting to create a chart which indicates the energy consumptions for the corresponding ventilation effectivenesses. This chart could be used as a guideline for choosing the desired ventilation effectiveness with minimum energy consumption. This could be conducted in future studies where there is possibility for cooling and heating cases.

-

Bibliography

Allard et al., 2007. Francis Allard, Hazim B. Awbi, Lars Davidson og Alois Schälin. *Computational fluid dynamics in ventilation design*. REHVA, 2007.

Ansys. Ansys. *ANSYS Fluent documentation*.

ASHRAE55, 2013. ASHRAE55. *Thermal Environmental Conditions for Human Occupancy*, 2013.

ASL, 2014. ASL. *Precision Thermometers F200 Series*, 2014. URL `https://www.instrumart.com/assets/ASL-f200-datasheet.pdf`.

Chen Q., 1995. Chen Q. *Comparison of different k-epsilon models for indoor air flow computations*. 1995.

Chen Zhang. Diffuse ceiling ventilation: Air distribution and thermal comfort. PhD thesis, Aalborg University, 2016.

Anna Diana Chodor og Piotr Paweł Taradajko. Experimental and Numerical Analysis of Diffuse Ceiling Ventilation. Master's thesis, Aalborg University, 2013.

Commission. European Commission. *2050 Energy Strategy*. URL `https://ec.europa.eu/energy/en/topics/energy-strategy/2050-energy-strategy`.

CR1752, 1999. CR1752. *CR 1752, Ventilation for buildings - Design criteria for the indoor environment*, 1999.

Danish Ministry of Energy, Utilities and Climate, May 2014. Danish Ministry of Energy, Utilities and Climate. *Strategi for energirenovering af bygninger*, 2014.

Daria et al., 2016. Zukowska-Tejsen Daria, Wolsing Marie, Grysbæk Malene og Hviid Christian Anker. *Field Study of Diffuse Ceiling Ventilation Performance in a Landscape Office*. 2016.

EN13779, 2007. EN13779. *EN 13779 Ventilation for non-residential buildings — Performance requirements for ventilation and room-conditioning systems*, 2007.

Fan et al., 2013. Jianhua Fan, Christian Anker Hviida og Honglu Yanga. *Performance analysis of a new design of office diffuse ceiling ventilation system*. 2013.

Fanger et al., 1988. P. O. Fanger, A. K. Melikov, H. Hanzawa og J. Ring. *Air Turbulence and Sensation of Draught*. 1988.

Horr et al., 2016. Yousef Al Horr, Mohammed Arif, Amit Kaushik, Ahmed Mazroei, Martha Katafygiotou og Esam Elsarrag. *Occupant productivity and office indoor environment quality: A review of the literature*. 2016.

Hviid og Terkildsen, **2012**. Christian Anker Hviid og Søren Terkildsen. *Experimental study of diffuse ceiling ventilation in classroom*. 2012.

Hviida og Svendsena, **2012**. Christian Anker Hviida og Svend Svendsena. *Experimental study of perforated suspended ceilings as diffuse ventilation air inlets*. 2012.

Hyldgaard et al., **1997**. Carl Erik Hyldgaard, M. Steen-Thoede og E.J. Funch. *Grundlæggende Klimateknik og Bygningsfysik*. Aalborg Universitet, 1997.

ICON. *ICON*. URL `http://icontestequipment.com/product/fluke-2287a/`.

INNOVA, **2016**. INNOVA. *Bruel And Kjaer 1302*, Bruel and Kjaer INNOVA AirTech Instruments, 2016. URL `https://www.testequipmentconnection.com/specs/Bruel_And_Kjaer_1302.PDF`.

Innova AirTech Instruments, **February 2005**. Innova AirTech Instruments. *Technical documentation 1412 Photoacoustic Field Gas-Monitor*. Innova AirTech Instruments, 2005.

ISO7730, **2005**. ISO7730. *Ergonomics of the thermal environment - Analytical determination and interpretation of thermal comfort using calculation of the PMV and PPD indices and local thermal comfort criteria (ISO 7730:2005)*, 2005.

Jacobs og Knoll, **2009**. Piet Jacobs og Bas Knoll. *Diffuce ceiling ventilation for fresh classroms*. 2009.

Martin Heine Kristensen og Jakob Søland Jensen. Impact of diffuse ceiling ventilation systems on indoor environmental quality in classrooms. Master's thesis, Aalborg University, 2015.

Kristensen et al., **2016**. Martin Heine Kristensen, Jakob Søland Jensen og Per Kvols Heiselberg. *Field study evaluation of diffuse ceiling ventilation in classroomduring real operating conditions*. 2016.

LumaSense technologies. LumaSense technologies. *Gas detection limits*. LumaSense technologies.

Mihai og Iordache, **2015**. Toderasc Mihai og Vlad Iordache. *Determining the indoor environment quality for an educational building*. 2015.

Mikeska og Fan, **2015**. Tomas Mikeska og Jianhua Fan. *Full scale measurements and CFD simulations of diffuse ceiling inlet for ventilation and cooling of densely occupied rooms*. 2015.

Nielsen et al., **2017**. Peter V Nielsen, Rasmus W Vilsbøll, Li Liu og Rasmus L Jensen. *Diffuse Ceiling Ventilation, Load Distribution and Ceiling Design*. 2017.

Nielsen, **2007**. Peter Vilhelm Nielsen. *Analysis and Design of Room Air Distribution Systems*. 13:6, 2007.

Nielsen, **2011**. Peter Vilhelm Nielsen. *The "Family Tree" of Air Distribution Systems*. Roomvent 2011, 2011.

Nielsen et al., 2013. Peter Vilhelm Nielsen, Tine Steen Larsen og Claus Topp. *Design methods for air distribution systems and comparison between mixing ventilation and displacement ventilation*. 2013.

Nielsen et al., 2015. P.V. Nielsen, R.W. Vilsbøll, L. Liu og R.L. Jensen. *Diffuse ceiling ventilation andthe influence of room height and heat load distribution*. 2015.

Parliament og the council of the European union, May 2010. The European Parliament og the council of the European union. *DIRECTIVE 2010/31/EU OF THE EUROPEAN PARLIAMENT AND OF THE COUNCIL of 19 May 2010 on the energy performance of buildings*. European union, 2010.

Ren et al., 2015. Shouhong Ren, Shuo Tian og Xiangyi Meng. *Comparison of Displacement Ventilation, Mixing Ventilation and Underfloor Air Distribution System*. 2015.

Srebric, 2011. Qingyan Chen & J. Srebric. *A Procedure for Verification, Validation, and Reporting of Indoor Environment CFD Analyses*. 2011.

Standard, 2007. Dansk Standard. *Indoor environmental input parameters for design and assessment of energy performance of buildings addressing indoor air quality, thermal environment, lighting and acoustics*. Dansk Standard, 2007.

Vilcekova et al., 2017. Silvia Vilcekova, Peter Kapalo, Ľudmila Meciarov, Eva Krídlová Burdová og Veronika Imreczeová. *Investigation of Indoor Environment Quality in Classroom - Case Study*. 2017.

Yu et al., 2015a. Tao Yu, Per Heiselberg, Bo Lei, Michal Pomianowski, Chen Zhang og Rasmus Jensen. *Experimental investigation of cooling performance of a novel HVAC system combining natural ventilation with diffuse ceiling inlet and TABS*. 2015.

Yu et al., 2015b. Tao Yu, Per Heiselberg, Bo Lei, Michal Pomianowski og Chen Zhangb. *A novel system solution for cooling and ventilation in office buildings:A review of applied technologies and a case study*. 2015.

Zhang et al., 2014. Chen Zhang, Heiselberg Per Kvols og Nielsen Peter Vilhelm. *Diffuse Ceiling Ventilation*. 2014.

Zhang et al., 2015a. Chen Zhang, Per Kvols Heiselberg, Michal Pomianowskia, Tao Yub og Rasmus Lund Jensena. *Integrated solution in an office room with diffuse ceiling ventilation and thermally activated building constructions*. 2015.

Zhang et al., 2015b. Chen Zhang, Martin Heine Kristensen, Jakob Søland Jensen, Per Kvols Heiselberg, Rasmus Lund Jensen og Michal Pomianowski. *Parametrical analysis on the diffuse ceiling ventilationby experimental and numerical studies*. 2015.

Part V

Appendix

A | Pressure drop experiment

In the present thesis, the investigation for the performance of this novel system of ventilation is performed by both experimental and numerical method. For the numerical investigation, it is necessary to define the inertial resistance and viscous resistance coefficient of the diffuse ceiling in the CFD model. These two parameters of the permeable ceiling determine the pressure drop between plenum and room and consequently the air flow pattern in the ventilated room. In addition to that, the supply air is released in plenum through a textile duct which means the air pattern in the plenum is influenced by the permeability and viscous resistance of the fabric material. In order to create a proper CFD model which can provide reliable predictions the porous properties of the textile duct material are needed to be defined too. In this Appendix A the pressure drop experiment for determining the previously mentioned coefficients will be presented and explained.

In order to obtain the coefficients of the porous materials it is necessary to conduct a pressure drop experiment. This experiment aims to log data of the pressure drop across the textile duct material and across the diffused ceiling panels for different air flow rates. After a quadratic regression analysis of the logged data the porous coefficients can be defined and then used as input to the CFD model.

The pressure drop can be measured by the use of the Digital micro manometer FC015 which can be seen in the Figure A.1. By connecting two tubes in the Digital micro manometer FC015 the pressure difference between the locations of the tubes is measured. Tubes for measuring the pressure drop across the fabric material have been placed inside the textile duct and plenum whereas tubes for measuring the pressure drop across the diffuse ceiling have been placed in plenum and room.

Figure A.1. FC015 Digital Micro manometer

For 15 different supply air flow rates, the pressure drop between fabric duct and plenum and also between plenum and room have been logged. Then the curves between pressure drop and superficial velocity can be plotted with their corresponding polynomials which are obtained after quadratic regression analyses. The superficial velocity is derived from the flow rate and cross sectional area as the below Equation A.1 states.

$$V_{sf} = \frac{q}{A} \tag{A.1}$$

Where:

V_{sf} - Superficial velocity $[m^3/(s \cdot m^2)]$
q - Flow rate $[m^3/s]$
A - Cross sectional area $[m^2]$

The pressure drop curve between textile duct and plenum can be seen in the Figure A.2 whereas the pressure drop curve between plenum and room is found in the Figure A.3. In the below Figures the corresponding polynomial of each curve can be seen too.

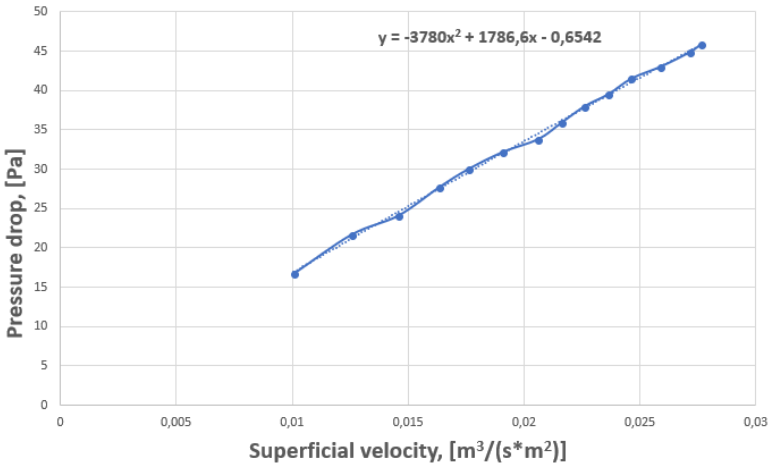

Figure A.2. Pressure drop between textile duct and plenum

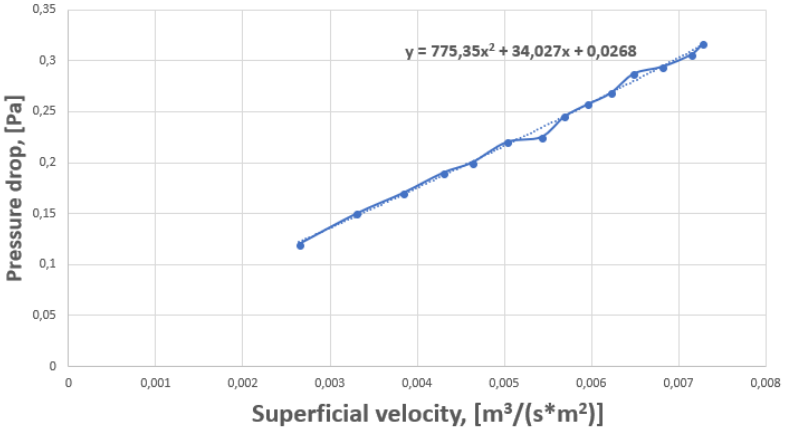

Figure A.3. Pressure drop between plenum and room

After the quadratic regression analysis the next step is to calculate the porous coefficients. In order to do that, the coefficients of the polynomials obtained by the quadratic regression analyses are used. The permeability α of a material can be calculated by the Equation $(A.2)$ and the inverse number of it equals with the the viscous resistance coefficient $\frac{1}{\alpha}$

$$\alpha = \frac{\mu \cdot \delta_X}{B} \tag{A.2}$$

Where:

α - Permeability $[m^2]$
μ - Dynamic viscosity of air $[Kg/(m \cdot s)]$
B - Coefficient from polynomial of form A· x^2+B· x+C $[Kg/(s \cdot m^2)]$
δ_X - Thickness of porous material [m]

By using the above Equation $(A.2)$ the permeability of the textile duct material and the viscous resistance of the porous ceiling can be calculated. The thickness of the fabric is 0,007m whereas the diffuse ceiling has a thickness of 0,025m. The B coefficient of each porous material corresponds to the second coefficient of each polynomial obtained by quadratic regression analysis. These coefficients can be seen in Figures A.2 and A.3. The calculated permeability of the textile duct material equals to 7·$10^{-11}m^2$ whereas the viscous resistance of the diffuse ceiling panels is equivalent to 7,6·10^7m^{-2}.

In addition to the permeabilities, inertial resistance coefficients of the porous materials need to be calculated. The below Equation $(A.3)$ shows how a inertial resistance coefficient of a porous material can be calculated.

$$C_2 = \frac{A \cdot 2 \cdot \delta_X}{\rho} \tag{A.3}$$

Where:

C_2 - Inertial coefficient $[m^{-1}]$
ρ - Density of air $[Kg/m^3]$
A - Coefficient from polynomial of form A· x^2+B· x+C $[Kg/(s \cdot m^2)]$
δ_X - Thickness of porous material [m]

By using the above Equation $(A.3)$ the inertial resistance coefficient of both porous materials, fabric and diffuse ceiling panels can be calculated. The A coefficient of each porous material corresponds to the first coefficient of each polynomial obtained by quadratic regression analysis. These coefficients can be seen in Figures A.2 and A.3. The calculated inertial coefficient of the fabric material equals to 8,8·10^5m^{-1} whereas for the porous ceiling equals to 50635m^{-1}. These calculated permeabilities and inertial resistances of both porous materials, fabric and diffuse ceiling are used as input boundaries in the numerical model for obtaining reliable predictions.

B | Experimental equipment

B.1 Pressure measurements

In order to control the supply flow rate to the room two Debro Meerbush manometers were used. One of these manometers can be seen in Figure B.1. The first manometer was connected with rubber pipes to an orifice plate joined to supply duct whereas the second manometer was connected with the same way to the exhaust duct. By reading the pressure from the manometers the supply flow rate could be adjusted as desired.

Figure B.1. Debro Meerbush manometer

B.2 Power measurements

To define with accuracy the total heat load of the system, RKT-2 voltage regulators connected with copper wires to HEWa-21 watt-meters were used. A combination of a voltage regulator and watt-meter is shown in Figure B.2. This allowed to read the actual power output in watts of each heat source placed in the room at any time.

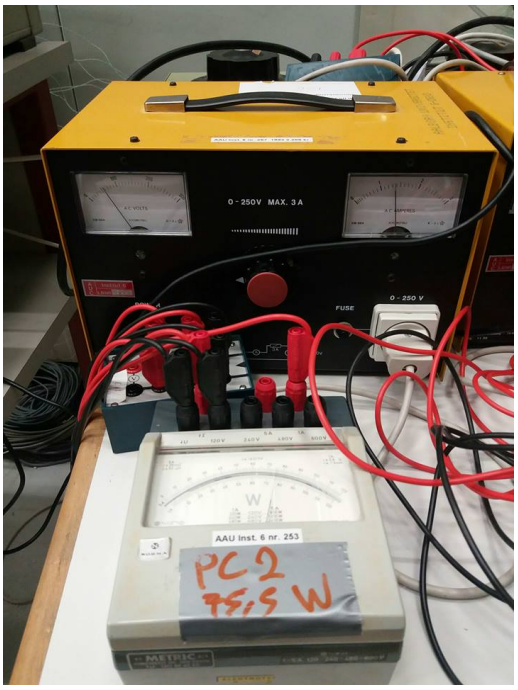

Figure B.2. RKT-2 voltage regulator combined with a HEWa-21 watt-meter

B.3 Airflow rate measurement

Nitrous oxide known as N_2O was used as tracer gas during the experimental measurements for representing pollutants in the room. The bottle of N_2O gas was connected to a manometer to adjust certain amount of N_2O delivered to room as it seems in Figure B.3. The airflow rate of tracer gas was controlled by a flowmeter which was connected to the manometer with rubber pipes. In Figure B.4 the D10A3239N flowmeter used for controlling the N_2O flow rate can be seen.

Figure B.3. N_2O bottle combined with a manometer

Figure B.4. D10A3239N flowmeter

B.4 Tracer gas measurement

As shown in Figure, tubes used to measure tracer gas concentration in the room were connected to two Multipoint Sample and Dozer devices type 1303. The concentration data were analysed by Tracer Gas Monitoring system and then logged in the PC. Each of these devices has six channels and it takes around 40 seconds to analyse the concentration in each channel.

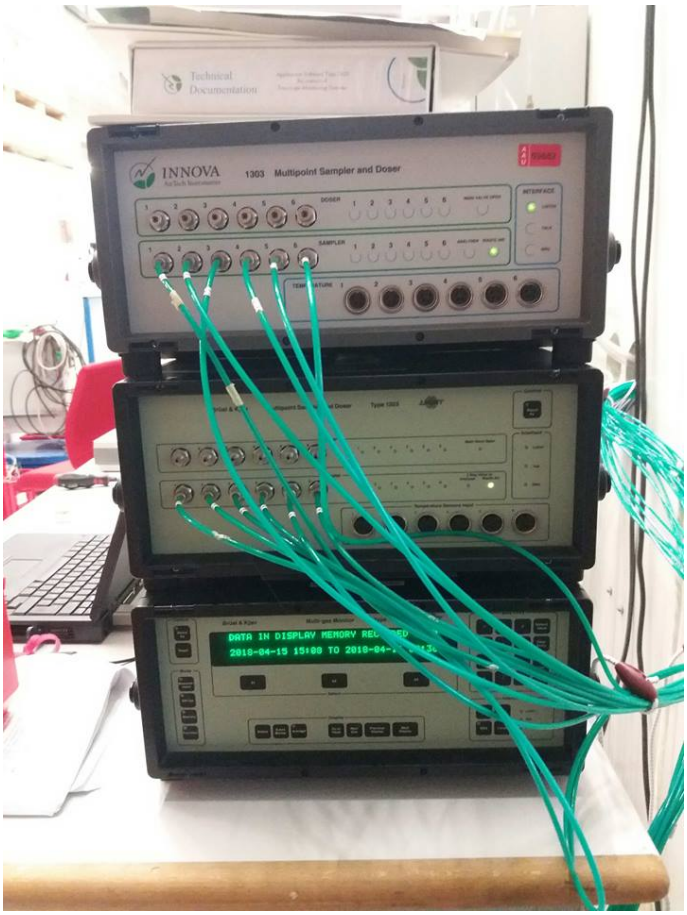

Figure B.5. Multipoint Sample and Dozer device type 1303

C | Calibration of equipment

C.1 Calibration of thermocouple

In this experiment K-type thermocouples were chosen as presented in the Figure C.1 below. Type K thermocouple consists of Chromel-Alumel, two dissimilar electrical conductors which form electrical junctions while differing in temperatures. Different temperatures generate different voltages due to thermoelectric effect where voltage is created because of different temperatures at each side of electrical conductor.

Figure C.1. K type thermocouple where white wire is Alumel (-) and green is Chromel (+)

K-type thermocouple is the most common type which is used for general purposes due to its low price and a wide variety of temperatures that it can measure from -200°C to +1350°C. Furthermore, its sensitivity is approximately $41\mu V/$°C

C.1.1 Calibration of thermocouple

In order to calibrate thermocouples a constant source of temperature needs to be used. Isocal 6 Venus 2140B was used to keep a constant temperature where the thermocouples were put inside and voltage readings were logged by Fluke Helios Plus 2287A data logger. To read precisely the temperature inside the Isocal device digital precision thermometer ASL F200 was used where its probe was put inside the Isocal device. Furthermore, KAYE K170-6 Ice reference point equipment was used to have reference point of 0°C from which the voltage was measured.

Figure C.2. ISOCAL 6 VENUS 2140B

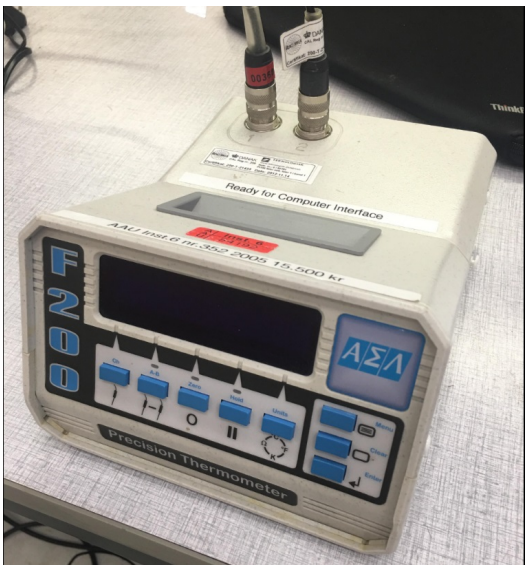

Figure C.3. ASL F200 Precision Digital Calibration Thermometer

Figure C.4. Fluke Helios Plus 2287A data logger [ICON]

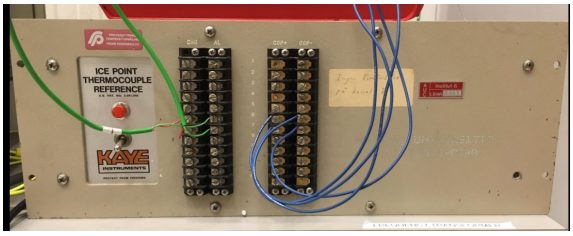

Figure C.5. KAYE K170-6 ice point reference

While changing the temperature in the Isocal device all thermocouples respond with different voltage output due to that each thermocouple has its own polynomial to represent that change. Figure C.6 below presents the generation of 2nd order polynomial for one thermocouple. In the below graph y-axis is the temperature difference (ΔT) between reference thermocouples in compensation box and Isocal device and x-axis is the voltage output in microvolts (mV).

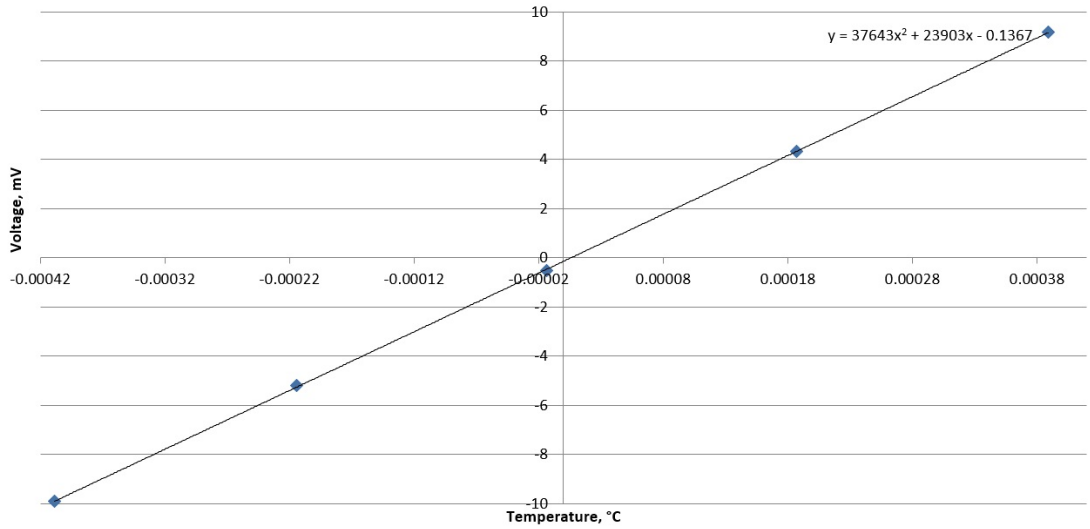

Figure C.6. Generation of thermocouple polynomial

Instead of variable 'x' voltage is input in the polynomial and the corresponding temperature can be calculated. An example of is presented in the Table C.1 below. It seems that the specific thermocouple is well calibrated since can read the same temperature as the precision thermometer with minor deviations.

Table C.1. Comparison between precision thermometer and thermocouple temperature

Precision thermometer temperature [°C]	Measured by thermocouple temperature [°C]	Difference [°C]
10.60	10.61	0.009
15.30	15.25	-0.048
20.00	20.03	0.033
24.84	24.84	0.003
29.67	29.66	-0.007

C.2 Anemometer calibration

For this experiment hot-sphere anemometers were used to measure air velocity in the room. A hot-sphere anemometer is shown in Figure C.7.

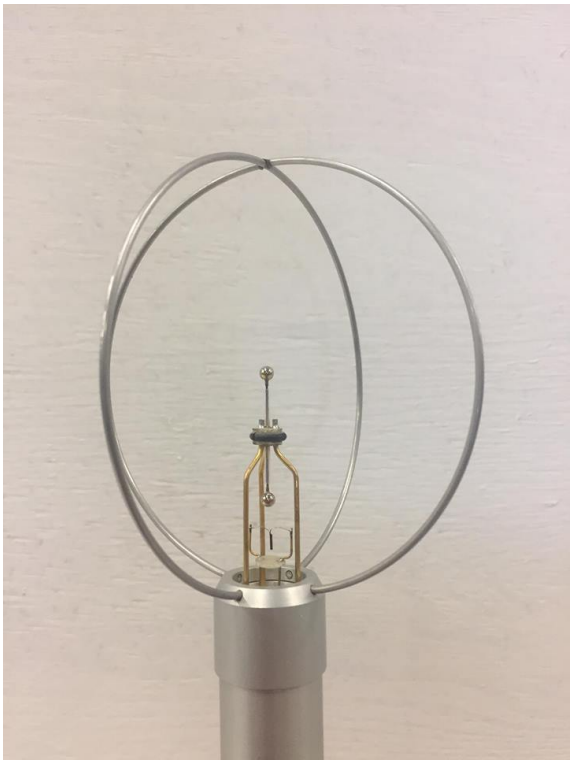

Figure C.7. Hot-sphere anemometer

Hot-sphere anemometers is the most commonly used anemometer for measuring air velocity in the room as it is able to measure very low air velocities with high precision. Since air velocities in the room are sought to be kept in range of 0-0,2 m/s in regards to thermal comfort.

C.2.1 Calibration of anemometer

To calibrate the hot-sphere anemometers a controllable source of constant air velocity must be used. In order to fulfil this purpose a jet wind tunnel is used. The jet wind tunnel is a tunnel fitted with a fan, an orifice plate and 2 filter boxes to ensure laminar flow at the "mouth" of the tunnel. The jet wind tunnel is shown in Figure C.8.

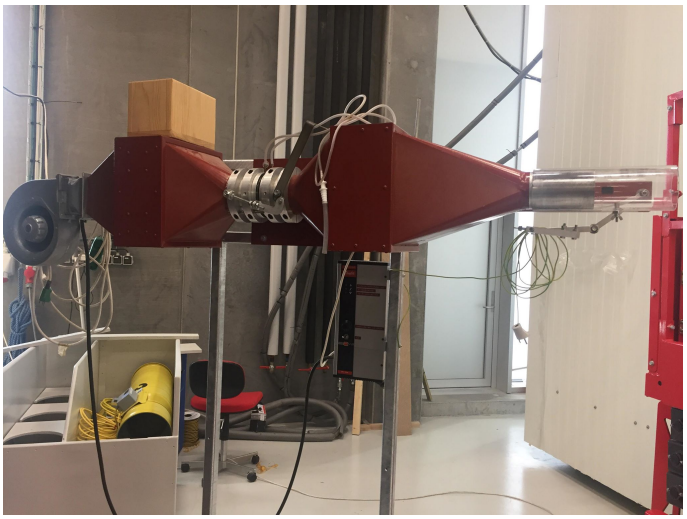

Figure C.8. Jet wind tunnel

The anemometers are placed 1 at a time at the "mouth" of the tunnel on a metal "arm" to hold it in place. The anemometer is then connected to the comfort sense where both are shown in Figure C.9 connected to the anemometer cables.

Figure C.9. Comfortsense connected to the anemometer cables.

The voltage from the hot-sphere anemometer is logged by the computer connected to the comfortsense. 8 air velocities were checked for the hot-sphere anemometers ranging from 0 to 0,4 m/s. To create the polynomials for calculating the air velocity from the voltage outputs of the anemometers the logged voltage is compared with the velocity set by the

jet wind tunnel creating a graph as shown in Figure C.10. In the below graph the y-axis and x-axis represent the air velocity (cm/s) and voltage (V) respectively.

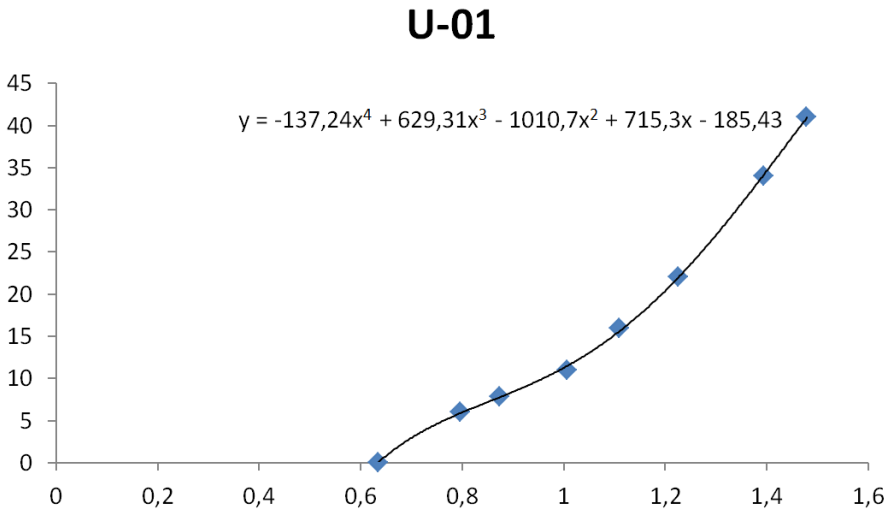

Figure C.10. Generation of anemometer polynomial for anemometer U-01

C.3 Control test of Gas-Monitor

To measure the concentration and distribution of the tracer gas in the hot box the Innova type 1412 Photoacoustic Field Gas-Monitor was used. Additionally the Innova and B & K type 1303 Multipoint Sampler and Doser were used too, as the name indicates, to enable the Innova type 1412 Photoacoustic Field Gas-Monitor to sample from multiple points simultaneously without having to exchange the sampling tube(s) to the Monitor. The Innova type 1412 Photoacoustic Field Gas-Monitor as well as the Innova and B & K type 1303 Multipoint Sampler and Doser are shown in Figure C.11. Technical documentation for the Innova type 1412 Photoacoustic Field Gas-Monitor [Innova AirTech Instruments, 2005] and Gas Detection limits by LumaSense Technologies was used for this control test [LumaSense technologies].

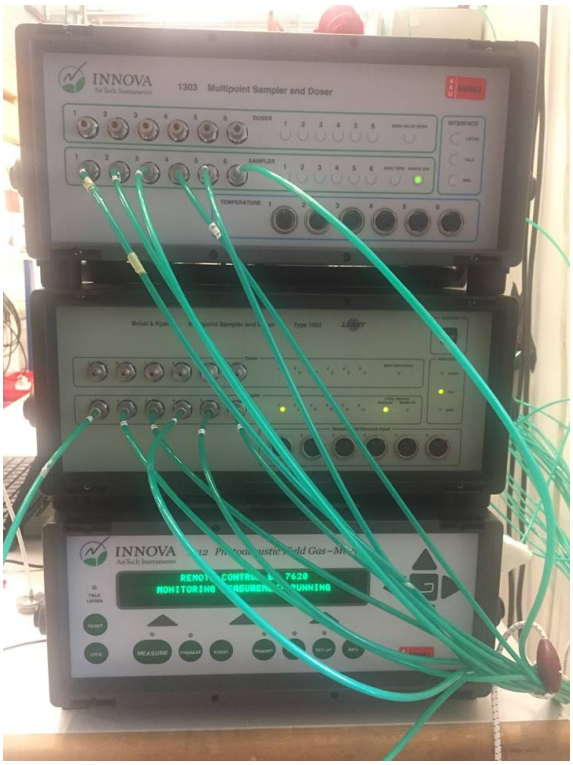

Figure C.11. The Innova type 1412 Monitor and Innova and B & K type 1303 Samplers as set-up for the experiments

The Innova type 1412 Monitor measuring principle is based on Infra-red Photo Acoustic Spectroscopy which in short works by pulsating an Infra-red light through an optical filter into a chamber containing the sampled gas in which the pulsating Infra-red light clashes with the particles of the gas and the resulting vibrations are recorded by microphones. This frequency is then translated into the reading the Monitor is calibrated for the particular optical filter(s) in use. There are 6 slots for optical filters in the instrument and 5 of them can be changed and recalibrated according to the need of the user. The 6th optical filter is not interchangeable and is the water vapour filter which is used to filter out the "noise" generated by the humidity of the sampled air. A scheme of the Monitor's construction is shown in Figure C.12. Furthermore the Innova type 1412 Monitor should be preheated to about 40-45 °C before conducting any calibration or measurement as the

core temperature of the instrument influences the readings.

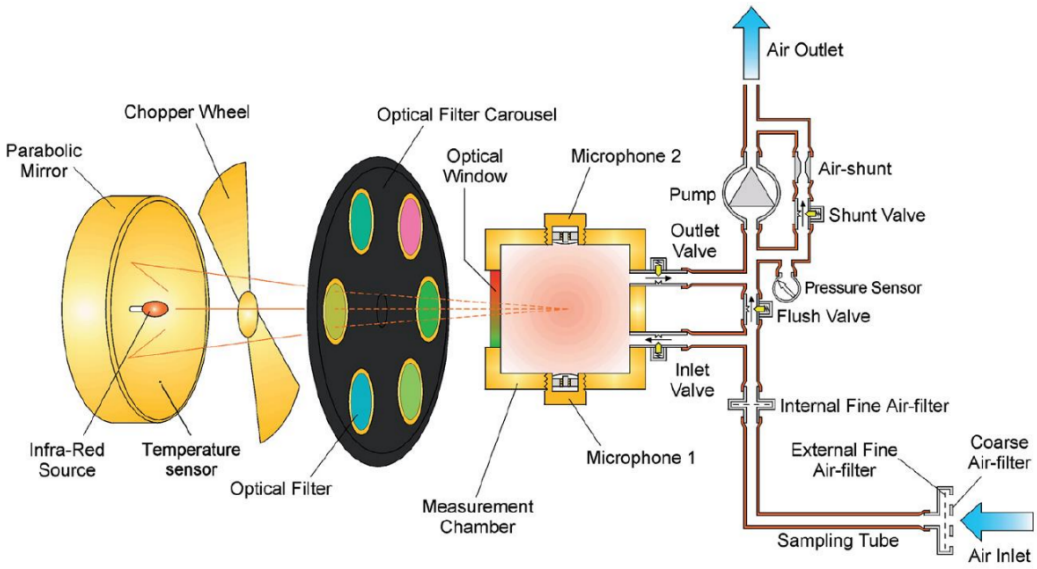

Figure C.12. System schematic principle for the Innova 1412 Monitor [LumaSense technologies]

Control test

Due to the time frame of the measurements a control test of the Innova 1412 Monitor was conducted instead of a full calibration. The control test for the Innova 1412 Monitor is set-up similar as for a full calibration. The principle of the set-up for the control test is shown in Figure C.13.

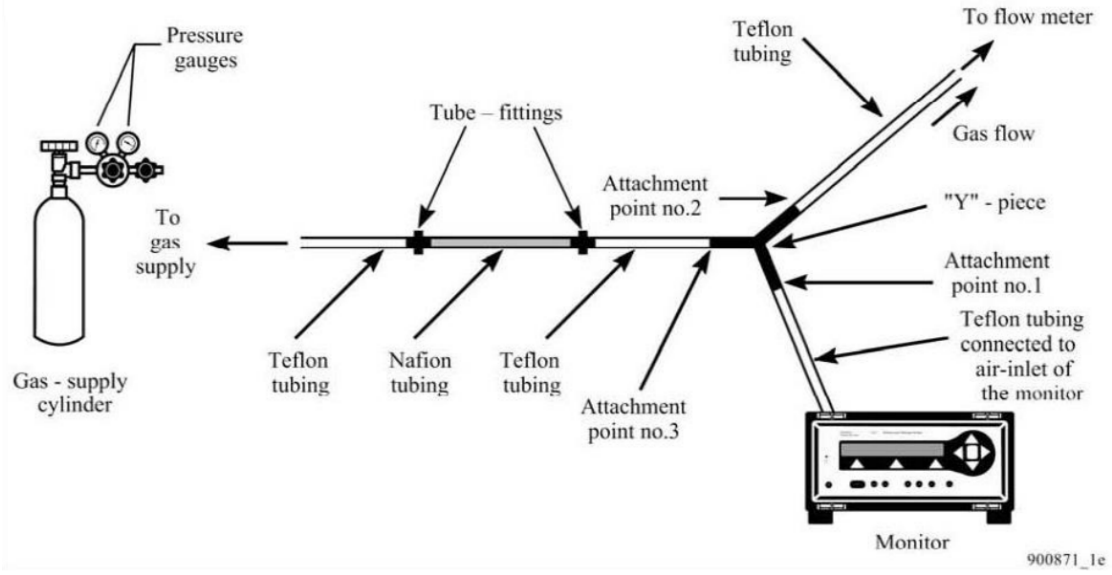

Figure C.13. Setup principle for calibration and control test of the Innova 1412 Monitor [Innova AirTech Instruments, 2005]

As shown in Figure C.13 a pressure gauge connected to a gas supply which for the control

test was pure N_2 gas and a control gas (0.1% N_2O and 99.9% N_2 mixture), via a Teflon tubing to a Nafion tube. The Nafion tubing is shown in Figure C.14.

Figure C.14. Example of nafion tubing

The Nafion tubing is used to humidify the air as the instrument cannot properly evaluate dry gas. The Nafion tube is permeable to water vapour so a wet towel is wrapped around the Nafion tubing to humidify the air. The Nafion tubing is then connected via another Teflon tube to a "Y"-piece. The "Y"-piece is connected via Teflon tubing to the Monitor through one leg and connected via Teflon tubing to a flowmeter through the other. The set-up is connected like this because if the gas was connected directly to the Monitor the pressure would break the instrument. The flowmeter is connected so that it is made sure that the Monitors pump does not suck in air as well as the gasses used for the control test. This is made sure by releasing enough pressure from the gas supply so that the flowmeter does not drop to zero when the Monitor is sampling the gas thereby preventing ambient air to interfere with the control test.

The results from the control test, with the pure N_2 gas and a control gas (0,1% N_2O and 99,9% N_2 mixture), are shown in Table C.2.

Table C.2. Results from the control test

Actual value [ppm]	**Measured Value [ppm]**
0	5.575
100	856.518

From the results shown in Table C.2 a conversion formula for the Innova 1412 Monitor can be created in the same fashion as for thermocouples and anemometers. More measurement points would be preferable but the control gas (0,1% N_2O and 99.9% N_2 mixture) was the only one available in the lab. The conversion formula for the Monitor is shown in Figure C.15.

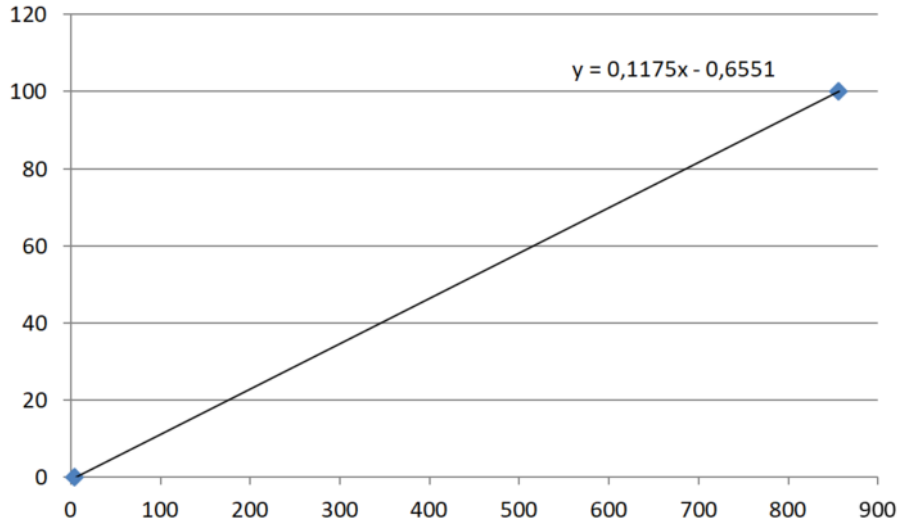

Figure C.15. Conversion formula for the Innova 1412 Monitor with Actual value along the y-axis and measured values along the x-axis

D | Case example

Table D.1. Case 1-transmission losses through envelope

Case 1	Structure	Temp Outside [°C]	Temp Room [°C]	U-value $[W^2/m \cdot K]$	Area $[m^2]$	Loss [W]
Transmission Losses	Wall E	22.0	22.0	8.00	8.9804	-4
	Wall W	21.1	22.0	0.18	9	-1
	Wall N	21.1	22.0	0.18	10.5	-2
	Wall S	21.0	22.0	0.18	10.5	-2
	Plenum E	22.0	22.0	8.00	3.7782	-2
	Plenum W	21.1	22.0	0.18	3.834	-1
	Plenum N	21.1	22.0	0.18	4.473	-1
	Plenum S	21.0	22.0	0.18	4.473	-1
	Window	22.0	22.0	8.00		0
	Floor	21.0	22.0	0.18	12.006	-2
	Carpet	21.0	22.0	0.18	2.952	-1
	Ceiling	21.9	22.0	0.18	15.12	0
	Dif_Wall E	22.0	22.0	8.00	0.09	0
	Dif_Wall W	21.1	22.0	0.18	0.09	0
	Diff_Wall N	21.1	22.0	0.18	0.105	0
	Dif_Wall S	21.0	22.0	0.18	0.105	0
				$\sum$	86.01	-15

Table D.2. Case 1-ventilation losses

Ventilation Losses	Parameters		Loss [W]
	T_Supply, [°C]	14.4	-845.0
	T_Exhaust, [°C]	22.0	
	Volumetric flow, $[m^3/h]$	326	

E Draught rate at specific heights

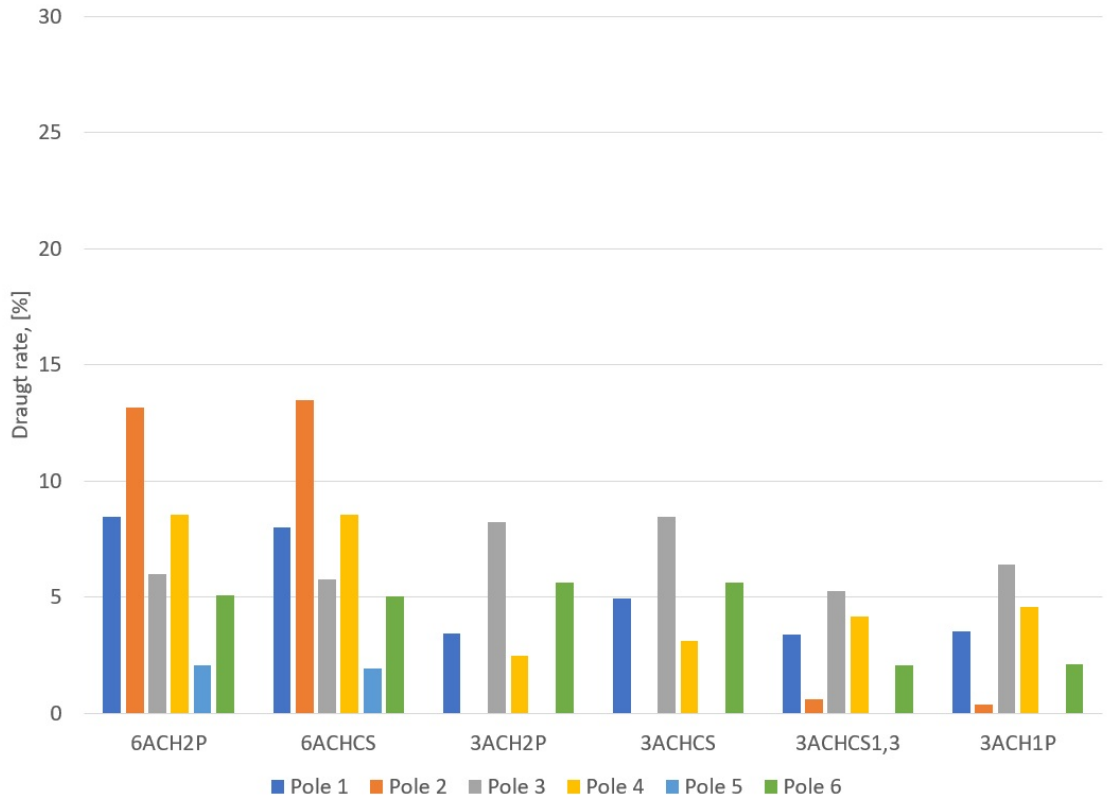

Figure E.1. Calculated draught rates at 0.6m height for each case and each pole

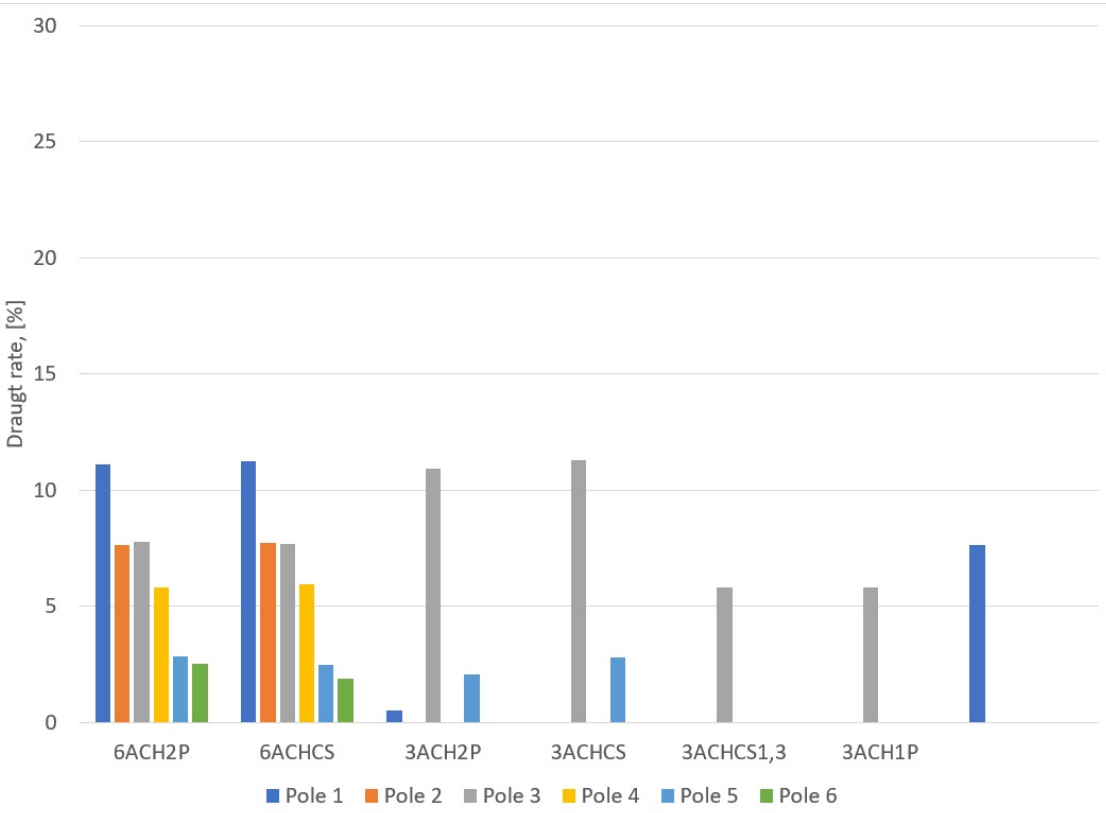

Figure E.2. Calculated draught rates at 1.7m height for each case and each pole

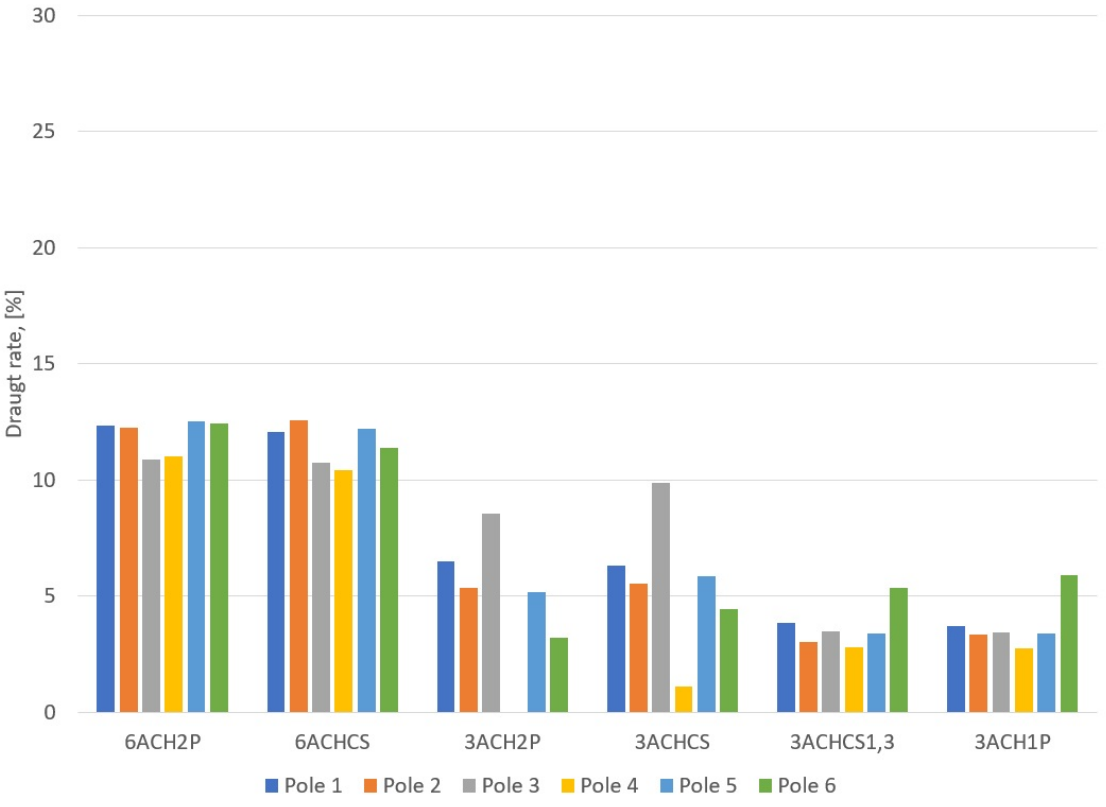

Figure E.3. Calculated draught rates at 2.2m height for each case and each pole

F | Resimulation of case 1

In this Appendix F the results of the re-simulation for case 1 will present. As mentioned in the Chapter 8 energy and mass unbalance occurred during the experiments that are why the results obtained from the simulation had deviations from the experimental data. In order to correct the temperatures in the CFD simulation, it is necessary to apply an energy source in the room which is equal to the energy unbalance rate happened during the experiments. In addition to that, to obtain correct predictions regarding the N_2O concentration the flow rate of the contaminants needs to be reduced according to the rate of mass unbalance.

The energy and mass unbalance occurred during the experiment for case 1 can be seen in the Table F.1.

Table F.1. Energy and N_2O mass unbalance rate occurred during the experiment for case 1

N_2O mass unbalance rate, [%]	Energy unbalance rate [%]
24.6	14.0

To obtain temperatures and pollutants concentration close to measurements an additional energy source and reduced supply flow rate of N_2O are used in the model as presented in the Table F.2.

Table F.2. Energy source and N_2O flow rate supplied to room used for the simulation correction

New N_2O flowrate, [l/h]	Extra energy source, [W/m^3]
31	-1.7

The comparison between temperatures measured during the experiment and calculated by the corrected numerical model are presented in the Figures F.1 - F.6 below.

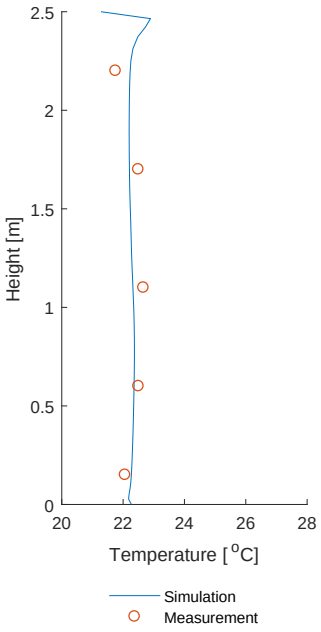

Figure F.1. Temperatures along pole 1

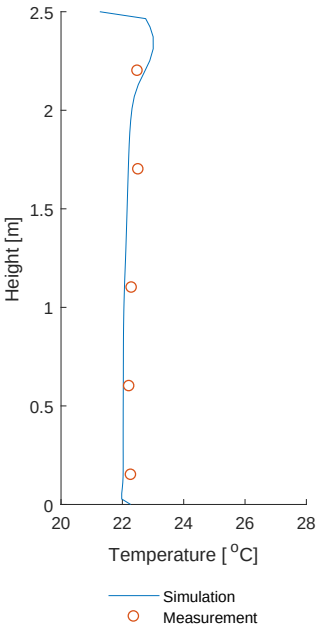

Figure F.2. Temperatures along pole 2

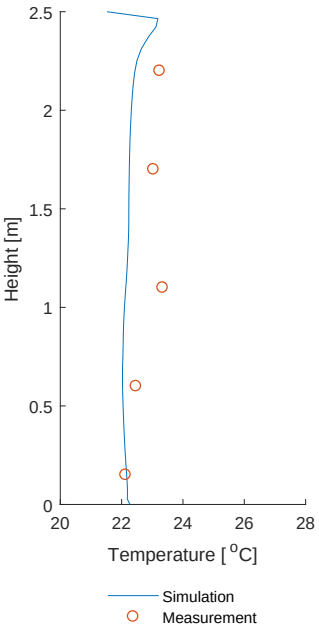

Figure F.3. Temperatures along pole 3

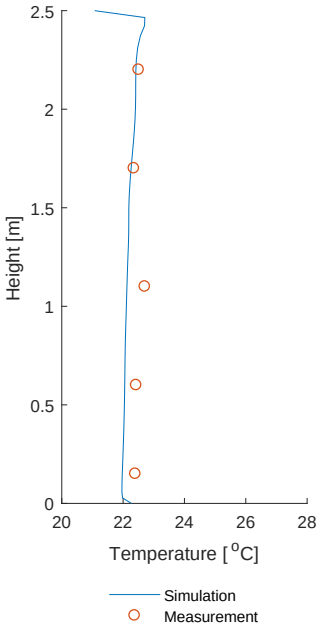

Figure F.4. Temperatures along pole 4

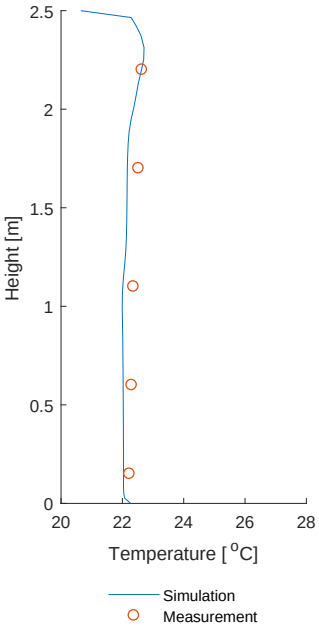

Figure F.5. Temperatures along pole 5

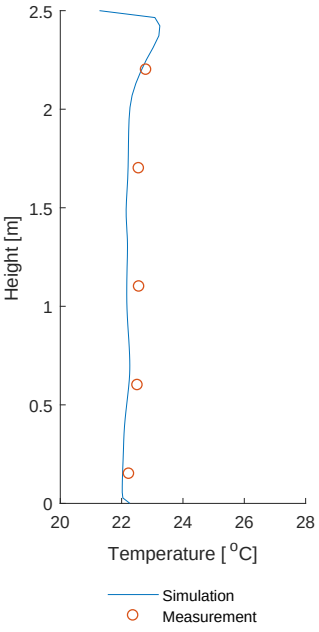

Figure F.6. Temperatures along pole 6

The comparison of temperature distribution in the plenum is presented in the Figure F.7

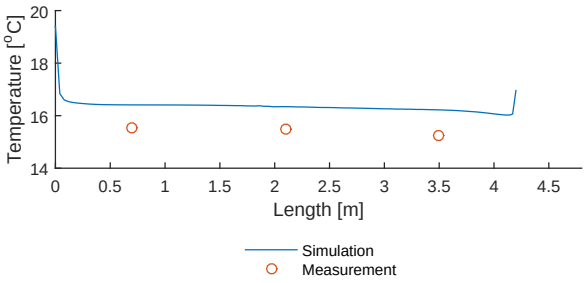

Figure F.7. Comparison of temperature distribution in plenum

From the Figures F.1 - F.6 it can be noticed that the numerical model estimates much more accurately temperature distribution along all poles. After the input of the extra energy source in the room the predictions regarding temperatures are closer to the measured ones. There are minor deviations between temperatures of corrected CFD model and experiment but is acceptable considering all the assumptions which are made when calculating the energy unbalance.

In addition to that, the temperatures in plenum calculated by the corrected CFD model is much closer to the measured ones compared to the previous simulation. The temperatures in the plenum deviate around 1 °C from these ones obtained from the experiment. However the improvement is obvious since before the correction of the model the deviations reached around 3 °C.

The comparison between air velocities measured during the experiment and calculated by the corrected numerical model are presented in the Figures F.8 - F.13 below.

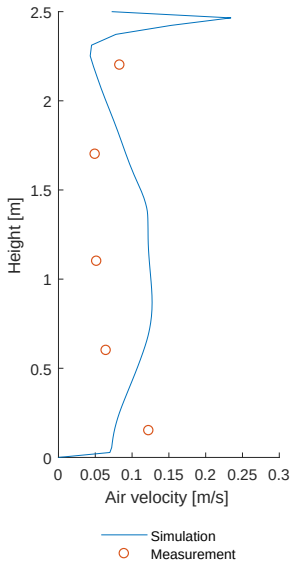

Figure F.8. Velocities along pole 1

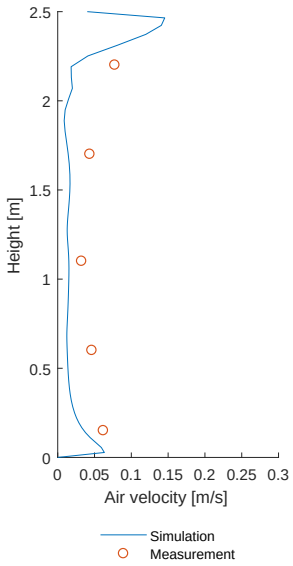

Figure F.9. Velocities along pole 2

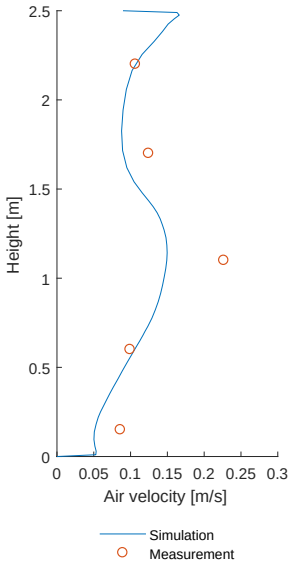

Figure F.10. Velocities along pole 3

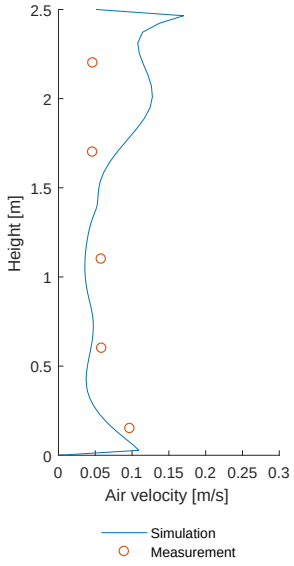

Figure F.11. Velocities along pole 4

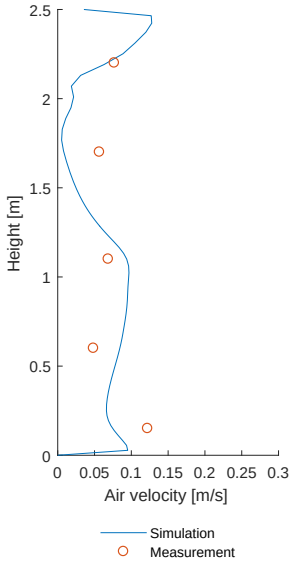

Figure F.12. Velocities along pole 5

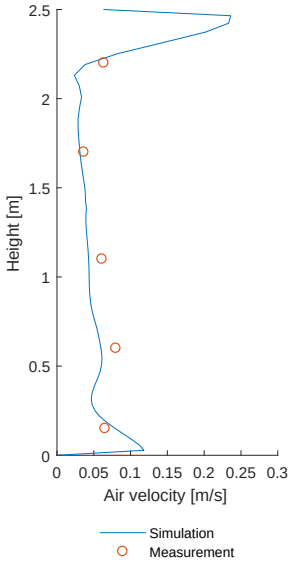

Figure F.13. Velocities along pole 6

Figures F.8 - F.13 show that corrected numerical model estimates the tendency of air velocities for most of the measurement points as the previous one. However if compare the previous and corrected simulation minor differences on air velocities will be noticed. These differences were expected since the extra heat applied in room consequently affects the air velocities within the room but they assumed negligible since not any significant difference is observed.

The comparison between N_2O measured during the experiment and calculated by the numerical model are presented in the Figures F.14 - F.19.

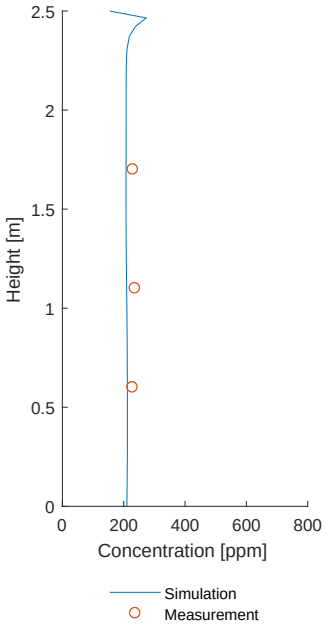

Figure F.14. N_2O along pole 1

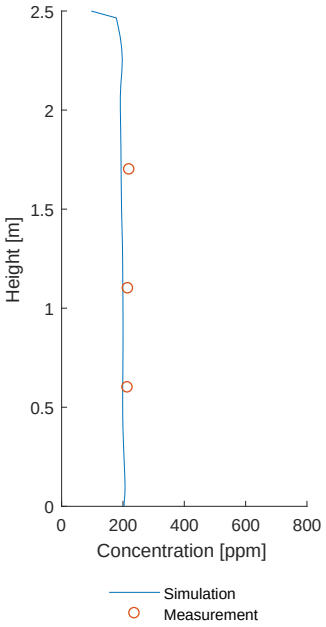

Figure F.15. N_2O along pole 2

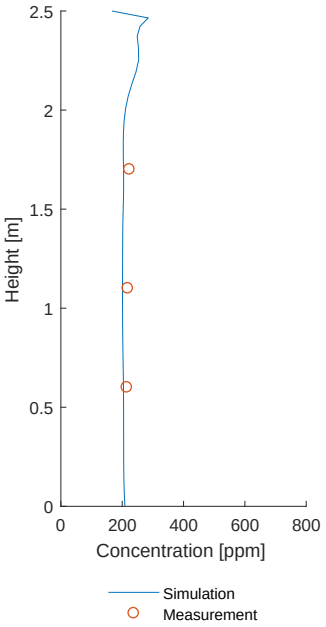

Figure F.16. N_2O along pole 3

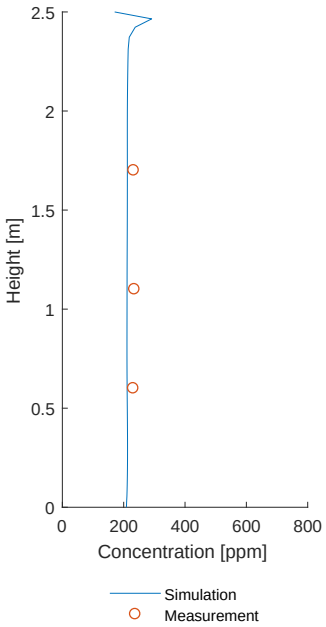

Figure F.17. N_2O along pole 4

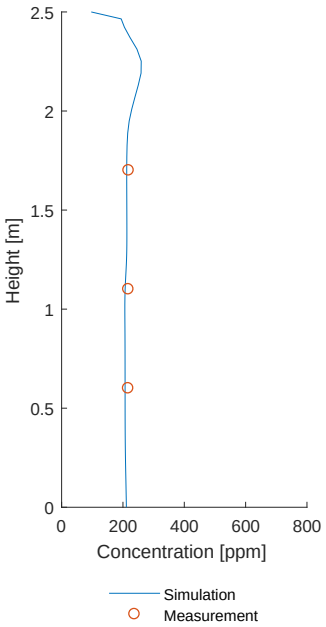

Figure F.18. N_2O along pole 5

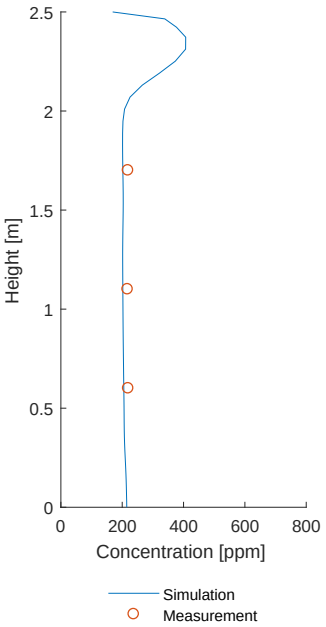

Figure F.19. N_2O along pole 6

The comparison between N_2O concentrations at inlet, plenum points, fabric points and outlet for can be seen in Figure F.20 and Figure F.21.

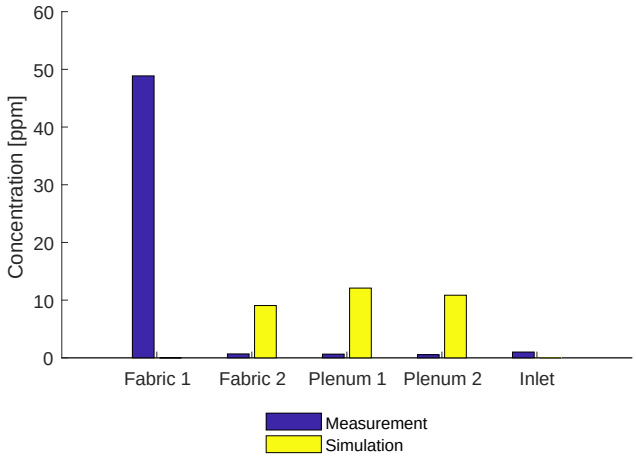

Figure F.20. Comparison of N_2O concentration at certain locations

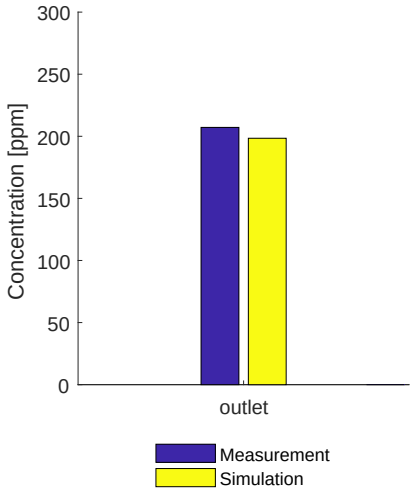

Figure F.21. Comparison of N_2O concentration at outlet

Figures F.14 - F.19 show that the corrected CFD model estimates accurately the N_2O distribution in the room. After reducing the supply contamination flow rate by 24% the calculated concentrations are very close to the experimental data. This means that the model can estimate accurately the N_2O concentration in such a case if model and experiment have the same boundary condition regarding contaminants.